

Reynolds-Averaged Navier–Stokes Simulations of Unyawed and Yawed Rotating Wheels

Ali Alsudani

Faculty of Aerospace Engineering



MASTER THESIS

*submitted in partial fulfilment of
the requirements for the award of the degree of*

Master of Science in Aerospace Engineering

Author:

Ali Alsudani - 4462769

Supervisor:

Dr. Davide Modesti

Koenigsegg:

Santiago Hernandez Medina

January 5, 2024



¹The cover image being a picture of the Koenigsegg Jesko retrieved from <https://wallpaperaccess.com/koenigsegg-jesko>
[Date accessed: 04-02-2022]

Preface

Dear reader,

This thesis marks the end of my academic career. This journey at the TU Delft began with an interest in sports cars since childhood. Therefore, I feel honoured that I can obtain my Master's degree working together with Koenigsegg. This was a dream come true.

I would like to express my deepest gratitude to my supervisors Dr. Davide Modesti and Santiago Hernandez Medina for their continuous guidance, availability and understanding. I am grateful for everything that they have done for me. I know that my journey had its major ups and downs. However, it was always reassuring knowing they were there for me when I needed them.

Furthermore, I want to thank my family and friends for believing in me and for their continuous support and love. We have made many great memories over the years and overcame obstacles together. You were always there when I needed you.

Finally, to my wife, without you this thesis would not have been what is now. From the sacrifices you had to make for me so I could pursue this thesis and obtain my degree to your endless love and support, which has pushed me to finish this. I would like to express my deepest gratitude for everything you do for me and I cannot thank you enough.

*Ali Alsudani
January 5, 2024, Delft*

Abstract

Aerodynamics has been an important aspect of the automotive industry for decades, as understanding its principles plays a key role in the design of modern vehicles. The aerodynamic forces affecting the vehicle directly impact its fuel consumption, performance, and stability, with a notable contributing factor being the wheels. They are responsible for up to 25% of the drag in the case of a general passenger car and up to 30%-50% for an open-wheeled race car. Therefore, understanding the aerodynamic characteristics of a wheel during the design process is essential.

In this research, the aerodynamic characteristics of an isolated rotating wheel in contact with the ground will be investigated using RANS simulations. Open-source software OpenFOAM is used to simulate the isolated rotating wheel and the mesh is generated using cfMesh. An extensive validation of the numerical method is carried out, including 2D isolated stationary and rotating cylinder simulations at a Reynolds number of 200 and 2D isolated stationary cylinder simulations at a Reynolds number of 1 000 000. Furthermore, a laminar simulation of a 3D rotating cylinder in contact with the ground is carried out as well. The wheel model used in this work is the "Fackrell A2" for which extensive literature is available. The region in contact with the ground is modelled using a step size approach to avoid highly skewed cells that will diverge the simulations or influence the accuracy.

Firstly, the sensitivity of the step size, mesh fineness and domain size is assessed and then unyawed wheel simulations are performed utilising the following three turbulence models: $k - \omega$ SST, Realizable $k - \varepsilon$ and Spalart-Allmaras. Among these models, the Realizable $k - \varepsilon$ model is chosen to investigate further the effect of yawing the wheel and the Reynolds number on the aerodynamic force coefficients, pressure coefficient distribution along the centerline and wake characteristics. The yaw effect is investigated by yawing the wheel up to 10° in increments of 2° and the Reynolds number effect is investigated for the Reynolds number range of 10 000 — 1 000 000.

The results show that yawing the wheel yields a fairly linear increase in C_D and C_S . A yaw angle of 10° shows an increase of approximately 16.4% in C_D . Regarding the C_L , only a significant increase of approximately 35.8% is observed when going from a yaw of 4° to 6° . Furthermore, the wake becomes asymmetric with increasing yaw. The vortex at the leeside on the ground becomes bigger while the vortex at the windward side becomes smaller. Additionally, a new vortex in the upper part of the wake further downstream is formed and the wake becomes shorter.

Increasing the Reynolds number, the value of C_D decreases and C_L stays approximately the same. Moreover, the Reynolds number seems to affect the pressure peaks upstream and downstream of the contact patch. A lower value results in larger magnitude peaks. Finally, in the investigated Reynolds number range the wake structures are the same. However, the wake is bigger when the Reynolds number is smaller and asymmetry was observed in the wake for $Re_D = 1\,000\,000$, which can be caused by the asymmetry of the wheel.

Contents

| | |
|--|-------------|
| Preface | I |
| Abstract | II |
| List of Figures | V |
| List of Tables | VIII |
| Abbreviations | IX |
| List of Symbols | X |
| 1 Introduction | 1 |
| 1.1 Problem Statement | 2 |
| 1.2 Thesis Outline | 2 |
| 2 Literature Review: Aerodynamics of Bluff Bodies | 3 |
| 2.1 Flow Past a Stationary Cylinder | 3 |
| 2.2 Flow Past a Rotating Cylinder | 6 |
| 2.3 Flow Past a Stationary Cylinder in Ground Effect | 10 |
| 2.4 Flow Past a Rotating Cylinder in Contact with the Ground | 11 |
| 3 Literature Review: Aerodynamics of an Isolated Rotating Wheel | 13 |
| 3.1 C_p Distribution | 13 |
| 3.1.1 Stationary vs Rotating | 13 |
| 3.1.2 Experiments vs Simulations | 14 |
| 3.2 Wake Characteristics | 16 |
| 4 Literature Review: Modelling of Rotating Wheels | 24 |
| 4.1 Modelling of a Detailed Rotating Wheel | 24 |
| 4.2 The Effects of Simplifications | 27 |
| 4.2.1 Modelling of the Contact Patch | 28 |
| 4.2.2 Influence of the Wheel Hub and Shoulder Geometry | 28 |
| 5 Numerical Methodology | 30 |
| 5.1 Reynolds-Averaged Navier-Stokes | 30 |
| 5.1.1 Spalart-Allmaras | 32 |
| 5.1.2 Realizable $k - \varepsilon$ | 33 |
| 5.1.3 $k - \omega$ SST | 34 |
| 5.2 OpenFOAM | 35 |
| 5.2.1 Time Schemes | 35 |
| 5.2.2 Gradient Schemes | 35 |
| 5.2.3 Divergence Schemes | 35 |
| 5.2.4 Laplacian Schemes | 36 |
| 5.2.5 Surface Normal Gradient Schemes | 36 |
| 5.3 CfMesh | 37 |
| 5.4 Solver Validation | 37 |
| 6 Wheel Simulations | 46 |
| 6.1 Geometry | 46 |
| 6.1.1 Wheel | 46 |
| 6.1.2 Contact Patch | 47 |
| 6.2 Mesh and Grid Sensitivity | 49 |

| | | |
|----------|---|------------|
| 6.3 | Domain Sensitivity | 51 |
| 6.4 | Boundary and Initial Conditions | 53 |
| 6.5 | Numerical Schemes and Solver Settings | 56 |
| 6.6 | Turbulence Models | 59 |
| 6.7 | Yawed Wheel | 63 |
| 7 | Results | 65 |
| 7.1 | Yawed Wheel | 65 |
| 7.1.1 | Force Coefficients | 66 |
| 7.1.2 | C_p Distribution | 68 |
| 7.1.3 | Streamlines | 69 |
| 7.1.4 | Q-criterion | 73 |
| 7.1.5 | $C_{p_{total}}$ Fields | 74 |
| 7.1.6 | Velocity Fields | 76 |
| 7.2 | Effect of the Reynolds Number | 82 |
| 7.2.1 | Force Coefficients | 82 |
| 7.2.2 | C_p Distribution | 83 |
| 7.2.3 | Streamlines | 84 |
| 7.2.4 | Q-criterion | 88 |
| 7.2.5 | $C_{p_{total}}$ Fields | 89 |
| 7.2.6 | Velocity Fields | 91 |
| 8 | Conclusion and Recommendations | 98 |
| 8.1 | Conclusion | 98 |
| 8.2 | Recommendations | 99 |
| | Bibliography | 100 |

List of Figures

| | | |
|------|--|----|
| 1.1 | The drag and rolling resistance plotted against vehicle velocity in km/h for a typical passenger car [2] | 1 |
| 2.1 | von Kármán vortex street [16] | 4 |
| 2.2 | The "drag crisis" [15] | 4 |
| 2.3 | Schematic overview of the different flow regimes for the flow past a stationary circular cylinder [17] | 5 |
| 2.4 | Schematic overview of the Magnus effect on a rotating circular cylinder [28] | 6 |
| 2.5 | The flowfields for different values of α at $Re_D = 4000$ (Prandtl) obtained from Zdravkovich [29] | 7 |
| 2.6 | St plotted against α from literature [32] | 7 |
| 2.7 | C_l , C_d and C_p distribution at $Re_D = 200$ obtained from 2D finite element method simulations [30] | 8 |
| 2.8 | Streamlines at $Re_D = 200$ and $Re_D = 1 \cdot 10^6$ for different values of α [37] | 9 |
| 2.9 | Instantaneous spanwise vorticity fields (DES) at $Re_D = 4 \cdot 10^4$ [42] | 10 |
| 2.10 | Isosurfaces of the magnitude of instantaneous vorticity (DES) at $Re_D = 4 \cdot 10^4$ [42] | 11 |
| 2.11 | Experimental and numerical results of the mean C_D versus h/D and the mean C_p distribution [42] | 11 |
| 2.12 | Streamlines (time-averaged) past a rotating 3D cylinder in contact with the ground [45] | 12 |
| 3.1 | Schematic overview of an isolated rotating wheel [52] | 13 |
| 3.2 | Experimental mean C_p distributions of stationary and rotating wheels | 14 |
| 3.3 | Numerically obtained mean C_p distribution compared to Fackrell using the 'A2' wheel geometry at a $Re_D = 5.3 \cdot 10^5$ | 15 |
| 3.4 | The theoretical vortex system as presented by Cogotti [55] | 16 |
| 3.5 | Vortex trailing systems behind a rotating wheel | 17 |
| 3.6 | Vortex structures of a stationary and rotating wheel by Wäschle [63] | 18 |
| 3.7 | Vortex structures of a stationary and rotating wheel by McManus and Zhang [53] | 18 |
| 3.8 | Isosurfaces obtained by Croner et al. [64] | 19 |
| 3.9 | The upper wake region past a rotating wheel by Dassanayake et al. [54] | 20 |
| 3.10 | The lower wake region past a rotating wheel by Dassanayake et al. [54] | 21 |
| 3.11 | The wake past a rotating wheel by Dassanayake et al. [54] | 21 |
| 3.12 | Streamlines averaged in time capturing the effect of yaw on the wake [9] | 22 |
| 3.13 | Top view of the averaged streamlines in the lower wake for a 4° yaw [9] | 22 |
| 3.14 | Streamlines averaged over 20 runs and Γ_2 cross-sectional contour plots at a yaw of -4° [9] | 23 |
| 4.1 | Deformation of the tire under the vehicle's load [12] | 24 |
| 4.2 | Visualisation of velocity distribution around a wheel for a RWBC and SM approach [12] | 25 |
| 4.3 | Empty rotating region comparison of MRF and SM [65] | 25 |
| 4.4 | The three different tread patterns [68] | 27 |
| 4.5 | The step size approach by Diasinos et al. [72] | 28 |
| 4.6 | C_L and C_D plotted against the step height by Diasinos et al. [72] | 28 |
| 4.7 | The three different wheel geometries [72] | 29 |
| 5.1 | Vorticity in the z-direction displaying the vortex shedding for an isolated stationary 2D cylinder at $Re_D = 200$ | 38 |
| 5.2 | Validation of the streamlines at $\alpha = 2$ for an isolated cylinder at $Re_D = 200$ | 38 |
| 5.3 | Validation of the streamlines at $\alpha = 4$ for an isolated cylinder at $Re_D = 200$ | 39 |
| 5.4 | 2D mesh for an isolated cylinder with domain size $40D$ | 40 |
| 5.5 | Layers near the cylinder with $y^+ \approx 1$ | 40 |
| 5.6 | Domain and mesh sensitivity study for a stationary 2D cylinder at $Re_D = 1 \cdot 10^6$ | 41 |
| 5.7 | u_x flowfield of a stationary 2D cylinder at $Re_D = 1 \cdot 10^6$ | 42 |
| 5.8 | Mean C_p distribution of a stationary 2D cylinder at $Re_D = 1 \cdot 10^6$ | 42 |
| 5.9 | u_x and u_y normalised at $x/D = 0.75$ | 43 |
| 5.10 | u_x and u_y normalised at $x/D = 1.5$ | 43 |

| | | |
|------|--|----|
| 5.11 | Mesh of the isolated 3D cylinder in contact with the ground | 44 |
| 5.12 | Contact patch for the 3D cylinder | 44 |
| 5.13 | 2D streamlines in the cross-sectional xy -plane at $Re_D = 100$ | 45 |
| 5.14 | 2D streamlines in the cross-sectional xz -plane at $Re_D = 100$ | 45 |
| 6.1 | Fackrell "A2" wheel | 46 |
| 6.2 | Highly non-orthogonal and skewed mesh cells due to edge of the Fackrell "A2" | 47 |
| 6.3 | Modified Fackrell "A2" wheel | 47 |
| 6.4 | Visualisation of contact patch regions | 48 |
| 6.5 | Step sizes: $0.0085D$, $0.005D$, $0.0028D$ and $0.002D$ sensitivity study | 48 |
| 6.6 | Mesh generated by cfMesh for an isolated rotating wheel | 49 |
| 6.7 | Mesh of contact region with the ground | 50 |
| 6.8 | Coarsest and finest mesh for convergence study | 50 |
| 6.9 | Mesh sensitivity study | 51 |
| 6.10 | Different domain sizes for the sensitivity study | 52 |
| 6.11 | Domain convergence study | 53 |
| 6.12 | The patches as defined in OpenFOAM | 53 |
| 6.13 | C_D and C_L convergence over 5000 iterations for $k - \omega$ SST, S-A and RKE | 59 |
| 6.14 | C_p distribution along the centerline for $k - \omega$ SST, S-A and RKE | 61 |
| 6.15 | C_p distribution along the centerline for $k - \omega$ SST and S-A | 62 |
| 6.16 | 2D streamlines validation | 63 |
| 6.16 | 2D streamlines validation | 63 |
| 6.17 | Coordinate system for the yaw effect | 64 |
| 6.18 | Wheel in domain with yaw = 10° | 64 |
| 7.1 | x/D , y/D and z/D planes for flow visualisation | 65 |
| 7.2 | The windward and leeside convention | 66 |
| 7.3 | C_D , C_L and C_S convergence over 5000 iterations for different yaw angles | 67 |
| 7.4 | C_D , C_L and C_S plotted against θ | 68 |
| 7.5 | The centerline of the wheel plane | 68 |
| 7.6 | C_p distribution of the bottom and upper half of the wheel along the centerline of the wheel | 69 |
| 7.7 | 2D streamlines for yaw angles of 0° , 4° and 10° at various x/D planes ($x/D = 0$, $x/D = 0.25$, $x/D = 0.75$ and $x/D = 1.5$) | 70 |
| 7.8 | 2D streamlines for yaw angles of 0° , 4° and 10° at various y/D planes ($y/D = 0.0014$, $y/D = 0.25$, $y/D = 0.5$ and $y/D = 0.75$) | 71 |
| 7.9 | 2D streamlines for yaw angles of 0° , 4° and 10° at $z/D = 0$ | 71 |
| 7.10 | 3D streamlines front view for yaw angles of 0° , 4° and 10° | 72 |
| 7.11 | 3D streamlines rear view for yaw angles of 0° , 4° and 10° | 72 |
| 7.12 | 3D streamlines of the jetting vortices emerging from the contact patch for yaw angles of 0° , 4° and 10° | 73 |
| 7.13 | Isosurface of $Q = 1000$ contour level for a yaw angle of 0° | 74 |
| 7.14 | Isosurface of $Q = 1000$ contour level for a yaw angle of 4° | 74 |
| 7.15 | Isosurface of $Q = 1000$ contour level for a yaw angle of 10° | 74 |
| 7.16 | $C_{p_{total}}$ fields for yaw angles of 0° , 4° and 10° at various x/D planes ($x/D = 0$, $x/D = 0.25$, $x/D = 0.75$ and $x/D = 1.5$) | 75 |
| 7.17 | $C_{p_{total}}$ fields for yaw angles of 0° , 4° and 10° at various y/D planes ($y/D = 0.0014$, $y/D = 0.25$, $y/D = 0.5$ and $y/D = 0.75$) | 76 |
| 7.18 | $C_{p_{total}}$ fields for yaw angles of 0° , 4° and 10° at $z/D = 0$ | 76 |
| 7.19 | Normalised u_x , u_y and u_z by u_∞ for yaw angles of 0° , 4° and 10° at $x/D = 0$ | 77 |
| 7.20 | Normalised u_x , u_y and u_z by u_∞ for yaw angles of 0° , 4° and 10° at $x/D = 0.25$ | 78 |
| 7.21 | Normalised u_x , u_y and u_z by u_∞ for yaw angles of 0° , 4° and 10° at $x/D = 0.75$ | 78 |
| 7.22 | Normalised u_x , u_y and u_z by u_∞ for yaw angles of 0° , 4° and 10° at $x/D = 1.5$ | 79 |
| 7.23 | Normalised u_x , u_y and u_z by u_∞ for yaw angles of 0° , 4° and 10° at $y/D = 0.75$ | 80 |
| 7.24 | Normalised u_x , u_y and u_z by u_∞ for yaw angles of 0° , 4° and 10° at $y/D = 0.5$ | 80 |

| | | |
|------|--|----|
| 7.25 | Normalised u_x , u_y and u_z by u_∞ for yaw angles of 0° , 4° and 10° at $y/D = 0.25$ | 81 |
| 7.26 | Normalised u_x , u_y and u_z by u_∞ for yaw angles of 0° , 4° and 10° at $y/D = 0.0014$ | 81 |
| 7.27 | Normalised u_x , u_y and u_z by u_∞ for yaw angles of 0° , 4° and 10° at $z/D = 0$ | 82 |
| 7.28 | C_D and C_L convergence over 5000 iterations for different Re_D values | 83 |
| 7.29 | C_D and C_L plotted against different Re_D values | 83 |
| 7.30 | C_p distribution along the centerline for different Re_D values | 84 |
| 7.31 | 2D streamlines for $Re_D = 10\,000$, $Re_D = 100\,000$ and $Re_D = 1\,000\,000$ at various x/D planes ($x/D = 0$, $x/D = 0.25$, $x/D = 0.75$ and $x/D = 1.5$) | 85 |
| 7.32 | 2D streamlines for $Re_D = 10\,000$, $Re_D = 100\,000$ and $Re_D = 1\,000\,000$ at various y/D planes ($y/D = 0.0014$, $y/D = 0.25$, $y/D = 0.5$ and $y/D = 0.75$) | 85 |
| 7.33 | 2D streamlines for $Re_D = 10\,000$, $Re_D = 100\,000$ and $Re_D = 1\,000\,000$ at $z/D = 0$ | 86 |
| 7.34 | 3D streamlines front view for $Re_D = 10\,000$, $Re_D = 100\,000$ and $Re_D = 1\,000\,000$ | 86 |
| 7.35 | 3D streamlines rear view for $Re_D = 10\,000$, $Re_D = 100\,000$ and $Re_D = 1\,000\,000$ | 87 |
| 7.36 | 3D streamlines of the jetting vortices emerging from the contact patch for $Re_D = 10\,000$, $Re_D = 100\,000$ and $Re_D = 1\,000\,000$ | 88 |
| 7.37 | Isosurface of $Q = 0.1$ contour level for $Re_D = 10\,000$ | 88 |
| 7.38 | Isosurface of $Q = 50$ contour level for $Re_D = 100\,000$ | 89 |
| 7.39 | Isosurface of $Q = 2500$ contour level for $Re_D = 1\,000\,000$ | 89 |
| 7.40 | $C_{p_{total}}$ fields for $Re_D = 10\,000$, $Re_D = 100\,000$ and $Re_D = 1\,000\,000$ at various x/D planes ($x/D = 0$, $x/D = 0.25$, $x/D = 0.75$ and $x/D = 1.5$) | 90 |
| 7.41 | $C_{p_{total}}$ fields for $Re_D = 10\,000$, $Re_D = 100\,000$ and $Re_D = 1\,000\,000$ at various y/D planes ($y/D = 0.0014$, $y/D = 0.25$, $y/D = 0.5$ and $y/D = 0.75$) | 91 |
| 7.42 | $C_{p_{total}}$ fields for $Re_D = 10\,000$, $Re_D = 100\,000$ and $Re_D = 1\,000\,000$ at $z/D = 0$ | 91 |
| 7.43 | Normalised u_x , u_y and u_z by u_∞ for $Re_D = 10\,000$, $Re_D = 100\,000$ and $Re_D = 1\,000\,000$ at $x/D = 0$ | 92 |
| 7.44 | Normalised u_x , u_y and u_z by u_∞ for $Re_D = 10\,000$, $Re_D = 100\,000$ and $Re_D = 1\,000\,000$ at $x/D = 0.25$ | 93 |
| 7.45 | Normalised u_x , u_y and u_z by u_∞ for $Re_D = 10\,000$, $Re_D = 100\,000$ and $Re_D = 1\,000\,000$ at $x/D = 0.75$ | 93 |
| 7.46 | Normalised u_x , u_y and u_z by u_∞ for $Re_D = 10\,000$, $Re_D = 100\,000$ and $Re_D = 1\,000\,000$ at $x/D = 1.5$ | 94 |
| 7.47 | Normalised u_x , u_y and u_z by u_∞ for $Re_D = 10\,000$, $Re_D = 100\,000$ and $Re_D = 1\,000\,000$ at $y/D = 0.75$ | 95 |
| 7.48 | Normalised u_x , u_y and u_z by u_∞ for $Re_D = 10\,000$, $Re_D = 100\,000$ and $Re_D = 1\,000\,000$ at $y/D = 0.5$ | 95 |
| 7.49 | Normalised u_x , u_y and u_z by u_∞ for $Re_D = 10\,000$, $Re_D = 100\,000$ and $Re_D = 1\,000\,000$ at $y/D = 0.25$ | 96 |
| 7.50 | Normalised u_x , u_y and u_z by u_∞ for $Re_D = 10\,000$, $Re_D = 100\,000$ and $Re_D = 1\,000\,000$ at $y/D = 0.0014$ | 96 |
| 7.51 | Normalised u_x , u_y and u_z by u_∞ for $Re_D = 10\,000$, $Re_D = 100\,000$ and $Re_D = 1\,000\,000$ at $z/D = 0$ | 97 |

List of Tables

| | | |
|------|---|-----|
| 2.1 | Approximate Re_D ranges of flow regimes regarding flow around a stationary circular cylinder [13, 14] | 3 |
| 2.2 | C_D , C_{pb} and St values obtained from stationary circular cylinder experiments at high Re_D [19] | 6 |
| 3.1 | Mean C_p values upstream and downstream of the contact patch area obtained from Computational Fluid Dynamics (CFD) simulations | 16 |
| 5.1 | S-A model constants | 33 |
| 5.2 | RKE model constants | 34 |
| 5.3 | $k - \omega$ SST model constants | 35 |
| 5.4 | Numerical schemes for the 2D isolated cylinder simulations at $Re_D = 1 \cdot 10^6$ using S-A | 36 |
| 5.5 | Numerical schemes for the 2D isolated cylinder simulations at $Re_D = 1 \cdot 10^6$ using $k - \omega$ SST | 36 |
| 5.6 | Solver settings using S-A | 37 |
| 5.7 | Solver settings using $k - \omega$ SST | 37 |
| 5.8 | Validation of C_d , C_l and St for an isolated 2D cylinder at $Re_D = 200$ | 39 |
| 5.9 | Validation of 2D URANS simulations for a 2D stationary cylinder at $Re_D = 1 \cdot 10^6$ | 41 |
| 5.10 | C_D and C_L compared to results of Pirozoli et al. [45] | 44 |
| 6.1 | Contact patch dimensions | 48 |
| 6.2 | Different mesh sizes for the mesh convergence studies | 50 |
| 6.3 | Type and number of mesh cells | 51 |
| 6.4 | Mesh quality parameters | 51 |
| 6.5 | Domain sensitivity dimensions | 51 |
| 6.6 | Domain 2x: type and number of mesh cells | 53 |
| 6.7 | Overview of boundary and initial conditions of the simulations utilising the $k - \omega$ SST turbulence model | 55 |
| 6.8 | Overview of boundary and initial conditions of the simulations utilising the RKE turbulence model | 56 |
| 6.9 | Overview of boundary and initial conditions of the simulations utilising the S-A turbulence model | 56 |
| 6.10 | Numerical schemes for the isolated rotating wheel in contact with the ground simulations at $Re_D = 5.3 \cdot 10^5$ | 57 |
| 6.11 | Divergence terms schemes for the S-A, $k - \omega$ SST and RKE turbulence models | 57 |
| 6.12 | Solver settings using S-A | 58 |
| 6.13 | Solver settings using $k - \omega$ SST | 58 |
| 6.14 | Solver settings using RKE | 58 |
| 6.15 | C_D and C_L values for an isolated wheel in contact with the ground validated by the results of Fackrell [6] and McManus and Zhang [53] | 60 |
| 6.16 | Layer parameters mesh and contact patch C_p values | 61 |
| 6.17 | Layer parameters mesh | 62 |
| 6.18 | C_p values upstream and downstream of the contact patch area obtained for different $k - \omega$ SST, S-A and RKE | 62 |
| 6.19 | C_p values upstream and downstream of the contact patch area obtained for different $k - \omega$ SST and S-A | 62 |
| 7.1 | C_D , C_L and C_S values for different yaw angles | 68 |
| 7.2 | C_D and C_L values for different Re_D values | 83 |
| 7.3 | C_p values upstream and downstream of the contact patch area obtained for different Re_D values | 84 |
| 1 | Overview of numerical research performed in the literature | 105 |

Abbreviations

| | |
|------------------|--|
| 2D | Two-dimensional |
| 3D | Three-dimensional |
| CAD | Computer-Aided Design |
| CFD | Computational Fluid Dynamics |
| CFL | Courant-Friedrichs-Lewy condition |
| DES | Detached Eddy Simulation |
| DDES | Delayed Detached Eddy Simulation |
| DILU | Diagonal-based Incomplete Lower-Upper |
| DNS | Direct Numerical Simulation |
| GAMG | Geometric Algebraic Multi-Grid |
| IBM | Immersed-Boundary-Method |
| LBM | Lattice-Boltzmann Method |
| LES | Large Eddy Simulation |
| MPI | Message Passing Interface |
| MRF | Moving Reference Frame |
| OpenFOAM | Open Source Field Operation and Manipulation |
| PBiCG | Preconditioned Bi-Conjugate Gradient |
| PBiCGstab | Preconditioned Bi-Conjugate Gradient Stabilized |
| PISO | Pressure Implicit with Splitting of Operators |
| PIV | Particle Image Velocimetry |
| RANS | Reynolds-Averaged Navier-Stokes |
| RKE | Realizable $k - \varepsilon$ |
| RWBC | Rotating Wall Boundary Condition |
| S-A | Spalart-Allmaras |
| SGS | Subgrid-scale stress |
| SIMPLE | Semi-Implicit Method for Pressure Linked Equations |
| SM | Sliding Mesh |
| SST | Shear Stress Transport |
| TrW | Transition in wake |
| TrSL | Transition in shear layer |
| TrBL | Transition in boundary layer |
| URANS | Unsteady Reynolds-Averaged Navier-Stokes |
| WALE | Wall Adapting Local Eddy-viscosity |

List of Symbols

| | | |
|----------------|--|-----------------------------------|
| α | rotational rate | [-] |
| δ_{ij} | Kronecker delta | |
| ε | turbulent dissipation rate | [m ² /s ³] |
| θ | position when determining pressure distribution along centerline | [°] |
| θ | yaw angle | [°] |
| κ | von Karman constant | [-] |
| μ | dynamic viscosity | [N·s/m ²] |
| ν | kinematic viscosity | [m ² /s] |
| ν_T | eddy viscosity | [m ² /s] |
| ρ | density | [kg/m ³] |
| τ_{ij} | specific Reynolds stress tensor | [m ² /s ²] |
| τ_w | wall shear stress | [kg / m · s ²] |
| ϕ | volumetric flux | [m ³ /s] |
| ω | rotational speed | [rad/s] |
| ω | specific turbulent dissipation rate | [1/s] |
| Π_{ij} | pressure strain correlation term | [m ² /s ³] |
| Ω | vorticity tensor | [rad/s] |
| $\vec{\Omega}$ | vector of rotation in MRF | [rad/s] |
| f | frequency | [Hz] |
| h | height between cylinder and ground | [m] |
| k | turbulent kinetic energy | [m ² /s ²] |
| ℓ | turbulent length scale | [m] |
| p | static pressure | [Pa] |
| t | time | [s] |
| \vec{r} | position vector in MRF | [m] |
| t_{ij} | viscous stress tensor | [kg / m · s ²] |
| u_i | velocity | [m/s] |
| u_τ | friction velocity | [m/s] |
| u_∞ | freestream velocity | [m/s] |
| u^+ | non-dimensional velocity | [-] |
| x_i | position | [m] |
| y | wall distance | [m] |
| y^+ | non-dimensional wall distance | [-] |
| A | frontal surface area | [m ²] |
| C_D | drag coefficient | [-] |
| C_L | lift coefficient | [-] |
| C_S | side force coefficient | [-] |
| C_p | pressure coefficient | [-] |
| C_μ | empirical constant | [-] |
| D | drag | [N] |
| D | diameter | [m] |
| E | roughness coefficient | [-] |
| L | lift | [N] |
| M | moment | [Nm] |
| P_{ij} | turbulent production term | [m ² /s ³] |
| R | radius | [m] |
| Re_D | Reynolds number | [-] |
| S_{ij} | strain-rate tensor | [1/s] |
| St | Strouhal number | [-] |

1. Introduction

Aerodynamics has been an important aspect of the automotive industry for decades, as understanding its principles plays a key role in the design of modern vehicles. The reason for this is that when a vehicle moves through the air it encounters aerodynamic forces that impact its fuel consumption, performance, and stability [1]. One of these forces that has a major impact is the drag. This force becomes the dominant resistance a standard passenger car experiences at speeds past 70 km/h [2] surpassing the rolling resistance as can be seen in Figure 1.1.

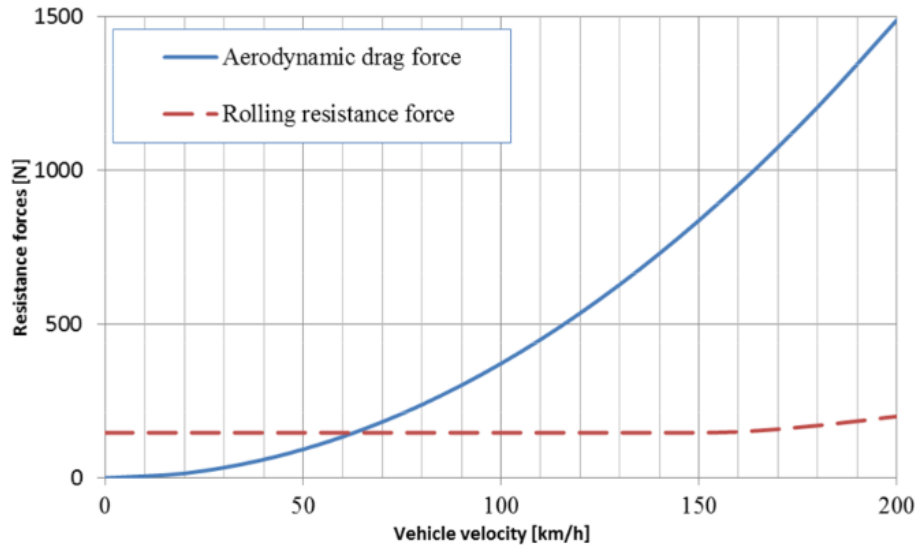


Figure 1.1: The drag and rolling resistance plotted against vehicle velocity in km/h for a typical passenger car [2]

Therefore, designers recognise the significance of minimising this drag force, which in turn results in less energy required to overcome the resistance. Hence, a lower fuel consumption that leads to an improved fuel efficiency. Moreover, performance-wise minimisation of the drag allows for higher top speeds that can be achieved and the generated downforce by the lift allows for better control and manoeuvrability, which enable drivers to push the limits of sport and racing cars further [3].

In pursuit of minimising the vehicle's drag, the wheels play a crucial role. Since, the wheels can attribute up to 25% of the drag in the case of a general passenger car [4] and up to 30%-50% for an open-wheeled race car, which in that case was the largest single source of drag that car experienced [5]. This drag is mainly caused by the pressure and only a small fraction can be attributed to friction. The reason for this is the relatively large separated region of flow downstream of the wheel [6].

This high contribution of the wheels to the overall drag signifies the importance of having a proper understanding of the aerodynamic characteristics of an isolated single wheel. Thus, over the years experimental research such as that of Rishabh Jakhar [7] and Siddharth Ghosh[8] and numerical research were performed to try and grasp the wheel's aerodynamic behaviour. However, even though there is great interest from the automotive industry, the research done is more limited compared to the other aspects of the vehicle, due to the difficulties that arise when investigating the transient nature of the wheel flow numerically as well as experimentally [9]. Furthermore, the aerodynamic characteristics can be affected by many aspects such as the types of rims used, the rim coverage [10], the contact patch area, the deformation of the tires and even the tire pattern features [11]. This means great care must be taken in accurately modelling all these aspects to achieve good results [12].

Additionally, the effect of yaw on a wheel's aerodynamics has been rarely investigated. Even though, in real-life scenarios, yaw can arise, due to crosswinds, disturbances caused by adjacent bodywork, uneven roads and steering the vehicle. One can say that practically yawed flow may occur more frequently than unyawed flow [9]. Moreover, research regarding isolated rotating wheels in contact with the ground is usually performed only at one particular Reynolds number. So, the effect of various Reynolds numbers on the aerodynamic characteristics has not been investigated to the author's knowledge.

1.1 Problem Statement

Hence, this thesis aims to perform simulations that will utilise Reynolds-Averaged Navier-Stokes (RANS) turbulence models due to their commercial attractiveness in the automotive industry to assess the effect of yaw and Reynolds number on the aerodynamic characteristics to bridge the gap in knowledge. From this, the thesis' research objective can be formulated as follows:

Research Objective

Assess the effect of yaw and Reynolds number by performing RANS simulations of unyawed and yawed isolated rotating wheels in contact with the ground.

From the research objective the following two research questions can be derived, which will be answered at the end of the thesis.

Research Question 1

What is the effect of yaw on the aerodynamic characteristics of an isolated rotating wheel in contact with the ground using RANS simulations?

Research Question 2

What is the effect of varying the Reynolds number on the aerodynamic characteristics of an isolated rotating wheel in contact with the ground using RANS simulations?

1.2 Thesis Outline

This thesis is structured as follows: in [Chapter 2](#) a literature review of the aerodynamics of bluff bodies will be given. This will contain the aerodynamics of both an isolated stationary and rotating circular cylinder. Furthermore, literature regarding cylinders in ground effect and rotating over the ground will be reviewed. [Chapter 3](#), reviews the literature regarding the aerodynamics of an isolated rotating wheel with the focus lying on the force coefficients, pressure coefficient distribution over the centerline and the wake. In addition, the effect of yawing the wheel will be discussed as well. [Chapter 4](#), discusses the approaches taken in the literature to numerically model a wheel. This consists of the techniques used to model rotation and the effects of simplifications generally made e.g. modelling the contact region with the ground. [Chapter 5](#) provides the theory behind the relevant turbulence models and presents the validation of the solver that is going to be used in the thesis by means of stationary and rotating 2D and 3D cylinder simulations. [Chapter 6](#) contains the wheel geometry and the approach taken for meshing the wheel and modelling the region in contact with the ground. Furthermore, the relevant boundary and initial conditions for the $k - \omega$ Shear Stress Transport (SST), Realizable $k - \epsilon$ (RKE) and Spalart-Allmaras (S-A) models are discussed. Moreover, the results of the sensitivity analysis regarding contact patch size, mesh fineness and domain size are presented in this chapter. In [Chapter 7](#) the results of the yaw effect and Reynolds number effect simulations are presented and discussed. The results consist of the obtained force coefficients, pressure coefficient distribution along the centerline, streamline plots, Q-criterion isosurface plots, total pressure field plots and velocity field plots. Finally, in [Chapter 8](#) a conclusion is drawn and recommendations for future work are given.

2. Literature Review: Aerodynamics of Bluff Bodies

In this chapter, literature regarding the aerodynamics of bluff bodies is discussed, which in this case is the flow past a circular cylinder as this serves as a very simplified version of a wheel. Literature from both experimental and numerical research is covered. The sections [Section 2.1](#) and [Section 2.2](#) review the flow past a stationary and rotating isolated cylinder respectively. Furthermore, [Section 2.3](#) discusses the effects of having a cylinder in ground effect and finally the literature of a rotating cylinder in contact with the ground is reviewed in [Section 2.4](#).

2.1 Flow Past a Stationary Cylinder

The flow past an isolated circular cylinder has been a subject of study for decades by researchers, as this geometry has multiple practical engineering applications. It is known to be a particularly difficult flow case due to the complex transient nature of its wake. One crucial factor affecting the flow characteristics is the Reynolds number (Re_D), which is defined as:

$$Re_D = \frac{\rho u_\infty D}{\mu_\infty} = \frac{u_\infty D}{\nu_\infty} \quad (2.1)$$

with ρ being the density in $[\text{kg}/\text{m}^3]$, u_∞ being the freestream air speed in $[\text{m}/\text{s}]$, D being the diameter in $[\text{m}]$, μ_∞ being the freestream dynamic viscosity of the air in $[\text{N}\cdot\text{s}/\text{m}^2]$ and ν_∞ being the freestream kinematic viscosity of the air in $[\text{m}^2/\text{s}]$.

Different Re_D ranges display different flow behaviours. These are divided into distinctive regimes by Zdravkovich [13]. An overview of these flow regimes is presented in [Table 2.1](#).

Table 2.1: Approximate Re_D ranges of flow regimes regarding flow around a stationary circular cylinder [13, 14]

| State | | Regime | | Re_D range |
|-------|------------------------------|---------------------|-------------------|---|
| L | Laminar | 1 | Creeping flow | $\approx < 1$ |
| | | 2 | Steady separation | $\approx 3 — 40$ |
| | | 3 | Periodic shedding | $\approx 30 — 200$ |
| TrW | Transition in wake | 1 | Far wake | $\approx 180 — 250$ |
| | | 2 | Near wake | $\approx 220 — 400$ |
| TrSL | Transition in shear layers | 1 | Lower | $\approx 350 — 2 \cdot 10^3$ |
| | | 2 | Intermediate | $\approx 1 \cdot 10^3 — 4 \cdot 10^4$ |
| | | 3 | Upper | $\approx 2 \cdot 10^4 — 2 \cdot 10^5$ |
| TrBL | Transition in boundary layer | 0 | Precritical | $\approx 1 \cdot 10^5 — 3.4 \cdot 10^5$ |
| | | 1 | Single bubble | $\approx 3 \cdot 10^5 — 4 \cdot 10^5$ |
| | | 2 | Two bubble | $\approx 3.8 \cdot 10^5 — 1 \cdot 10^6$ |
| | | 3 | Supercritical | $\approx 5 \cdot 10^5 — 6 \cdot 10^6$ |
| | | 4 | Postcritical | $\approx 3.5 \cdot 10^6 — 8 \cdot 10^6$ |
| T | Fully turbulent | Complete transition | | $\approx > 8 \cdot 10^6$ |

As can be seen in [Table 2.1](#), Zdravkovich [13] described that the flow for different Re_D experiences 5 distinctive states namely: laminar, transition in the wake, transition in the shear layers, transition in the boundary layer and fully turbulent.

The laminar state of the flow consists of three distinctive regimes. The first one is creeping flow, which is also known as Stokes flow. This occurs at small Re_D values $\approx < 1$ where the viscous forces are dominating and the flow is unseparated from the cylinder. This regime is named **L1** by the author. The next regime **L2** is characterised by its steady behaviour with two symmetric vortices also known as Föppl vortices placed on each side of the wake. Finally, in the last laminar regime (**L3**) the flow starts to become asymmetric and unsteady, displaying the well-known alternating shedding of vortices also known as the von Kármán vortex street. Visualisation of this von Kármán vortex street is presented in [Figure 2.1](#). Also, note that up to a $Re_D \approx 190$ in this regime the flow can be considered 2D. From this Re_D and higher, 3D effects appear such as the appearance of spanwise vortices, formation of vortex loops and deformation of primary vortices [15].

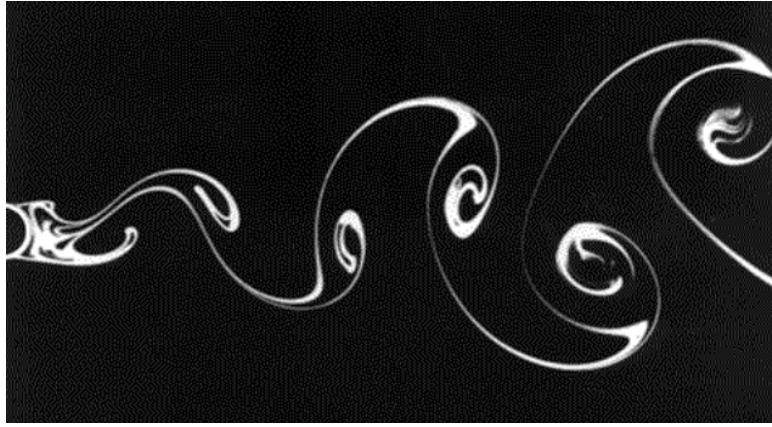


Figure 2.1: von Kármán vortex street [16]

Eventually, all laminar flows become unstable and transition to turbulence after a particular Re_D . The flow of the wake does not instantly turn into a fully turbulent flow. Instead, there is a transition region. It is observed that the flow first starts to transition in the wake bringing us to the next state that follows up the laminar state. This transition in the wake state (**TrW**) consists of two separate regimes (**TrW1** & **TrW2**). **TrW1** is characterised by the vortices being formed laminar and regular. However, further downstream in the far wake, they become irregular and transition to turbulence. This transition moves upstream with increasing Re_D until **TrW2** where the vortices are formed laminar and irregular. However, they turn partly turbulent before being shed downstream.

The next transitional state is when the free shear layers start to transition to turbulent (**TrSL**). This state is usually also known as the subcritical state and it has three regimes, which are characterised by transition waves that develop along the free shear layers that stabilise near the wake (**TrSL1**). Then when increasing Re_D vortices form as a chain along the free shear layer (**TrSL2**) and finally the shear layers will burst into turbulence near the cylinder (**TrSL3**).

Note, that in the previously mentioned states the boundary layers on both sides of the cylinder are laminar. However, when increasing Re_D further they become turbulent as well. Therefore, the next state identified is based on the transition of the boundary layers (**TrBL**). In this state, a well-known phenomenon occurs often referred to as the "drag crisis". This is when a significant reduction of C_D is experienced by the cylinder when increasing Re_D , due to the fact that separation of the flow from the cylinder surface is delayed by having a turbulent boundary layer. The "drag crisis" is shown in Figure 2.2 where the mean drag coefficient ($\overline{C_D}$) is plotted against the Reynolds number.

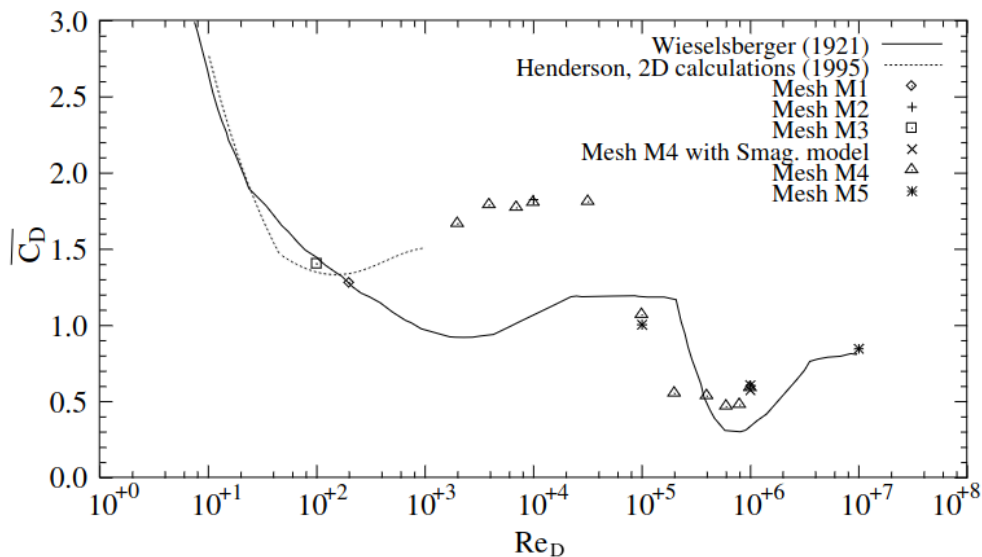


Figure 2.2: The "drag crisis" [15]

The C_D and respectively the lift coefficient (C_L) are defined as follows:

$$C_D = \frac{D}{\frac{1}{2}\rho u_\infty^2 A}, \quad (2.2)$$

$$C_L = \frac{L}{\frac{1}{2}\rho u_\infty^2 A} \quad (2.3)$$

with D and L being the drag and lift force respectively in [N] and A being the frontal surface area in [m²]. In [Figure 2.2](#) it can be seen that experimentally as well as with simulations this behaviour is observed. Generally the **TrBL** state is also named the critical regime. In this state, there are five different regimes. The first one **TrBL0** is known as the precritical regime, which is characterised by the start of transition at a separation point. This is followed by **TrBL1**, where a single separation bubble is present. This bubble is created due to first having laminar separation followed by turbulent reattachment and then eventually turbulent separation. Increasing Re_D yields a second bubble on the other side of the cylinder (**TrBL2**). Note, that **TrBL1** and **TrBL2** are both very sensitive to disturbances. Thus depending on the cylinder's roughness the flow can go from **TrBL0** to **TrBL3** immediately. **TrBL3** is named the supercritical regime and is recognised by the fragmented separation bubbles. Finally, **TrBL4** is characterised by having the transition occurring in between the stagnation and separation lines. Finally, the final state is achieved when a complete transition to turbulence is achieved. A schematic overview of the different flow regimes is presented in [Figure 2.3](#). Note that "A" denotes *laminar boundary layer separation*, "B" denotes a *separation bubble*, and "C" denotes *transition in between stagnation and separation lines*. Finally, "D" denotes *boundary layer completely turbulent*.

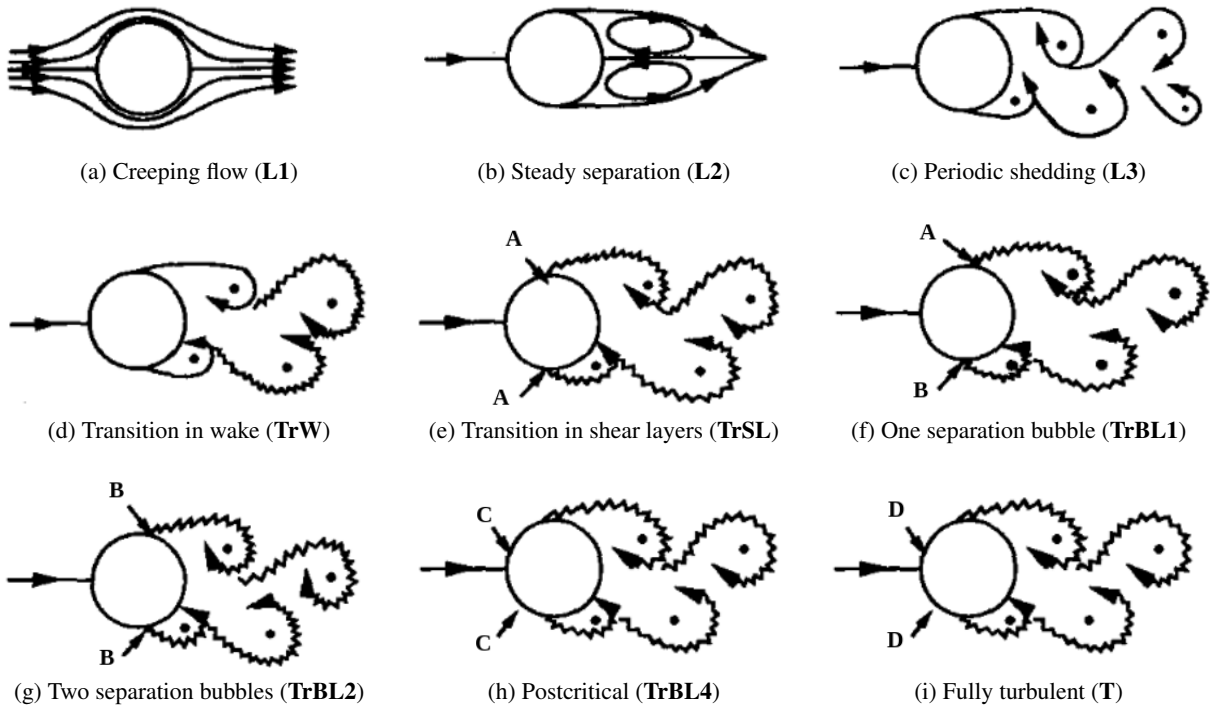


Figure 2.3: Schematic overview of the different flow regimes for the flow past a stationary circular cylinder [\[17\]](#)

In this report the focus will lie more on the higher Re_D flow as it is more of practical interest for eventually investigating a rotating automotive wheel. One of the earlier experimental investigations performed for stationary circular cylinders at high Re_D is performed by Roshko [\[18\]](#). A great overview created by Andrew Porteous [\[19\]](#) contains several experiments performed at high Re_D . This is presented in [Table 2.2](#). As can be seen, the results of the experiments contain the C_D values, base pressure coefficient (C_{pb}) and the Strouhal number (St). The pressure coefficient (C_p) in this report is defined as follows:

$$C_p = \frac{p_s - p_\infty}{\frac{1}{2}\rho u_\infty^2}, \quad (2.4)$$

with p_s being the relevant static pressure in [Pa] and p_∞ the static freestream pressure in [Pa]. The Strouhal number is a non-dimensional number that gives insight into the unsteadiness of the flow. It is defined as:

$$St = \frac{fD}{u_\infty}, \quad (2.5)$$

with f being the frequency of vortex shedding in [Hz] and D being the diameter in [m]. The experiments show that generally, the C_D increases and C_{pb} decreases with an increasing Re_D .

Table 2.2: C_D , C_{pb} and St values obtained from stationary circular cylinder experiments at high Re_D [19]

| <i>Experiment</i> | $Re_D \cdot 10^6$ [-] | C_D [-] | $-C_{pb}$ [-] | St [-] |
|-------------------|-----------------------|-------------|---------------|------------|
| Roshko [18] | 1 - 3.5 | 0.3 - 0.7 | 0.62 - 0.85 | 0.27 |
| Schmidt [20] | 1 - 5 | 0.18 - 0.53 | 0.35 - 0.60 | — |
| Achenbach [21] | 0.5 - 5 | 0.6 - 0.76 | 0.85 | — |
| Jones et al. [22] | 0.5 - 8 | 0.15 - 0.54 | 0.53 - 0.63 | 0.3 |
| Schewe [23] | 1 - 5 | 0.22 - 0.52 | — | 0.2 - 0.27 |
| Shih et al. [24] | 0.3 - 8 | 0.16 - 0.50 | 0.1 - 0.6 | 0.2 - 0.25 |

2.2 Flow Past a Rotating Cylinder

Similarly, over the years multiple studies have been conducted regarding rotating circular cylinders. One of the earliest authors that investigated this is Prandtl [25]. He concluded that there is a maximum lift coefficient of 4π . However, experiments later showed that this limit could be exceeded [26, 27].

The effect discovered by rotating the cylinder is known as the "Magnus effect". A schematic overview is depicted in Figure 2.4. As can be seen, due to the rotation of the cylinder a resulting lift force is obtained. The lift force is generated by deflecting the airflow downwards and due to Newton's third law, a lift force is generated.

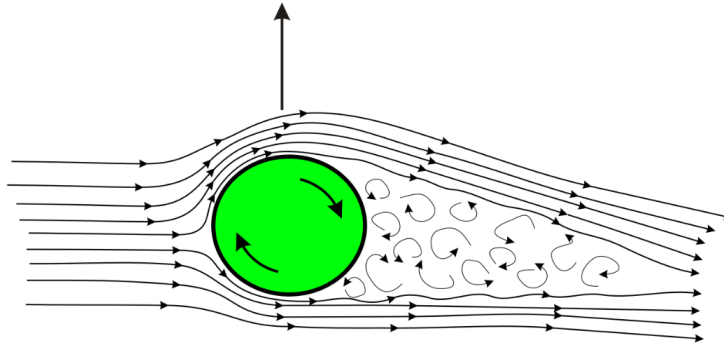


Figure 2.4: Schematic overview of the Magnus effect on a rotating circular cylinder [28]

When investigating rotational cylinders a non-dimensional ratio: the rotational rate (α) is used to be able to compare different rotations. This α is defined as:

$$\alpha = \frac{\omega R}{u_\infty} \quad (2.6)$$

with ω being the rotational speed in [rad/s] and R being the radius in [m]. Note, that ωR is the circumferential speed of the cylinder, which is normalised by dividing by u_∞ .

Zdravkovich described the findings of Prandtl regarding flow patterns in [29]. Visualisations of streamline patterns obtained from these experiments for different values of α are presented in Figure 2.5. Note, that the

cylinder is rotating clockwise. As can be seen for $\alpha = 0$ and 1, there is vortex shedding present. However, for values of $\alpha > 2$ this is no longer the case. Moreover, the stagnation points move more towards the side of the cylinder that moves against the free stream flow. Furthermore, the wake seems to move to that side as well and is considerably smaller for larger values of α .

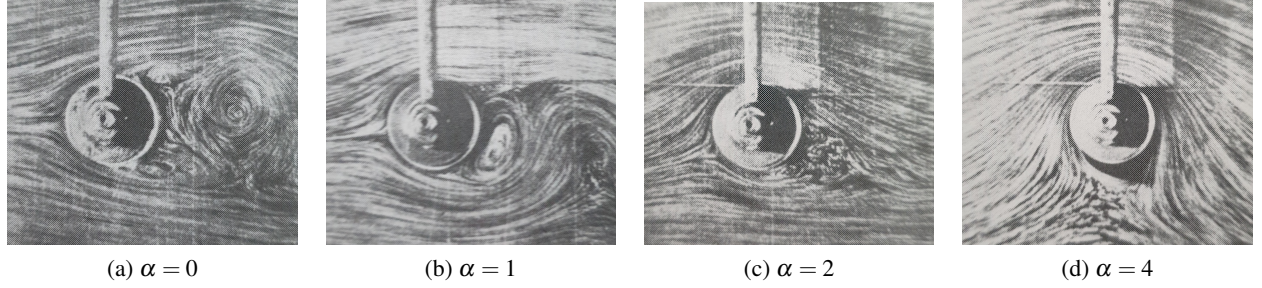


Figure 2.5: The flowfields for different values of α at $Re_D = 4000$ (Prandtl) obtained from Zdravkovich [29]

Numerically, Mittal and Kumar [30] investigated laminar flows past a 2D rotating cylinder at values of $Re_D = 200$ and $Re_D = 1000$ for $0 \leq \alpha \leq 5$. Their results showed the mean lift to be exceeding the limit proposed by Prandtl as well. Furthermore, they have observed a von Karman vortex street in the range of $0 \leq \alpha \leq 1.9$, which is in agreement with the aforementioned experiment and the results of other researchers such as Stojkovic et al. [31].

However, both groups of researchers observe the reappearance of a second shedding phase at the range of $4.35 \leq \alpha \leq 4.8$ (Mittal and Kumar [30]) and $4.8 \leq \alpha \leq 5.15$ (Stojkovic et al. [31]). Note, that Stojkovic et al. [31] performed their simulations at a different $Re_D = 100$.

In the region $0 < \alpha < 2$ where the literature agrees that there is still vortex shedding there are discrepancies in the behaviour of St . As can be seen in the plot of Chen and Rheem [32], some authors such as Diaz and Gavadal [33] and Chew and Cheng [34] observe an increasing St in this range with increasing α , others state that St stays constant (Mittal and Kumar [30]) and a decreasing St from $\alpha \approx 1$ (Kumar and Cantu [35]) and $\alpha \approx 1.5$ (Kang and Choi [36]) is observed as well. The plot of the different results is presented in Figure 2.6 where St is plotted against α in the range of $0 < \alpha < 2$.

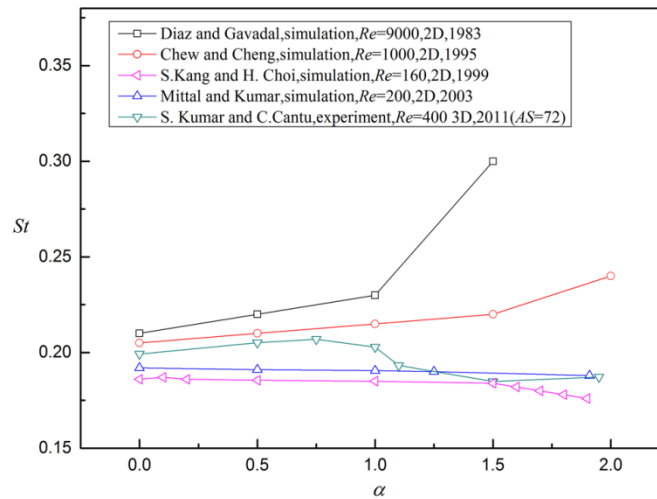


Figure 2.6: St plotted against α from literature [32]

The effect of increasing the rotational rate on the aerodynamic coefficients C_d and C_l is shown in Figure 2.7. Note, that lowercase letters are used to indicate 2D, and uppercase letters are used for 3D cases. In Figure 2.7 it can be observed that with increasing α the corresponding Magnus force becomes stronger. Hence, a bigger C_l in magnitude. This is confirmed by the bigger suction peaks in the C_p distribution. Furthermore, it can be seen that C_d starts decreasing with increasing α initially and then after the second shedding phase it starts to increase a small amount. This varying behaviour can be attributed to the dominating Magnus effect reducing

the pressure drag. However, at high rotational rates, other factors may contribute to an increase in C_d . Also, note that it is important to recognise that aspects such as Re_D and the roughness of the cylinder could play a role in the obtained coefficients.

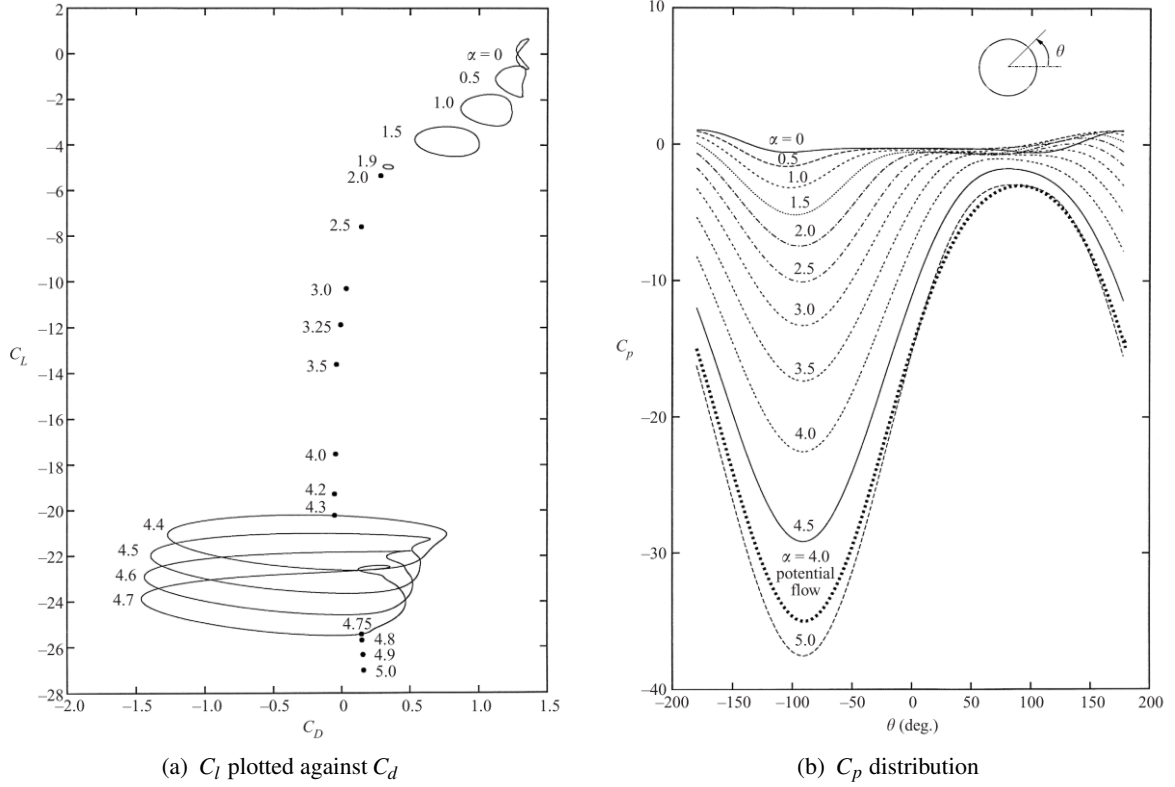


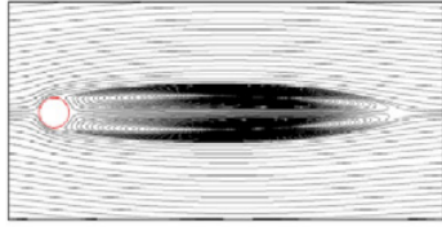
Figure 2.7: C_L , C_d and C_p distribution at $Re_D = 200$ obtained from 2D finite element method simulations [30]

Regarding flow past a rotating cylinder at high Re_D limited research is performed. Even though it is an interesting subject with respect to industrial applications.

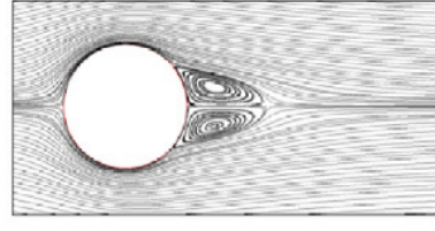
Karabelas et al. [37] investigated three Re_D values, namely: $Re_D = 5 \cdot 10^5$, $Re_D = 1 \cdot 10^6$ and $Re_D = 5 \cdot 10^6$ by means of 2D RANS and Unsteady Reynolds-Averaged Navier-Stokes (URANS). The numerical simulations carried out are performed for α ranging from $\alpha = 0$ and $\alpha = 8$ and utilised the standard $k - \varepsilon$ model. The results gave insights into the flow structures, aerodynamic loads and contribution of the pressure and viscous components of the forces for different values of Re_D and α .

Furthermore, Yao et al. [38] carried out similar simulations as Karabelas et al. [37]. These simulations were conducted in FLUENT 6.3 with the chosen turbulence model being the RNG $k - \varepsilon$ model (with standard wall treatment), due to it being able to provide good results for rotational flows. The Re_D values examined ranged from $Re_D = 6.5 \cdot 10^5$ up to $Re_D = 5.2 \cdot 10^6$ [37].

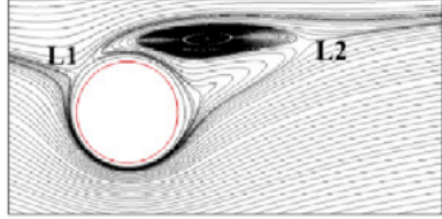
The findings at high Re_D did not display significantly different relations between the force coefficients and α compared to the laminar flow. In addition, both found that at high Re_D the vortex shedding is suppressed as is the case with laminar flow. However, at higher Re_D the flow patterns differ from the laminar case as can be seen in Figure 2.8. Also, it is stated that the Magnus effect is not as pronounced in higher Re_D as it is for the laminar case [37].



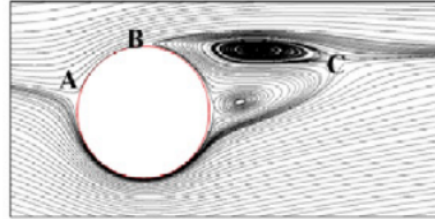
(a) $Re_D = 200, \alpha = 0$



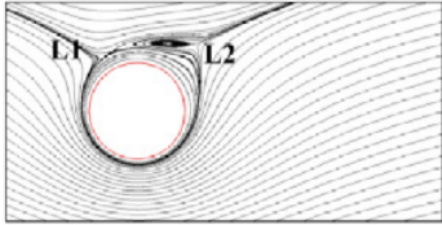
(b) $Re_D = 1 \cdot 10^6, \alpha = 0$



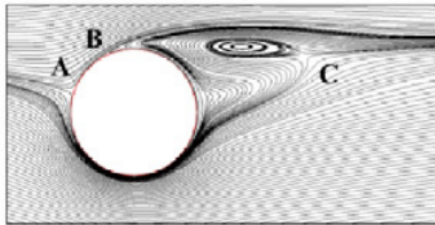
(c) $Re_D = 200, \alpha = 2$



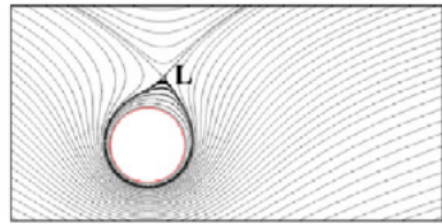
(d) $Re_D = 1 \cdot 10^6, \alpha = 2$



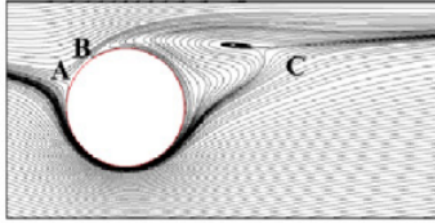
(e) $Re_D = 200, \alpha = 3$



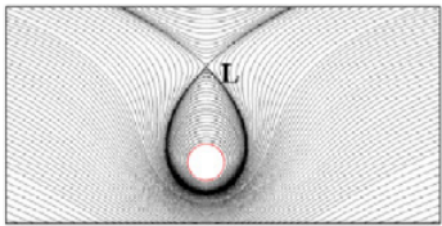
(f) $Re_D = 1 \cdot 10^6, \alpha = 3$



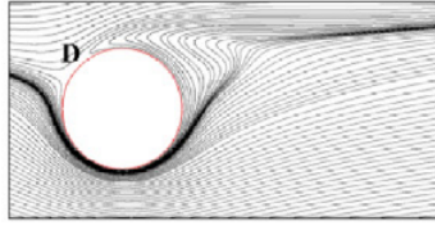
(g) $Re_D = 200, \alpha = 4$



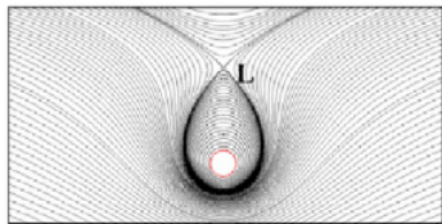
(h) $Re_D = 1 \cdot 10^6, \alpha = 4$



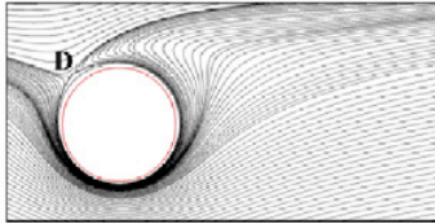
(i) $Re_D = 200, \alpha = 6$



(j) $Re_D = 1 \cdot 10^6, \alpha = 6$



(k) $Re_D = 200, \alpha = 8$



(l) $Re_D = 1 \cdot 10^6, \alpha = 8$

Figure 2.8: Streamlines at $Re_D = 200$ and $Re_D = 1 \cdot 10^6$ for different values of α [37]

2.3 Flow Past a Stationary Cylinder in Ground Effect

The incompressible flow of a stationary circular cylinder near the ground is determined by Re_D and the gap ratio (h/D) with h being the height between the cylinder and ground in [m]. Bringing the cylinder close to a parallel plane, such as the ground alters the behaviour of the typical vortex shedding.

One of the early investigations of a circular cylinder close to a plane was performed by Taneda [39] at a low $Re_D = 170$. He observed the presence of the von Karman vortex street at a gap ratio of 0.6. However, at $h/D = 0.1$, only a single row of vortices was observed.

Further research by Bearman and Zdravkovich [40] at $Re_D = 4.5 \cdot 10^4$ demonstrated that shedding of vortices are suppressed for gap ratios smaller than $h/D = 0.3$. Furthermore, gap ratios larger than 0.3 had a fairly constant St value, with the ground's only influence being to make the vortex shedding more highly tuned as the gap was decreasing in size.

Major work in this field was performed by Nishino [41]. He performed experiments at $Re_D = 4 \cdot 10^4$ and $Re_D = 1 \cdot 10^5$. He tried to minimise the boundary layer influence on the flowfield by moving the ground at the same speed as the freestream flow to avoid the effect that the differences in boundary layers introduce to these cases. From his results, he found that generally a cylinder in ground effect can be divided into three categories based on the gap sizes:

- Large gap ($h/D > 0.5$)
- Intermediate-gap ($0.35 < h/D < 0.5$)
- Small-gap ($h/D < 0.35$)

Between these three categories there are major differences. In the case of the large gap the von Kármán vortices were clearly observed behind the cylinder. Contrary, to the small-gap case where these vortices were absent resulting in a low-momentum-fluid zone bounded by two nearly parallel shear layers producing small-scale vortices. This can be seen in Figure 2.9 and Figure 2.10. These figures present the Detached Eddy Simulation (DES) results of the instantaneous spanwise vorticity fields and the isosurfaces of the magnitude of instantaneous vorticity at $Re_D = 4 \cdot 10^4$ respectively.

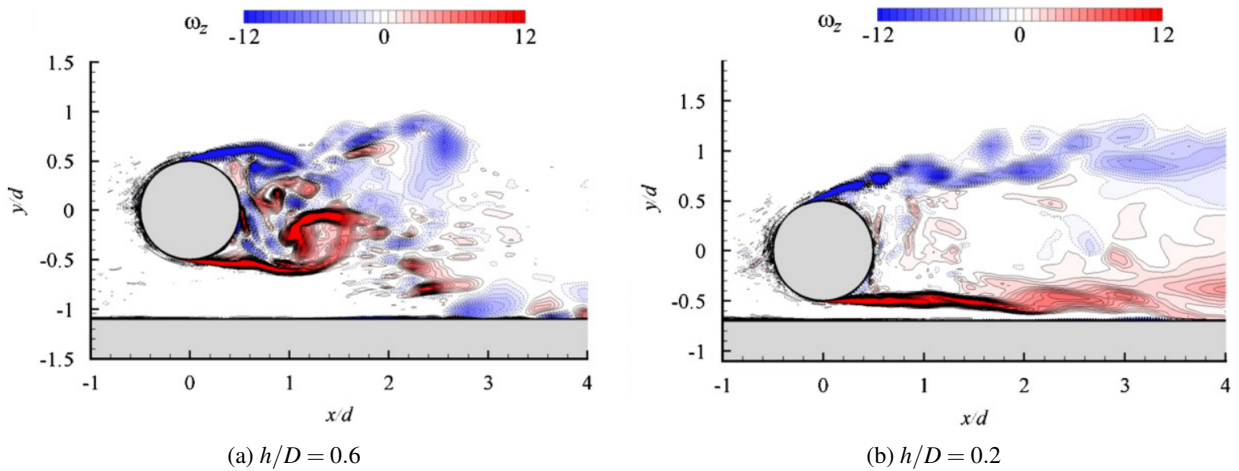


Figure 2.9: Instantaneous spanwise vorticity fields (DES) at $Re_D = 4 \cdot 10^4$ [42]

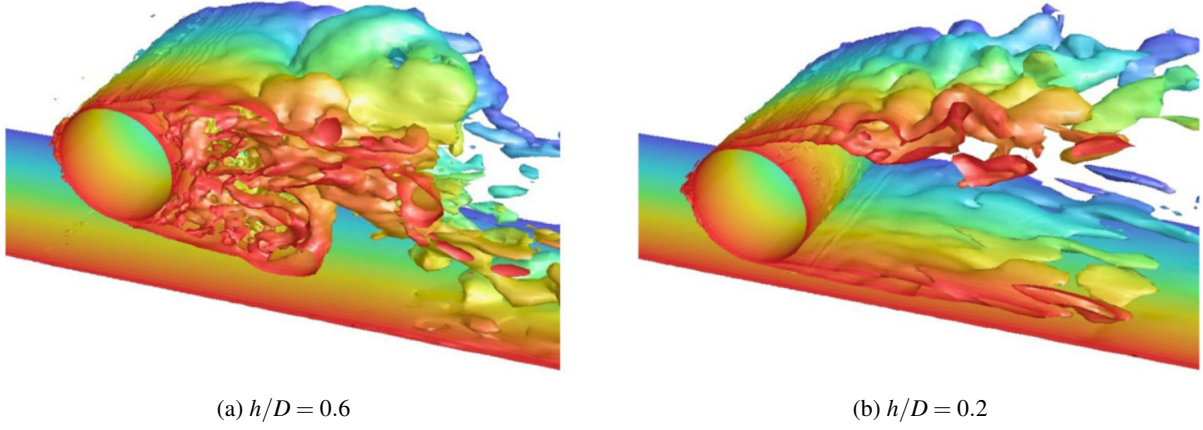


Figure 2.10: Isosurfaces of the magnitude of instantaneous vorticity (DES) at $Re_D = 4 \cdot 10^4$ [42]

Moreover, it was found that C_D rapidly decreased when the cylinder moved closer to the ground in the intermediate-gap region. Also, in the small-gap region, a constant value of C_D was observed indicating the correlation between the drag reduction and the cessation of the von Kármán vortices. This is observed in Figure 2.11, which also shows that next to experiments a numerical investigation was performed by using DES and URANS. They found that DES captured the main features of the ground effect while URANS did not capture them. Furthermore, it was also observed that the suction became less (lower negative C_p) with a decreasing gap size and with a decreasing gap size up to $h/D = 0.2$, the URANS simulations show an increasing C_D , which was not observed in the DES and experimental results. There a more constant behaviour followed by a sudden drop when getting close to the ground was observed.

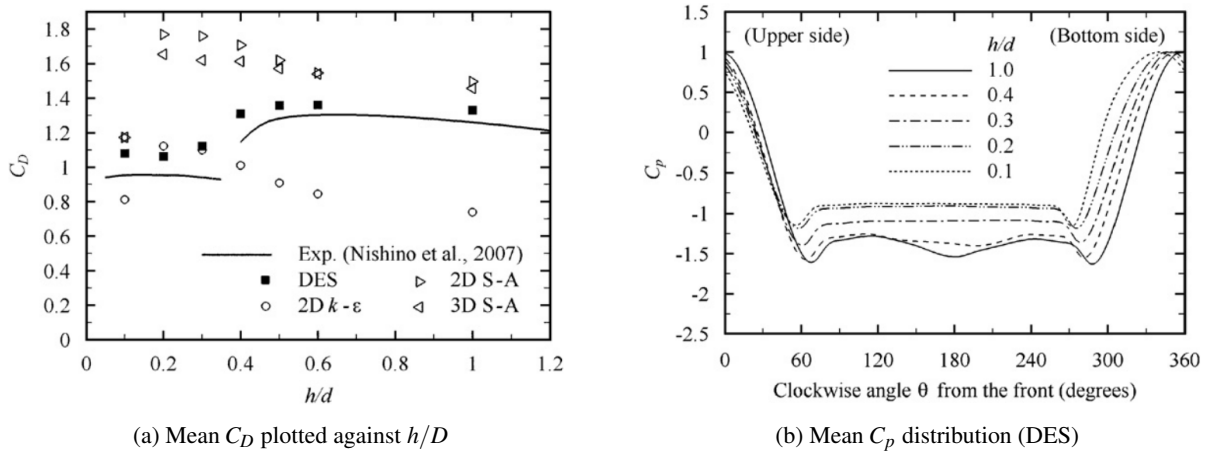


Figure 2.11: Experimental and numerical results of the mean C_D versus h/D and the mean C_p distribution [42]

2.4 Flow Past a Rotating Cylinder in Contact with the Ground

In the literature, there are only a limited amount of articles discussing rotating cylinders in contact with the ground. Namely, research performed by Stewart [43] and Houdroge et al. [44] investigated the effects of 2D rotating cylinders and Pirozoli et al. [45] investigated the case of a 3D cylinder. Note, that all of these studies performed simulations at very low values of Re_D ranging between 200 and 1000.

Pirozoli et al. [45] performed a Direct Numerical Simulation (DNS) of a 3D rotating cylinder in contact with the ground at $Re_D \leq 1000$. The main differences between their research and other research regarding rotating wheels are the geometry and the Re_D . Pirozoli et al. [45] used a finite 3D cylinder and simulated at $Re_D \leq 1000$, while wheel geometries are more complicated (hubs, rims, grooves) and the Re_D practical values range in the order of magnitude of 10^5 — 10^6 . Therefore, there may be differences in the flowfield and the obtained force

coefficients (substantially larger $C_D \approx 1$ & $C_L \approx 1.05$ at $Re_D = 1000$).

When analysing the flow past this rotating cylinder in this Re_D range a strong shear layer at the upper edge of the wheel caused by boundary layer detachment is observed, which becomes unstable around values approximately $Re_D > 400$. When it becomes unstable hairpin vortices are formed that dominate the wake. Furthermore, near the contact region, a higher pressure in front of the contact patch and a negative pressure is observed downstream of the contact patch. This is a characteristic, which is also observed in wheels and will be discussed more in detail in [Chapter 3](#). Moreover, they found three vortex pairs in the wheel wake. The streamlines for $Re_D = 500$ and $Re_D = 1000$ are presented [Figure 2.12](#) respectively.

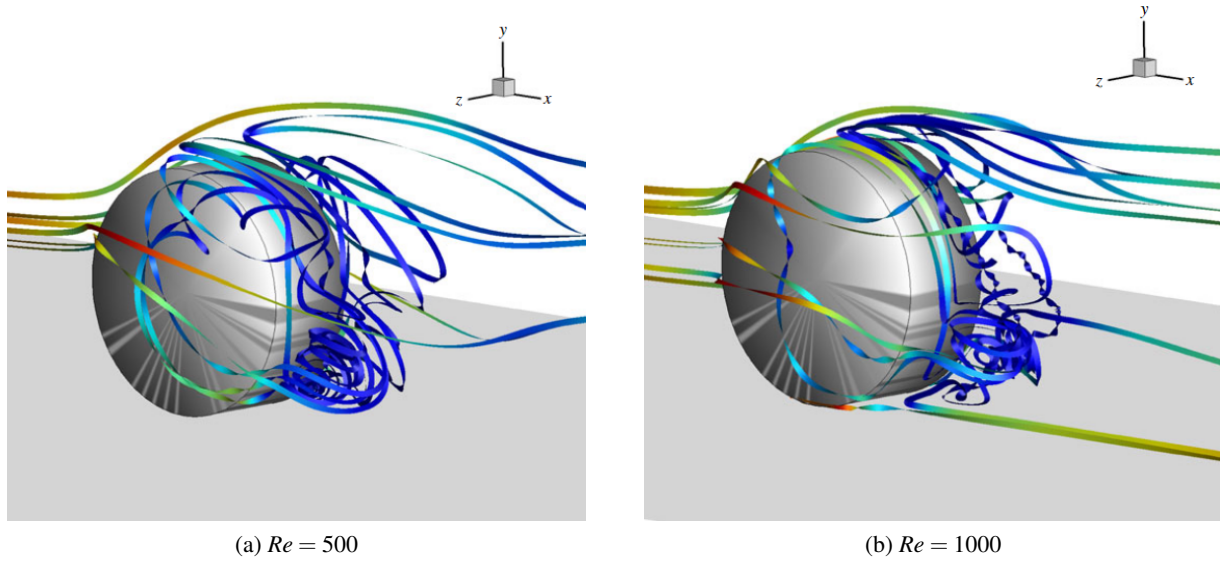


Figure 2.12: Streamlines (time-averaged) past a rotating 3D cylinder in contact with the ground [\[45\]](#)

3. Literature Review: Aerodynamics of an Isolated Rotating Wheel

In this chapter, the aerodynamic characteristics of an isolated rotating wheel in contact with the ground are discussed. Mainly, attention is paid to the surface pressure distribution over the centerline of the wheel in [Section 3.1](#) and the wake characteristics in [Section 3.2](#).

One of the earliest experiments investigating an isolated wheel near the ground were performed by Morelli [46] and Stapleford and Carr [47]. These experiments were the first to indicate the significance of the rotation of the wheel and its contact with the ground. It was observed that when there was a small gap between the wheel and the ground, the measured time-averaged lift force was negative. This is due to the Venturi effect creating a low-pressure region (suction) underneath the wheel. When this gap was sealed a positive time-averaged lift force was detected.

A few years after, the first experimental investigations conducted of an isolated rotating wheel in contact with a moving ground were performed by Fackrell and Harvey [6, 48, 49] at $Re_D = 5.3 \cdot 10^5$. These experiments gave insight into the behaviour of the pressure distribution of a rotating wheel and to this day serve as a benchmark for validation. These experiments were recreated with a different wheel geometry over the years by Mears et al. [50, 51].

A schematic overview of the behaviour of the flow over a rotating wheel is presented in [Figure 3.1](#). Fackrell [6] discovered that the flow separates from a thin boundary layer following the rotation of the wheel instead of the surface. This region of free separation is indicated by *A*. Furthermore, region *B* indicates the contact area of the wheel with the ground. This region will be the source of jetting vortices [6].

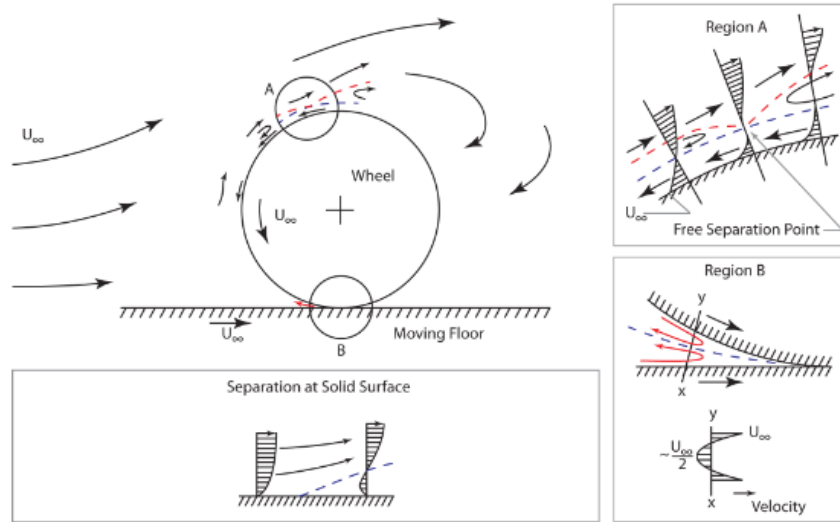


Figure 3.1: Schematic overview of an isolated rotating wheel [52]

3.1 C_p Distribution

In this section, the mean pressure distribution along the centerline of a wheel is discussed. In [Subsection 3.1.1](#) comparisons between a stationary and a rotating wheel are made, followed by a comparison between the mean C_p distribution obtained from experiments and simulations in [Subsection 3.1.2](#).

3.1.1 Stationary vs Rotating

The experiments performed by Fackrell [6] were the first experiments to measure the surface pressure of a rotating wheel in contact with a moving ground. These measurements were compared to similar measurements performed for a stationary wheel.

Again Mears et al. [50] conducted experiments in a similar fashion as Fackrell [6]. However, Mears et al. [50] did use a different wheel geometry. Therefore, the obtained results of the experiments could only be

used to validate the main structures and phenomena found in the flowfield. The obtained results of the mean C_p distribution of a stationary and rotational wheel are presented in Figure 3.2.

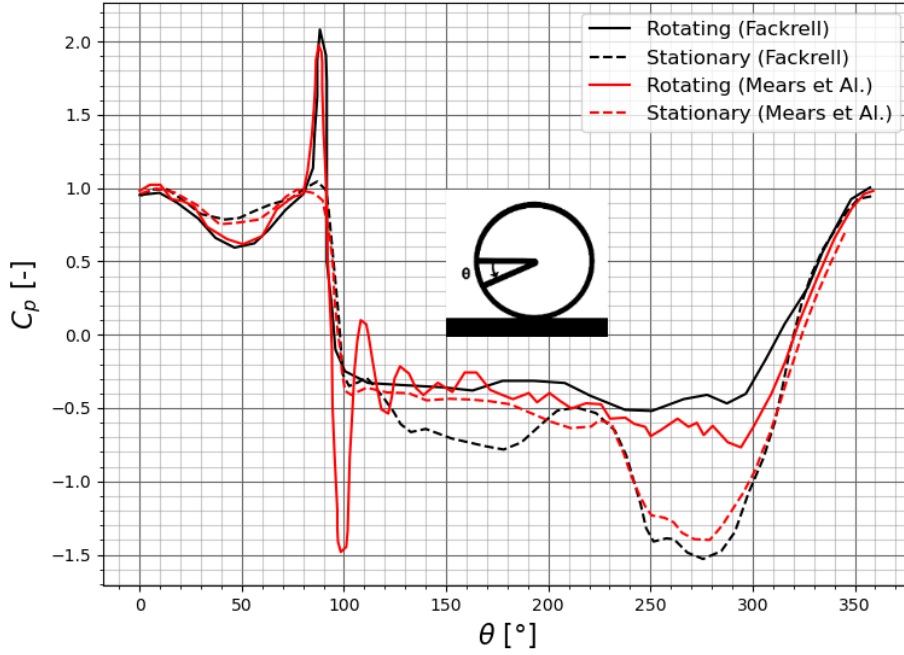


Figure 3.2: Experimental mean C_p distributions of stationary and rotating wheels

Multiple conclusions were drawn from these experiments. When analysing the mean C_p distribution, certain aspects stand out and the differences between a stationary and a rotating wheel can be identified. Firstly, in the case of a rotating wheel, a large pressure peak was observed upstream of the contact patch area with a $C_p \approx 2$ for both rotating cases, contrary to what was found for a stationary wheel where in this region the C_p value approaches 1 indicating stagnation of the flow. This phenomenon was caused by the moving ground and the boundary layer of the rotating wheel, which due to their converging movement (Region B) in Figure 3.1 results in the region acting as a 'viscous pump' increasing the pressure. This results in two vortices near the ground that roll up past both sides of the wheel's contact patch. These vortices are well known as the jetting vortices.

Furthermore, directly downstream of the contact patch, a negative pressure peak was observed by Mears et al. [50]. However, this peak was not observed by Fackrell [6] even though he had predicted it, due to the opposite divergent movement of the ground and rotating wheel. He argued that the absence of this peak was caused by the moving ground lifting. Hence, touching the wheel in the low-pressure region. However, another explanation could be that the transient response of the pressure sensor, electronics, tubing etc. distorts the measurement signal, indicating that near the line of contact, simulations could be giving more reliable results of the behaviour compared to experiments [53]. However, the fact that Mears et al. [50] did observe this negative peak shows that either the measurement technology progressed enough over the years or that the first explanation is more feasible.

Moreover, moving towards the upper side of the wheel ($250^\circ < \theta < 320^\circ$) a significant difference is noticeable. In the case of a stationary wheel, lower C_p values were observed indicating a region of higher suction. This contributes largely to the fact that a stationary wheel generates more lift than a rotating wheel. In addition, separation occurs further upstream and lower drag is measured in the case of a rotating wheel. Thus, the conclusion is that the action of having the wheel rotating in itself significantly affects the flowfield.

3.1.2 Experiments vs Simulations

It is important to compare the mean C_p distributions obtained from experiments and simulations, as this will give insight into certain limitations that may arise when modelling and simulating a rotating wheel. The results of the mean C_p distributions obtained from the URANS simulations of McManus and Zhang [53] and URANS,

DES and Large Eddy Simulation (LES) of Dassanayake et al. [54] compared to the experiment performed by Fackrell [6] using the 'A2' wheel geometry at a $Re_D = 5.3 \cdot 10^5$ are presented in Figure 3.3. These simulations were performed with the same conditions as the experiment to be able to compare the results.

At first glance it can be seen that in general, the simulations capture the main flow behaviour significantly well. The flow around the rotating wheel stagnated slightly below the front wheel at $\theta = 5.6^\circ$ compared to the URANS simulations of McManus and Zhang [53] where a value of $\theta = 4.2^\circ$ was observed. Then up to $\theta \approx 50^\circ$ the C_p slightly falls and from there it starts increasing before sharply rising to a pressure peak. This slight decrease and increase in pressure was fairly well captured by all the performed simulations.

However, discrepancies were found near the contact patch when the pressure peak was reached. Upstream of the contact patch the URANS simulations by McManus and Zhang [53] overpredicted the pressure peak with $\approx 36\%$ compared to the experimental value found by Fackrell [6]. Contrary, the simulations by Dassanayake et al. [54] underpredicted the peak by $\approx 39\%$.

Downstream of the contact patch McManus and Zhang [53] observed a large negative C_p , which is similar to the behaviour found by Mears et al. [50]. However, Dassanayake et al. [54] observed a minor peak. An overview of the observed mean C_p values upstream and downstream of the contact area is presented in Table 3.1.

Furthermore, flow separation during the experiment occurred at $\theta = 280^\circ$, which is in excellent agreement with the separation obtained by Dassanayake et al. [54]. Their URANS and DES simulations predicted separation at $\theta = 280^\circ$ as well. Their LES however predicted separation further downstream at $\theta = 272^\circ$. This was attributed to the large mesh resolution required in the boundary layer to obtain accurate results for LES. In the case of McManus and Zhang [53], the separation location was predicted further downstream with both turbulence models predicting: $\theta = 270^\circ$ (S-A) and $\theta = 255^\circ$ (RKE).

Finally, all simulations captured a fairly similar value for the mean base pressure, which is comparable to what was obtained in the experiment. This value lies near $C_p = -0.39$.

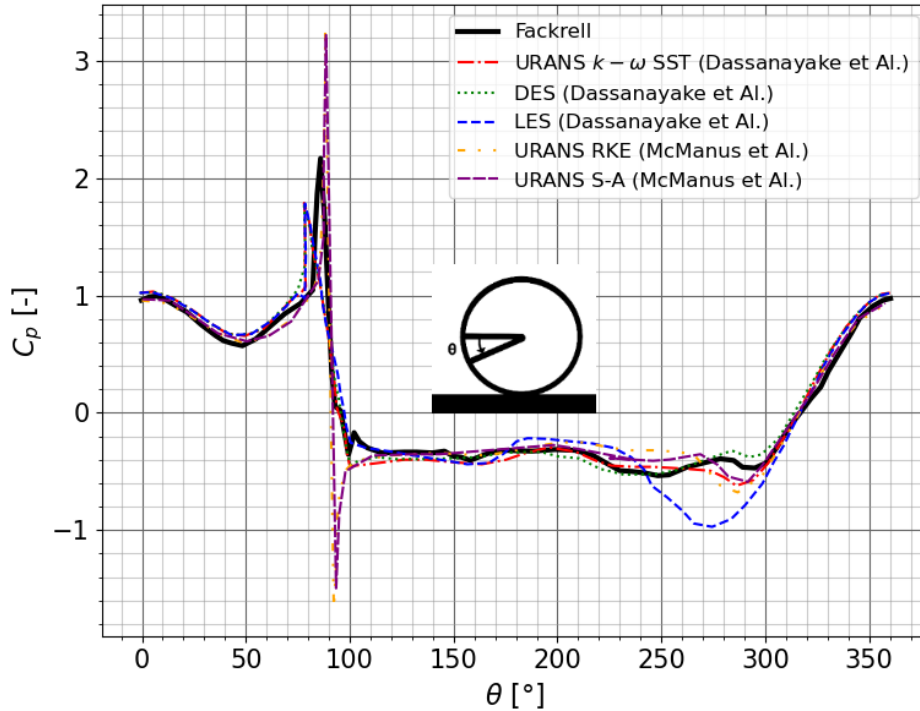


Figure 3.3: Numerically obtained mean C_p distribution compared to Fackrell using the 'A2' wheel geometry at a $Re_D = 5.3 \cdot 10^5$

Table 3.1: Mean C_p values upstream and downstream of the contact patch area obtained from Computational Fluid Dynamics (CFD) simulations

| | C_p upstream | C_p downstream |
|--|----------------|------------------|
| McManus and Zhang (S-A) [53] | 3.22 | -1.49 |
| McManus and Zhang (RKE) [53] | 3.24 | -1.69 |
| Dassanayake et al. $k - \omega$ SST [54] | 1.62 | -0.45 |
| Dassanayake et al. (DES) [54] | 1.73 | -0.44 |
| Dassanayake et al. (LES) [54] | 1.74 | — |

3.2 Wake Characteristics

Understanding the wake of a rotating wheel is crucial during the design phase. The vortical structures can interact with the rest of the vehicle leading to vibrations. In this section, the main general phenomena observed for a rotating wheel in the literature are discussed. Furthermore, the difference between the wake of a stationary wheel and a rotating wheel is highlighted as well and the effect of yaw is mentioned.

Cogotti [55] was one of the early researchers to theoretically describe the vortex system of an isolated rotating wheel. This vortex system is presented in Figure 3.4.

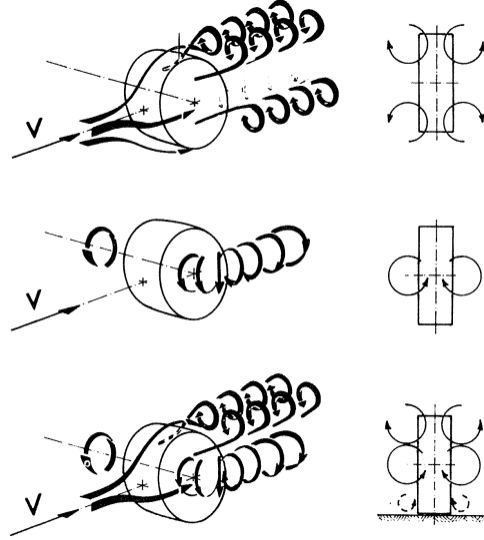


Figure 3.4: The theoretical vortex system as presented by Cogotti [55]

As can be seen, Cogotti [55] theorised based on the shape of the wheel and rotation induced that there are three distinct vortex pairs. The top vortex pattern of Figure 3.4 describes the vortex pattern caused by the shape of the wheel, while the middle vortex pattern indicates the predicted pattern due to the rotation of the wheel. Finally, combining the two results yields the last vortex system seen at the bottom of Figure 3.4, which is the vortex system trailing a rotating wheel.

Another theoretical vortex model was proposed by Mercker and Berneburg [56]. This vortex trailing system is presented in Figure 3.5b. The difference between this system and Cogotti's is the direction and magnitude of the counter-rotating vortices near the ground. So, the lower vortex pair rotates in the same direction as the upper vortex pair.

Experiments performed by Bearman et al. [57] investigated the near wake of an isolated stationary and rotating wheel. The results yielded a contra-rotating vortex pair dominating the near wake being located approximately $0.25D$ above the ground in the case of a rotating wheel. Contrary, to a stationary wheel where the vortex pair was located near the ground. These results did not agree with the theoretical vortex systems mentioned.

So, Saddington et al. [58] derived a vortex trailing system based on experiments. They examined different planes downstream of the wheel, resulting in the following main wake characteristics:

- There exists a region with a velocity deficit in the shape of an inverted T.
- The vortex trailing systems consists of two contra-rotating vortex pairs located at the upper half of the wheel and near the ground in the near wake ($x/D < 1$). It is observed that the upper vortex pair will merge with the more dominant pair near the ground ($x/D > 1$).
- There exist large regions of reverse flow, which extend beyond the projected profile of the tire.

A schematic overview of the vortex system proposed by Saddington et al. [58] is presented in Figure 3.5c and Figure 3.5d.

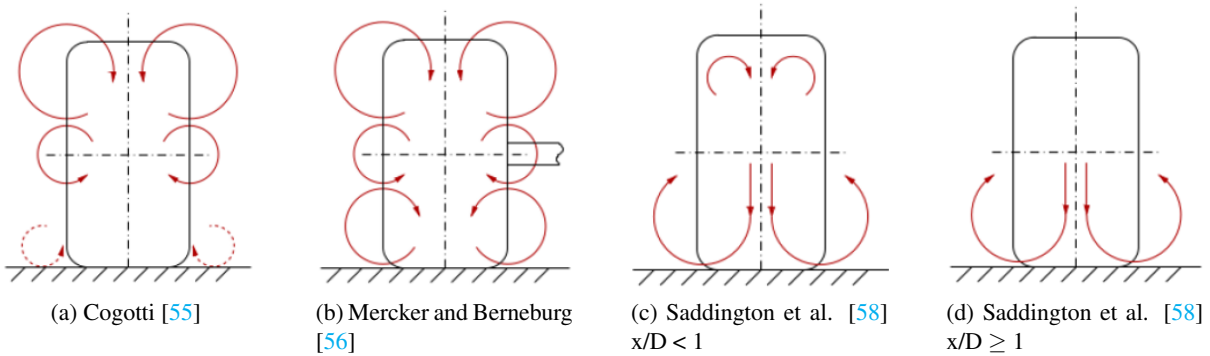


Figure 3.5: Vortex trailing systems behind a rotating wheel

However, in the literature itself there is less agreement regarding the flow structures within the wake compared to the mean C_p distribution [59]. The findings of Saddington et al. [58] of having an upper and lower vortex pair with the lower vortex pair being the stronger are in agreement with the findings of Axerio and Laccarino [60]. However, Patel et al. [59] found the opposite. So, they found that the upper vortex pair was the dominant pair. For their research, they performed an experimental Particle Image Velocimetry (PIV) and numerical (DES) investigation to identify the existing instantaneous and time-averaged flow structures within the wake. They investigated it by decomposing the unsteady flowfield by means of proper orthogonal decomposition, which filtered the complex unsteady flowfield revealing the underlying mechanisms that cause the temporal fluctuation relative to the mean flowfield. The findings of Patel et al. [59] were in agreement with the research of Heyder-Bruckner [61] and Knowles et al. [62].

Both the research of Wäschle [63] and McManus and Zhang [53] investigated the differences between the vortex structures of the time-averaged flowfield of a stationary and rotating wheel. The vortex structures as found by Wäschle [63] are presented in Figure 3.6 and the vortex structures found by McManus and Zhang [53] are presented in Figure 3.7.

Wäschle [63] observed that the main dominating vortex for a stationary wheel, as well as a rotating wheel, is the wake-horseshoe vortex indicated by (1) in Figure 3.6. This vortex appeared to be weaker in the case of the rotating wheel. In addition, both cases displayed a wheel squash vortex (3), due to separation at the tire shoulders in the frontal area of the wheel contact patch. Note, that the rotation of the wheel introduced additional energy into the flowfield diminishing the wheel squash vortex. Furthermore, important differences that were observed are the stagnation horseshoe vortex (4) in the case of a stationary wheel (very weak and not present for the rotating wheel) and the vortex ring being present at the upper half of the rotating wheel. Contrary, to the upper half of the stationary wheel where a C-shoulder vortex pair occurred that kept the flow attached and increased the acceleration of the flow over the upper half, while a vortex ring increased the pressure over the upper half and behind the wheel. Hence, reducing the lift and drag for a rotating wheel. This reduction of aerodynamic forces agrees with the experimental findings of Fackrell [6].

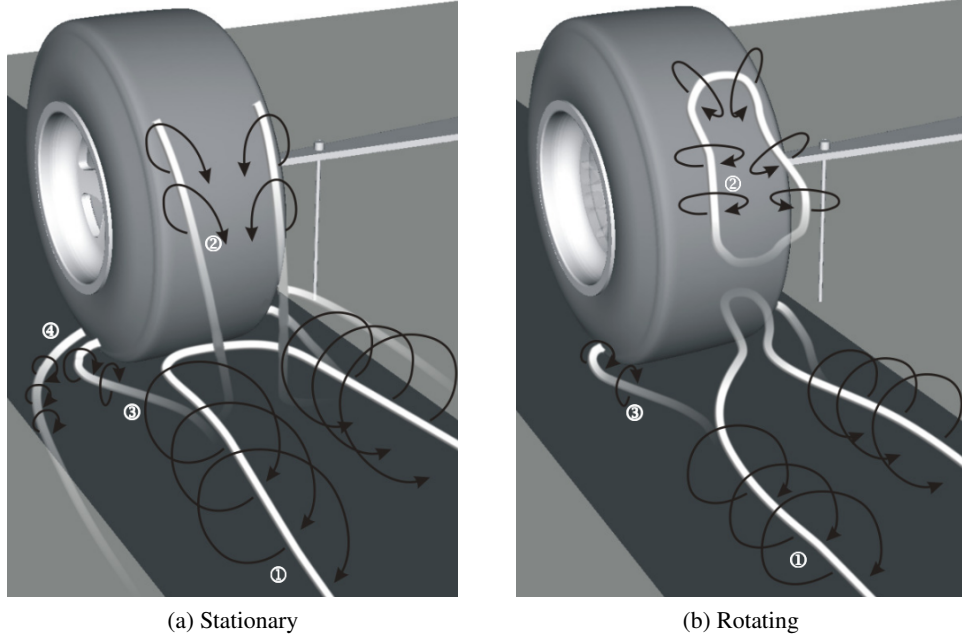


Figure 3.6: Vortex structures of a stationary and rotating wheel by Wäschle [63]

The results of McManus and Zhang [53] displayed good qualitative and quantitative agreement with the experiments of Fackrell [6]. Moreover, similar mean vortex structures were observed compared to the results obtained by Wäschle [63], such as the counter-rotating vortices for both cases. Furthermore, as can be seen in the case of a stationary wheel a larger region of attached flow was found that is directed down the rear face of the wheel towards the ground. This is also in agreement with the findings of Wäschle [63]. However, for a rotating wheel at the upper half after the flow separates an arch-shaped vortex was observed by McManus and Zhang [53]. Also, McManus and Zhang [53] found no evidence of a stagnation horseshoe vortex like (4). Note, that they found that the differences in mechanisms causing the vortices resulted in the vortices behind a rotating wheel being noticeably weaker and less spread laterally in agreement with the experiments of Fackrell [6] and Wäschle [63].

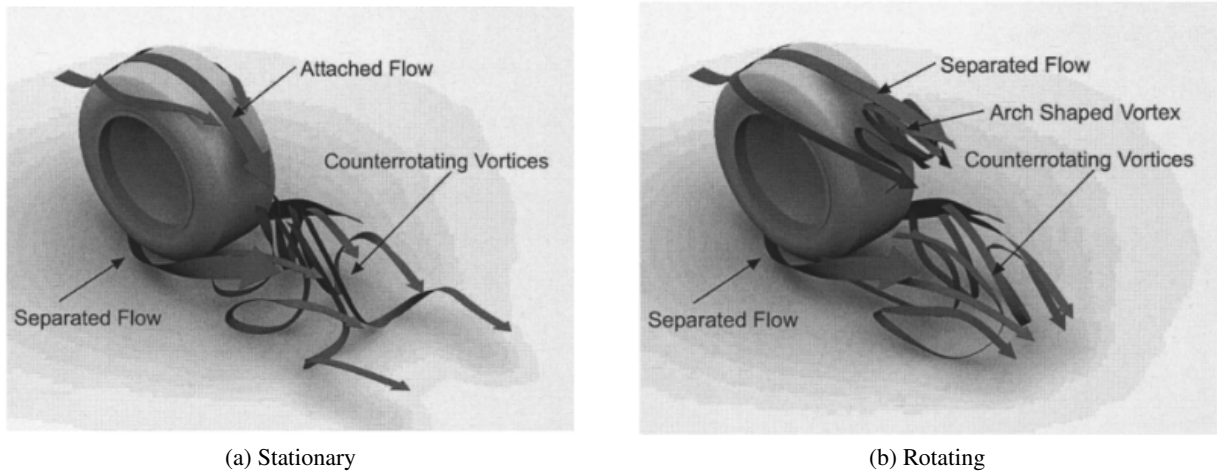


Figure 3.7: Vortex structures of a stationary and rotating wheel by McManus and Zhang [53]

Croner et al. [64] took the next step by aiming to characterise the unsteady behaviour of the wake of a rotating wheel, as it is known that in the case of bluff bodies, unsteady calculations provide more accurate aerodynamic forces and spatial features. The importance of understanding this unsteady behaviour will give insight into the influence that the vortical structures have on the aerodynamic forces.

The results of the URANS simulations displayed the main flow characteristics, which consisted of large

boundary layer separations, re-circulation areas and vortical structures. Not only did they perform a numerical investigation, they also performed an experimental investigation using PIV and Hot-Wire Anemometry to obtain instantaneous data, such as the velocities in the wake. During the experiments, real road conditions were achieved by way of a moving belt, which is synchronised at the speed of the freestream flow and attention was paid to making sure that there is no boundary layer by placing a suction system ahead of the belt. Note, that the experiment and simulations were performed with a sting attached to the wheel. This increased the asymmetry of the results compared to a fully isolated wheel.

Their research has shown that the base area ($100^\circ - 270^\circ$) is highly unsteady, which is in agreement with the findings of Fackrell [6]. In this area, the discrepancies follow from the re-circulation areas, which are dependent on the wheel geometry (e.g. aspect ratio & tire shoulders) and Re_D . Also, the importance of simulating the upper boundary layer separation is stressed as it could lead to major discrepancies in the obtained flowfields compared to real life. When the mean base C_p was computed a fairly constant value was observed.

Looking at the vortical structures of the wake, at the upper half and behind the wheel, which are caused by the rotation and boundary layer separation an arch-shaped vortex is detected. The isosurface and streamlines of this are presented in Figure 3.8a, with I indicating the arch-shaped vortex and II indicating a contra-rotative upper vortex pair. So, contrary to the findings of Wäschle [63] a ring vortex is not observed.

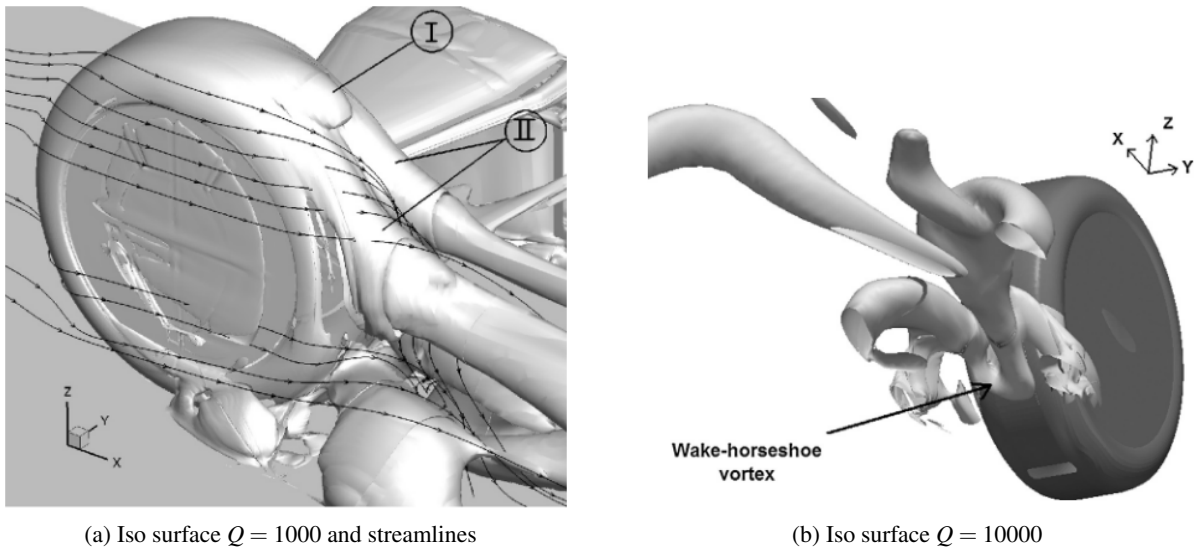


Figure 3.8: Isosurfaces obtained by Croner et al. [64]

In the near wake of the wheel ($x \leq D$) the PIV and CFD results both showed two upper vortices, which are caused by the boundary layer separation. Furthermore, two vortices near the ground were observed as well. However, note that this vortex pair does not originate from the jetting vortices but is connected in a massive wake horse-shoe vortex as can be seen in Figure 3.8b.

Finally, an additional pair of vortices near the middle was observed, which have their origin at the wheelbase and merge either with the upper or near-ground pair further downstream. So, in total three vortex pairs were observed. Moreover, the upper vortices were more correlated than the ones near the ground and the behaviour of the upper vortex pair was not linked to that of the lower vortex pair.

The unsteadiness of the flow in the wake was also studied at different locations by means of velocity spectra. From the experimental results it was found that for each component and each position in the wake, two parts of the main frequencies were observed. The first frequency matched the wheel's rotation frequency and the second frequency characterised the wake dynamics. The harmonics of these frequencies were also detected. The difference between the simulations and experimental results was fairly small, which showed that CFD and especially wall-resolved URANS simulations could considerably predict the temporal characteristics, with accuracy closely matched to that of experiments.

Further investigation of the wake showed that the main frequency f_1 was predominant in all the inspected wake locations. Furthermore, near the ground downstream of the jetting vortices large variations in u_x and u_y were observed. Hence, large differences in time. While in the central-plane large differences in u_y and a decrease in the variations of u_x were observed. Also, the upper separation region and the region downstream of

the contact patch were investigated for the simulations. This was not possible in the experimental setup, due to the limitations of the experimental setup and the intrusiveness of the probes affecting the results. Analysing the upper separation region it displayed stable behaviour with variations below 1% and the region downstream of the contact region was dominated by the first harmonic of the frequency.

Investigation of the force coefficients like the side force coefficient C_S , C_D and C_L showed that the largest variations were found with the C_S , with it being dominated by the main frequency. This side force is caused mainly by having an asymmetric setup, which deviates from the direction of the wake and is the reason that a side force is generated. Also, note that C_L and C_D had a slightly higher dominant first harmonic frequency. Finally, the viscous components of the forces were observed to be quasi-steady. Hence, pressure modifications caused the variations in forces.

Dassanayake et al. [54] simulated a rotating wheel in contact with the ground using URANS, DES and LES. This allowed for comparison of the unsteady flow features captured by URANS to that of the more accurate methods DES and LES. Just like McManus and Zhang [53] they used the same wheel as Fackrell's experiment [6], which is known as the Fackrell "A2".

When comparing the results of the upper region, all three cases captured the flow separation. Furthermore, an arched-shape vortex, which was nearly as wide as the wheel was present in the results of the URANS. This is in agreement with the observations of McManus and Zhang [53]. This arched-shape vortex was also present in the results of the DES simulations, due to it behaving as an URANS near the walls. However, the results of LES showed a vortex pair. Figure 3.9 presents the results of the upper wake region of the three methods.

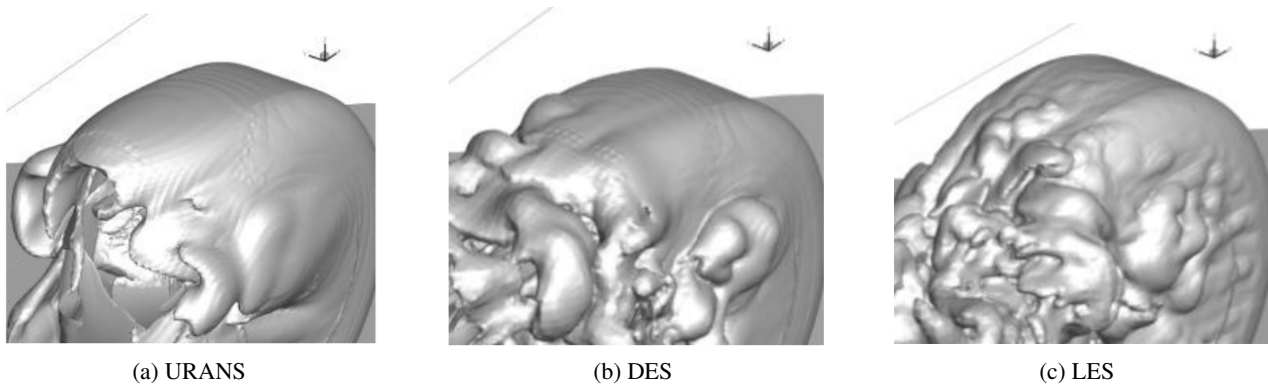


Figure 3.9: The upper wake region past a rotating wheel by Dassanayake et al. [54]

Near the contact region, due to the high-pressure region of the converging boundaries, flow to the side directions was captured by URANS, DES and LES. As can be seen, this flow mixed with the flow at the hub in the DES and LES simulations. This was due to the vortices leaving the hub region and the rotation of the wheel, which is contrary to the results obtained from the URANS simulations where the flow from the hub and the lower separation region flow were not interacting. The structures found in the lower region of the wake are presented in Figure 3.10.

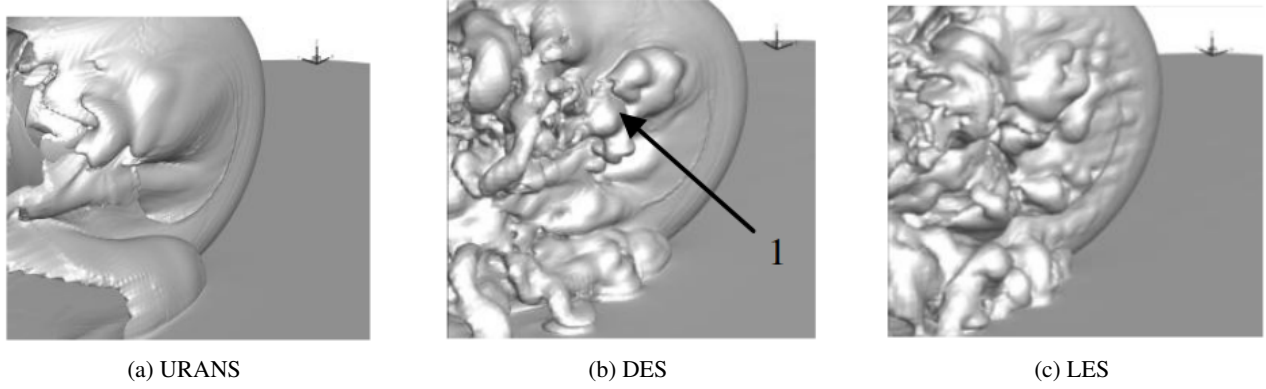


Figure 3.10: The lower wake region past a rotating wheel by Dassanayake et al. [54]

Looking at the entire wake region, the vortices near the wall were much more prominently captured and the vortex pair extended downstream in the case of LES, while for DES the interaction between the hub vortices and the upper region vortices yielded vortices that roll upon themselves. Moreover, the interaction between the separation and the hub allowed the vortices to break down and spread laterally as can be seen. Finally, even though it is obvious, the URANS simulations captured fewer details compared to the other two and the expected vortex pair near the ground was barely visible as can be seen in Figure 3.11.

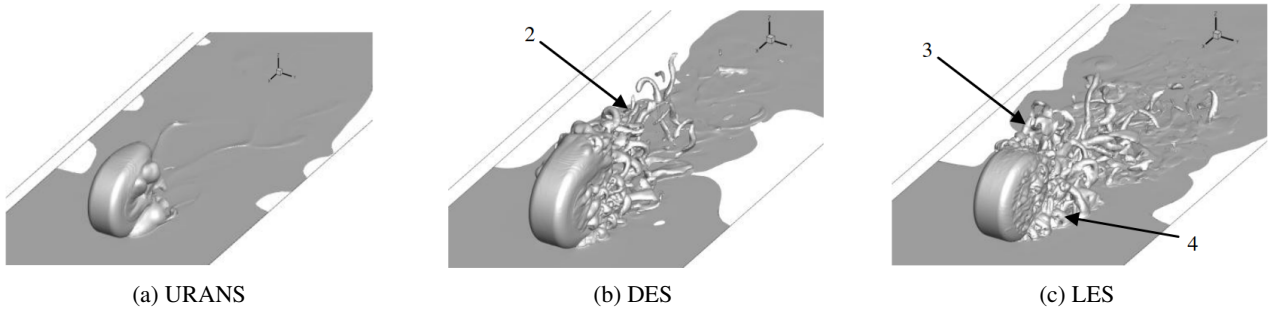


Figure 3.11: The wake past a rotating wheel by Dassanayake et al. [54]

An overview of isolated rotating wheel simulations performed in the literature is presented in Table 1 of the Appendix. This table contains the researchers with their type of simulations performed and chosen turbulence models at the respective Re_D . Furthermore, their approaches taken to model the rotation and contact patch region are stated. These aspects will be discussed more in-depth in the following chapter. Finally, additional notes and their wheel geometries of choice are mentioned as well

Yaw

Regarding the effect of yaw limited research is performed even though it is very important for wheel aerodynamics since it arises in many different practical situations, such as crosswinds, disturbances caused by adjacent bodywork and when steering the wheel [9].

Parfett et al. [9] performed experiments with a smooth wheel for angles up to $\pm 6^\circ$ and measured the flowfield by means of PIV. They found that the structures in the wake are highly sensitive to yawing the wheel. The time-averaged streamlines they found for yaw angles of 0° (unyawed), 2° , 4° and 6° are visualised in Figure 3.12. As can be seen, less of the wake originated upstream of the wheel on the windward side (B) with an increasing yaw angle and more was drawn up from the top of the wheel indicated by C . Moreover, Figure 3.13 shows that yaw drove the entire flow towards the leeside in the lower wake, which is a phenomenon not observed in the case of an unwyawed wheel. One of their major conclusions regarding the effect of yaw is that yawing the wheel results in the stagnation point moving towards the windward side of the wheel shoulder. They found that this caused the vortex on the ground at the leeside to be strengthened while the windward ground vortex is weakened.

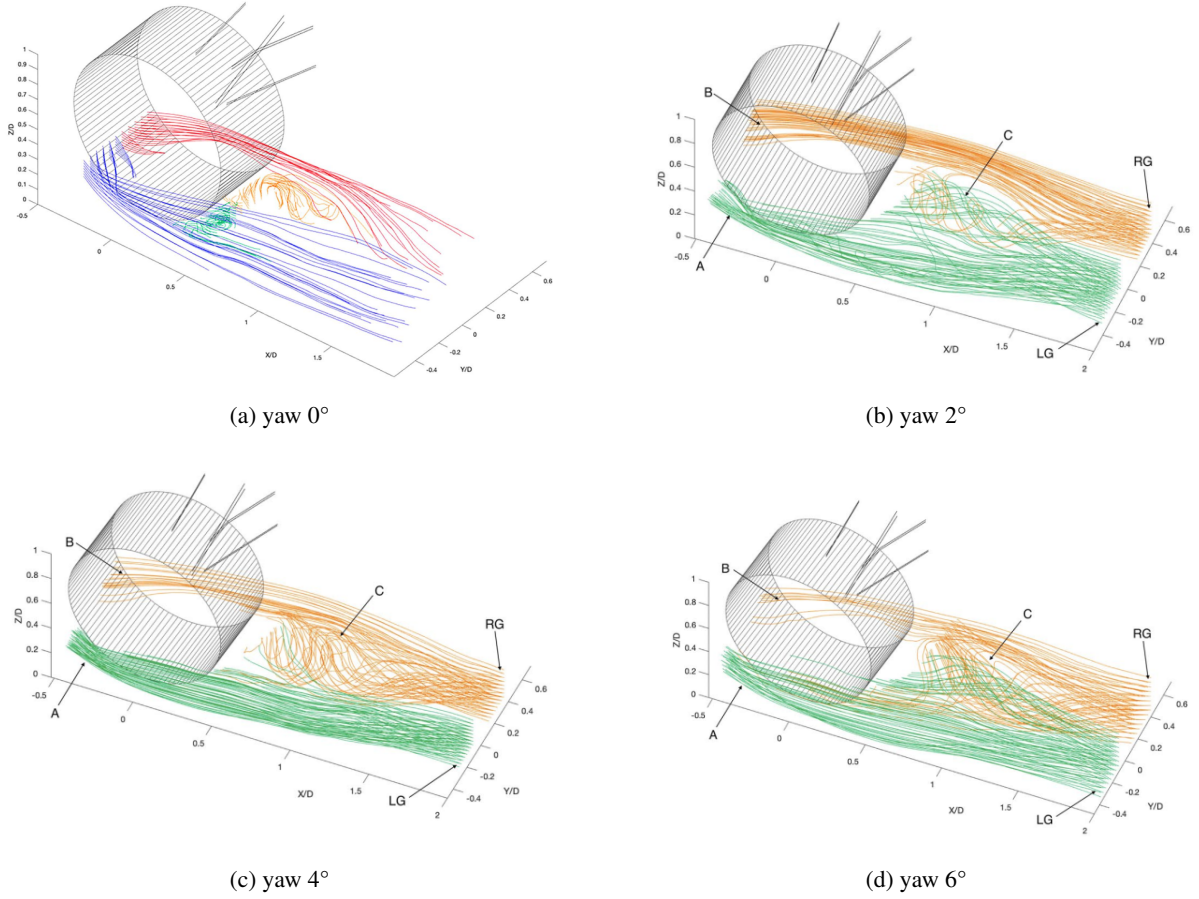


Figure 3.12: Streamlines averaged in time capturing the effect of yaw on the wake [9]

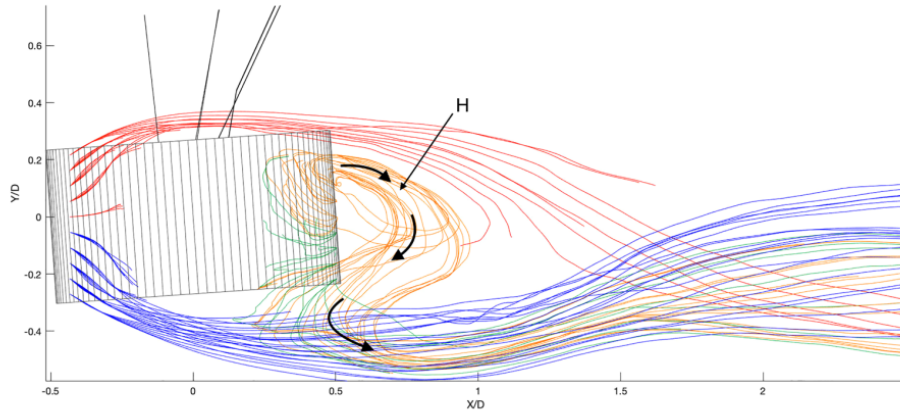
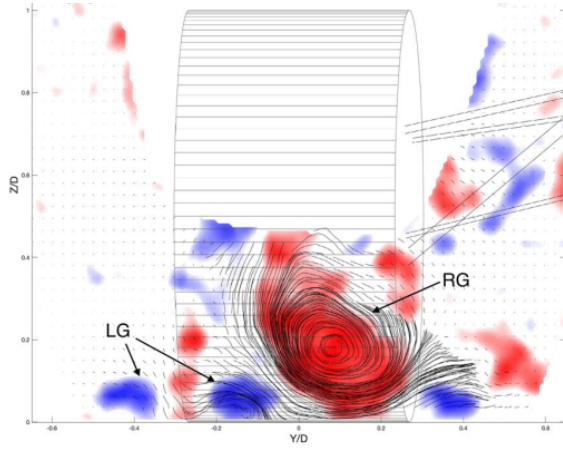
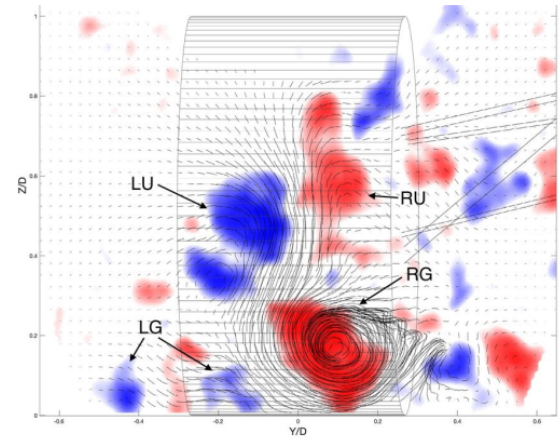


Figure 3.13: Top view of the averaged streamlines in the lower wake for a 4° yaw [9]

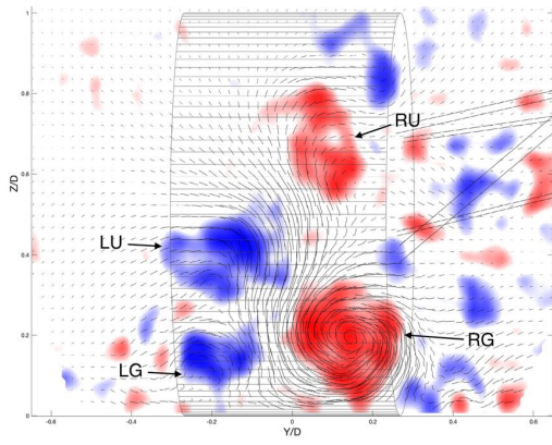
Furthermore, the progression of the wake downstream can be seen in [Figure 3.14](#). So, close to the wheel at $x/D = 0.7$ only ground vortices were present with the right one being large and dominant while the presence of the left ground vortex was almost negligible. Then further downstream the upper vortex pair appeared at $x/D = 1$ and slowly the left upper vortex started to merge with the left ground vortex further downstream until they merged at around $x/D = 1.6$. Note, that the right upper vortex stayed identifiable. This newly merged left ground vortex was of comparable size to the right ground vortex. Finally, further on the wake was dominated by a pair of counter-rotating vortices as seen at $x/D = 2.2$. Note, that another interesting aspect that they discovered was that yawing the wheel stabilised the wake as well.



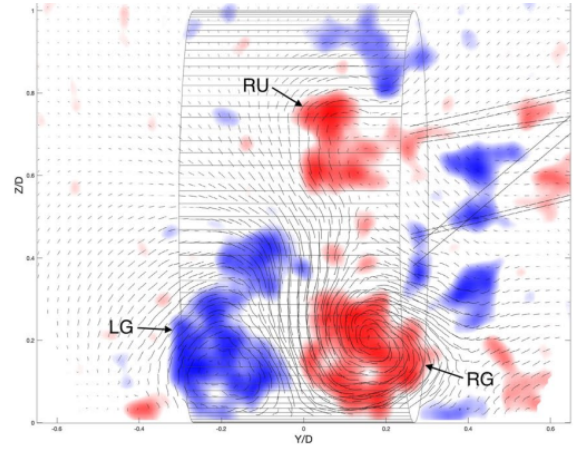
(a) $x/D = 0.7$



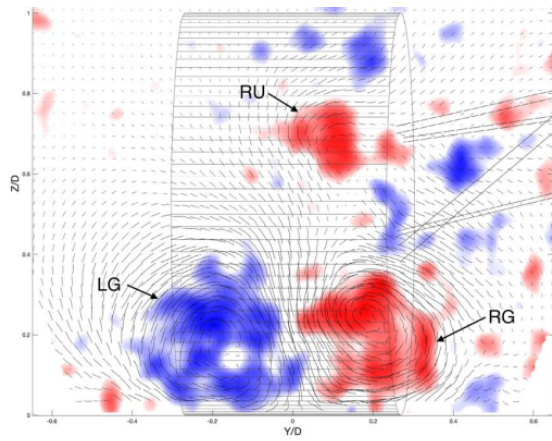
(b) $x/D = 1$



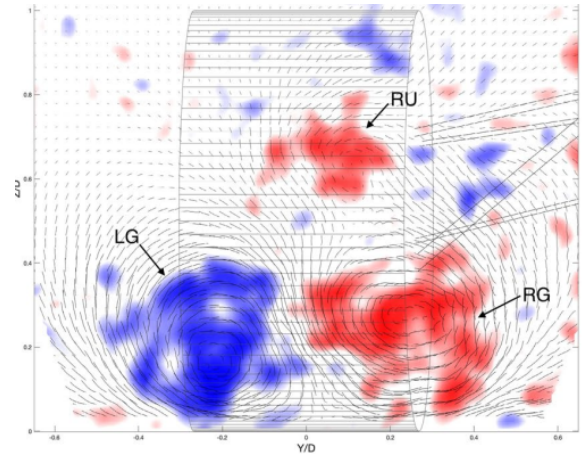
(c) $x/D = 1.3$



(d) $x/D = 1.6$



(e) $x/D = 1.9$



(f) $x/D = 2.2$

Figure 3.14: Streamlines averaged over 20 runs and Γ_2 cross-sectional contour plots at a yaw of -4° [9]

4. Literature Review: Modelling of Rotating Wheels

In this chapter, the approach of modelling rotating wheels in the literature is discussed with a focus on more detailed wheels, such as wheels with treads and rims as this requires more techniques to be modelled. This is explained more in-depth in [Section 4.1](#). Furthermore, approaches in modelling the contact patch area and the effect of general simplifications made are presented in [Section 4.2](#)

4.1 Modelling of a Detailed Rotating Wheel

The flow around a rotating wheel is complex, due to the small tire features and contact region with the ground. These require correct modelling making it necessary to accurately represent the wheel geometry and impose proper boundary conditions. In order to achieve accurate simulations it is important that one implements a sliding movement according to the speed of rotation on the mesh part that rotates. This is fairly simple to implement for the rims of the wheel. However, it becomes impossible to utilise in the case when a wheel has tires, due to the area, which is in contact with the ground deforming due to the experienced load as can be seen in [Figure 4.1a](#). This deformation results in the tire bulging out from the sides near the ground ([Figure 4.1b](#)) and a contact patch area ([Figure 4.2b](#)) [12].

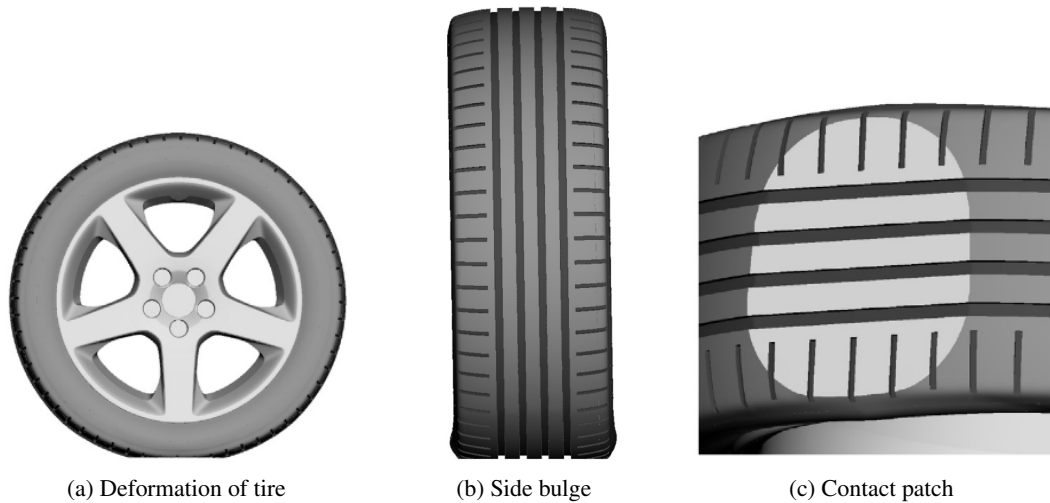


Figure 4.1: Deformation of the tire under the vehicle's load [12]

Generally, three different approaches to implement rotation in CFD are the Rotating Wall Boundary Condition (RWBC), Moving Reference Frame (MRF) and Sliding Mesh (SM) approach.

The easiest and most frequently used method of imposing a rotation is by means of RWBC. In this approach, one introduces a tangential velocity at the wall of the wheel. Note, that due to the conservation of mass, the normal velocity should equal zero creating a solid wall condition, as flow cannot physically pass through the object. The drawback of this is that complex geometrical parts of a wheel, such as the rim and lateral grooves on the tire cannot be correctly modelled. This is evident from [Figure 4.2](#), as the lateral grooves and the inside of the rim display lower velocities (note that the darker colours indicate lower velocities). This is caused by the fact that the surfaces are normal to the desired tangential velocity direction. Hence, when projecting the velocity vector to the surface, a significant part will be lost. Therefore, RWBC is recommended to only be used for simplified wheel geometries with a smooth/slick tire and closed rim. Only then will the obtained results be representative.

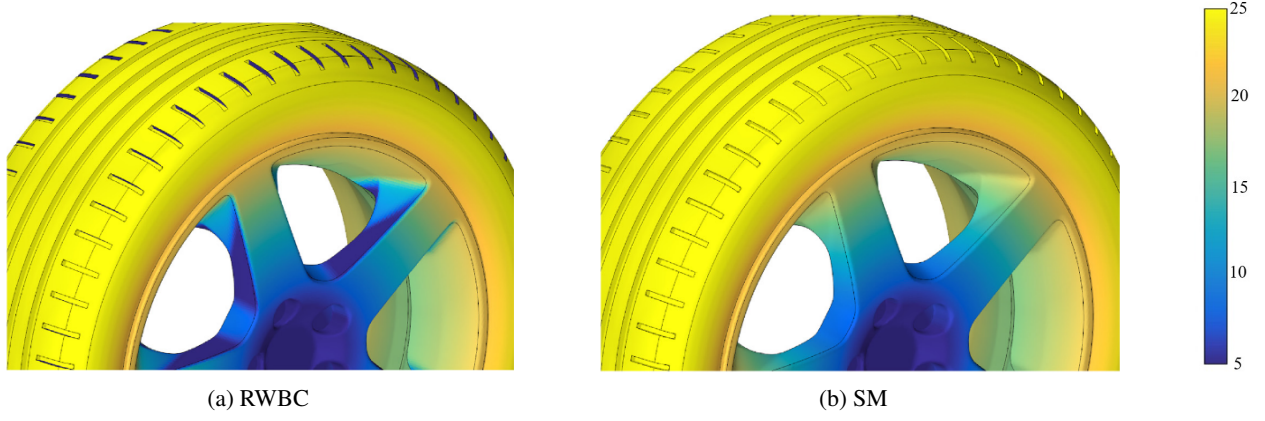


Figure 4.2: Visualisation of velocity distribution around a wheel for a RWBC and SM approach [12]

An effective method that solves this issue is the MRF. In this method, the fluid will be locally placed in a rotating reference frame. This fixes the issue encountered by the RWBC, due to the fact that it allows for normal velocity components. The incompressible Navier-Stokes equations in the moving frame of reference can be written for unsteady flows as follows:

$$\frac{\partial \vec{u}_R}{\partial t} + \frac{\partial \vec{\Omega}}{\partial t} \times \vec{r} + \nabla \cdot (\vec{u}_R \otimes \vec{u}_I) + \vec{\Omega} \times \vec{u}_I = -\nabla(p/\rho) + \nu \nabla \cdot \nabla(\vec{u}_I), \quad (4.1)$$

$$\nabla \cdot \vec{u}_I = 0,$$

with I and R indicating inertial and rotating respectively. Furthermore, $\vec{\Omega}$ is the vector of rotation and \vec{r} is the position vector originating from the origin of rotation all the way up to the mesh cell. However, note, that in an empty region containing uniform flow the equation reduces to

$$\nabla p = -\rho(\vec{\Omega} \times \vec{u}_I). \quad (4.2)$$

Therefore, there will be an additional value induced in the velocity, which will cause inaccuracies as seen in Figure 4.3a. Moreover, a major drawback of this method is that the obtained results are dependent on the wheel's initial position, due to the fact that the wheel itself is not moved when the MRF method is used.

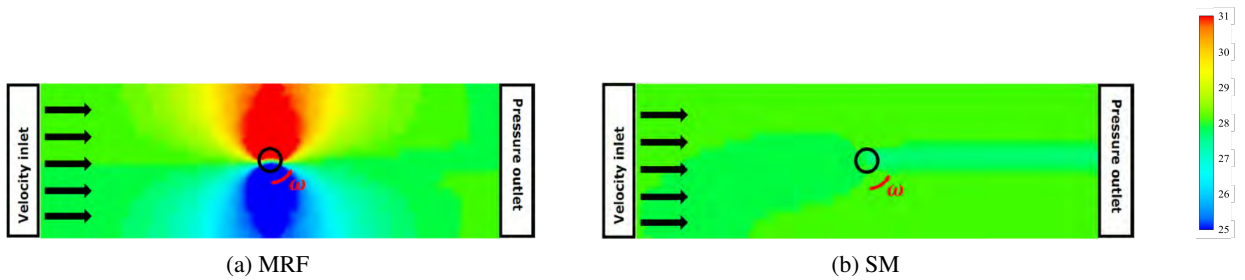


Figure 4.3: Empty rotating region comparison of MRF and SM [65]

One of the more costly methods when trying to model a rotating wheel is the SM method. This is the most realistic way to model a rotating wheel and is used in the research field. This unsteady modelling method requires the mesh to rotate each time step. However due to the side bulging and contact patch area, this method is not really feasible for tires. Therefore, it is usually applied to the rims. This method has a higher computational cost compared to the previous two mentioned, due to the movement of the mesh, which requires proper interfacing between the rotated and neighbouring fixed cells. This can take up to 50 % when the method is applied to the entire wheel and up to 20 % in runtime when it is applied to the rim only [12]. However, obviously, this is dependent on the parallelisation of the simulation and the number of cells used. Note, that the SM approach does not induce an extra gradient as can be seen in Figure 4.3b.

Finally, Hobeika and Sebben [12] proposed a method that combines the advantages of both the RWBC and MRF methods, which is called the MRFg method. As mentioned before the RWBC method falls short near the lateral grooves. So, these areas where the rotational effects are the largest will make use of the MRF approach (lateral grooves). Furthermore, RWBC is applied to the external tire area where the tangential velocity correctly projects on the surface. By combining these two approaches, an SM method is not needed, which saves computational time. Note, that MRFg is independent of modelling the rim. So, SM could still be used for rim rotation when using MRFg. It is concluded that the MRFg in the case of an isolated wheel when compared to full SM simulations yields accurate results with less computational time, making it a good alternative approach.

Reiß et al. [66] implemented this proposed MRFg method when performing Delayed Detached Eddy Simulation (DDES) with Open Source Field Operation and Manipulation (OpenFOAM) V1712+ by ESI-OpenCFD. They also performed experiments to validate the results of these simulations to prove the applicability of the proposed method. The first simulations performed were for a lifted rotating wheel where the most accurate results in this case were obtained by applying the SM method to the rim and tire. With these results, they compared the hybrid approach, which produced similar results. This indicated that the MRFg method is an efficient and reliable way to perform the simulations.

The next step they took was performing simulations for a rotating wheel in contact with the ground. They compared the results for two types of wheels. One consisting of only longitudinal grooves and one consisting of both longitudinal and lateral grooves. Before they performed the simulations, the wheel was deformed by the weight of an Audi A4 2015 model and 3D scanned. Moreover, the contour of the contact patch was captured as well using a scanned silicone paste imprint. This allowed for a more accurate model of the bulge and contact patch. The obtained results of the simulations showed that the presence of a tread resulted in a higher pressure in the longitudinal grooves, which yielded higher lift compared to a tire without lateral grooves. Moreover, a higher pressure region was found upstream of the contact patch area of the treaded wheel, due to less mass flow passing through the longitudinal grooves. Thus leading to more jetting. In addition, stronger vortices were observed near the contact patch and bulge resulting in a wider wake there locally. Finally, in the case of a treaded tire smaller vortices were observed at the top of the tire shoulder, which improved the flow attachment.

At last, to obtain even more accurate results a model with dynamic tire deformation was investigated. This displayed the importance of capturing the actual tire geometry. So, the deformations were not negligible. The effect of the dynamic deformation of the tire seemed to have a decreasing effect on the vehicle drag. This was confirmed by investigating a dynamic deformed tire with longitudinal grooves. A reduction of $\Delta C_D = 0.004$ was observed. However, when investigating a treaded dynamically deformed tire an increase of $\Delta C_D = 0.001$ was observed on the vehicle drag. Hence, the presence of treads increased the vehicle drag by $\Delta C_D = 0.005$. Furthermore, larger effects were found with respect to the lift as both dynamic deformation and the treads seemed to increase the C_L of the vehicle. Thus, the conclusion is that the accurate modelling of the wheel geometry including the tire patterns and deformation is a must to obtain accurate results.

A follow-up research performed by Reiß et al. [67] performed a numerical and experimental investigation for different tire and rim configurations. Experimentally the wake was captured by means of PIV, which serves as validation material for the DDES simulations performed in OpenFOAM v1712+. The aim of this research was to provide insight into the complex wake around a rotating wheel. For the simulation a SM method is implemented for the rim and the MRF is implemented for the lateral grooves. Furthermore, the geometry of the rotating wheel under deformation is measured to get the results as close to the experiment as possible, which is the same approach as by Reiß et al. [66].

Three different tires and six different rims were investigated in this research. In the wind tunnel early on the high drag combinations of tire and rim compared to other configurations were detected. From the results it was concluded from comparing the simulations to the experimental results, that the simulation method required improvement to predict the flowfield in the wake area, even though the fairly good predictions of the changes in drag.

Zhou et al. [68] investigated the aerodynamic characteristics of isolated loaded tires having different tread patterns experimentally and numerically by means of RANS using the $k - \omega$ SST model and DES simulations. They researched three different tire types. Namely, straight lateral grooves, axis symmetrical and point sym-

metrical grooves. An overview of the different tread patterns is presented in [Figure 4.4](#). Note, that the view is from below the wheel. So, the contact patch is visible.

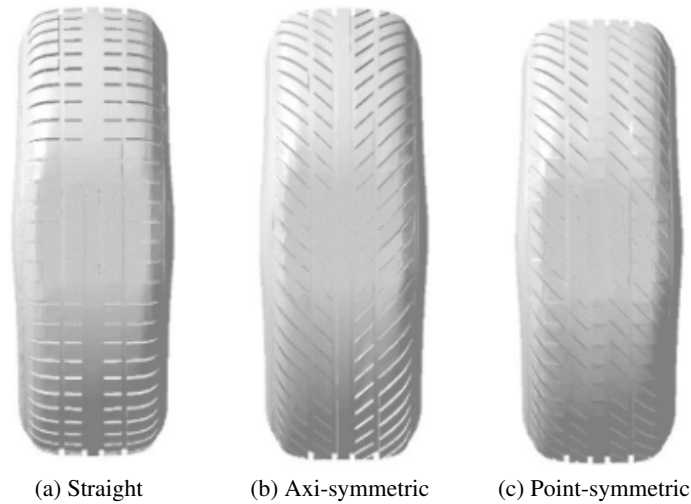


Figure 4.4: The three different tread patterns [\[68\]](#)

They concluded that the angle of a tire lateral groove affects the vortices generated, the pressure and the flow-field. The more the angle of the lateral groove aligns with the freestream flow direction, the values of surface pressure and drag become less. However, one should keep in mind that the conclusion drawn is made based on a half-wheel. Obviously, an entire wheel will have a different flowfield worth investigating. Furthermore, the effect of rotation was not investigated as well, which also is worth investigating in the future.

Another method of modelling the tire tread that can yield fairly accurate results is the Immersed-Boundary-Method (IBM) together with the Lattice-Boltzmann Method (LBM). This was implemented by Lew et al. [\[69\]](#) and the simulations were set up to closely match the experiment of Schnepf et al. [\[70\]](#). This method showed encouraging results compared to a typical rotating RWBC.

Note, that in the simulations of Lew et al. [\[69\]](#), the tires were in an unloaded state. Hence, the tire bulge caused by a load was absent and this bulge plays an important role in determining the wake shape near the ground [\[70\]](#). So, the bulge's absence leads to a different flowfield near the ground. Also, the load on a wheel determines the size of the contact patch area, which again could affect the flow near the ground if the contact patch area is not the correct size as the wheel is not deformed.

Therefore, a follow-up study was performed by Mortazawy et al. [\[71\]](#), which makes use of the IBM and LBM for a standalone and deforming treaded tire. The state of the deformed tire could either be obtained from a scan of a similar experiment or from Computer-Aided Design (CAD) software. The obtained results displayed a considerable improvement and encouraging results regarding the mean total pressure right behind the tire and at the contact patch. Furthermore, the floor wake structures found were closer to that of the experiment.

4.2 The Effects of Simplifications

When one wants to numerically investigate the aerodynamic forces and flow features of a rotating wheel, generally simplifications and compromises are made. The effects of these commonly used methods are investigated by Diasinos et al. [\[72\]](#) regarding four different aspects. Namely, the geometric fidelity in the wheel hub regions, the modelling of the contact patch, the ground representation and the effect of rotation on separation. In this section, only the first two points will be discussed. Note, that the performed simulations are RANS. So, the effects of the simplifications could be even amplified for unsteady flows.

4.2.1 Modelling of the Contact Patch

An important and difficult aspect of simulating rotating wheels is the modelling of the contact patch area. This area would require highly fine mesh cells and usually the result is highly skewed cells in that area, which leads to a mesh of bad quality. A common method as proposed by Diasinos et al. [72] is the step size approach. A schematic sketch of this approach is presented in Figure 4.5a. This approach allows for more control over the mesh resulting in non-skewed cells as can be seen in Figure 4.5b, which in turn yields more reliable converged results.

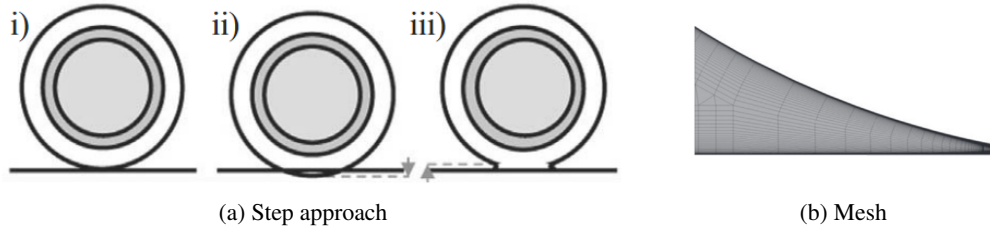


Figure 4.5: The step size approach by Diasinos et al. [72]

It was observed that even the most minor changes in modelling the step had a major impact on the thickness of the wake and the aerodynamic forces. An increased step resulted in a narrower wake, which affects the force coefficients. A sensitivity study of C_L and C_D with respect to the step size is presented in Figure 4.6. As can be seen, it is of high importance to assess the step size beforehand since it can affect up to 30% of the lift value if it is a bigger size patch.

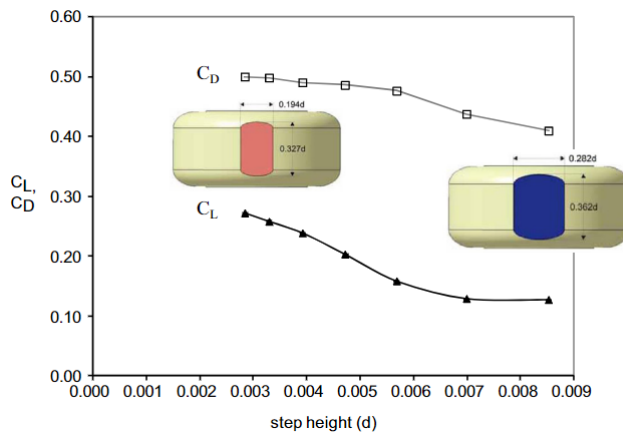


Figure 4.6: C_L and C_D plotted against the step height by Diasinos et al. [72]

Other approaches used in the literature are e.g. cutting the wheel at an appropriate ground level trying to obtain the correct area of the contact patch, such as performed by Croner et al. [64] or scanning the wheel to obtain a highly accurate model like Reiß et al. [66, 67].

4.2.2 Influence of the Wheel Hub and Shoulder Geometry

Another major aspect investigated by Diasinos et al. [72] was the influence of the wheel hubs on a rotating wheel. As in some literature wheel hubs are removed, which means basically rotating cylinders with "shoulders" are simulated as is the case with e.g. Axon et al. [73]. Figure 4.7 displays the wheel geometries used for these simulations.

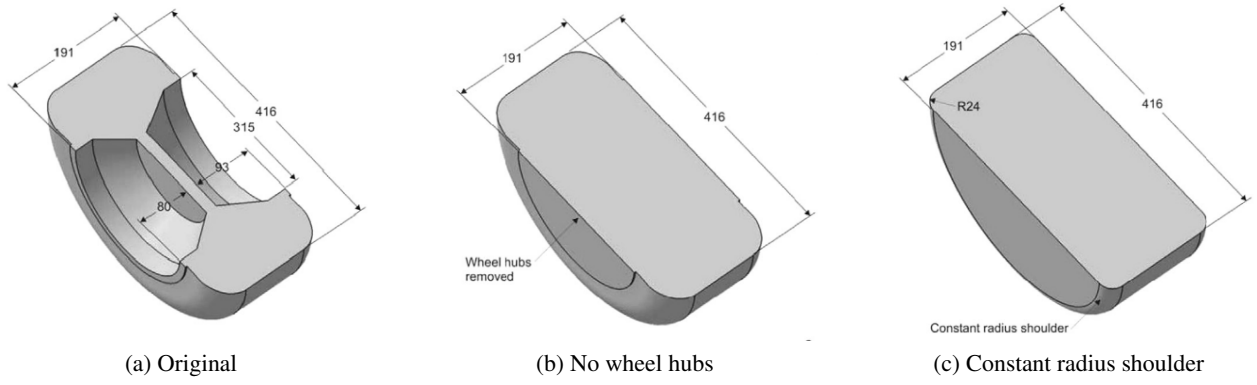


Figure 4.7: The three different wheel geometries [72]

From the results it was observed that the removal of the wheel hubs yielded major changes in the lift ($\approx 30\%$ less). However, less change in the drag ($\approx 8\%$) even though it had a significant effect on the wake. In addition, a constant-radius wheel shoulder had a similar impact of $\approx 30\%$ on the lift. So, one could not just use a cylindrical shape (wheel without hubs) to simulate the effects of a wheel with hubs. Moreover, two additional significantly smaller vortices were observed in the near wake of the wheel without hubs. This additional vortex pair was also observed by Pirozoli et al. [45], which means that it is a characteristic of the cylindrical shape itself. These additional vortices are formed by the shear interaction with the wheel's side walls and dissipate downstream leaving the initial two other vortex pairs at the top and bottom. Also, the wheel without hubs produced a taller narrower wake compared to the original due to the separation point moving approximately 5° forward.

5. Numerical Methodology

In this chapter, the RANS turbulence models are described in [Section 5.1](#). Furthermore, OpenFOAM and the relevant schemes used are described in [Section 5.2](#). [Section 5.3](#) presents the mesh software that will be used in the thesis and the use of the solver is validated step by step in [Section 5.4](#).

5.1 Reynolds-Averaged Navier-Stokes

Turbulence models are required due to the fact that DNS requires too much computational power. Hence, in the case of RANS the entire effect of turbulence is modelled. The RANS equations are derived from the incompressible Navier-Stokes equations for an isotropic fluid with the constant fluid properties of density and viscosity. The equations of conservation of mass and momentum in Cartesian coordinates are presented in [Equation 5.1](#) and [Equation 5.2](#):

$$\frac{\partial u_i}{\partial x_i} = 0, \quad (5.1)$$

$$\rho \frac{\partial u_i}{\partial t} + \rho u_j \frac{\partial u_i}{\partial x_j} = -\frac{\partial p}{\partial x_i} + \frac{\partial t_{ij}}{\partial x_j}. \quad (5.2)$$

With u_i being the velocity, x_i being the position, t being the time, ρ being the density and t_{ij} being the viscous stress tensor, which is defined as $t_{ij} = 2\mu S_{ij}$. The μ is the molecular viscosity of the fluid and S_{ij} is known as the strain-rate tensor:

$$S_{ij} = \frac{1}{2} \left(\frac{\partial u_i}{\partial x_j} + \frac{\partial u_j}{\partial x_i} \right). \quad (5.3)$$

The principle of RANS is based on the concepts introduced by Reynolds. This consists of the decomposition of u_i into a mean and fluctuating part:

$$u_i = \langle u_i \rangle + u'_i \quad (5.4)$$

with the mean being defined as the ensemble-averaged solution $\langle u_i \rangle = \frac{1}{N} \sum_{\mu=1}^N u_i \Big|_{\mu}$, or as follows in the case of statistically stationary processes $\langle u_i \rangle = \lim_{t \rightarrow \infty} \frac{1}{t} \int_0^t u_i(t') dt'$.

The next step is to substitute the decomposed velocity into the Navier-Stokes equation and apply an averaging operator to the equations. However, prior to that one can rewrite the convective term to simplify the averaging process. This yields the following convective term:

$$u_j \frac{\partial u_i}{\partial x_j} = \frac{\partial}{\partial x_j} (u_j u_i) - u_i \frac{\partial u_j}{\partial x_j} = \frac{\partial}{\partial x_j} (u_j u_i) \quad (5.5)$$

with the second term dropping out due to [Equation 5.1](#). Note, that the average of the mean is still the mean and that the average of the fluctuation equals zero. Furthermore, applying the average operator, dividing by ρ and rearranging the equations results in the RANS equations:

$$\frac{\partial \langle u_i \rangle}{\partial x_i} = 0, \quad (5.6)$$

$$\frac{\partial \langle u_i \rangle}{\partial t} + \frac{\partial}{\partial x_j} (\langle u_j \rangle \langle u_i \rangle) + \frac{1}{\rho} \frac{\partial \langle p \rangle}{\partial x_i} = \frac{\partial}{\partial x_j} (2\nu \langle S_{ji} \rangle - \langle u'_j u'_i \rangle). \quad (5.7)$$

Here $-\langle u'_i u'_j \rangle$ is defined as the specific Reynolds stress tensor τ_{ij} , which indicates the rate of momentum transfer due to turbulence averaged over time and must be entirely modelled in the case of RANS simulations. Also, due to the tensor being symmetric, the following relation holds: $\tau_{ij} = \tau_{ji}$ [74].

Due to the Reynolds averaging, one introduces a closure problem as there are more unknowns than equations. Therefore, a transport equation can be derived for τ_{ij} by multiplying the momentum equation in the i -direction

with the fluctuating component in the j -direction u'_j and the momentum equation in the j -direction by the fluctuating component of the i -direction u'_i . Then adding the results and applying an average operator results in:

$$\langle u'_i \mathcal{N}(u_j) + u'_j \mathcal{N}(u_i) \rangle = 0 \quad (5.8)$$

with $\mathcal{N}(u_i)$ being a Navier-Stokes operator:

$$\mathcal{N}(u_i) = \rho \frac{\partial u_i}{\partial t} + \rho u_k \frac{\partial u_i}{\partial x_k} + \frac{\partial p}{\partial x_i} - \mu \frac{\partial^2 u_i}{\partial x_k \partial x_k}. \quad (5.9)$$

Rearranging the terms and dividing by ρ results in a transport equation for τ_{ij} :

$$\frac{\partial \tau_{ij}}{\partial t} + \langle u_k \rangle \frac{\partial \tau_{ij}}{\partial x_k} = P_{ij} + \varepsilon_{ij} - \Pi_{ij} + \frac{\partial}{\partial x_k} \left[\nu \frac{\partial \tau_{ij}}{\partial x_k} + C_{ijk} \right]. \quad (5.10)$$

$$P_{ij} = - \left(\tau_{ik} \frac{\partial \langle u_j \rangle}{\partial x_k} + \tau_{jk} \frac{\partial \langle u_i \rangle}{\partial x_k} \right) \quad (5.11)$$

$$\varepsilon_{ij} = 2\nu \left\langle \frac{\partial u'_i}{\partial x_k} \frac{\partial u'_j}{\partial x_k} \right\rangle \quad (5.12)$$

$$\Pi_{ij} = \left\langle \frac{p'}{\rho} \left(\frac{\partial u'_i}{\partial x_j} + \frac{\partial u'_j}{\partial x_i} \right) \right\rangle \quad (5.13)$$

$$C_{ijk} = \langle u'_i u'_j u'_k \rangle + \frac{1}{\rho} (\langle p' u'_i \rangle \delta_{jk} + \langle p' u'_j \rangle \delta_{ik}) \quad (5.14)$$

with $\langle u_k \rangle \partial \tau_{ij} / \partial x_k$ being the advection term, P_{ij} being the production term, ε_{ij} representing the dissipation, Π_{ij} giving the pressure strain correlation and the last term of Equation 5.10 describing the diffusion. Note, the diffusion can be divided into a viscous diffusion:

$$\nu \frac{\partial^2 \tau_{ij}}{\partial x_k \partial x_k}, \quad (5.15)$$

a turbulent diffusion:

$$\frac{\partial \langle u'_i u'_j u'_k \rangle}{\partial x_k} \quad (5.16)$$

and a diffusion due to pressure:

$$\frac{1}{\rho} \frac{\partial}{\partial x_k} (\langle p' u'_i \rangle \delta_{jk} + \langle p' u'_j \rangle \delta_{ik}). \quad (5.17)$$

As can be seen when setting up the transport equation for τ_{ij} , six new equations together with 22 new unknowns are generated. This requires turbulence modelling, which makes use of empirical approximations to be able to solve this.

There are two main categories of turbulence models. Namely, the eddy viscosity models and the Reynolds stress models. The first one can be categorised in 0-equation models, one or more transport equations or non-linear models. The principle behind them is that due to turbulence leading to momentum exchange between fluid elements, it can be assumed that τ_{ij} is proportional to the mean strain rate by a constant, named the eddy viscosity. So, the aforementioned Equation 5.10 — Equation 5.17 are not solved in this case and the following approximation is made for the specific Reynolds-stress tensor:

$$\tau_{ij} \cong 2\nu_T S_{ij} - \frac{2}{3} \delta_{ij} k \quad (5.18)$$

with ν_T being the eddy viscosity, S_{ij} being the mean strain rate, δ_{ij} being the Kronecker delta and k being the turbulence kinetic energy, which is defined as follows:

$$k \equiv \frac{1}{2} \langle u'_i u'_i \rangle = \frac{1}{2} (\langle u'^2 \rangle + \langle v'^2 \rangle + \langle w'^2 \rangle) \quad (5.19)$$

which as can be seen is the sum of the three specific normal Reynolds stress components in the x -, y - and z -direction respectively. Following this relevant turbulence models will be discussed that will be used eventually for the solver validation and wheel simulation. These turbulence models are the one-equation Spalart-Allmaras model and the two-equations RKE and $k - \omega$ SST.

5.1.1 Spalart-Allmaras

Spalart and Allmaras introduced a one-equation turbulence model [75], which is commercially used significantly, due to its robustness and simulation time. The transport equation for the eddy viscosity is presented in Equation 5.20 followed by the corresponding definitions and model constants in Table 5.1:

$$\frac{\partial \tilde{\nu}}{\partial t} + u_j \frac{\partial \tilde{\nu}}{\partial x_j} = c_{b1} (1 - f_{t2}) \tilde{S} \tilde{\nu} - \left[c_{w1} f_w - \frac{c_{b1}}{\kappa^2} f_{t2} \right] \left(\frac{\tilde{\nu}}{d} \right)^2 + \frac{1}{\sigma} \left[\frac{\partial}{\partial x_j} \left((v + \tilde{\nu}) \frac{\partial \tilde{\nu}}{\partial x_j} \right) + c_{b2} \frac{\partial \tilde{\nu}}{\partial x_i} \frac{\partial \tilde{\nu}}{\partial x_i} \right] + f_{t1} \Delta U^2, \quad (5.20)$$

$$v_T = \tilde{\nu} f_{u1}, \quad (5.21)$$

$$f_{v1} = \frac{\chi^3}{\chi^3 + c_{v1}^3}, \quad (5.22)$$

$$\chi = \frac{\tilde{\nu}}{v}, \quad (5.23)$$

$$\tilde{S} = \sqrt{2\Omega_{ij}\Omega_{ij}} + \frac{\tilde{\nu}}{\kappa^2 d^2} f_{v2}, \quad (5.24)$$

$$f_{v2} = 1 - \frac{\chi}{1 + \chi f_{v1}}, \quad (5.25)$$

$$f_w = g \left[\frac{1 + C_{w3}^6}{g^6 + C_{w3}^6} \right]^{\frac{1}{6}}, \quad (5.26)$$

$$g = r + C_{w2} (r^6 - r), \quad (5.27)$$

$$r \equiv \frac{\tilde{\nu}}{\tilde{S} \kappa^2 d^2}, \quad (5.28)$$

with d being the distance closest to the surface

$$f_{t1} = C_{t1} g_t e^{-C_{t2} \frac{\omega_t^2}{\Delta U^2} [d^2 + g_t^2 d_t^2]}, \quad (5.29)$$

$$f_{t2} = C_{t3} e^{-C_{t4} \chi^2}. \quad (5.30)$$

Table 5.1: S-A model constants

| Constant | Value |
|----------|---|
| σ | $\frac{2}{3}$ |
| κ | 0.41 |
| c_{b1} | 0.1355 |
| c_{b2} | 0.622 |
| c_{w1} | $\frac{c_{b1}}{\kappa^2} + \frac{(1+c_{b2})}{\sigma}$ |
| c_{w2} | 0.3 |
| c_{w3} | 2 |
| c_{v1} | 7.1 |
| c_{t1} | 1 |
| c_{t2} | 2 |
| c_{t3} | 1.1 |
| c_{t4} | 2 |

5.1.2 Realizable $k - \varepsilon$

The RKE is a two-equation model that closes the RANS equations by adding a transport equation for k and ε modified from the originally developed $k - \varepsilon$ by Jones et al. [76]. The RKE model is shown to perform better for rotational flows, large separation regions, boundary layers encountering adverse pressure gradients and recirculation bubbles [77]. That is why it is a commonly chosen turbulence model during the simulation of rotating wheels. The transport equations of k and ε are presented in the following equations respectively:

$$\frac{\partial}{\partial t}(\rho k) + \frac{\partial}{\partial x_i}(\rho k u_i) = \frac{\partial}{\partial x_j} \left[\left(\mu + \frac{\mu_T}{\sigma_k} \right) \frac{\partial k}{\partial x_j} \right] + P_k + P_b - \rho \varepsilon - Y_M + S_k, \quad (5.31)$$

$$\frac{\partial}{\partial t}(\rho \varepsilon) + \frac{\partial}{\partial x_j}(\rho \varepsilon u_j) = \frac{\partial}{\partial x_j} \left[\left(\mu + \frac{\mu_T}{\sigma_\varepsilon} \right) \frac{\partial \varepsilon}{\partial x_j} \right] + \rho C_1 S \varepsilon - \rho C_2 \frac{\varepsilon^2}{k + \sqrt{\nu \varepsilon}} + C_{1\varepsilon} \frac{\varepsilon}{k} C_{3\varepsilon} P_b + S_\varepsilon, \quad (5.32)$$

with

$$C_1 = \max \left[0.43, \frac{\eta}{\eta + 5} \right], \quad (5.33)$$

$$\eta = S \frac{k}{\varepsilon}, \quad (5.34)$$

$$S = \sqrt{2 S_{ij} S_{ij}}. \quad (5.35)$$

The turbulent viscosity term is modelled as follows:

$$\mu_T = \rho C_\mu \frac{k^2}{\varepsilon} \quad (5.36)$$

with

$$\frac{1}{A_0 + A_s \frac{k U^*}{\varepsilon}}, \quad (5.37)$$

$$U^* \equiv \sqrt{S_{ij} S_{ij} + \tilde{\Omega}_{ij} \tilde{\Omega}_{ij}}, \quad (5.38)$$

$$\tilde{\Omega}_{ij} = \Omega_{ij} - 2 \varepsilon_{ijk} \omega_k, \quad (5.39)$$

$$\Omega_{ij} = \overline{\Omega_{ij}} - \varepsilon_{ijk} \omega_k, \quad (5.40)$$

$$A_s = \sqrt{6} \cos \phi, \quad (5.41)$$

$$\phi = \frac{1}{3} \cos^{-1}(\sqrt{6}W), \quad (5.42)$$

$$W = \frac{S_{ij}S_{jk}S_{ki}}{\tilde{S}^3}, \quad (5.43)$$

$$\tilde{S} = \sqrt{S_{ij}S_{ij}}. \quad (5.44)$$

The RKE model constants are presented in [Table 5.2](#).

Table 5.2: RKE model constants

| Constant | Value |
|----------------------|-------|
| A_0 | 4.04 |
| $C_{1\varepsilon}$ | 1.44 |
| C_2 | 1.9 |
| σ_k | 1.0 |
| σ_ε | 1.2 |

5.1.3 $k - \omega$ SST

Another two-equation turbulence model, which is commonly used in engineering applications is the $k - \omega$ SST [78]. This model requires the transport equations of k and ω to be solved, with ω being the specific dissipation rate and it combines the best of both worlds regarding the $k - \varepsilon$ and $k - \omega$ model by means of a blending function. The relevant equations regarding the $k - \omega$ SST are presented respectively as follows:

$$\mu_T = \frac{\rho \alpha_1 k}{\max(\alpha_1 \omega, SF_2)}, \quad (5.45)$$

$$\frac{\partial(\rho k)}{\partial t} + \frac{\partial(\rho u_j k)}{\partial x_j} = \tau_{ij} \frac{\partial u_i}{\partial x_j} - \beta^* \rho \omega k + \frac{\partial}{\partial x_j} \left[(\mu + \sigma_k \mu_T) \frac{\partial k}{\partial x_j} \right], \quad (5.46)$$

$$\frac{\partial(\rho \omega)}{\partial t} + \frac{\partial(\rho u_j \omega)}{\partial x_j} = \frac{\gamma}{\nu_T} \tau_{ij} \frac{\partial u_i}{\partial x_j} - \beta \rho \omega^2 + \frac{\partial}{\partial x_j} \left[(\mu + \sigma_\omega \mu_T) \frac{\partial \omega}{\partial x_j} \right] + 2(1 - F_1) \frac{\rho \sigma_{\omega 2}}{\omega} \frac{\partial k}{\partial x_j} \frac{\partial \omega}{\partial x_j}, \quad (5.47)$$

with the closure coefficients and auxiliary relations being:

$$\tau_{ij} = \mu_T \left(\frac{\partial u_i}{\partial x_j} + \frac{\partial u_j}{\partial x_i} - \frac{2}{3} \frac{\partial u_k}{\partial x_k} \delta_{ij} \right) - \frac{2}{3} \rho k \delta_{ij}, \quad (5.48)$$

$$\phi = F_1 \phi_1 + (1 - F_1) \phi_2, \quad (5.49)$$

$$F_1 = \tanh \left\{ \left\{ \min \left[\max \left(\frac{\sqrt{k}}{\beta^* \omega d}, \frac{500 \nu}{d^2 \omega} \right), \frac{4 \rho \sigma_{\omega 2} k}{CD_{k\omega} d^2} \right] \right\}^4 \right\}, \quad (5.50)$$

$$F_2 = \tanh \left[\left[\max \left(\frac{2\sqrt{k}}{\beta^* \omega d}, \frac{500\nu}{d^2 \omega} \right) \right]^2 \right], \quad (5.51)$$

$$CD_{k\omega} = \max \left(2\rho \sigma_{\omega 2} \frac{1}{\omega} \frac{\partial k}{\partial x_j} \frac{\partial \omega}{\partial x_j}, 10^{-20} \right). \quad (5.52)$$

Also, for the $k - \omega$ SST model there are model constants, which are presented in [Table 5.3](#).

Table 5.3: $k - \omega$ SST model constants

| Constant | Value |
|---------------------|---|
| β^* | 0.09 |
| β_1 | 0.075 |
| β_2 | 0.0828 |
| γ_1 | $\frac{\beta_1}{\beta^*} - \frac{\sigma_{\omega 1} \kappa^2}{\sqrt{\beta^*}}$ |
| γ_2 | $\frac{\beta_2}{\beta^*} - \frac{\sigma_{\omega 2} \kappa^2}{\sqrt{\beta^*}}$ |
| κ | 0.41 |
| σ_{k1} | 0.85 |
| σ_{k2} | 1 |
| $\sigma_{\omega 1}$ | 0.65 |
| $\sigma_{\omega 2}$ | 0.856 |
| a_1 | 0.31 |

5.2 OpenFOAM

OpenFOAM is an open-source library written in C++, that contains multiple solvers one may choose from to perform CFD simulations. One of its unsteady solvers is PimpleFOAM, which is a large-step incompressible transient solver, utilising the PIMPLE algorithm [79]. The PIMPLE algorithm is a merge between the Pressure Implicit with Splitting of Operators (PISO) and Semi-Implicit Method for Pressure Linked Equations (SIMPLE) algorithms. Note, that the PISO algorithm is used in transient simulations, while SIMPLE is used for steady-state simulations.

Furthermore, there are several schemes that one can choose for the discretised Navier-Stokes equations. These are different time, gradient, divergence, laplacian and surface normal gradient schemes, which are explained in the following subsections respectively.

5.2.1 Time Schemes

The time scheme that solves for the first order time derivative ($\partial/\partial t$), which is indicated as `ddtSchemes` in the `fvSchemes` file is chosen to be the **backward Euler** method. Also known as the implicit Euler method, this method has a second-order accuracy and is known to be stable since it is an implicit method. Note, for steady-state simulations the scheme **steadyState** should be chosen.

5.2.2 Gradient Schemes

In the `fvSchemes` file the gradient schemes are defined under `gradSchemes`. The gradients (∇) are solved by the **Gauss linear** numerical scheme, with Gauss being the finite volume discretisation of the Gauss integration. This finite volume scheme requires interpolation between cell centre and face centre values. This is specified to be executed linearly by the term `linear`.

5.2.3 Divergence Schemes

The divergence schemes are specified by `divSchemes`. The divergence terms ($\nabla \cdot$) could only be solved by the **Gauss** numerical scheme. However, the interpolation schemes must be specified by the user, which again is chosen to be **linear**.

5.2.4 Laplacian Schemes

The Laplacian schemes are specified by `laplacianSchemes`. The Laplacian ($\Delta = \nabla^2$) terms are solved using **Gauss linear corrected**.

5.2.5 Surface Normal Gradient Schemes

The scheme chosen is the **corrected** scheme, with the term corrected indicating an explicit non-orthogonal correction [79].

An overview of the schemes used for the solver validation simulations with the S-A and $k - \omega$ SST turbulence models can be found in Table 5.4 and Table 5.5 respectively. The solver settings for these validation cases are given in Table 5.6 and Table 5.7. The numerical schemes used for the wheel simulations and the parameters are discussed more in detail further in Section 6.5.

Table 5.4: Numerical schemes for the 2D isolated cylinder simulations at $Re_D = 1 \cdot 10^6$ using S-A

| | |
|-----------------------------------|----------------------------|
| <code>ddtSchemes</code> | backward |
| <code>gradSchemes</code> | Gauss linear |
| <code>div(phi,U)</code> | Gauss linearUpwind grad(U) |
| <code>div(phi,v)</code> | Gauss linear |
| <code>laplacianSchemes</code> | Gauss linear corrected |
| <code>interpolationSchemes</code> | linear |
| <code>snGradSchemes</code> | corrected |

Table 5.5: Numerical schemes for the 2D isolated cylinder simulations at $Re_D = 1 \cdot 10^6$ using $k - \omega$ SST

| | |
|-----------------------------------|----------------------------|
| <code>ddtSchemes</code> | backward |
| <code>gradSchemes</code> | Gauss linear |
| <code>div(phi,U)</code> | Gauss linearUpwind grad(U) |
| <code>div(phi,k)</code> | Gauss linear |
| <code>div(phi,omega)</code> | Gauss linear |
| <code>laplacianSchemes</code> | Gauss linear corrected |
| <code>interpolationSchemes</code> | linear |
| <code>snGradSchemes</code> | corrected |

Table 5.6: Solver settings using S-A

| Solver | |
|------------------------------|---|
| p | solver: GAMG smoother: DICGaussSeidel tolerance: 1e-6 relTol: 0.01 |
| U, \tilde{v} | solver: smoothSolver smoother: symGaussSeidel tolerance: 1e-6 relTol: 0.01 |
| $U, \tilde{v}(\text{final})$ | solver: smoothSolver smoother: symGaussSeidel tolerance: 1e-8 relTol: 0 |
| PIMPLE | |
| nCorrectors | 2 |
| nNonOrthogonal-Correctors | 0 |
| pRefCell | 0 |
| pRefValue | 0 |
| Relaxation factors | |
| fields | — |
| equations | — |

Table 5.7: Solver settings using $k - \omega$ SST

| Solver | |
|---------------------------|---|
| p | solver: GAMG smoother: DICGaussSeidel tolerance: 1e-6 relTol: 0.01 |
| U, k | solver: smoothSolver smoother: symGaussSeidel tolerance: 1e-6 relTol: 0.01 |
| U, k (final) | solver: smoothSolver smoother: symGaussSeidel tolerance: 1e-8 relTol: 0 |
| ω | solver: PBiCGStab preconditioner: DILU tolerance: 1e-10 relTol: 0.1 |
| ω (final) | solver: PBiCGStab preconditioner: DILU tolerance: 1e-10 relTol: 0 |
| PIMPLE | |
| nCorrectors | 2 |
| nNonOrthogonal-Correctors | 0 |
| pRefCell | 0 |
| pRefValue | 0 |
| Relaxation factors | |
| fields | p : 0.3 |
| equations | $U \mid k \mid \omega$: 0.7 $U \mid k \mid \omega$ (final): 1.0 |

5.3 CfMesh

This section describes the chosen meshing software. The one that will be used to mesh the wheel geometry is cfMesh. This software was chosen due to it being open source and being suitable to easily mesh complex 3D geometries. Furthermore, it is a cross-platform library that is built on top of OpenFOAM. It allows for both 2D and 3D automatic mesh generation in parallel using both shared memory parallelisation and distributed memory parallelisation by means of Message Passing Interface (MPI) [80].

5.4 Solver Validation

In this section, the solver pimpleFoam of OpenFOAM v2106 will be validated with existing literature. This is an incompressible transient solver that will be validated in a stepwise approach by first performing 2D laminar simulations of an isolated stationary cylinder. Then, rotation will be added to the cylinder, to check if it is correctly implemented. After this, the use of turbulence models in this solver is validated by performing stationary simulations for an isolated 2D cylinder at ($Re_D = 1 \cdot 10^6$). Furthermore, the effect of the ground and its movement in contact with a rotating 3D bluff body (cylinder) is validated as well.

$Re_D = 200$

In this subsection the results of stationary and rotating 2D laminar simulations of an isolated cylinder are presented and validated. The simulations are performed at $Re_D = 200$ and the stationary case is validated with the results of Rajani et al. [81]. The rotating simulations are validated with the results of Mittal and Kumar [30] and the streamlines are compared to the results of Karabelas et al. [37]. An overview of the validation of the force coefficients and St is presented in Table 5.8.

Stationary

In the case of a stationary isolated cylinder, the mean values of the transient C_d and C_l are presented in Table 5.8 together with the ΔC_d and ΔC_l , which are the magnitudes of the fluctuations. As can be seen, excellent agreement is achieved for both C_d and C_l . Furthermore, the vorticity field is shown in Figure 5.1. This shows that the simulation captures the vortex shedding phenomena perfectly, which is in agreement with the behaviour that is to be expected from literature [13].

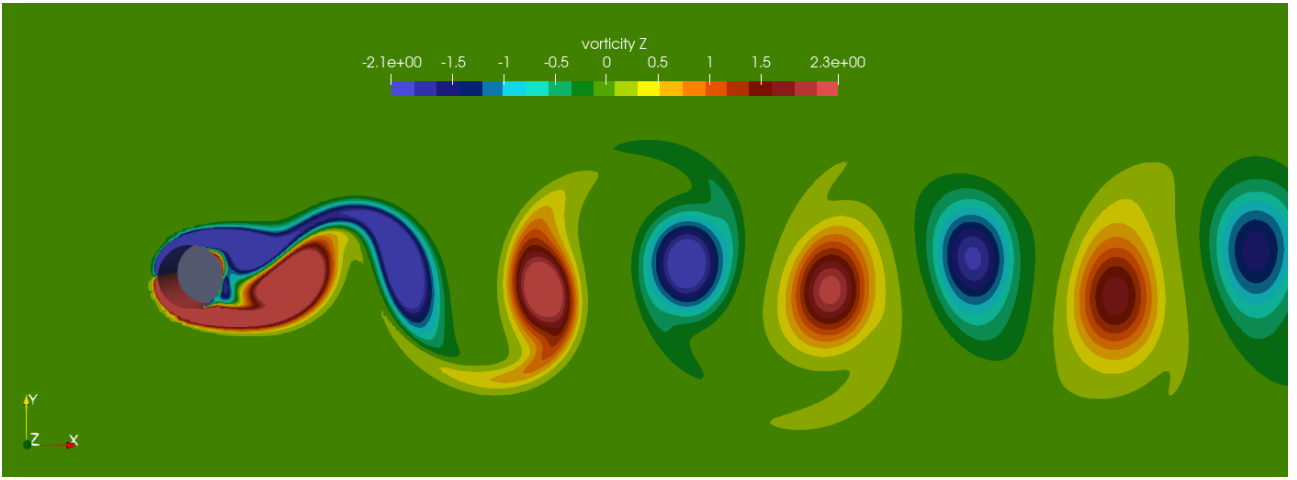
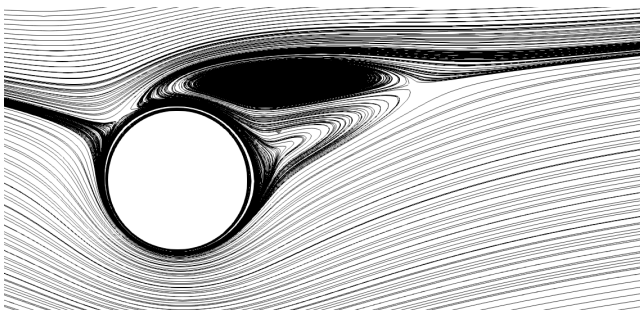


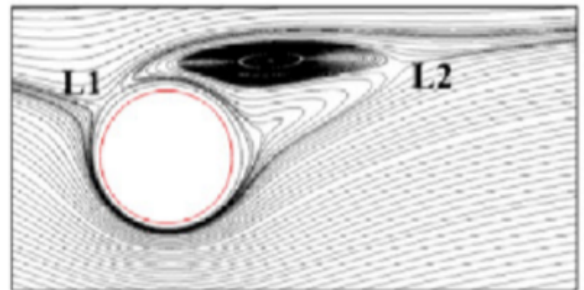
Figure 5.1: Vorticity in the z -direction displaying the vortex shedding for an isolated stationary 2D cylinder at $Re_D = 200$

Rotating

The streamlines of an isolated rotating cylinder at $Re_D = 200$ are presented in Figure 5.2 and Figure 5.3. As can be seen, the behaviour of the flow past the cylinder is captured excellently. Hence, the effect of rotation is correctly simulated. This is further confirmed by the excellent agreement of the force coefficients as can be seen in Table 5.8.



(a) OpenFOAM v2106



(b) Karabelas et al. [37]

Figure 5.2: Validation of the streamlines at $\alpha = 2$ for an isolated cylinder at $Re_D = 200$

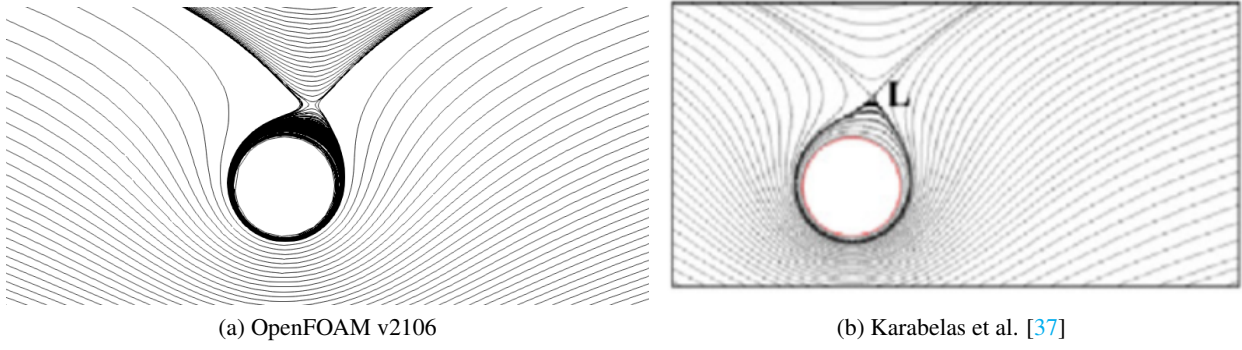


Figure 5.3: Validation of the streamlines at $\alpha = 4$ for an isolated cylinder at $Re_D = 200$

Table 5.8: Validation of C_d , C_l and St for an isolated 2D cylinder at $Re_D = 200$

| Stationary | | | | | |
|---------------------------|-----------|------------------|-------------|------------------|----------|
| | C_d [-] | ΔC_d [-] | C_l [-] | ΔC_l [-] | St [-] |
| OpenFOAM v2106 | 1.3253 | 0.04 | ≈ 0 | 0.66 | 0.195 |
| Rajani et al. [81] | 1.3365 | 0.04 | ≈ 0 | 0.61 | 0.1957 |
| Rotating ($\alpha = 2$) | | | | | |
| | C_d [-] | ΔC_d [-] | C_l [-] | ΔC_l [-] | St [-] |
| OpenFOAM v2106 | 0.2825 | — | -5.4362 | — | — |
| Mittal and Kumar [30] | 0.29 | — | -5.42 | — | — |

$Re_D = 1 \cdot 10^6$

Stationary

One of the earliest simulations in the relatively high Re_D range for a stationary cylinder were performed by Travin et al. [82]. They performed DES simulations of a smooth circular cylinder at Re_D ranging from $1.4 \cdot 10^6$ up to $3 \cdot 10^6$. As turbulence models, they used the one-equation S-A model near the wall and a subgrid-scale stress (SGS) model moving away from the wall.

Catalano et al. [83] performed LES with wall modelling and compared the results with RANS and URANS simulations. Moreover, they compared their results with the available experimental literature at that time. They found that the mean C_p was fairly well captured. Hence, their results are often used as a benchmark to validate one's simulations at high Re_D . Their simulations were performed at $Re_D = 5 \cdot 10^5$, $Re_D = 1 \cdot 10^6$ and $Re_D = 2 \cdot 10^6$ with the standard $k - \varepsilon$ turbulence model by Jones et al. [76] with wall functions. The obtained results consisted of the time averaged C_d , C_p , St and their dependence on Re_D .

Ong et al. [84] performed 2D URANS simulations at $Re_D = 1 \cdot 10^6$, $Re_D = 2 \cdot 10^6$ and $Re_D = 3.6 \cdot 10^6$. They also chose the standard $k - \varepsilon$ turbulence model like Catalano et al. [83].

Furthermore, Stringer et al. [85] carried out 2D URANS for a wide range of Re_D values ($40 < Re_D < 1 \cdot 10^6$). They used the commercial solver ANSYS CFX-13.0 and OpenFOAM 1.7.1 to perform their simulations with their turbulence model of choice being $k - \omega$ SST. Their main finding was that in the case of low Re_D values ($Re_D < 1 \cdot 10^3$) both solvers achieved accurate results when compared to experiments. However, in the case of high Re_D the results became less conclusive.

The aforementioned literature can be used to verify the applicability of the turbulence models and the ability of the solver to perform simulations at high Re_D for these types of flow cases. So, the first step is to generate a 2D mesh for an isolated cylinder, which is shown in Figure 5.4. As can be seen, the wake is refined, due to it being the region of interest.

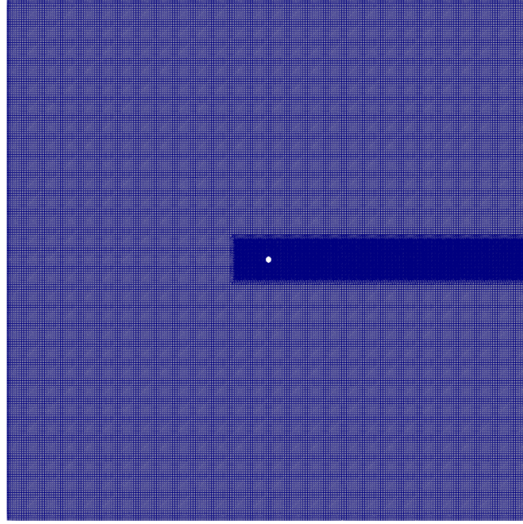


Figure 5.4: 2D mesh for an isolated cylinder with domain size $40D$

Furthermore, the mesh is generated to achieve $y^+ \approx 1$ near the cylinder. This allows the first cell to be in the viscous sublayer of the boundary layer, which allows you to resolve the boundary layer. Note, that y^+ is defined as follows:

$$y^+ = \frac{yu_\tau}{\nu} \quad (5.53)$$

with y being the distance from the wall and u_τ being the friction velocity, which is defined as follows:

$$u_\tau = \sqrt{\frac{\tau_w}{\rho}} \quad (5.54)$$

with τ_w being the wall shear stress. The generated layers to resolve the boundary layer are presented in [Figure 5.5](#).

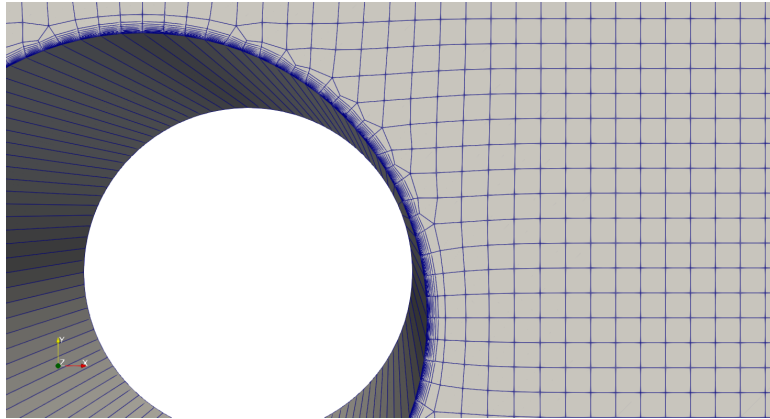


Figure 5.5: Layers near the cylinder with $y^+ \approx 1$

Since the results could be influenced by the computational domain size and mesh size, one has to perform a sensitivity study. The approach for this sensitivity study was to first try different domain sizes of $20D$, $30D$, $40D$ and $60D$ in all directions since the domain is a square. The results were considered converged when the C_d value did not change more than 2% when increasing the domain size. Similarly, the mesh was refined until again the C_d value did not change more than 2%. The simulations of these domain and mesh sensitivity studies were carried out using the S-A, due to its computational efficiency (one-equation) and the results are presented in [Figure 5.6](#). The results show that for the simulations a domain size of $40D$ and a mesh size of approximately $2 \cdot 10^5$ cells are sufficient.

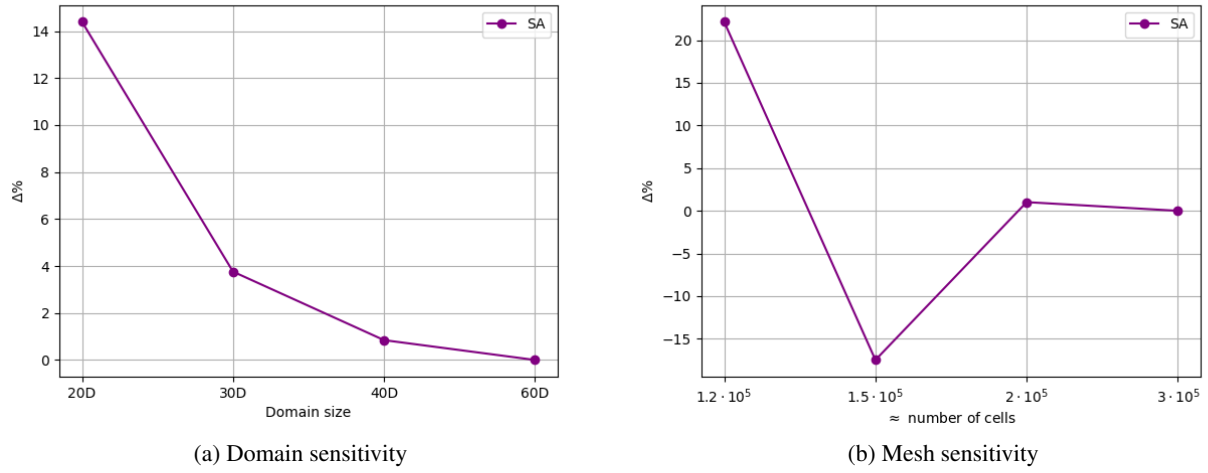


Figure 5.6: Domain and mesh sensitivity study for a stationary 2D cylinder at $Re_D = 1 \cdot 10^6$

With the obtained domain and mesh size, two turbulence models will be used to simulate flow past a 2D stationary cylinder. Namely, the S-A and $k - \omega$ SST turbulence models respectively. Furthermore, regarding the time step, a Courant-Friedrichs-Lewy (CFL) condition of 0.7 was chosen. This condition for multiple degrees of freedom is defined as follows:

$$CFL = \max \left(\frac{u_x \Delta t}{\Delta x}, \frac{u_y \Delta t}{\Delta y}, \frac{u_z \Delta t}{\Delta z} \right) \leq 1. \quad (5.55)$$

Thus, by setting the CFL value and depending on the fineness of the mesh the appropriate time step Δt will be calculated and used. Note, for stability and accuracy purposes the value of 1 is set as a limit. Therefore, to be below this a value of 0.7 was chosen. The obtained results of C_d and St compared to literature are found in Table 5.9 and the u_x flowfields for the two turbulence models are presented in Figure 5.7.

Table 5.9: Validation of 2D URANS simulations for a 2D stationary cylinder at $Re_D = 1 \cdot 10^6$

| | Method | Model | C_d [-] | St [-] |
|----------------------|------------|----------------------|-----------|----------|
| OpenFOAM v2106 | 2D URANS | SA | 0.491 | 0.242 |
| | | $k - \omega$ SST | 0.4355 | 0.322 |
| Catalano et al. [83] | 3D RANS | $k - \varepsilon$ | 0.39 | — |
| | 3D URANS | | 0.40 | 0.31 |
| | LES | SGS + wall modelling | 0.31 | 0.35 |
| Ong et al. [84] | 2D URANS | $k - \varepsilon$ | 0.5174 | 0.2823 |
| Stringer et al. [85] | 2D URANS | $k - \omega$ SST | 0.54 | 0.3 |
| Roshko [18] | experiment | — | 0.3 | 0.27 |

As can be seen, the range of C_d lies approximately between 0.3 – 0.54 and the value of St lies around 0.3. The C_d values of the 2D URANS simulations seem to be a bit higher near ≈ 0.5 . The results of the simulations seem to align with the results in the literature with the values of ≈ 0.49 and ≈ 0.436 . Moreover, the values obtained for St seem to be in agreement with the range of the literature as well. This gives the indication that the high Re_D is handled well by the solver. This is confirmed by looking at the flowfield, which shows that the vortex shedding at high Re_D is captured just as was observed in Roshko's experiment [18].

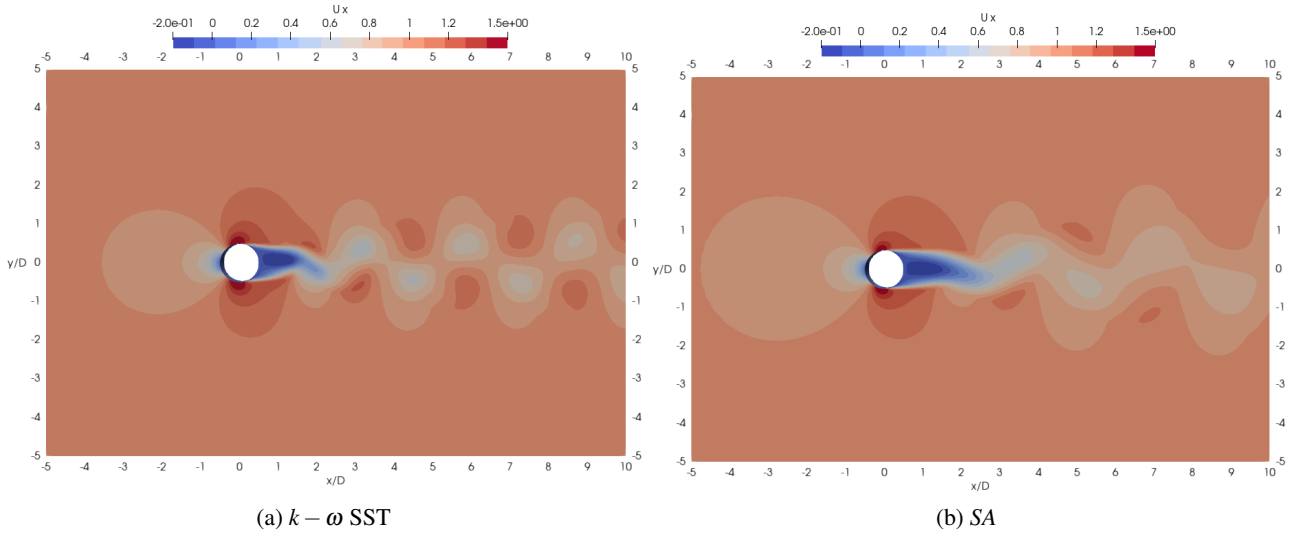


Figure 5.7: u_x flowfield of a stationary 2D cylinder at $Re_D = 1 \cdot 10^6$

Furthermore, the validation of the mean C_p distribution is given in Figure 5.8. In the simulations, the flow seems to separate earlier compared to the results of Catalano et al. [83]. Moreover, lower suction is captured as well. However, looking at the initial part up to $\theta \approx 50^\circ$, the C_p coincides perfectly with the literature. Additionally, the C_p values around $\theta \approx 110^\circ$ (separation region indicated by a horizontal straight line in Figure 5.8) agree with the LES results of Catalano et al. [83].

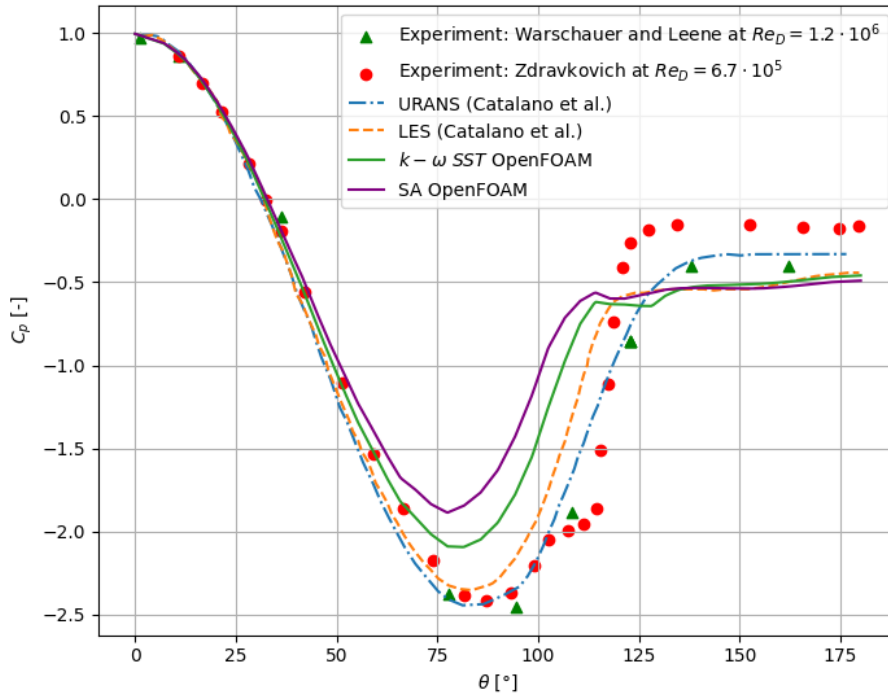


Figure 5.8: Mean C_p distribution of a stationary 2D cylinder at $Re_D = 1 \cdot 10^6$

The results of the wake display similar behaviour as seen in the results of Catalano et al. [83]. The validation of the normalised u_x and u_y in the wake at $x/D = 0.75$ and $x/D = 1.5$ are presented in Figure 5.9 and Figure 5.10. The behaviour is captured well. However, there are some differences in the magnitudes of the normalised velocities, which could be caused by e.g. 3D effects since the simulations of Catalano et al. [83] were performed

for 3D cylinders. Note, that it was mentioned in [Section 2.1](#) that after $Re_D \approx 190$ 3D effects appear.

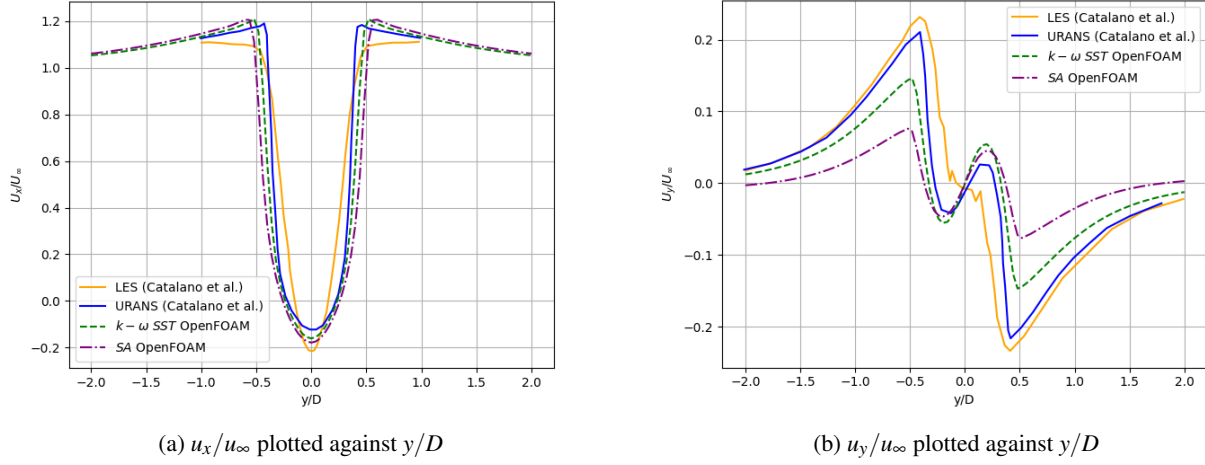


Figure 5.9: u_x and u_y normalised at $x/D = 0.75$

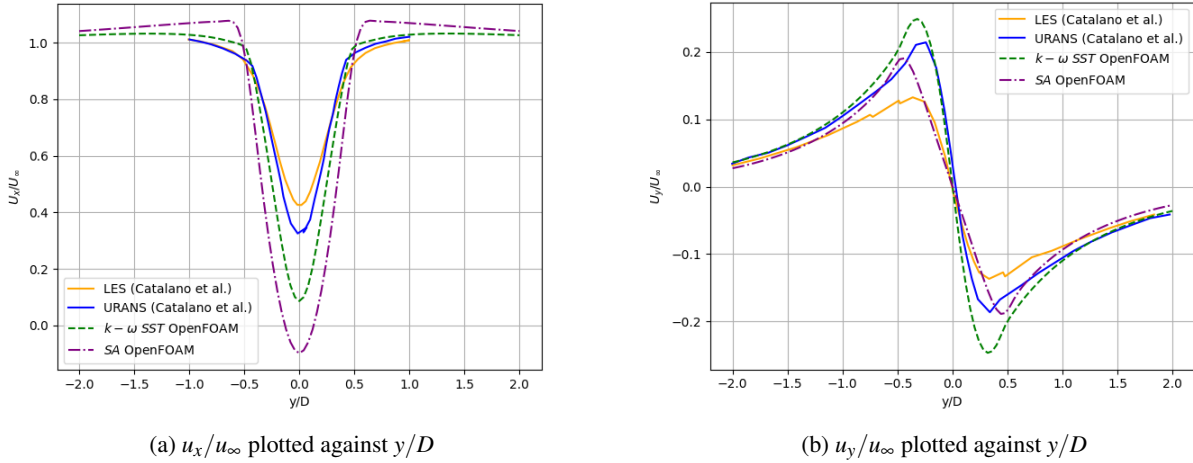


Figure 5.10: u_x and u_y normalised at $x/D = 1.5$

Rotating Cylinder in Contact with the Ground

In this final validation case a rotating isolated cylinder in contact with the ground is simulated as was done by Pirozoli et al. [45]. The purpose of these simulations is to see if the solver could properly simulate the necessary conditions regarding a rotating bluff body like a cylinder in contact with a moving ground. Moreover, it will also validate the 3D mesh obtained from cfMesh and the abilities of OpenFOAM to perform similar 3D simulations.

Note, that Pirozoli et al. [45] performs DNS simulations and the complexity of the problem is handled through the immersed boundary method. Furthermore, for their simulations, they use a $768 \times 256 \times 385$ mesh, which is a way larger mesh than will be used for the validation simulations due to RAM memory limitations.

For these simulations the simpleFoam solver is used to validate it as well since this solver will be used to perform RANS simulations for the wheel. Furthermore, a 3D mesh with approximately 4.4 million cells is created with $y^+ < 1$ and a refined wake. An overview of this mesh can be seen in [Figure 5.11](#). Regarding the contact region with the ground a step size approach is taken, such as that of Diasinos et al. [72].

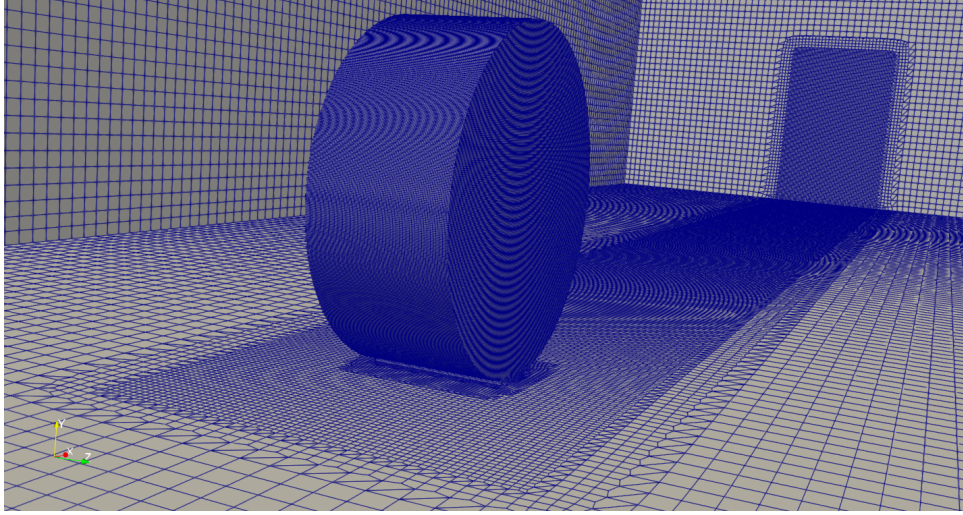


Figure 5.11: Mesh of the isolated 3D cylinder in contact with the ground

The simulations are performed for $Re_D = 100$, $Re_D = 200$, $Re_D = 500$ and $Re_D = 1000$ with the results of the force coefficients being presented in [Table 5.10](#).

As can be seen, the values of C_D are in very good agreement, while the C_L values are completely off. An explanation for this could be the different approaches taken in modelling the contact region. In the case of Pirozoli et al. [45], since it is an immersed boundary method no additional measure is needed when modelling the contact with the ground. However, for the validation simulations that are performed a step size approach must be taken to avoid highly skewed bad cells in that region.

Regarding this approach, the aforementioned literature has stated the importance of modelling the contact patch correctly, due to the major influence it can have on the C_L value. Therefore, it is believed that the contact patch plays a more important role for cylinders in contact with the ground, because the cross-section of the cylinder is a square, meaning no "wheel" shoulders are present. Hence, when the contact patch is generated it is way wider stretching the entire cylinder's width and is not able to properly enclose as can be observed in [Figure 5.12](#). This difference in size and shape could significantly influence the results of C_L and apparently not that of C_D , which seems to be way less sensitive to it.

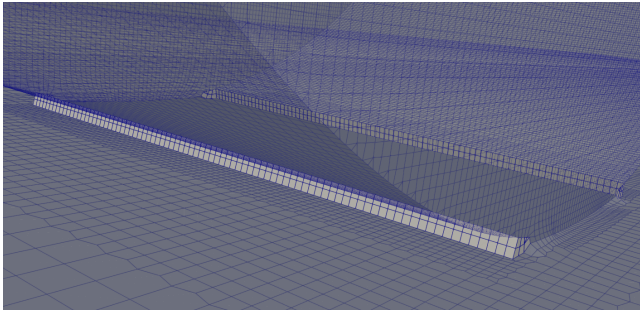
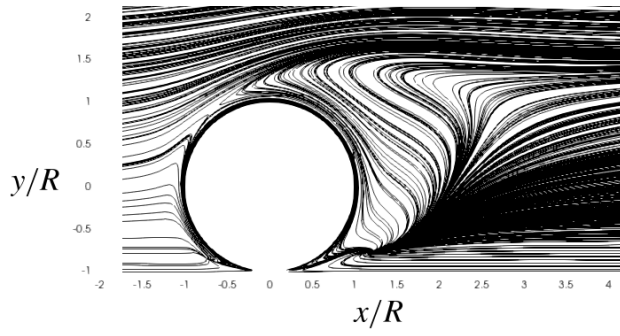


Figure 5.12: Contact patch for the 3D cylinder

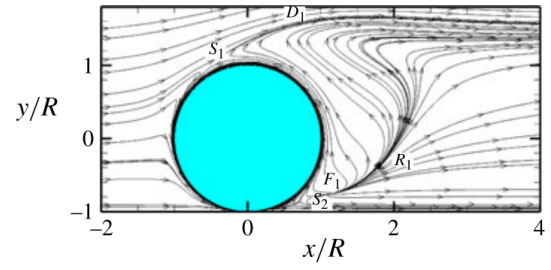
Table 5.10: C_D and C_L compared to results of Pirozoli et al. [45]

| | OpenFOAM v2106 | | Pirozoli et al. [45] | |
|--------|----------------|---------|----------------------|-------|
| Re_D | C_D | C_L | C_D | C_L |
| 100 | 2.354 | -0.0185 | 2.35 | 1.44 |
| 200 | 1.653 | -0.0156 | 1.68 | 1.19 |
| 500 | 1.186 | 0.0888 | 1.24 | 0.91 |
| 1000 | 1.0065 | 0.3289 | 1.00 | 1.05 |

Furthermore, to validate if the obtained flowfield is realistic 2D cross-sectional streamlines of the xy - and xz -planes are compared for one of the simulations at $Re_D = 100$ and presented in [Figure 5.13](#) and [Figure 5.14](#) respectively. As can be seen, the streamlines are in excellent agreement, indicating that the obtained flowfield corresponds to what is found in the literature and that the solver is capable of performing similar 3D rotating bluff body simulations in contact with a moving ground.

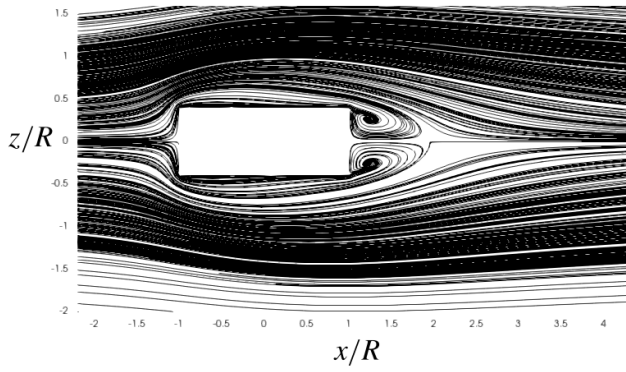


(a) OpenFOAM v2106

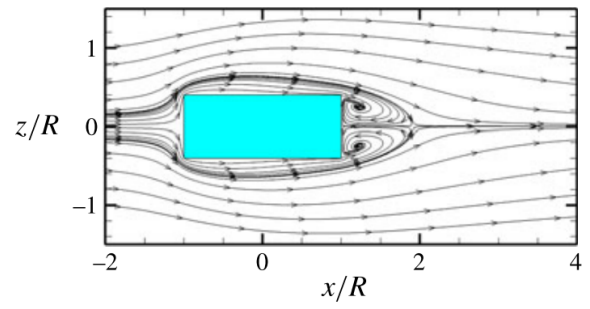


(b) Pirozoli et al. [45]

Figure 5.13: 2D streamlines in the cross-sectional xy -plane at $Re_D = 100$



(a) OpenFOAM v2106



(b) Pirozoli et al. [45]

Figure 5.14: 2D streamlines in the cross-sectional xz -plane at $Re_D = 100$

6. Wheel Simulations

In this chapter, the simulation set-up for the RANS simulations of an isolated rotating wheel will be presented and discussed. Firstly, the wheel geometry and the sensitivity of its contact patch region will be described and discussed in [Section 6.1](#). Then the approach taken to generate the mesh and find the suitable parameters by means of a grid sensitivity study can be found in [Section 6.2](#). Furthermore, the results of the domain sensitivity study are described in [Section 6.3](#). [Section 6.4](#) contains the boundary and initial conditions utilised for the simulations and [Section 6.5](#) mentions the numerical schemes and solver settings used. [Section 6.6](#) presents and compares the results of the S-A, RKE and $k - \omega$ SST turbulence models to the force coefficients and 2D streamlines of Fackrell [6] and McManus and Zhang [53] to validate the results of the wheel simulations. Finally, the method behind the approach taken to yaw the wheel is found in [Section 6.7](#).

6.1 Geometry

In this section, the wheel geometry will be described and the modelling of the contact patch with the ground. Furthermore, the results of the sensitivity study are also presented from which a step size is chosen.

6.1.1 Wheel

In this research, it is decided to use the Fackrell "A2" wheel, due to its available dimensions and experimental results [6, 53]. For this wheel, the RWBC method is used to model rotation. This is beneficial in terms of setting up the simulations and the cost of running them.

A cross-sectional view of the Fackrell "A2" wheel can be seen in [Figure 6.1a](#) with the dimensions being in mm. These dimensions are used to create a CAD model of the wheel using SolidWorks, which is shown in [Figure 6.1b](#). This CAD model is then exported as an STL file and converted to an FMS file since this is the preferred format of cfMesh.

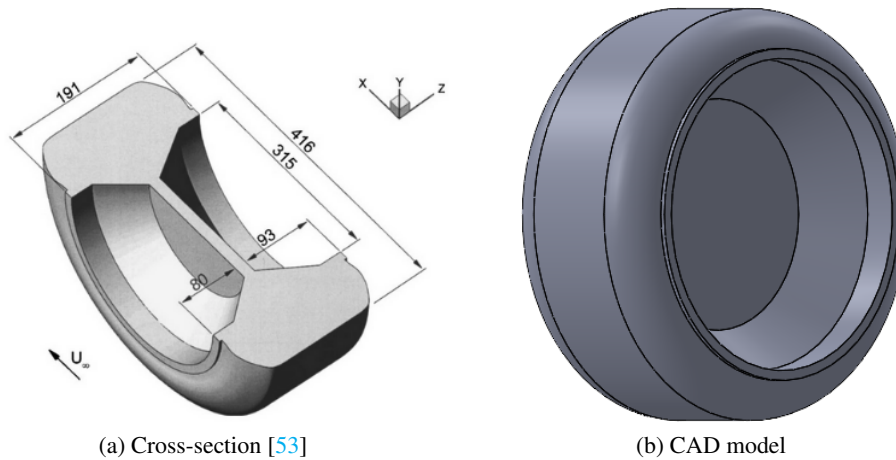


Figure 6.1: Fackrell "A2" wheel

However, before this wheel could be used for simulations two modifications were necessary to be able to achieve a good mesh with $y^+ \approx 1$. The first one was getting rid of the edge at the wheel hub. This edge is very small and preliminary simulations with and without this edge showed that its effect on the results is negligible. The reason to get rid of this edge was due to the highly non-orthogonal and skewed cells generated for small first cell heights trying to achieve $y^+ \approx 1$. These are to be avoided since they can have a detrimental effect on the results and/or solver stability. A visualisation of these bad cells is given in [Figure 6.2](#) with green indicating the highly non-orthogonal cells in [Figure 6.2a](#) and red indicating the highly skewed cells in [Figure 6.2b](#).

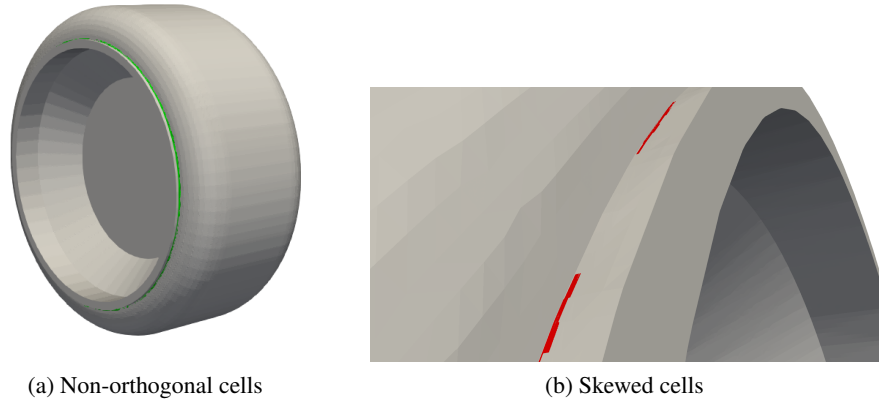


Figure 6.2: Highly non-orthogonal and skewed mesh cells due to edge of the Fackrell "A2"

The second modification was to round the angles in the cross-sectional view (indicated by R0.005 in Figure 6.3a). This was necessary since these corners lead to poor cells in terms of non-orthogonality and skewness. Additionally, the layers generated could collapse at these locations. This was especially the case for non-rounded corners with the meshing software SnappyHexMesh, which is one of the reasons why cfMesh was preferred. The actual geometry of the wheel used for the simulations is presented in Figure 6.3. The cross-sectional view is given in Figure 6.3a and the CAD model can be seen in Figure 6.3b.

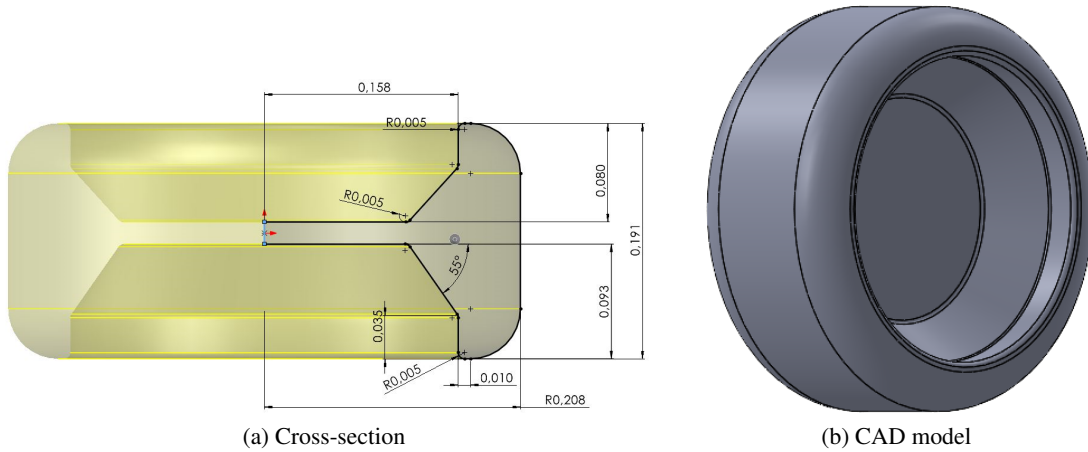


Figure 6.3: Modified Fackrell "A2" wheel

6.1.2 Contact Patch

The same approach as Diasinos et al. [72] is taken to model the region where the wheel makes contact with the ground. In this research, the effect of different step sizes on the force coefficients will be examined as well. Therefore, different contact patches should be generated and tested. Diasinos et al. [72] tested different sizes of contact patches as well. In the end, they used a step size of $0.0028D$, which was the smallest size they could achieve without compromising on the mesh quality in that region. So, for this research, a simulation with an even smaller contact patch will be performed to see if going even smaller is worth it.

The first simulations were performed with the step sizes of $0.0085D$ and $0.005D$. Then the results were compared and a smaller step size was chosen. This was done until the obtained force coefficients were converged. Hence independent of the chosen step size. Therefore, after $0.0085D$ and $0.005D$ the step sizes of $0.0028D$ and $0.002D$ were tested as well. These four step sizes correspond to heights of approximately 3.5, 2, 1.2 and 0.83 mm for this particular wheel. A visualisation of the contact patches when looking from the ground upwards is presented in Figure 6.4 and the dimensions are given in Table 6.1. Note, that the values in the table indicate the largest distance of the patch in that specific direction.

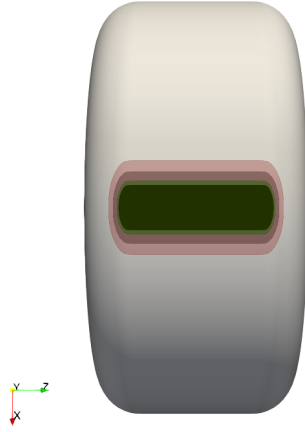


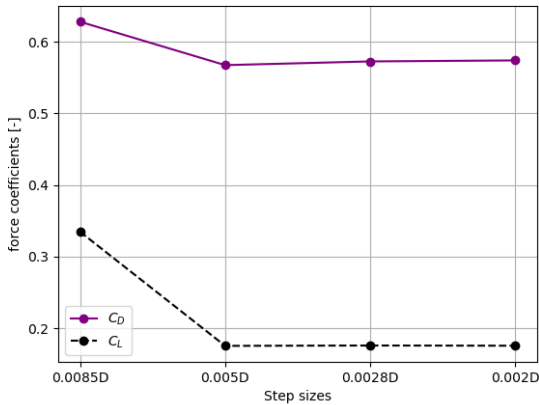
Figure 6.4: Visualisation of contact patch regions

Table 6.1: Contact patch dimensions

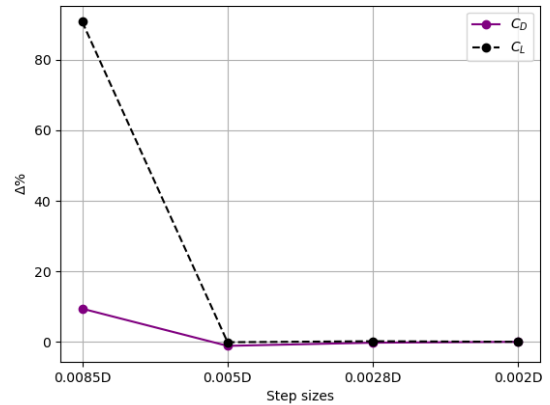
| Step size | Δx [m] | Δy [m] | Δz [m] |
|-----------|----------------|----------------|----------------|
| $0.0085D$ | 0.076368 | 0.003536 | 0.1430966 |
| $0.005D$ | 0.058664 | 0.00208 | 0.1356237 |
| $0.0028D$ | 0.043946 | 0.0011648 | 0.1292836 |
| $0.002D$ | 0.037138 | 0.000832 | 0.1263305 |

The importance of performing these simulations is to find a suitable contact patch that achieves a balance between accuracy and computational cost. Since, using a step size that is too small requires more mesh refinement in that region (smaller mesh cells are needed), which increases the computational cost. Furthermore, to keep the simulations consistent the same number of layers (10) was used with $y^+ \approx 1$. The reason that this number of layers was chosen is due to the restriction caused by the small contact patch of the step size $0.002D$. So, this is the maximum number of layers that will fit this space with a thickness ratio of 1.25.

The results of the C_D and C_L for the different step sizes can be found in Figure 6.5a and the difference in the percentage of these coefficients with respect to the force coefficients of the smallest step size ($0.002D$) in Figure 6.5b. From these results, a suitable step size can be determined for the simulations of this research. As can be seen, there are major differences between the results of the step sizes $0.0085D$ and $0.005D$ ($C_D \approx 9.4\%$ and $C_L \approx 91\%$). That the value of C_L is sensitive to the contact patch region was also observed by Diasinos et al. [72]. It can be observed that from the step size of $0.005D$ and going smaller to $0.0028D$ and $0.002D$ the values C_D and C_L barely change. So, from a step size of $0.005D$ and smaller, the results seem independent of the step size. Hence, choosing the step size $0.005D$ will be computationally the wise choice. However, the difference in computational cost is so small between $0.005D$ and $0.0028D$, that the step size $0.0028D$ was chosen to conduct the simulations with. The main reason for this is the fact that Diasinos et al. [72] also used this step size for their simulations. This allows for a better comparison of e.g. the C_p distribution along the centerline of the wheel by having the pressure peaks at the same position. This benefit outweighs the small computational cost benefit the step size $0.005D$ has over the step size $0.0028D$.



(a) C_D and C_L for different step sizes



(b) $\Delta\%$ changes w.r.t $0.002D$

Figure 6.5: Step sizes: $0.0085D$, $0.005D$, $0.0028D$ and $0.002D$ sensitivity study

6.2 Mesh and Grid Sensitivity

In this section, the approach to generating the mesh will be explained. As mentioned before the software used will be cfMesh. Moreover, a mesh convergence study is performed and the results show the level of fineness required for the mesh. From that the necessary cfMesh parameters can be obtained.

A visualisation of the generated mesh is presented in Figure 6.6. As can be seen, a hexahedral structured mesh is obtained. The mesh is created by defining a maximum cell size in the (*maxCellsize*) entry of the *meshDict* file. Then the refinement regions or refinement levels of the patches can be specified. In the case of the wheel as is evident from Figure 6.6b there were three refinement boxes created. The first and largest refinement box, which will be named *RefinementBox 1* stretches out to the outlet and its purpose is to refine the wake region $2x$ compared to the *maxCellsize*. The reason for this is the wake being a region of interest. Furthermore, *RefinementBox 2* is a refinement box that refines $3x$ in the near-wake of the wheel to more accurately capture the behaviour of the vortices close to the wheel. Finally, *RefinementBox 3*, which is enclosing the wheel geometry refines that region $4x$. This refinement box is placed to make it possible to have cell layers without too large of a gradient between the last cell of the layer and the mesh in that domain. This also allows the mesh cells near the ground to fit the contact patch nicely. The mesh near the contact region together with its cross-sectional view can be seen in Figure 6.7. Finally, to avoid issues with snapping the geometry near the edges, a separate VTK file is generated of the curves of these edges. This is used to specify a specific edge refinement cell size of 0.001171875.

After refining the cells, layers are added on the wheel, contact patch and ground. The number of layers that can be chosen depends on the step size, the cell size as a result of *RefinementBox 3* and the thickness ratio. When generating the layers the aim is to have the first cell height being around $y^+ \approx 1$. The layers are visible in Figure 6.7b, each of these 12 layers is generated with a thickness ratio of 1.25. The reason for this is to try and minimise having large cells next to each other since that could lead to inaccurate results or even a divergent simulation. Hence, having an increasing cell size around 25% - 30% is a good rule of thumb. It is decided to have 12 layers due to the limitation imposed by the step size.

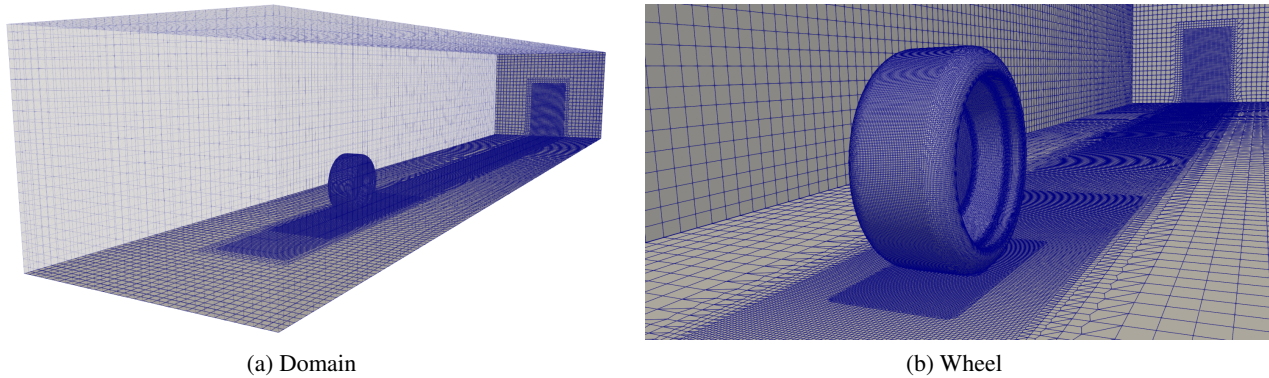


Figure 6.6: Mesh generated by cfMesh for an isolated rotating wheel

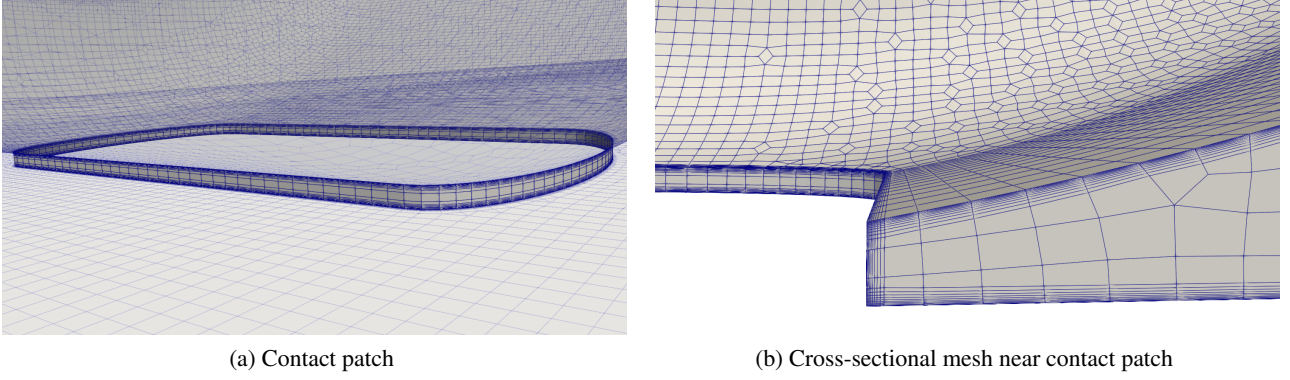


Figure 6.7: Mesh of contact region with the ground

In a similar fashion different meshes are generated to conduct a mesh convergence study. The way different meshes are generated is by changing the *maxCellSize* entry. An overview of the different meshes is given in Table 6.2. As can be seen, there were four different meshes generated for the mesh convergence study with *Level 1* being the finest mesh and *Level 4* being the coarsest. These two meshes can be seen in Figure 6.8. It was decided to vary the *maxCellSize* since it is the easiest way to refine the nodes in the wake and on the wheel surface evenly. The *maxCellSize* values were mainly chosen by trial and error, since the mesh generation process was sensitive to collapsing cells near the contact region. These different values resulted in meshes consisting of approximately $4.31 \cdot 10^6$, $5.19 \cdot 10^6$, $6.82 \cdot 10^6$ and $7.68 \cdot 10^6$ cells. Note, that for the mesh convergence study the original domain size was used as was used for the experiments of Fackrell [6] and the simulations of McManus and Zhang [53].

Table 6.2: Different mesh sizes for the mesh convergence studies

| Mesh | maxCellSize | number of cells | number of cells (wheel surface) |
|---------|-------------|-----------------|---------------------------------|
| Level 1 | 0.0475 | 7 676 568 | 225 756 |
| Level 2 | 0.05 | 6 819 646 | 204 922 |
| Level 3 | 0.057 | 5 192 821 | 176 352 |
| Level 4 | 0.0625 | 4 305 384 | 154 418 |

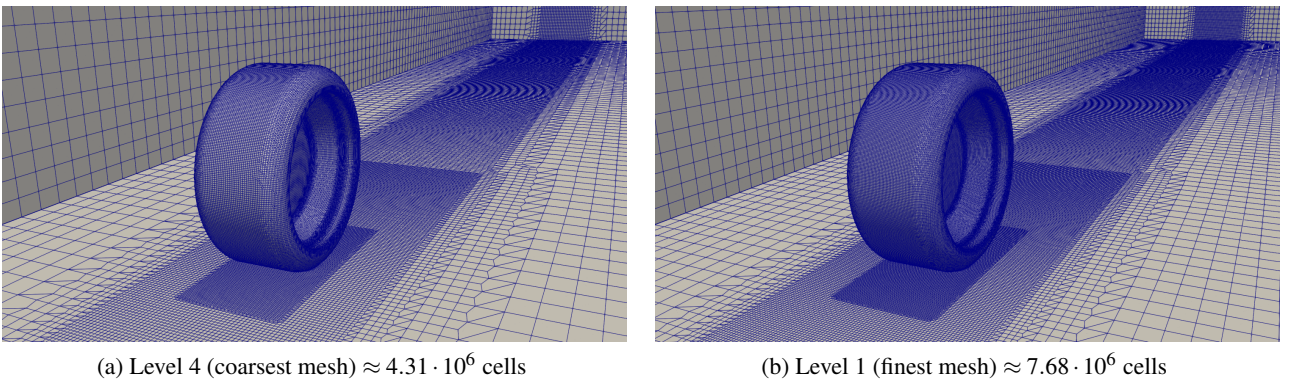


Figure 6.8: Coarsest and finest mesh for convergence study

The result of the mesh convergence study is presented in Figure 6.9. This study was conducted with a step size of $0.0085D$ since a bigger step size is easier to mesh near the contact region. The results of the mesh convergence study show that C_D and C_L change minimally after *Level 2*. Thus this mesh is considered converged. Hence, for the simulations a *maxCellSize* of 0.05 will be used.

The exact type of cells present in this mesh and its quality parameters are presented in Table 6.3 and Table 6.4. Note, that the high value of the maximum aspect ratio is remarkable. However, this is caused by

the transition from the final layer of the ground to the far-field mesh cells, which are the largest. This seems to not have an effect due to the fact that these cells are aligned with the direction of the flow. The other quality parameters such as maximum non-orthogonality ($< 70^\circ$ [79]) and maximum skewness of the cells are within the realm of what could be expected for such a complex 3D geometry. Hence, the mesh is of quality.

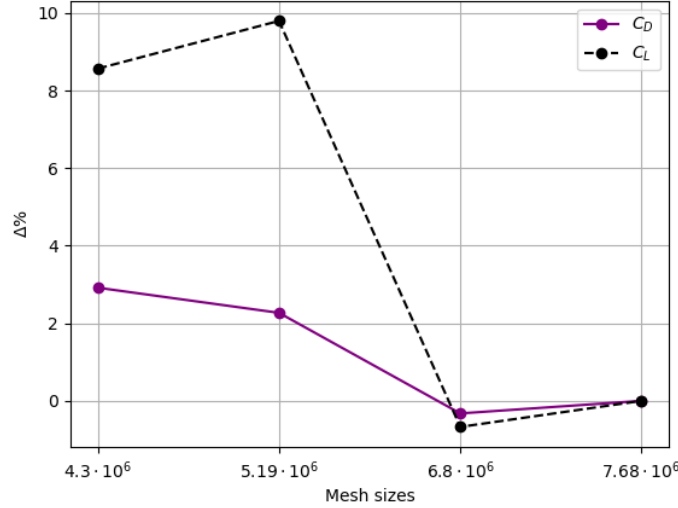


Figure 6.9: Mesh sensitivity study

Table 6.3: Type and number of mesh cells

| Type | Number of cells |
|--------------|------------------|
| Hexahedral | 6 539 933 |
| Prism | 576 |
| Pyramids | 48 |
| Tetrahedral | 48 |
| Polyhedral | 279 041 |
| Total | 6 819 646 |

Table 6.4: Mesh quality parameters

| | |
|---------------------------|-----------|
| Max aspect ratio | 2861.358 |
| Max non-orthogonality | 45.66239 |
| Average non-orthogonality | 5.5077709 |
| Max skewness | 1.4936722 |

6.3 Domain Sensitivity

The size of the domain could affect the results of the simulations. Therefore, it is important to conduct a domain size sensitivity study as well. For this study, it is decided to start with the original domain and enlarge it until there is no significant change in the force coefficients. An overview of the different domains and their dimensions normalised by D is given in Table 6.5. In this table the distance Δx_{inlet} stretches from the inlet up to the centre of the wheel. Similarly, Δx_{outlet} is the distance from the centre of the wheel up to the outlet in the x -direction. Furthermore, Δy is the distance from the ground upwards and Δz is the distance sideways with the centre of the wheel being in the middle of Δz .

Table 6.5: Domain sensitivity dimensions

| Domain | $\Delta x_{inlet}/D$ | $\Delta x_{outlet}/D$ | $\Delta y/D$ | $\Delta z/D$ |
|--------------|----------------------|-----------------------|--------------|--------------|
| 1 (original) | 5 | 15 | 2.93 | 3.66 |
| 2 (2x) | 10 | 30 | 5.86 | 7.32 |
| 3 (3x) | 15 | 45 | 8.79 | 10.98 |
| 4 (largest) | 20 | 45 | 11.72 | 21.95 |

As mentioned before the smallest domain of this sensitivity study is the original domain of Fackrell's experiment [6] and McManus and Zhang's simulations [53]. Then the distances of $\Delta x_{inlet}/D$, $\Delta x_{outlet}/D$, $\Delta y/D$ and

$\Delta z/D$ are doubled. The reason for this is the sensitivity of cfMesh near the contact patch area. So, for a slightly different distance that is not a multiple of the original distances, the cells near the contact patch region collapse with a *maxCellsize* of 0.05. Hence, for the third domain the distances are enlarged 3x from the original in every direction. Finally, for the last domain it was specifically decided to have significantly bigger values for $\Delta y/D$ and $\Delta z/D$ to see if that has a significant effect on the results. A visualisation of the domains around the wheel can be seen in [Figure 6.10](#). The green domain is the original domain, the purple domain is the 2x larger, the red domain is the 3x larger and the largest domain is the yellow box.

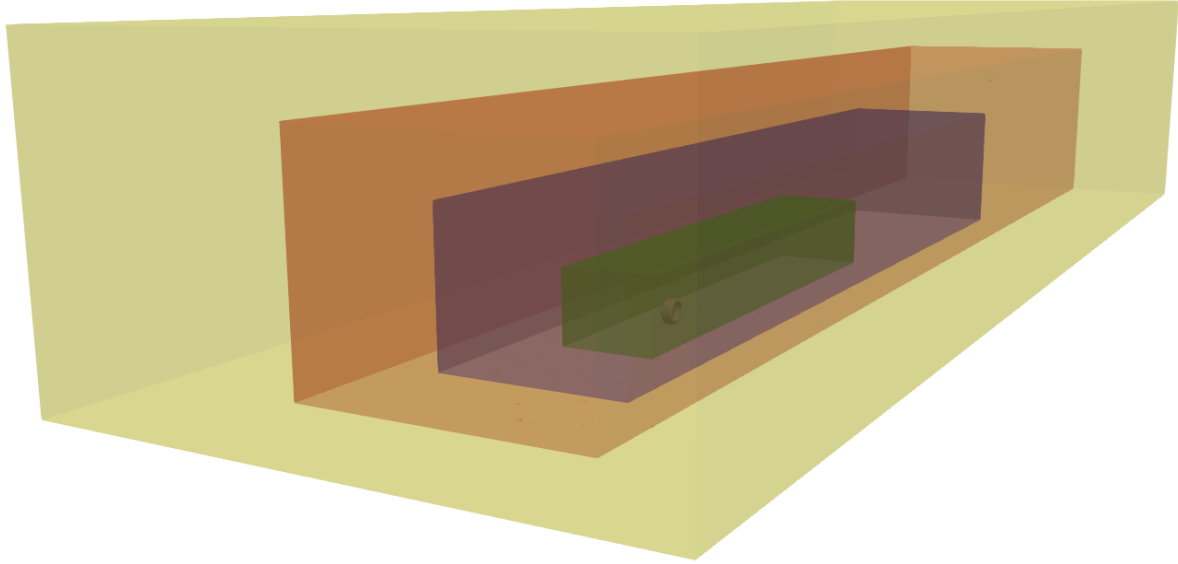


Figure 6.10: Different domain sizes for the sensitivity study

The results of the domain convergence study are presented in [Figure 6.11](#). The results show that increasing the size of the domain larger than 2x barely affects the force coefficients, since the difference in C_D and C_L compared to the largest domain equals 0.66% and 1.24% respectively. Therefore, for further simulations, it is decided to use domain 2. Additionally, enlarging the domain means that more mesh cells are required. Therefore, the new number of cells can be found in [Table 6.6](#). Note, that for this domain sensitivity study, the *maxCellsize* of 0.05 obtained from the mesh convergence study is doubled to 0.1. However, the sizes of the cells on the wheel and wake are kept the same by adding an additional refinement level to all the refinement boxes. The reason for this is that larger cells near the boundaries for larger domains are computationally preferable. So those larger cells outside the regions of interest (wake and wheel) will not affect the results.

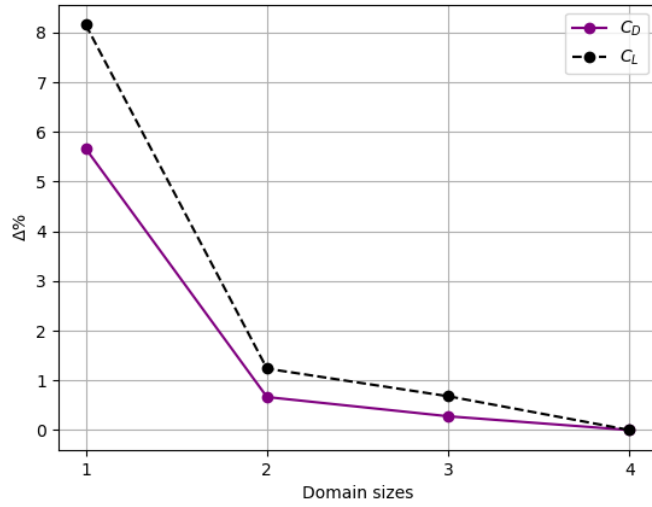


Figure 6.11: Domain convergence study

Table 6.6: Domain 2x: type and number of mesh cells

| Type | Number of cells |
|--------------|------------------|
| Hexahedral | 9 612 947 |
| Prism | 1440 |
| Pyramids | 144 |
| Tetrahedral | 144 |
| Polyhedral | 293 427 |
| Total | 9 908 102 |

6.4 Boundary and Initial Conditions

This section contains the relevant boundary and initial conditions for the simulations. So, to assign boundary conditions, the domain with the geometry inside it should be divided into patches. This is done into seven different patches of which six can be seen in Figure 6.12. The seventh is the contact patch. The type of boundary condition assigned to the wheel and ground is *wall*. The contact patch is assigned the *symmetry* type and the rest is assigned the type *patch*.

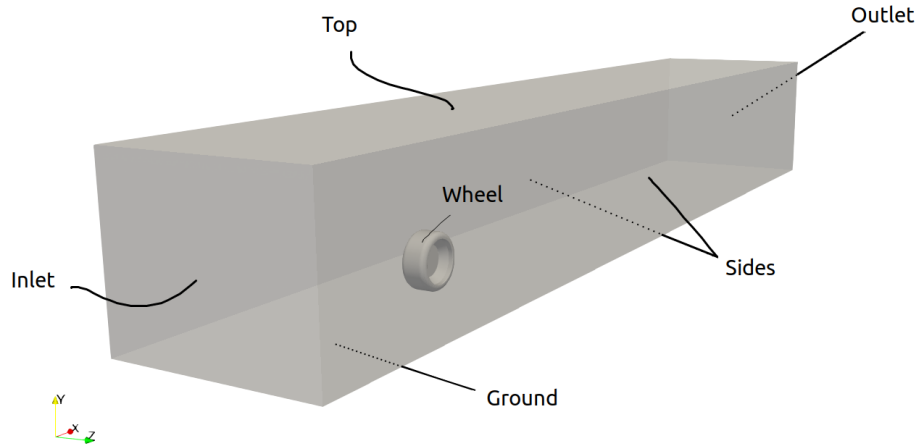


Figure 6.12: The patches as defined in OpenFOAM

The simulations will be performed with a $Re_D = 5.3 \cdot 10^5$. So, initial conditions should be specified depending on the turbulence model. In the case of the $k - \omega$ SST model they should be specified for the following parameters: U , p , v_T , k and ω . For RKE ε should be initialised instead of ω and for S-A: U , p , v_T and \tilde{v} should be initialised.

Velocity (U)

The simulations are initialised with a uniform flowfield of 18.6 m/s in the x -direction. Since, the wheel is simulated isolated and rotating in an empty space this condition is applied at the inlet, sides and top. Furthermore,

the *zeroGradient* boundary condition is applied to the outlet, which means the value of U is constant at the outlet. Moreover, multiple research indicated the importance of the moving ground. Hence, the ground speed is initialised with 18.6 m/s in the x -direction. Since, the ground velocity matches the u_∞ a boundary layer will not be present on the ground, which is physically accurate. The prescription of the velocity is done using the boundary type *fixedValue* with the value as *uniform (18.6 0 0)*. Regarding the wheel, the *rotatingWallVelocity* condition is used. This allows for a rotating wall to rotate around an axis. The value for this condition is prescribed in rad/s and the value is chosen in a way that the rotational speed of the wheel results in the circumferential speed of the wheel matching the speed of the ground. Hence, the rotational speed of the wheel is prescribed to be approximately 89.42 rad/s. Finally, at the contact patch, condition symmetry is applied to avoid flow passing through it.

Pressure (p)

Since the simulations are assumed to be incompressible, the exact value of pressure is not of interest, only the pressure differences. Therefore, a fixed value of 0 Pa is set on the outlet and *zeroGradient* boundary condition is applied to the inlet, sides and top. Moreover, *zeroGradient* is applied to the ground and wheel as well as *symmetry* to the contact patch.

Eddy viscosity (ν_T)

In the case of ν_T the boundary condition calculated is used for all the far-field patches. This is chosen because the value of ν_T can be calculated from the initial values. Moreover, at the wheel and ground a wall function is required. At these patches, the *nutkWallFunction* is utilised. This wall function checks the y^+ value. If it is smaller than a particular value named *Ypluslam* it means the viscous sublayer region solution is used, which sets the value of $\nu_T = 0$ in the cells adjacent to the wall. If y^+ is larger than *Ypluslam* the log-law region equation to calculate ν_T is used, which is

$$\nu_T = \nu \cdot \left(\frac{\kappa y^+}{\ln(E y^+)} - 1 \right) \quad (6.1)$$

with $\kappa = 0.41$ being the von Karman constant and $E = 9.8$ being the roughness coefficient [86].

Turbulence kinetic energy (k)

An initial turbulent kinetic energy value k is calculated based on u_∞ and the turbulent intensity I as follows:

$$k = \frac{3}{2} (u_\infty I)^2. \quad (6.2)$$

Like McManus and Zhang [53] the value of I was set to 0.2%. Hence, this results in a value of $k = 0.00207576$, which is prescribed to the far-field inflow patches: inlet, sides and top by means of the *inletOutlet*. Therefore, the outflow patch outlet requires the *zeroGradient* boundary condition. Furthermore, at the wall patches wheel and ground it is known that $k = 0$. Therefore a *fixedValue* condition is set on both with the value of 0.

Turbulent dissipation rate (ε) and specific turbulent dissipation rate (ω)

The initial value of ω is calculated based on the value of k , ε and a turbulent length scale ℓ in the following way:

$$\omega = \frac{1}{C_\mu} \frac{\varepsilon}{k} \quad (6.3)$$

with $C_\mu = 0.09$ being an empirical constant. Furthermore, ε is computed in the following way:

$$\varepsilon = \frac{C_\mu k^{3/2}}{0.1 \ell} \quad (6.4)$$

with $\ell \approx 0.0045D$ being a value for the turbulent length scale. Hence an initial value for $\varepsilon \approx 0.0455$ and $\omega \approx 243.4$ is calculated. Therefore, these values are prescribed for far-field patches that have an *inletOutlet*

condition at the inflow (inlet, sides and top) and zeroGradient at the outflow patch (outlet). At the wheel and ground the epsilonWallFunction and omegaWallFunction are used depending on the chosen turbulence model. The omegaWallFunction computes the value of ω based on the y^+ value [86]. In the viscous sub-layer the value is calculated as follows:

$$\omega_{viscous} = \frac{6.0\nu}{\beta_1 y^2} \quad (6.5)$$

and in the logarithmic region it is computed as:

$$\omega_{log} = \frac{k^{1/2}}{C_\mu^{1/4} \kappa y}. \quad (6.6)$$

Note, that in the buffer-layer (intermediate region) the value of ω is calculated based on the values of the viscous sub-layer and logarithmic region

$$\omega = \sqrt{\omega_{viscous}^2 + \omega_{log}^2}. \quad (6.7)$$

In the case of the wheel simulations since $y^+ < 1$, ω will be computed using [Equation 6.5](#).

An overview of the boundary and initial conditions when utilising the $k - \omega$ SST and RKE turbulence model are given in [Table 6.7](#) and [Table 6.8](#) respectively.

Table 6.7: Overview of boundary and initial conditions of the simulations utilising the $k - \omega$ SST turbulence model

| | U | p | v_T | k | ω |
|---------|----------------------------------|---------------------------|------------------|---------------------------|-------------------|
| Inlet | fixedValue uniform (18.6 0 0) | zeroGradient | calculated | inletOutlet | inletOutlet |
| Sides | fixedValue uniform (18.6 0 0) | zeroGradient | calculated | inletOutlet | inletOutlet |
| Top | fixedValue uniform (18.6 0 0) | zeroGradient | calculated | inletOutlet | inletOutlet |
| Outlet | zeroGradient | fixedValue (uniform 0) | calculated | zeroGradient | zeroGradient |
| Ground | fixedValue uniform (18.6 0 0) | zeroGradient | nutkWallFunction | fixedValue (uniform 0) | omegaWallFunction |
| Wheel | rotatingWallVelocity | zeroGradient | nutkWallFunction | fixedValue (uniform 0) | omegaWallFunction |
| Contact | symmetry | symmetry | symmetry | symmetry | symmetry |

Table 6.8: Overview of boundary and initial conditions of the simulations utilising the RKE turbulence model

| | U | p | v_T | k | ε |
|---------|----------------------------------|---------------------------|------------------|---------------------------|---------------------|
| Inlet | fixedValue uniform (18.6 0 0) | zeroGradient | calculated | inletOutlet | inletOutlet |
| Sides | fixedValue uniform (18.6 0 0) | zeroGradient | calculated | inletOutlet | inletOutlet |
| Top | fixedValue uniform (18.6 0 0) | zeroGradient | calculated | inletOutlet | inletOutlet |
| Outlet | zeroGradient | fixedValue (uniform 0) | calculated | zeroGradient | zeroGradient |
| Ground | fixedValue uniform (18.6 0 0) | zeroGradient | nutkWallFunction | fixedValue (uniform 0) | epsilonWallFunction |
| Wheel | rotatingWallVelocity | zeroGradient | nutkWallFunction | fixedValue (uniform 0) | epsilonWallFunction |
| Contact | symmetry | symmetry | symmetry | symmetry | symmetry |

For the S-A turbulence model the difference compared to the previously mentioned turbulence models is the use of the nutUSpaldingWallFunction at the wall-type patches, which approximates based on the following relation:

$$y^+ = u^+ + \frac{1}{E} \left[e^{\kappa u^+} - 1 - \kappa u^+ - \frac{1}{2} (\kappa u^+)^2 - \frac{1}{6} (\kappa u^+)^3 \right] \quad (6.8)$$

with u^+ being the dimensionless velocity. Furthermore, the far-field type values of v_T and \tilde{v} are initialised with a value of $5 \cdot v$. The overview of the S-A turbulence model initial and boundary conditions are presented in [Table 6.9](#).

Table 6.9: Overview of boundary and initial conditions of the simulations utilising the S-A turbulence model

| | U | p | v_T | \tilde{v} |
|---------|----------------------------------|---------------------------|--------------------------|---------------------------|
| Inlet | fixedValue uniform (18.6 0 0) | zeroGradient | inletOutlet | inletOutlet |
| Sides | fixedValue uniform (18.6 0 0) | zeroGradient | inletOutlet | inletOutlet |
| Top | fixedValue uniform (18.6 0 0) | zeroGradient | inletOutlet | inletOutlet |
| Outlet | zeroGradient | fixedValue (uniform 0) | zeroGradient | zeroGradient |
| Ground | fixedValue uniform (18.6 0 0) | zeroGradient | nutUSpaldingWallFunction | fixedValue (uniform 0) |
| Wheel | rotatingWallVelocity | zeroGradient | nutUSpaldingWallFunction | fixedValue (uniform 0) |
| Contact | symmetry | symmetry | symmetry | symmetry |

6.5 Numerical Schemes and Solver Settings

In this section, the numerical schemes and solver settings that will be used for the simulations are discussed. The schemes used are based on the OpenFoam tutorials by means of preliminary simulations and comparison with literature. The numerical schemes used for the simulations are found in [Table 6.10](#). The numerical schemes of the divergence terms specific for a particular turbulence model are given in [Table 6.11](#). Since the schemes also impact the obtained results, simulations are also performed with a different set of divergence schemes for the RKE turbulence model. Here, instead of the *Gauss upwind* scheme the *Gauss linear* scheme is used for the $\text{div}(\phi, k)$ and $\text{div}(\phi, \varepsilon)$ terms.

Table 6.10: Numerical schemes for the isolated rotating wheel in contact with the ground simulations at $Re_D = 5.3 \cdot 10^5$

| | |
|----------------------|----------------------------|
| ddtSchemes | steadyState |
| gradSchemes | Gauss linear |
| div(phi,U) | Gauss linearUpwind grad(U) |
| laplacianSchemes | Gauss linear corrected |
| interpolationSchemes | linear |
| snGradSchemes | corrected |

Since RANS simulations are steady state and simpleFoam is used, the steadyState ddtScheme must be used to set the time derivatives to zero and avoid erroneous results. Furthermore, for all the cases of the spatial discretisation of the gradient terms the *Gauss linear* scheme is used, which indicates that Gauss integration is used with linear interpolation from the cell centres to faces. Looking at the divergence terms, in the case of incompressible flows the phi will denote the volumetric flux of velocity on the cell faces ($\phi = \mathbf{u}_f \cdot \mathbf{S}_f$) [79]. So, div(phi,U) specifies the advection of velocity and the scheme that will be used is the *Gauss linearUpwind grad(U)*, which is a second-order, upwind-biased and unbounded scheme that requires the specification of the velocity gradient. Gauss integration is the only choice for the Laplacian schemes as well and since the entry requires both an interpolation scheme and a surface normal gradient scheme the *Gauss linear corrected* scheme is chosen. The interpolationSchemes entry will be *linear*. Hence, interpolations of values generally from cell centres to face centres will be done linearly. Regarding the snGradSchemes a corrected scheme is used since non-orthogonality of the mesh cells is way below 70° . This applies an explicit non-orthogonal correction [79].

Table 6.11: Divergence terms schemes for the S-A, $k - \omega$ SST and RKE turbulence models

| S-A | |
|------------------------|--------------|
| div(phi, \tilde{v}) | Gauss upwind |
| $k - \omega$ SST | |
| div(phi,k) | Gauss upwind |
| div(phi, ω) | Gauss upwind |
| RKE [Gauss upwind] | |
| div(phi,k) | Gauss upwind |
| div(phi, ϵ) | Gauss upwind |
| RKE [Gauss linear] | |
| div(phi,k) | Gauss linear |
| div(phi, ϵ) | Gauss linear |

Note, that the difference between *Gauss upwind* and *Gauss linear* is that *Gauss upwind* is first-order bounded and *Gauss linear* is second-order unbounded. Here the bounded scheme is more stable even though less accurate. That is the reason that it was initially chosen for the divergence terms as seen in Table 6.11. The reason to perform simulations using *Gauss linear* with the RKE instead of the $k - \omega$ SST turbulence model was the stability of the simulations.

The solver settings of the simulations with the S-A, $k - \omega$ SST and RKE turbulence models are presented in Table 6.12, Table 6.13 and Table 6.14 respectively. These tables contain the relevant solvers, tolerances and relaxation factors used.

Table 6.13: Solver settings using $k - \omega$ SST

| Solver | |
|---------------------------|---|
| p | solver: GAMG smoother: GaussSeidel tolerance: 1e-6 relTol: 0.1 |
| U, k | solver: PBiCG preconditioner: DILU tolerance: 1e-8 relTol: 0.1 |
| ω | solver: PBiCGStab preconditioner: DILU tolerance: 1e-8 relTol: 0.1 |
| SIMPLE | |
| nNonOrthogonal-Correctors | 0 |
| residualControl | p : 1e-06 U : 1e-08 k : 1e-08 ω : 1e-08 |
| Relaxation factors | |
| fields | p : 0.3 |
| equations | $U \mid k \mid \omega$: 0.7 |

Table 6.12: Solver settings using S-A

| Solver | |
|---------------------------|---|
| p | solver: GAMG smoother: GaussSeidel tolerance: 1e-6 relTol: 0.1 |
| U, \tilde{v} | solver: smoothSolver smoother: GaussSeidel tolerance: 1e-8 relTol: 0.1 |
| SIMPLE | |
| nNonOrthogonal-Correctors | 0 |
| residualControl | p : 1e-06 U : 1e-08 \tilde{v} : 1e-08 |
| Relaxation factors | |
| fields | p : 0.3 |
| equations | $U \mid \tilde{v}$: 0.7 |

Table 6.14: Solver settings using RKE

| Solver | |
|---------------------------|---|
| p | solver: GAMG smoother: GaussSeidel tolerance: 1e-6 relTol: 0.1 |
| U, k | solver: PBiCG preconditioner: DILU tolerance: 1e-8 relTol: 0.1 |
| ϵ | solver: PBiCGStab preconditioner: DILU tolerance: 1e-8 relTol: 0.1 |
| SIMPLE | |
| nNonOrthogonal-Correctors | 0 |
| residualControl | p : 1e-06 U : 1e-08 k : 1e-08 ϵ : 1e-08 |
| Relaxation factors | |
| fields | p : 0.3 |
| equations | $U \mid k \mid \epsilon$: 0.7 |

6.6 Turbulence Models

In this section, the three turbulence models S-A, $k - \omega$ SST and RKE will be utilised and the results will be compared to that of the experiment and simulations from literature [6, 53, 72]. These results consist of the C_D , C_L , the C_p distribution over the centerline and 2D streamlines in the $z/D = 0$ plane.

Convergence

The simulations are considered converged when the force coefficients achieve a steady behaviour. In Figure 6.13 it can be seen that this is achieved from approximately 1500 iterations.

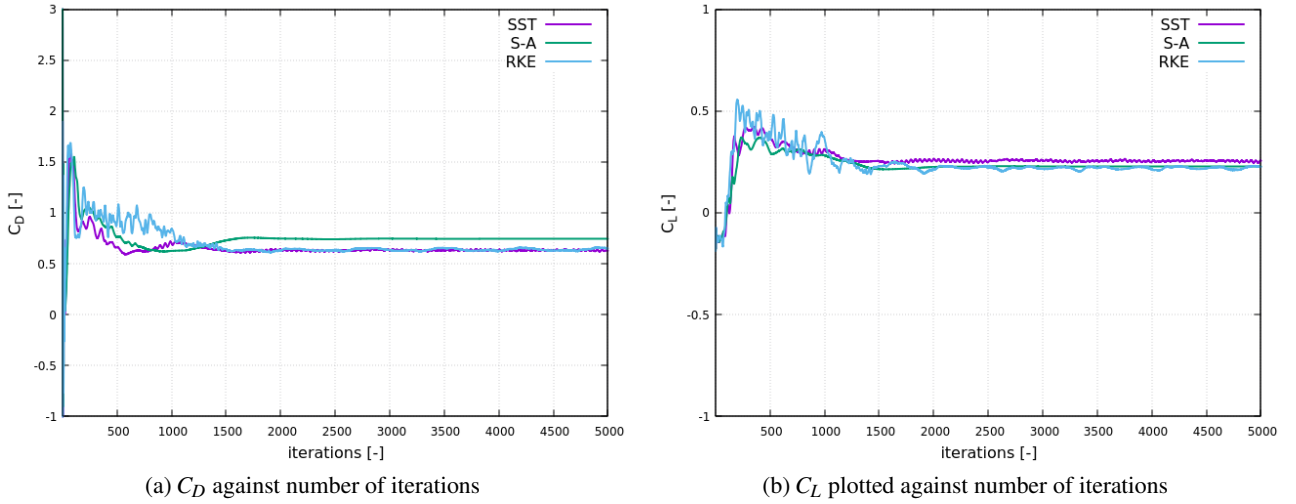


Figure 6.13: C_D and C_L convergence over 5000 iterations for $k - \omega$ SST, S-A and RKE

The obtained results of C_D and C_L are compared to the results of Fackrell [6] and McManus and Zhang [53] in Table 6.15. As can be seen, the obtained C_D for the three turbulence models is overestimated compared to the other results and the value of C_L is underestimated. Note, that Fackrell [6] has stated that there is a margin error of 5% in his results. From the the three turbulence models the $k - \omega$ SST obtains $C_D \approx 0.63$ and $C_L \approx 0.26$, which are the closest values to what was observed by Fackrell [6]. However, the results also depend on the schemes used for the simulations e.g. using the *Gauss linear* term for the divergence terms: $\text{div}(\phi, k)$ and $\text{div}(\phi, \epsilon)$ yield lower $C_D \approx 0.57$ and $C_L \approx 0.18$.

The results obtained are overall in good agreement with the literature. The values obtained were not expected to match exactly due to RANS simulations containing modelling errors, which are more prominent at higher Re_D values. However, generally, it is expected that C_D is in more agreement with the results than C_L . The reason in this case could be the *Gauss upwind* scheme used for the divergence terms, due to it being less accurate and when the *Gauss linear* scheme is used for the RKE model a $C_D \approx 0.57$ was observed, which is closer to the value of Fackrell's experiment [6]. So, this is an indication that RKE with *Gauss linear* gives a more accurate force coefficient result. Then the question becomes why is $C_L \approx 0.18$ so much more underestimated compared to the experimental results? There can be multiple explanations for this e.g. modelling of the contact patch region or modelling error from RANS. Also, note Fackrell [6] achieved the C_L value by integrating the C_p distribution along the mean centerline.

Furthermore, the differences between the results and those of McManus and Zhang [53] are caused by differences in mesh size. The "fine" mesh size used by McManus and Zhang [53] had a total number of cells of 2.94 million with an average of $y^+ \approx 2.5$ near the wheel. Moreover, their simulations were unsteady and as seen before the used schemes and solvers could influence the results as well.

Table 6.15: C_D and C_L values for an isolated wheel in contact with the ground validated by the results of Fackrell [6] and McManus and Zhang [53]

| | C_D | C_L |
|-------------------------------|-------|-------|
| Fackrell [6] | 0.51 | 0.28 |
| McManus and Zhang (S-A) [53] | 0.475 | 0.152 |
| McManus and Zhang (RKE) [53] | 0.434 | 0.156 |
| OpenFOAM ($k - \omega$ SST) | 0.63 | 0.26 |
| OpenFOAM (S-A) | 0.75 | 0.23 |
| OpenFOAM (RKE) [Gauss upwind] | 0.64 | 0.22 |
| OpenFOAM (RKE) [Gauss linear] | 0.57 | 0.18 |

C_p Distribution

The C_p distribution along the centerline of the wheel for the three turbulence models is given in Figure 6.14 together with the results of the experiment of Fackrell [6] and the RANS $k - \omega$ SST simulation of Diasinos et al. [72].

It can be seen that the results from the simulations of the three turbulence models behave similarly. In all cases the flow stagnates near the front of the wheel. Then up to $\theta \approx 50^\circ$ the C_p slightly falls and from there it starts increasing before sharply rising to a positive pressure peak followed by a minor negative peak. An overview of the C_p peak values is given in Table 6.18. The obtained positive peaks are larger than what was observed by Fackrell [6] ($C_p \approx 2.15$) and are really close to what was observed by Diasinos et al. [72] ($C_p \approx 2.7$). Note, that the slight difference in θ location of the peaks is due to small differences in contact patch size even though they should be the same size since the contact patch is constructed based on the method proposed by Diasinos et al. [72]. As shown the largest peak is observed with the RKE model. However, the difference is small. Regarding the negative peak, it is obvious that this peak is more negative in the cases of $k - \omega$ SST ($C_p \approx -0.53$) and S-A ($C_p \approx -0.53$) compared to RKE ($C_p \approx -0.37$). These are very minor peaks and they are smaller than the one observed by Diasinos et al. [72] ($C_p \approx -0.62$) and as mentioned before Fackrell [6] did not observe a negative peak. However, he hypothesised that there should be one. Then moving further along the centerline it can be seen that the behaviour up to the end ($\theta = 360^\circ$) is in great agreement with the experiment since the values lie within the blue shaded area. This is a good indication that the results obtained from the simulation are good and give good insight into how the wheel behaves. Within the turbulence models themselves, looking past the contact patch in more detail, the three turbulence models behave similarly up to $\theta \approx 160^\circ$ then the value of RKE stays relatively constant around $C_p \approx -0.4$ and shifts linearly to $C_p \approx -0.47$ around $\theta \approx 250^\circ$, while $k - \omega$ SST and S-A follow the trend of Fackrell's experiment [6]. From there when looking further along the centerline the region of flow separation is reached. In this region the C_p becomes more negative. This is visible from the results of Diasinos et al. [72]. The same behaviour is observed for RKE and $k - \omega$ SST only less severe in magnitude. So, it agrees more with the C_p distribution of Fackrell's experiment [6]. In the case of S-A this behaviour is not observed. After the separation region, the θ value of the centerline goes up to 360° , back to the front of the wheel.

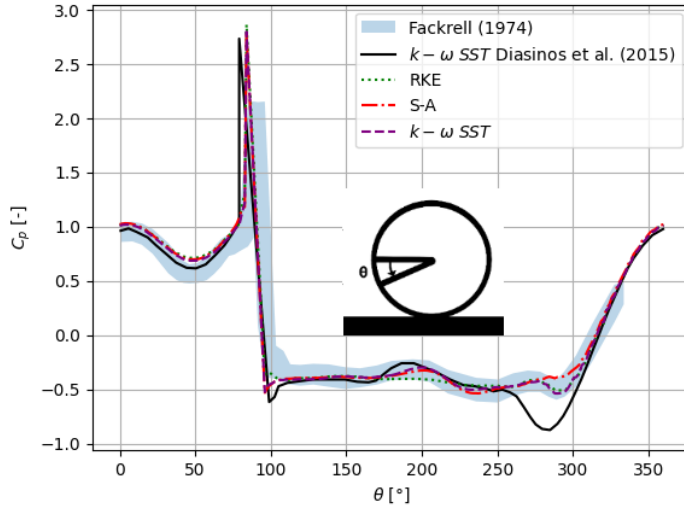


Table 6.16: Layer parameters mesh and contact patch C_p values

| | |
|-------------------|----------------------|
| number of layers | 10 |
| thickness ratio | 1.25 |
| first cell height | 0.0000176491027988 m |

Figure 6.14: C_p distribution along the centerline for $k - \omega$ SST, S-A and RKE

The results of the C_p distribution seem to be in good agreement with the results of Fackrell [6] and Diasinos et al. [72]. However, the results from other research such as that of McManus and Zhang [53] and Dassanayake et al. [54] obtain varying magnitudes regarding the pressure peaks even though the same wheel is used. In addition, Croner et al. [64] used a different wheel and they found peaks of $C_p = 15.6$ and $C_p = -13.5$. Each of these researchers has their approach to modelling the contact patch and generating the mesh and Diasinos et al. [72] did not see major differences in peak value when changing the contact patch size. Therefore, it is also interesting to investigate the sensitivity of the C_p peaks by changing the first cell height. The result of making the first cell height smaller and obtaining $y^+ \approx 0.25$ is presented in Figure 6.15. As can be seen, the peaks indeed become larger. The values of these peaks upstream and downstream of the contact patch are summarised in Table 6.19. Note, that the simulation with the RKE turbulence model diverged which is why only the results of $k - \omega$ SST and S-A are presented. The results show that the positive peak indeed becomes larger going from $C_p \approx 2.80$ to $C_p \approx 3.93$ for $k - \omega$ SST and $C_p \approx 2.77$ to $C_p \approx 3.91$ for S-A. Downstream of the contact patch only $k - \omega$ SST seems to be less sensitive since the C_p value goes from $C_p = -0.53$ to $C_p = -0.58$. In the case of S-A the negative peak increases in magnitude from $C_p = -0.53$ to $C_p = -0.71$. Furthermore, in the separation region the C_p becomes more negative for the $k - \omega$ SST coming closer to the result of Diasinos et al. [72] in that region of the flow.

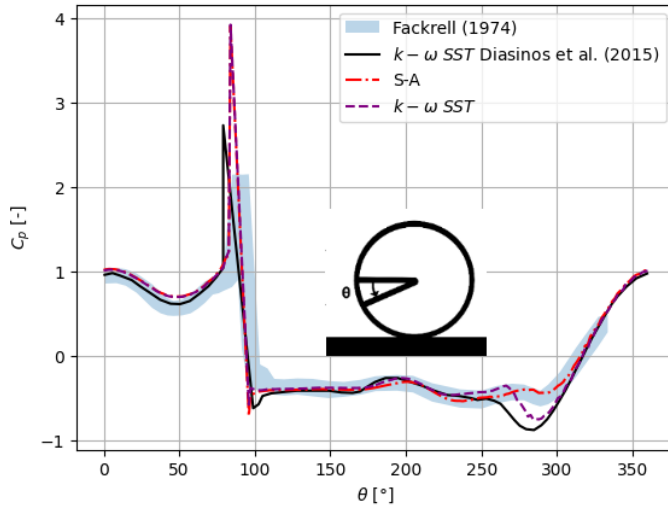


Figure 6.15: C_p distribution along the centerline for $k - \omega$ SST and S-A

Table 6.18: C_p values upstream and downstream of the contact patch area obtained for different $k - \omega$ SST, S-A and RKE

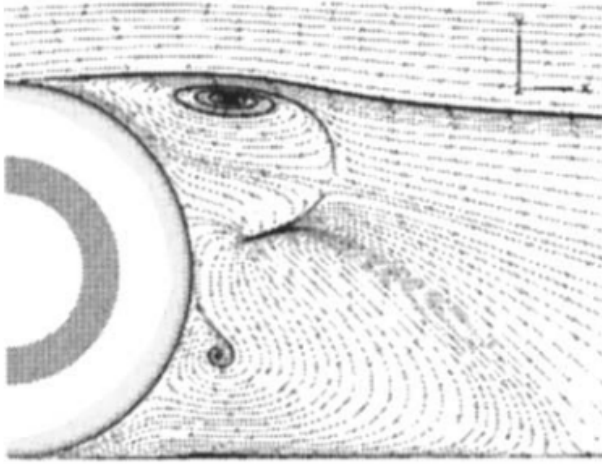
| Turbulence model | C_p upstream | C_p downstream |
|------------------|----------------|------------------|
| $k - \omega$ SST | 2.80 | -0.53 |
| RKE | 2.86 | -0.37 |
| S-A | 2.77 | -0.53 |

Table 6.19: C_p values upstream and downstream of the contact patch area obtained for different $k - \omega$ SST and S-A

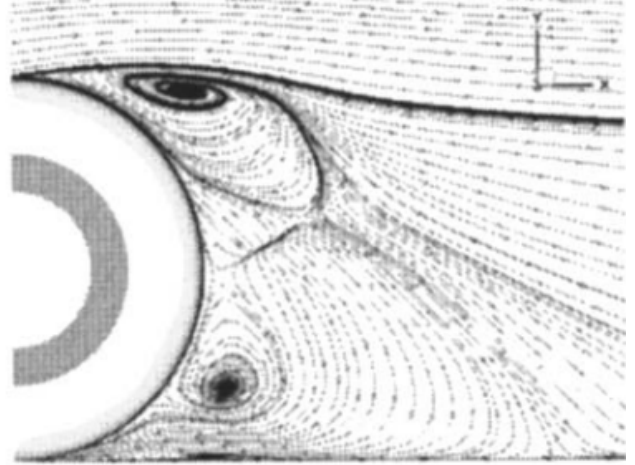
| Turbulence model | C_p upstream | C_p downstream |
|------------------|----------------|------------------|
| $k - \omega$ SST | 3.93 | -0.58 |
| S-A | 3.91 | -0.71 |

2D Streamlines

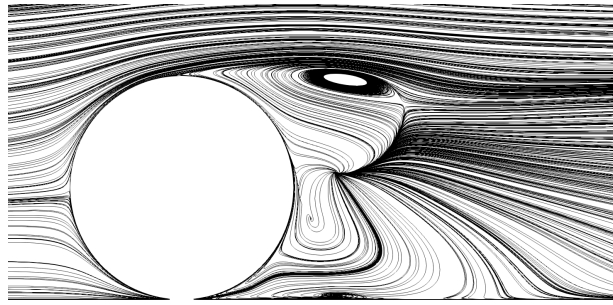
Finally, investigating the flowfield of the three turbulence models and comparing them to the results of McManus and Zhang [53] will show if the three turbulence models predict the same basic flow structures and if they agree with literature. This will be done by analysing the 2D streamlines in the $z/D = 0$ plane. The 2D streamlines results are found in Figure 6.16. The results of McManus and Zhang[53] are found in Figure 6.16a and Figure 6.16b for RKE and S-A respectively. The 2D streamlines obtained from the simulations of RKE, S-A and $k - \omega$ SST are given in Figure 6.16c, Figure 6.16d and Figure 6.16e respectively. As can be seen, all the turbulence models captured the vortex on top caused by separation and the vortex behind the wheel in the near-wake on the ground. The results of McManus and Zhang[53] show that with the S-A turbulence model, a larger vortex on the ground is present compared to RKE, which is the same from the obtained results of Figure 6.16c and Figure 6.16d. Therefore, the obtained flowfields of the three turbulence models are in excellent agreement with the results of McManus and Zhang [53]. Hence, the obtained flowfields are validated.



(a) RKE [53]

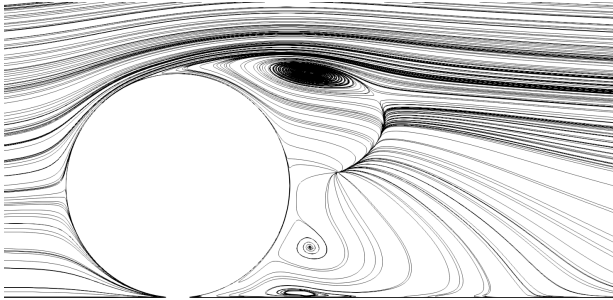


(b) S-A [53]

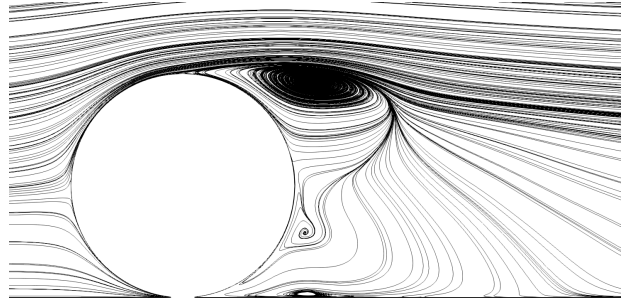


(c) RKE

Figure 6.16: 2D streamlines validation



(d) S-A



(e) $k - \omega$ SST

Figure 6.16: 2D streamlines validation

6.7 Yawed Wheel

The effect of yawing the wheel will be investigated for angles up to $\pm 10^\circ$. Therefore an additional coordinate system is created. This can be seen in Figure 6.17. So, the x -direction aligns with the inflow and normal to it is the z -axis. The other additional coordinate system is a body axis system, which aligns the x' -axis parallel to the wheel geometry and normal to it is the z' -axis. The angle θ these axes make with the xz coordinate system is the angle under which the wheel is yawed.

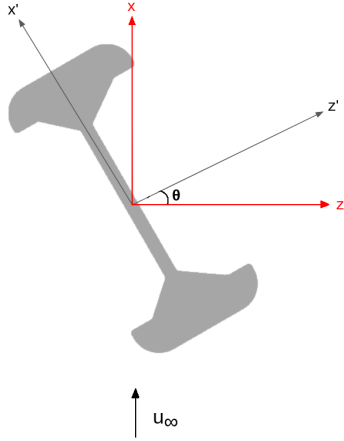


Figure 6.17: Coordinate system for the yaw effect

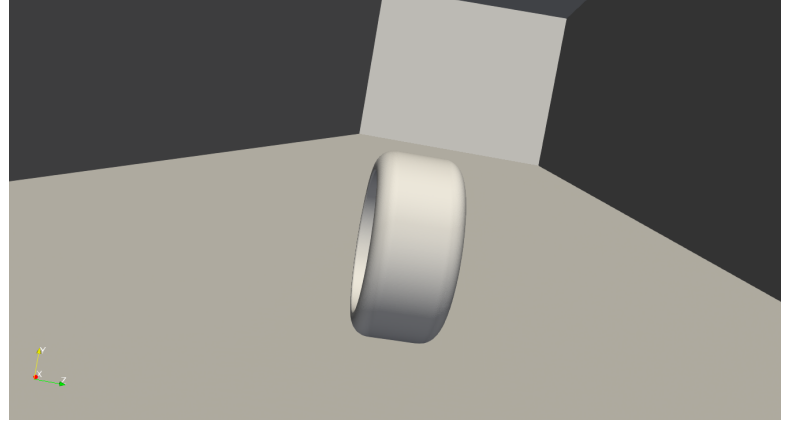


Figure 6.18: Wheel in domain with yaw = 10°

The way this is modelled for the simulations is by yawing the wheel including the contact patch instead of rotating the entire domain. This is shown in [Figure 6.18](#). The reason for this approach is the limitation of regional refinement in cfMesh.

Furthermore, the approach taken to model yaw is to have $u_{x'} = 18.6$ m/s and to match u_∞ accordingly. This is a comparable situation to having a crosswind or yawing the wheel without slipping and keeping the rotational speed the same. Note, that Re_D should be corrected with the new u_∞ . So, to keep the Re_D the same for the simulations to compare the flowfields, the value of ν will be slightly altered. Note, that the $u_{x'}$ and $u_{z'}$ components can be calculated as follows:

$$u_{x'} = u_\infty \cos \theta, \quad (6.9)$$

$$u_{z'} = u_\infty \sin \theta. \quad (6.10)$$

Moreover, an important aspect to keep in mind is to avoid slipping the wheel during the simulations. Therefore, the flow velocity component in $u_{x'}$ is also the ground velocity. Hence, $u_{z'} = 0$ for the ground.

Also, note for the following yaw effect simulations the RKE turbulence model will be used with the *Gauss linear* scheme for the divergence terms. However, compared to what is mentioned in [Section 6.4](#) preliminary yaw simulations showed that the use of the `kLowReWallFunction` for k instead of a `fixedValue` of 0 on the wall types (wheel and ground) resulted in better converging behaviour of the simulations. Therefore, this is used from here on for the yaw simulations and even the Re_D effect simulations.

7. Results

In this chapter, the results of the yawed and Re_D effect RANS simulations are presented and discussed respectively in [Section 7.1](#) and [Section 7.2](#). These sections contain the obtained force coefficients, C_p distribution along the centerline, streamline plots, Q-criterion contour plots, total pressure field plots and velocity field plots. The visualisation of the flowfield results will be given for nine planes. Namely, four x/D planes to investigate the flow behaviour at the wheel ($x/D = 0$ and $x/D = 0.25$) and in the near- and far-wake ($x/D = 0.75$ and $x/D = 1.5$). Then another four y/D planes, which will show the behaviour of the flow moving downstream near the contact patch region ($y/D = 0.0014$), the lower wake region ($y/D = 0.25$), the centre of the wheel ($y/D = 0.5$) and upper wake region ($y/D = 0.75$). Finally, one plane at $z/D = 0$ to observe the behaviour in the flow direction. An overview of these planes is presented in [Figure 7.1](#).

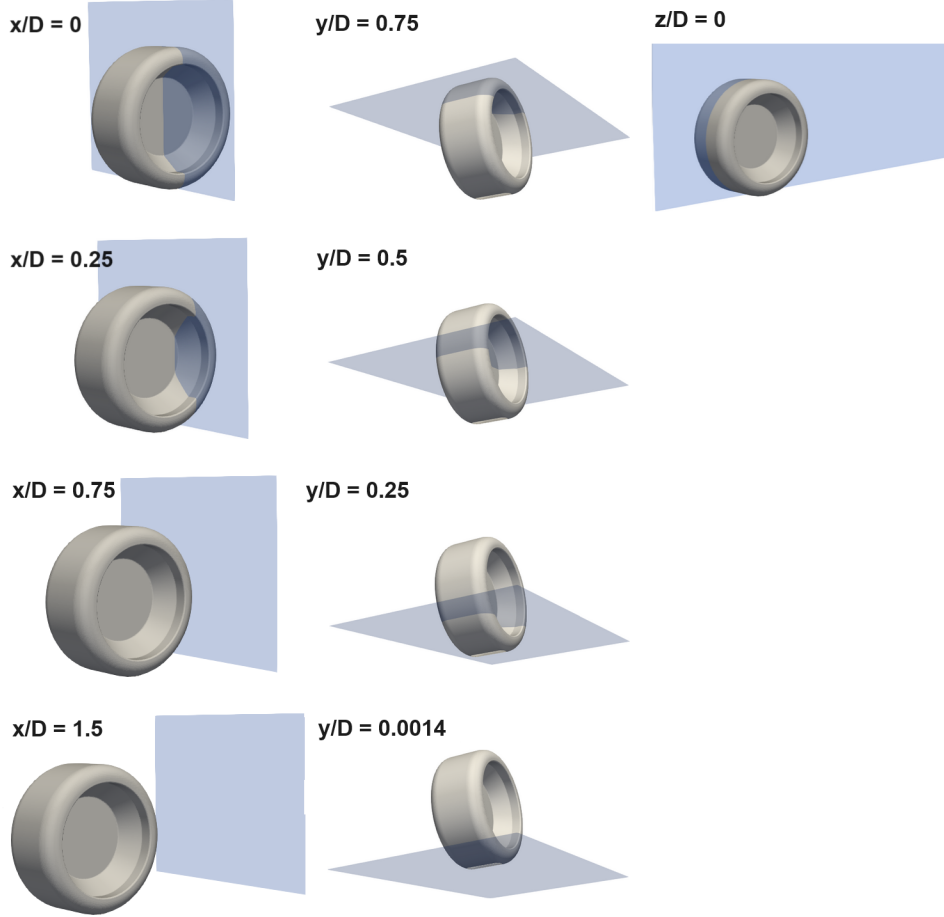


Figure 7.1: x/D , y/D and z/D planes for flow visualisation

7.1 Yawed Wheel

The results of yawing the wheel are presented in this section. The simulations were performed in increments of 2° up to 10° . In the case of the force coefficients and C_p distribution, the results for all the angles are given. However, for the visual plots, the results of 0° , 4° and 10° are given and discussed. The angles 0° and 10° are chosen to clearly show the difference between an unyawed and yawed wake. Furthermore, the yaw angle 4° is chosen as an intermediate step to see if the effects are as pronounced at a smaller yaw angle. Moreover, to describe changes in the flowfield due to yaw the same convention is used as Parfett et al. [9], which can be seen in [Figure 7.2](#).

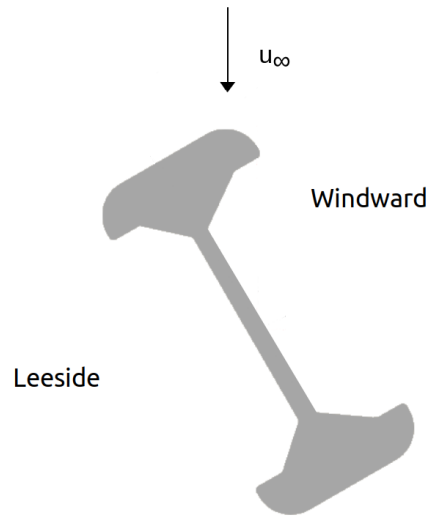
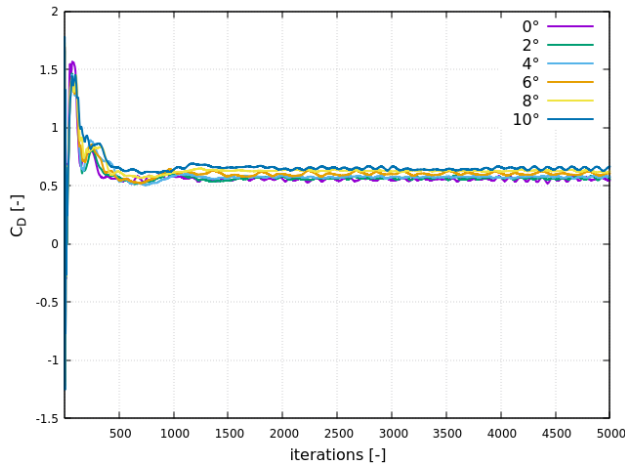


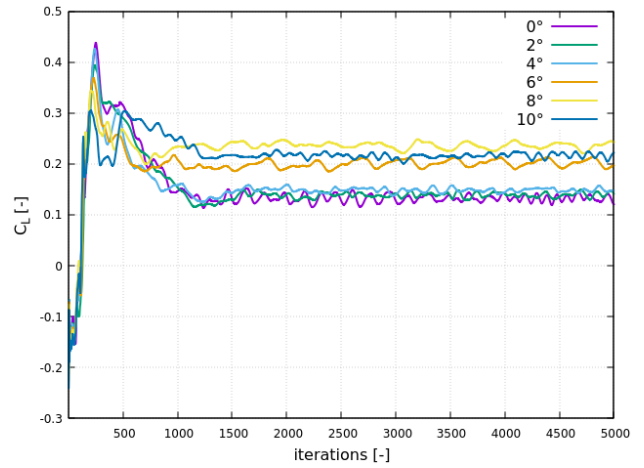
Figure 7.2: The windward and leeward convention

7.1.1 Force Coefficients

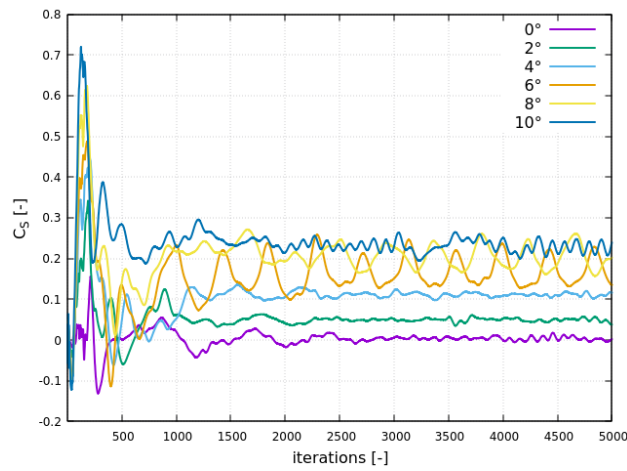
The values obtained for C_D , C_L and C_S plotted against the number of iterations are given in [Figure 7.3](#). These graphs show that the simulations can be considered converged from approximately 1500 iterations since the average force coefficient value does not necessarily change with increasing iterations. The oscillations seen can be attributed to the fact that the flow over a rotating wheel at higher Re_D values is highly unsteady. Another aspect that could play a role is that the higher Re_D value of this complex unsteady flow can be more sensitive to numerical dissipation introduced by the discretization schemes. Also, due to the way the contact patch region is modelled a limited number of layers can be fit in that region. Furthermore, $y^+ \approx 1$ for the first cell height needs to be achieved to resolve the viscous sublayer of the boundary layer. So, a very small first height cell must be chosen for a high Re_D . Generally, as a rule of thumb 25% - 30 % is used as the ratio between mesh cells when gradually increasing the cell size. This is useful since it allows for a smooth transition that can capture the boundary layer and other flow characteristics like the vortices. However, due to the way the contact patch is modelled a limited amount of mesh cells can be fit in that region, which results in a relatively abrupt change in mesh cell size from the last mesh cell in the layer to the rest of the grid. This abrupt change in cell size may lead to numerical instability or convergence difficulties. Therefore, these aspects can attribute to the fact that still some oscillations are present in the force coefficient results and the simulations are considered converged since the average value does not change anymore after a certain number of iterations.



(a) C_D plotted against number of iterations



(b) C_L plotted against number of iterations



(c) C_S plotted against number of iterations

Figure 7.3: C_D , C_L and C_S convergence over 5000 iterations for different yaw angles

The results of the obtained force coefficients are summarised in [Table 7.1](#) and the effect of yawing the wheel on the force coefficients is visualised in [Figure 7.4](#). As can be seen, all C_D , C_L and C_S initially increase when the wheel gets yawed. Both the values of C_D and C_S seem to increase fairly linearly with an increasing yaw angle. Contrary, to C_L which seems to increase initially and stabilise around a value past $\theta \approx 6^\circ$. Furthermore, at $\theta \approx 9^\circ$ C_S becomes larger than C_L . This is obvious since yawing the wheel is relatively the same as having a crosswind from the side. Hence, if the angle becomes larger the effect it will have on C_S becomes larger as well.

Table 7.1: C_D , C_L and C_S values for different yaw angles

| yaw angle [°] | C_D [-] | C_L [-] | C_S [-] |
|---------------|-----------|-----------|-----------|
| 0 | 0.5557 | 0.1322 | 0.0035 |
| 2 | 0.5645 | 0.1387 | 0.0492 |
| 4 | 0.5750 | 0.1484 | 0.1117 |
| 6 | 0.6035 | 0.2016 | 0.1655 |
| 8 | 0.6289 | 0.2356 | 0.2049 |
| 10 | 0.6470 | 0.2162 | 0.2308 |

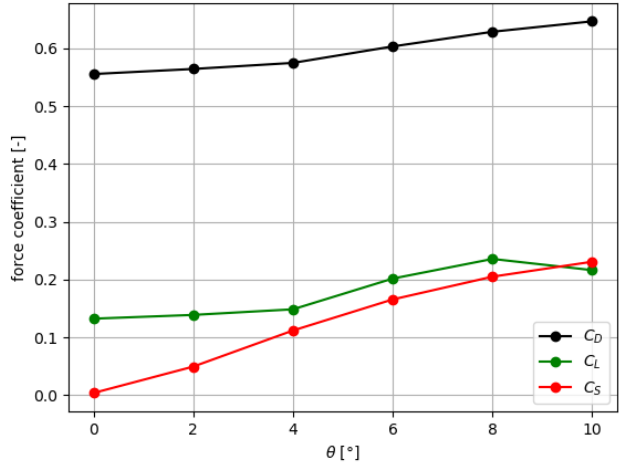


Figure 7.4: C_D , C_L and C_S plotted against θ

7.1.2 C_p Distribution

The results of the C_p distribution along the centerline of the wheel (Figure 7.5) are presented in Figure 7.6. The C_p distribution is plotted against x/D for the sake of convenience. Therefore, two separate graphs are given for the top and bottom half of the wheel.

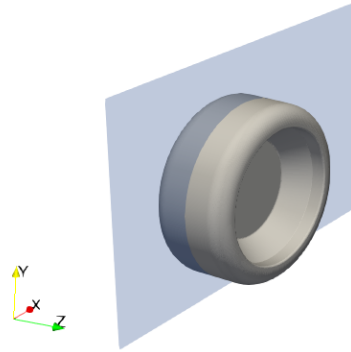


Figure 7.5: The centerline of the wheel plane

The results show that even though there is a yaw angle, the C_p distribution along the centerline of the wheel displays similar behaviour. As can be seen from the bottom half initially the behaviour of the C_p distribution does not change up to the contact patch region where the peaks are achieved. The location of the C_p peaks seems not to be affected by yaw. However, the magnitude of the C_p peaks seems to slightly differ depending on the yaw angle. This difference in magnitude is so small that it can be considered negligible.

Then looking at C_p distribution of the wheel at the part of the wheel where the flow is separated, which is x/D past the lower peak in the bottom half graph and near $x/D > -0.2$ in the upper half plot, the C_p generally becomes more negative for $\theta > 4^\circ$ (more suction). This agrees with the increasing C_L results of the previous subsection.

Furthermore, yawing the wheel does not seem to affect the separation location since the behaviour of the distribution is the same for each angle in Figure 7.6b. Note, that the squiggly behaviour of the lines can be attributed to the interpolation schemes used in OpenFOAM.

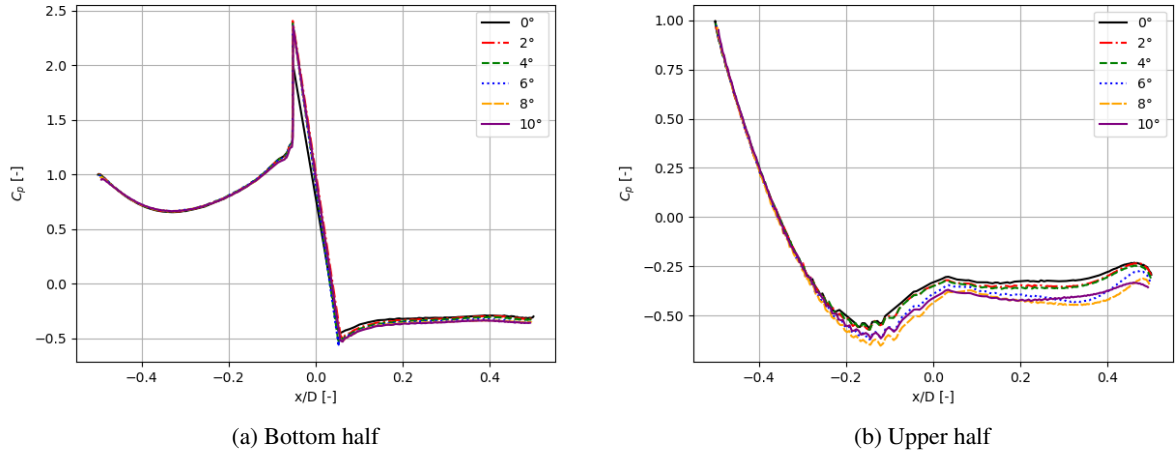


Figure 7.6: C_p distribution of the bottom and upper half of the wheel along the centerline of the wheel

7.1.3 Streamlines

In this subsection visualisations of the streamlines will be given, which will aid in understanding the behaviour of the wake. The results of the streamlines consist of 2D and 3D plots. The 2D streamlines plots for the x/D , y/D and z/D can be found in [Figure 7.7](#), [Figure 7.8](#) and [Figure 7.9](#) respectively. [Figure 7.10](#) and [Figure 7.11](#) show the 3D streamlines from a front and rear view. Finally, [Figure 7.12](#) shows the jetting vortices.

Firstly, when looking at the streamlines of the unyawed wheel an arch-shaped vortex at the upper part of the wake and counter-rotating vortices in the lower part of the wake are observed. This is in agreement with the URANS results of McManus and Zhang [53] and Dassanayake et al. [54].

Furthermore, looking at the x/D planes of the 2D streamlines for $\theta = 0^\circ$ in [Figure 7.7](#) the flow behaves symmetrically. As can be seen, an increasing yaw angle results in an asymmetrical wake. This behaviour is seen in every x/D plane starting from $x/D = 0$. Initially, there are vortices inside the wheel hub on both sides. Then increasing the yaw angle seems to suppress the vortex at the windward side in this plane. Moreover, the counter-rotating vortex pair in the near-wake ($x/D = 0.75$) and far-wake ($x/D = 1.5$) becomes dominated by the leeside vortex, which becomes bigger, while the windward side vortex becomes smaller. In addition, in the near-wake, a vortex starts forming in the upper region of the wake and it moves downstream since it is also present in the far wake of $\theta = 10^\circ$.

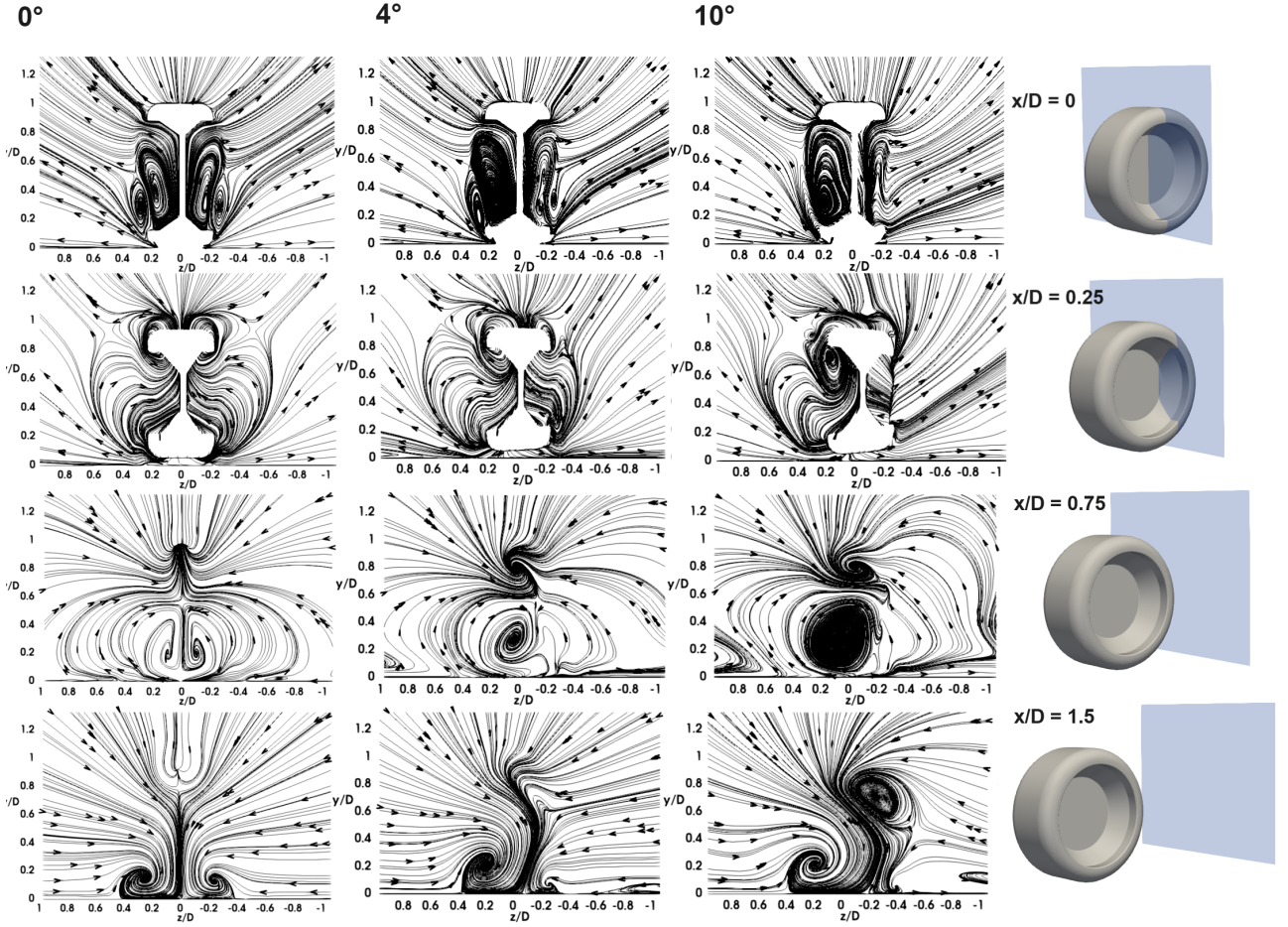


Figure 7.7: 2D streamlines for yaw angles of 0° , 4° and 10° at various x/D planes ($x/D = 0$, $x/D = 0.25$, $x/D = 0.75$ and $x/D = 1.5$)

The results of the y/D planes in Figure 7.8 show that again for an unyawed wheel, the flow structures are symmetric. Then in the upper region of the wake ($y/D = 0.75$) the arch-shaped vortex seems to interact with the flow inside the wheel hub at the leeside for an increasing yaw angle ($\theta = 10^\circ$). Additionally, it looks like when the yaw angle is increased even more then the vortex will also interact with the flow in the hub at the windward side. At the centre of the wheel ($y/D = 0.5$) it is shown that the effect of yaw causes the vortex at the windward side to disappear and the streamlines to move from the leeside to the windward side in the wake. In the lower wake region ($y/D = 0.25$), the symmetry is broken as well. As can be seen, after a small yaw angle (4°) the vortex at the leeside becomes larger as it was initially up to $x/D \approx 1$ for $\theta = 0^\circ$ and then becomes $x/D \approx 1.5$ for $\theta = 4^\circ$. Near the contact patch region, the effect yaw has on the counter-rotating vortex pair seen in the far-wake ($x/D = 1.5$) is also visible here. As can be seen, the leeside vortex becomes more dominant by how the streamlines move downstream.

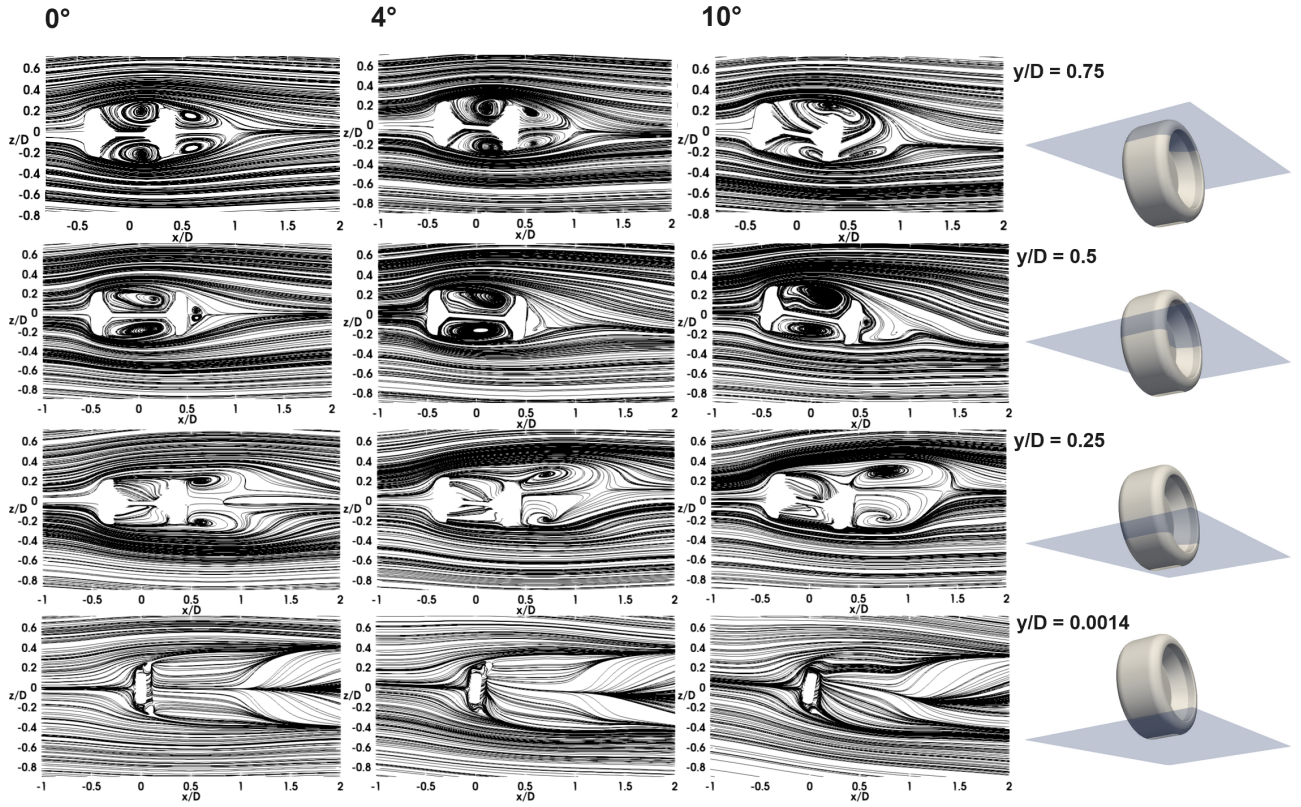


Figure 7.8: 2D streamlines for yaw angles of 0° , 4° and 10° at various y/D planes ($y/D = 0.0014$, $y/D = 0.25$, $y/D = 0.5$ and $y/D = 0.75$)

Finally, [Figure 7.9](#) shows that the vortex in the lower part of the wake becomes larger by increasing the yaw of the wheel. This is due to the fact that the vortex at the leeside in the lower wake increases in size as a result of yaw, which was seen in the previous planes.

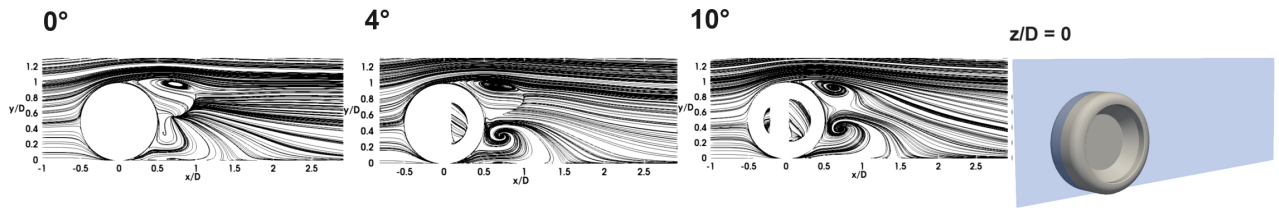
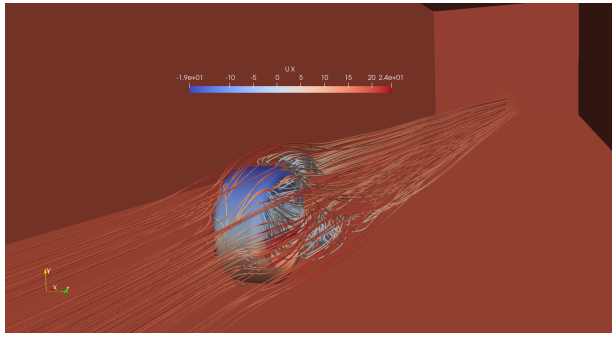
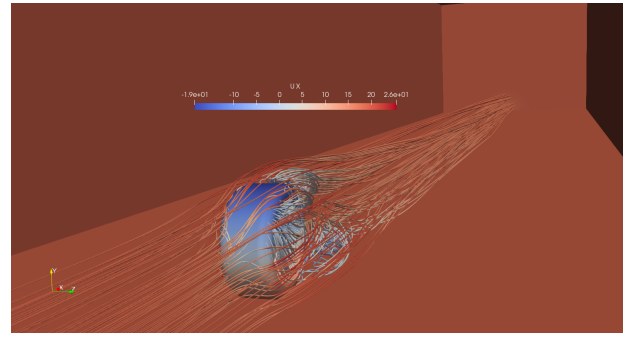


Figure 7.9: 2D streamlines for yaw angles of 0° , 4° and 10° at $z/D = 0$

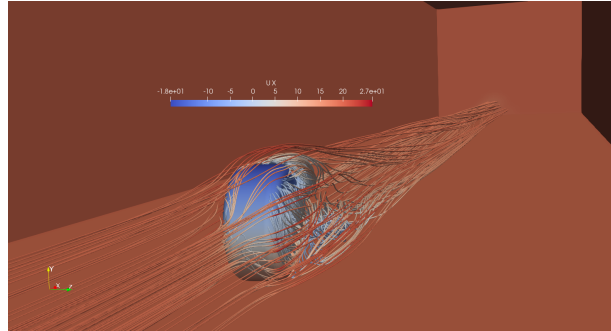
In the 3D streamlines plot of the front view ([Figure 7.10](#)) it is clearly visible that the arch-shaped vortex starts to merge with the flow in the wheel hub at the leeside. Furthermore, the increasing size of the lower wake vortex is very obvious when looking at the rear view ([Figure 7.11](#)). Note, that the streamlines are truncated in that view to make the Figure clearer. Finally, [Figure 7.12](#) shows the jetting vortices emerging from the contact patch. As can be seen, the effect of yaw is that the vortex at the windward side starts to become smaller as well while at the leeside the vortex is still present.



(a) 0°

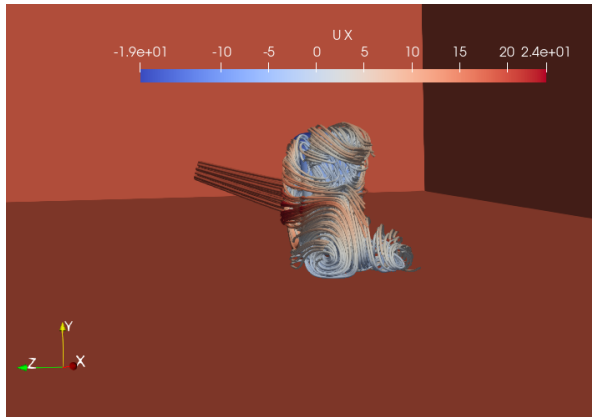


(b) 4°

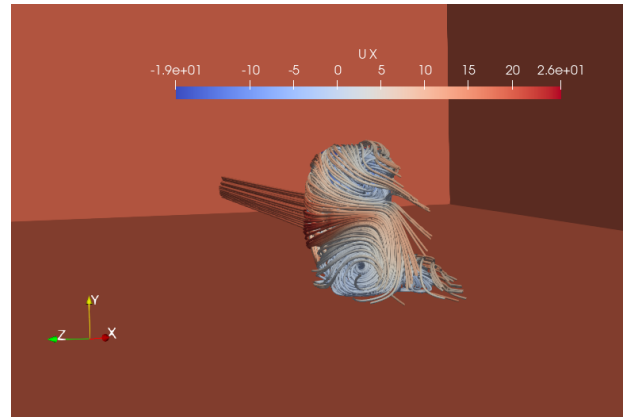


(c) 10°

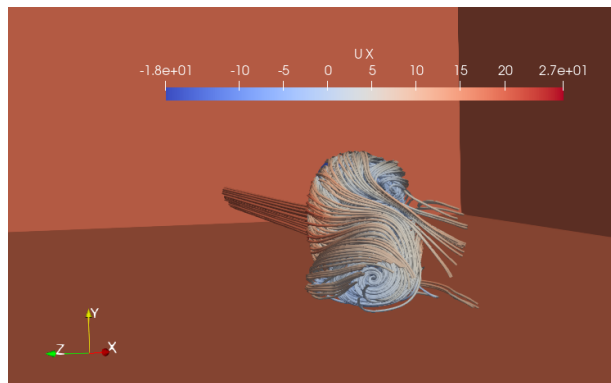
Figure 7.10: 3D streamlines front view for yaw angles of 0°, 4° and 10°



(a) 0°



(b) 4°



(c) 10°

Figure 7.11: 3D streamlines rear view for yaw angles of 0°, 4° and 10°

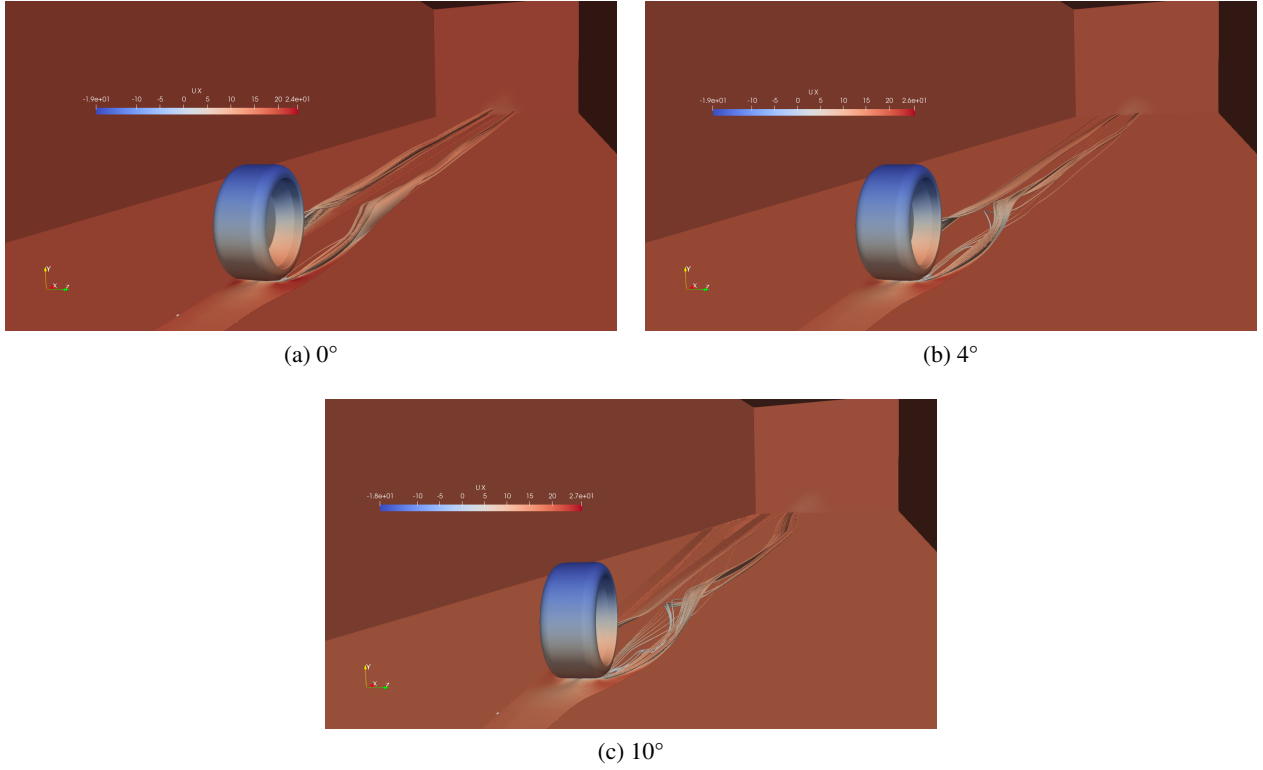


Figure 7.12: 3D streamlines of the jetting vortices emerging from the contact patch for yaw angles of 0° , 4° and 10°

7.1.4 Q-criterion

The Q-criterion is a method that allows for visualisation of the flow structures. The definition is given as follows:

$$Q = \frac{1}{2} (\|\Omega\|^2 - \|S_{ij}\|^2) > 0, \quad (7.1)$$

with Ω being the vorticity tensor and S_{ij} being the strain-rate tensor. According to this criterion vortices of an incompressible flow are identified as a "connected fluid region with a positive second invariant of ∇u ". So, vortices are identified when the magnitude of the vorticity is larger than the magnitude of the strain rate. Furthermore, an additional condition is set requiring the pressure in the vortex to be lower than the ambient pressure [87].

The results of the obtained isosurfaces for $Q = 1000$ seen from the front and rear side for $\theta = 0^\circ$, $\theta = 4^\circ$ and $\theta = 10^\circ$ are presented in Figure 7.13, Figure 7.14 and Figure 7.15 respectively. The first thing that is observed in all the figures are the structures on the ground, which are present at the borders of the refinement regions. The appearance of spurious structures is most likely a result of the way gradients are calculated in Paraview, which is different than in OpenFOAM.

Furthermore, the other structures are present in the wheel hub, in the upper region of the wake and in the lower region of the wake. The side shown from the front view is the leeside of the wheel. As can be seen for increasing yaw, structures are still present inside the leeside wheel hub. Moreover, from the front view already it can be observed that the structure trailing the wheel at the leeside becomes bigger indicating a larger vortex at that side. This is confirmed with the rear view. Firstly, as can be seen in Figure 7.13b from the rear view at an unyawed wheel the structures are symmetrical. In the upper wake region, the arch-shaped vortex caused by the flow separating is clearly visible and in the lower wake region, first larger structures are observed in the near-wake, which become smaller structures moving downstream indicating the vortices become smaller moving downstream. When the yaw is increased to $\theta = 4^\circ$ it can be observed that the leeside structure indeed slightly starts to become larger than the windward structure in the lower near-wake region. For this yaw the

arch-shaped vortex is still present and very slightly tilted towards the leeside. Eventually, when the yaw is increased enough ($\theta = 10^\circ$) as can be seen in Figure 7.15b the structures changed significantly compared to the unyawed case. As can be seen, after the arch-shaped structure there is a vortical structure moving downstream in the upper wake region at the windward side. Additionally, in the lower near-wake region the leeside structure becomes even bigger and the windward structure even smaller.

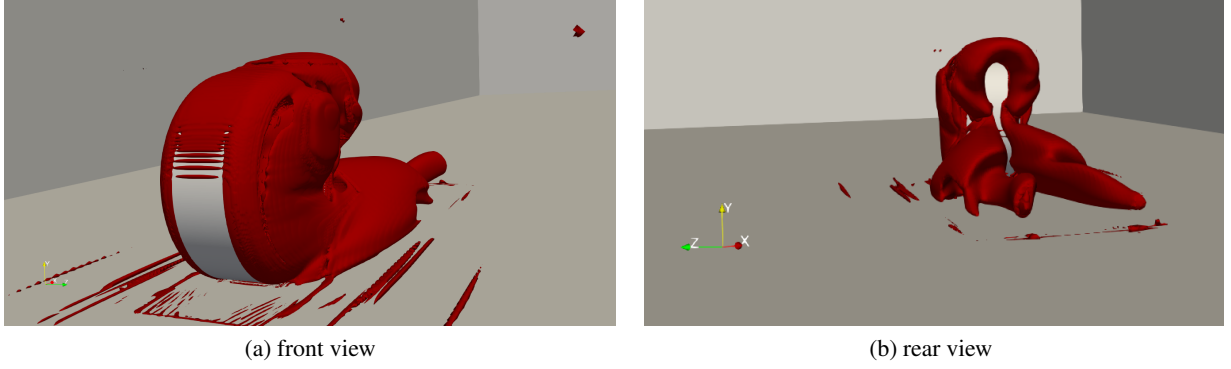


Figure 7.13: Isosurface of $Q = 1000$ contour level for a yaw angle of 0°

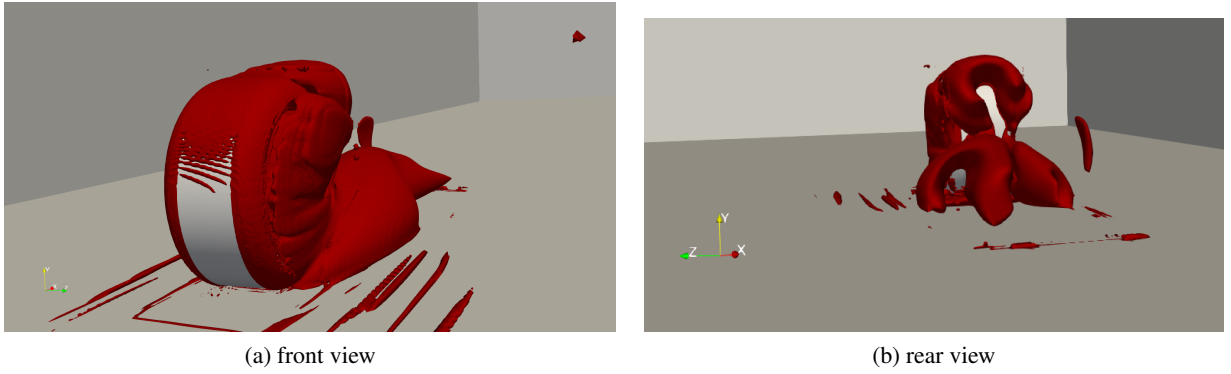


Figure 7.14: Isosurface of $Q = 1000$ contour level for a yaw angle of 4°

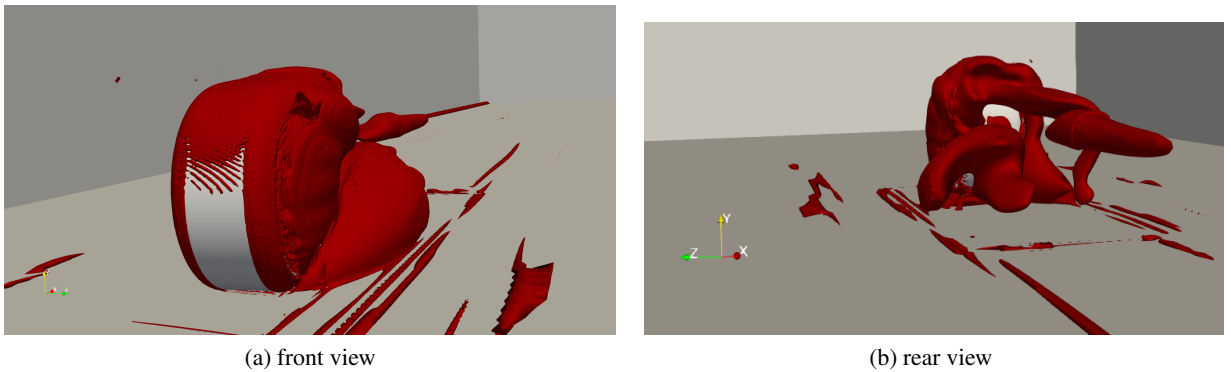


Figure 7.15: Isosurface of $Q = 1000$ contour level for a yaw angle of 10°

7.1.5 $C_{p_{total}}$ Fields

The results of the $C_{p_{total}}$ fields are presented in this subsection. The reason to visualise the $C_{p_{total}}$ is due to the fact that it easily shows the outline of the wake. The total pressure is computed as follows:

$$p_t = p_{ref} + p + 0.5\rho|\mathbf{u}|^2 \quad (7.2)$$

with $p_{\text{ref}} = 0$ [79]. The results of the x/D planes can be found in Figure 7.16. For the cases of the y/D planes and the $z/D = 0$ plane the results are presented in Figure 7.17 and Figure 7.18 respectively. The figures consist of the plots with the most left column being for the unyawed wheel. The column next to it contains the results for a yaw angle of 4° and next to those plots are the results of $\theta = 10^\circ$. The corresponding planes can be seen on the right side of the figure.

The results as seen in Figure 7.16 clearly show the change in the wake with an increase in the yaw of the wheel. As can be seen, the wake starts to become larger at the positive z/D side and smaller at the negative z/D side. This effect on the wake is more pronounced when moving more downstream. Moreover, when specifically looking at the far-wake $x/D = 1.5$ plane, the upper region of the wake shifts towards the right and the wake becomes shorter as well.

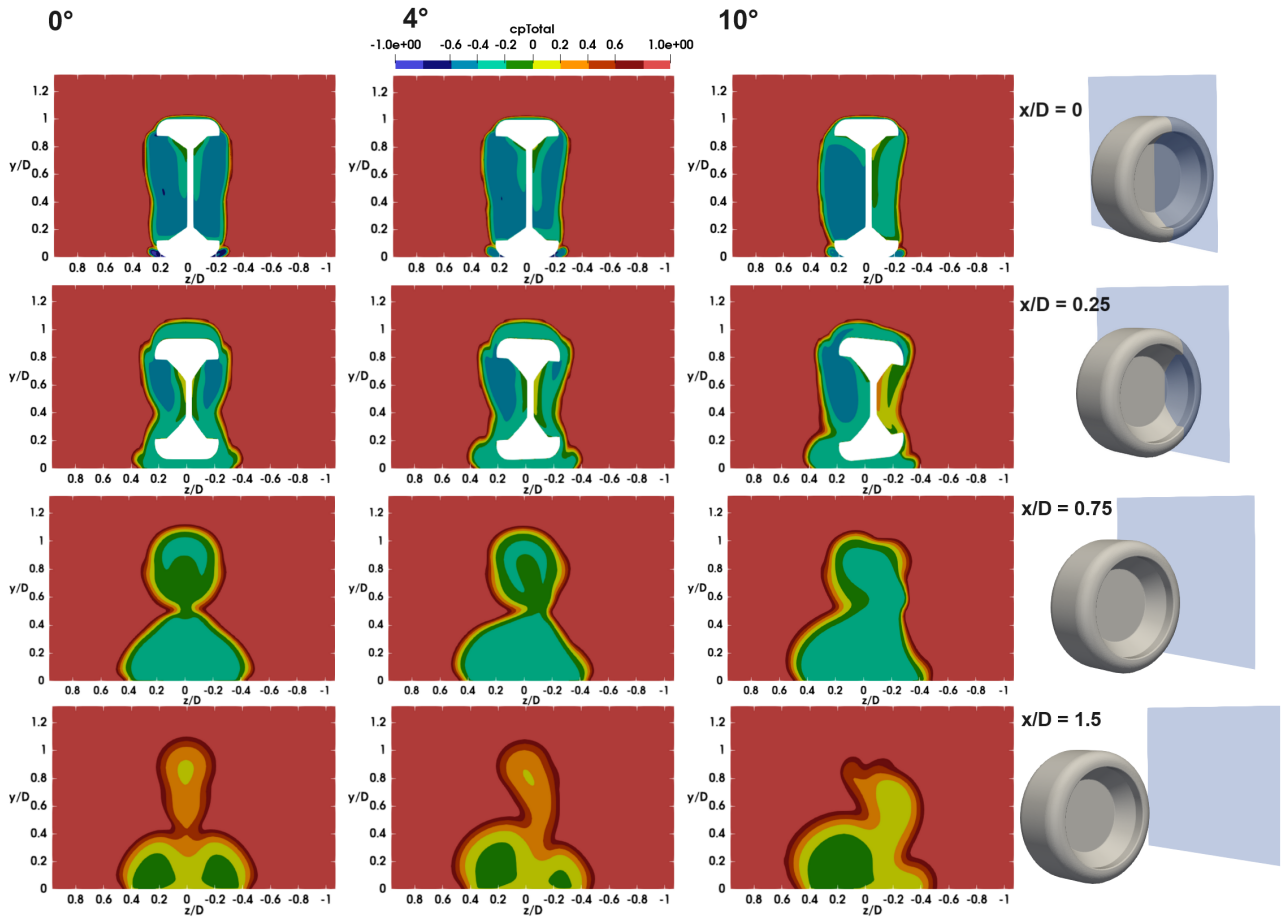


Figure 7.16: $C_{p\text{total}}$ fields for yaw angles of 0° , 4° and 10° at various x/D planes ($x/D = 0$, $x/D = 0.25$, $x/D = 0.75$ and $x/D = 1.5$)

The results of Figure 7.17 show that looking at the upper plane at $y/D = 0.75$ the wake will rotate with the yaw angle moving downstream. Furthermore, the wake is bigger at the centre plane due to the yaw. Also, the increase in size at the leeside is clearly visible moving downstream in the lower wake.

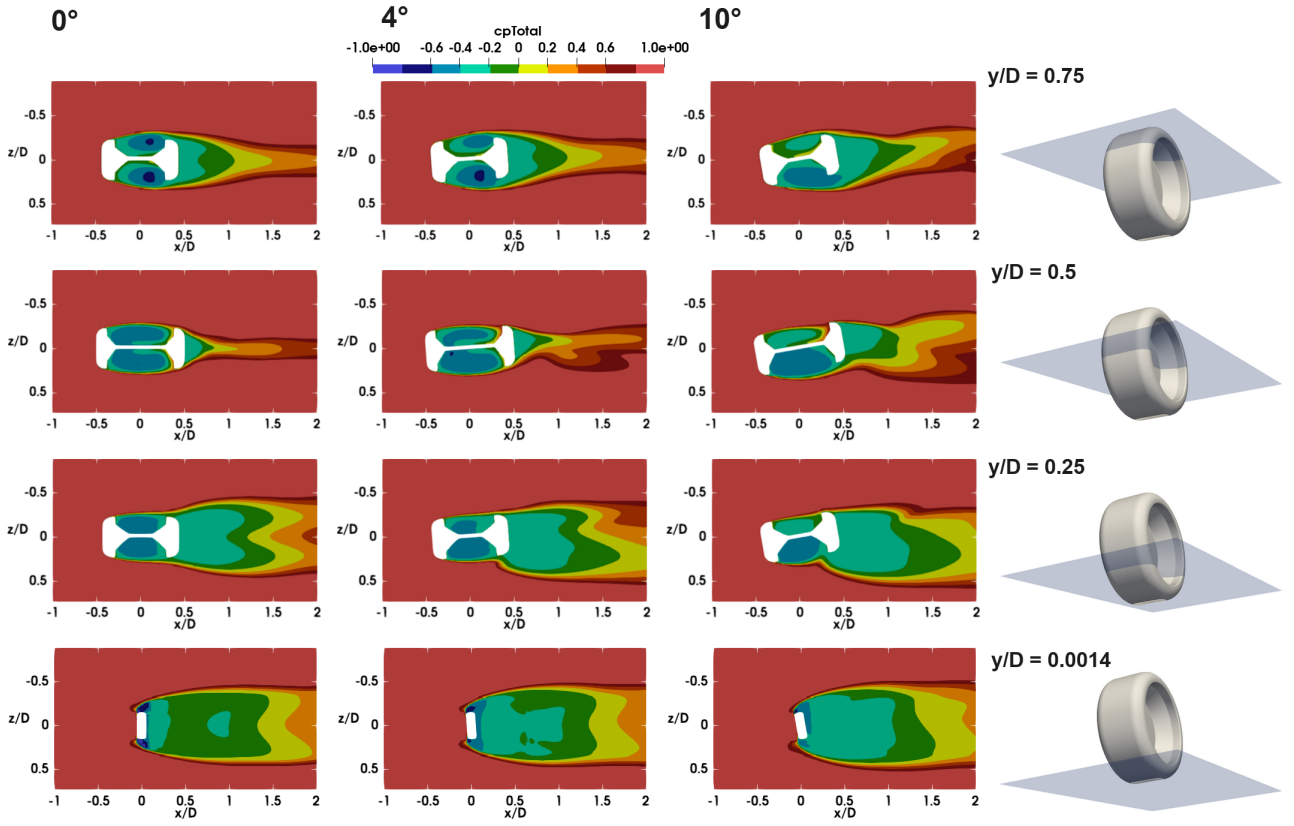


Figure 7.17: C_{pTotal} fields for yaw angles of 0° , 4° and 10° at various y/D planes ($y/D = 0.0014$, $y/D = 0.25$, $y/D = 0.5$ and $y/D = 0.75$)

In Figure 7.18 it is visible that at $z/D = 0$ the wake is shorter (smaller in the y/D direction) downstream in the wake with an increasing yaw angle. This is clearly visible when comparing the plots of $\theta = 0^\circ$ and $\theta = 10^\circ$.

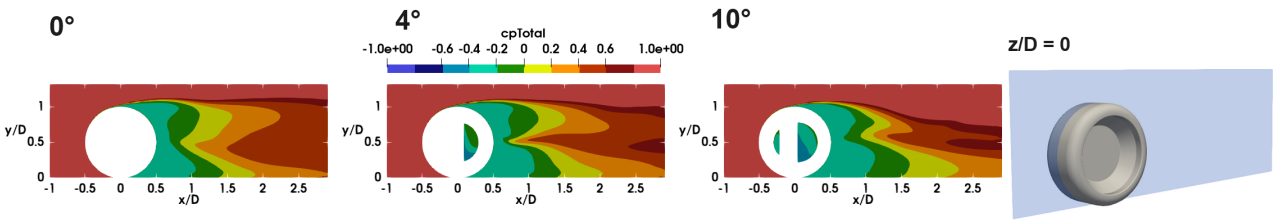


Figure 7.18: C_{pTotal} fields for yaw angles of 0° , 4° and 10° at $z/D = 0$

7.1.6 Velocity Fields

In this subsection, the velocity fields in the x –, y – and z –direction normalised by u_∞ for the different planes (Figure 7.1) are given. The results of the x/D planes are given in Figure 7.19 - Figure 7.22 and the results of the y/D planes are given in Figure 7.23 - Figure 7.26. Finally, the velocity fields of $z/D = 0$ are shown in Figure 7.27. The figures contain the field plots for $\theta = 0^\circ$ on the first row, $\theta = 4^\circ$ on the second row and $\theta = 10^\circ$ on the bottom third row. The left column represents u_x/u_∞ , the middle column u_y/u_∞ and the column most to the right u_z/u_∞ .

The plane looking at the velocity fields at the centre of the wheel $x/D = 0$ is presented in Figure 7.19. The results show that at the upper side of the wheel hub, there is backwards flow (negative u_x/u_∞). This is the most severe close to the wheel since the largest negative u_x/u_∞ values are observed there. As can be seen in the left column is that increasing the yaw angle results in less negative u_x/u_∞ in the leeside wheel hub while

the magnitude remains the same in the windward side. Furthermore, the u_y/u_∞ plots clearly show that at the leeside the area of negative u_y/u_∞ becomes larger, which indicates more flow is moving downwards there and at the windward this becomes smaller. So, these are the main observations at the centre x/D plane of the wheel from the velocity field plots.

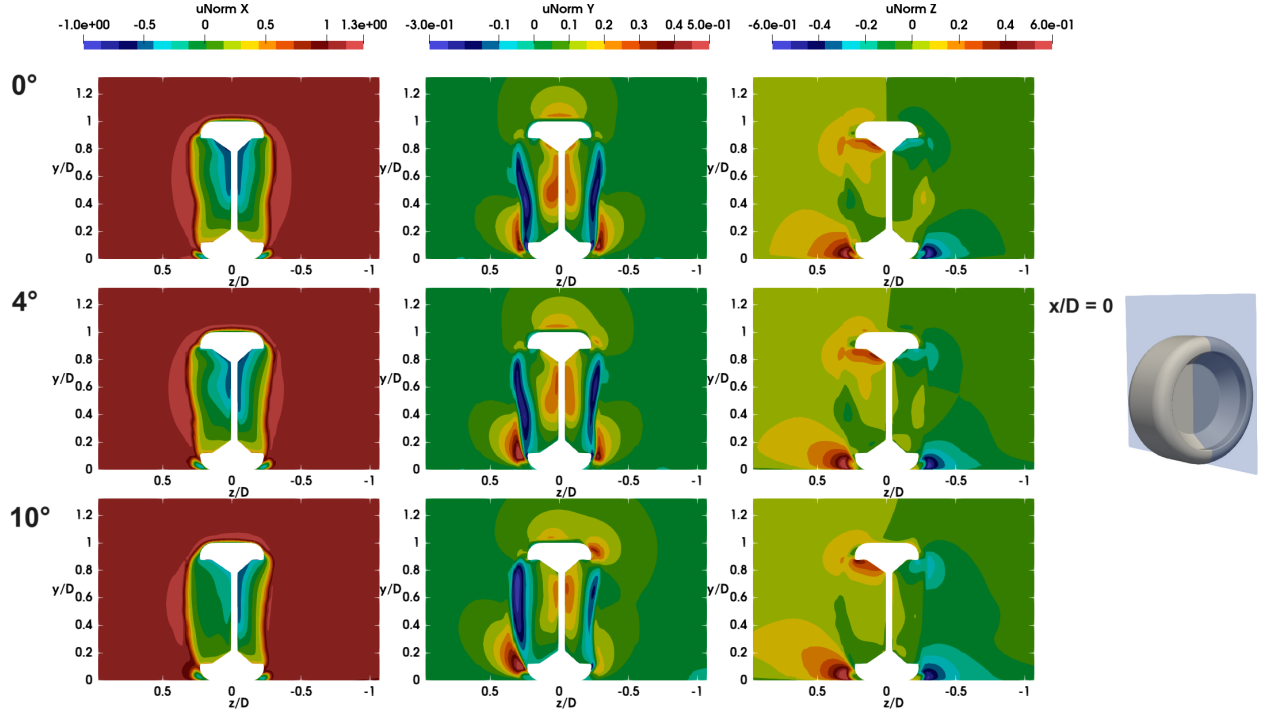


Figure 7.19: Normalised u_x , u_y and u_z by u_∞ for yaw angles of 0° , 4° and 10° at $x/D = 0$

Moving more downstream at $x/D = 0.25$ (Figure 7.20) similar behaviour is observed as seen in Figure 7.19 regarding the flow at the leeside and windward side. In this plane, the asymmetry of the flow with increasing yaw angle is more visible. As can be seen in the middle column, the area (blue) with negative u_y/u_∞ at the top of the wheel for $\theta = 0^\circ$ at the windward side and the red area below it diminish with increasing yaw while the same areas at the leeside become more pronounced.

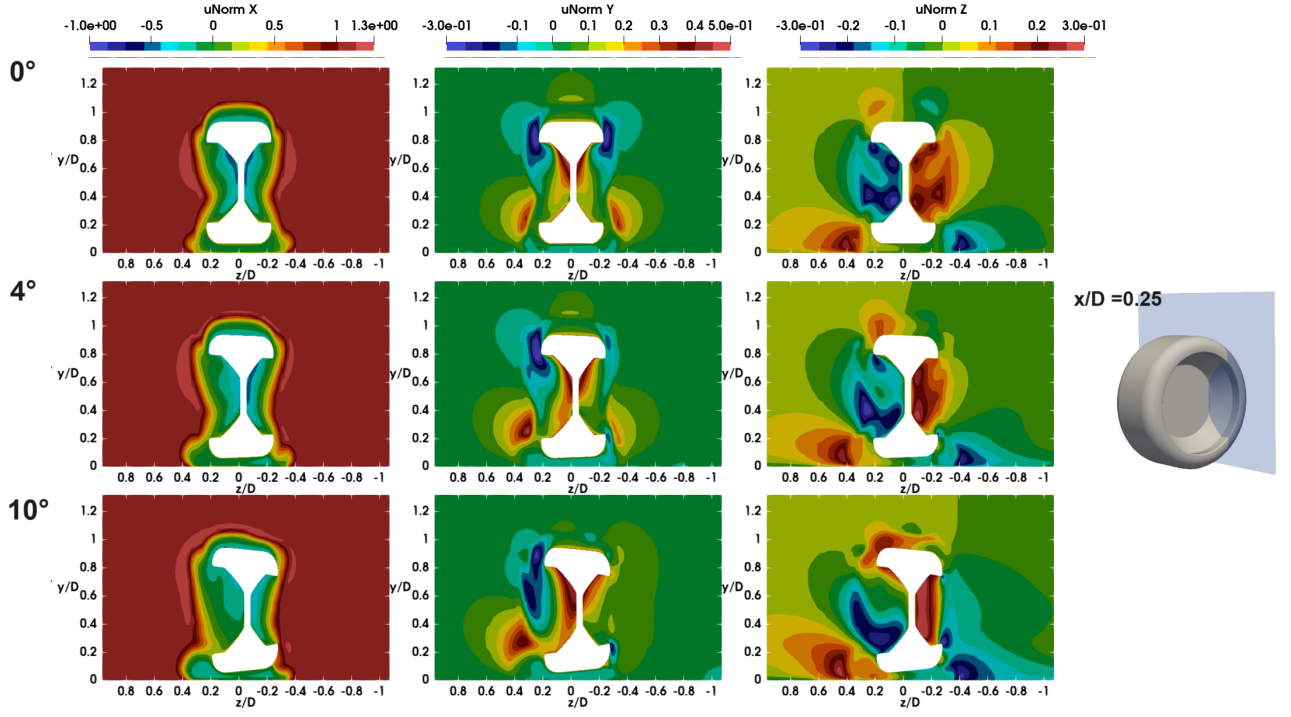


Figure 7.20: Normalised u_x , u_y and u_z by u_∞ for yaw angles of 0° , 4° and 10° at $x/D = 0.25$

In the near-wake [Figure 7.21](#) the regions with the most backward flow are the light blue areas in the upper part of the wake and in the lower part of the wake. They correspond to the arch-shaped vortex and the counter-rotating vortex pair. Additionally, due to yaw when $\theta = 10^\circ$ is compared to $\theta = 0^\circ$ it can be seen that there is more backwards flow in the near-wake for $\theta = 10^\circ$. Again the yawing enforces the structures at the leeside and the magnitudes become smaller at the windward side when looking at u_y/u_∞ and u_z/u_∞ .

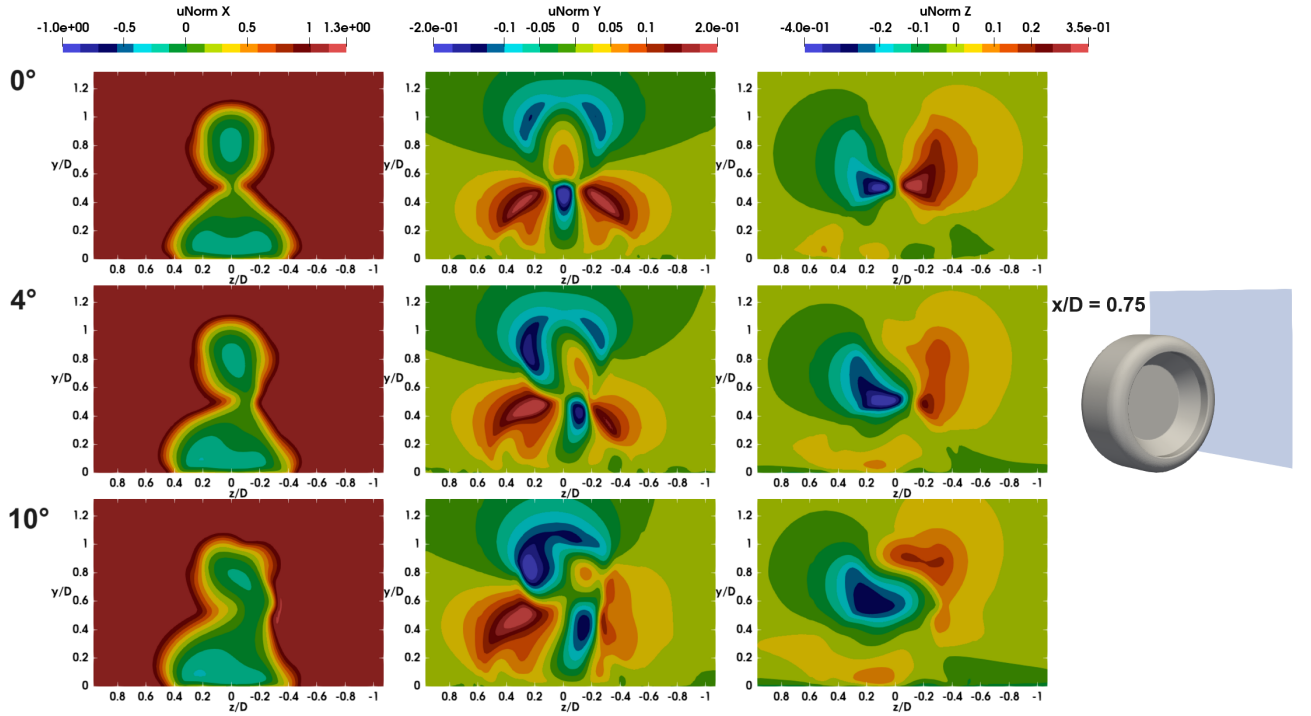


Figure 7.21: Normalised u_x , u_y and u_z by u_∞ for yaw angles of 0° , 4° and 10° at $x/D = 0.75$

Finally, in the far-wake ([Figure 7.22](#)) the asymmetry is the most obvious. The regions with backward flow shift more towards the positive z/D direction (leeside) and increase in size in the y/D direction when looking

at the lower part of the wake. At the upper part of the wake, the regions with reversed flow seem to move to the negative z/D direction. Moreover, in the u_z/u_∞ plots it can be seen that the blue area with negative u_z/u_∞ increases in size with an increasing yaw angle.

Additionally, the red area with positive u_z/u_∞ (negative z/D -direction) shifts upwards and increases in magnitude. Furthermore, in the positive z/D -direction the u_z/u_∞ on the ground also increases in magnitude. As can be seen, the red and blue areas become more intense and larger.

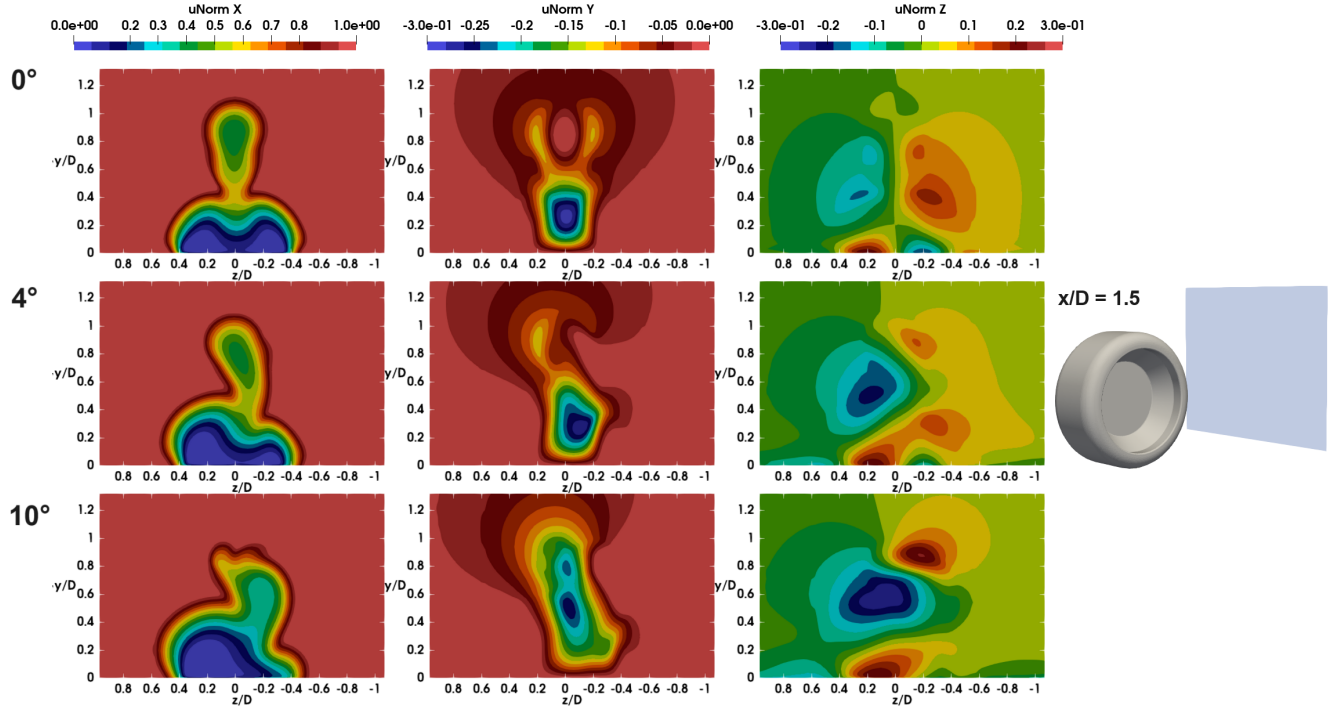


Figure 7.22: Normalised u_x , u_y and u_z by u_∞ for yaw angles of 0° , 4° and 10° at $x/D = 1.5$

The y/D planes are interesting due to the fact that they show the effect of yaw over those planes downstream. As can be seen for the upper plane of the wheel $y/D = 0.75$ yawing only tends to rotate the wake and does not affect the magnitudes of u_x/u_∞ . However, regarding u_z/u_∞ the blue region becomes bigger (negative) and the red region becomes smaller (positive). Moreover, regarding $y/D = 0.5$ the wake in that plane becomes bigger including the region of backward flow with increasing θ . Also, the yellow/orange region in the near wake near the leeside becomes bigger and the windward side smaller with yaw as seen in the u_y/u_∞ plots. Furthermore, the big red region in the wake for u_z/u_∞ seems to become way smaller as well with increasing yaw.

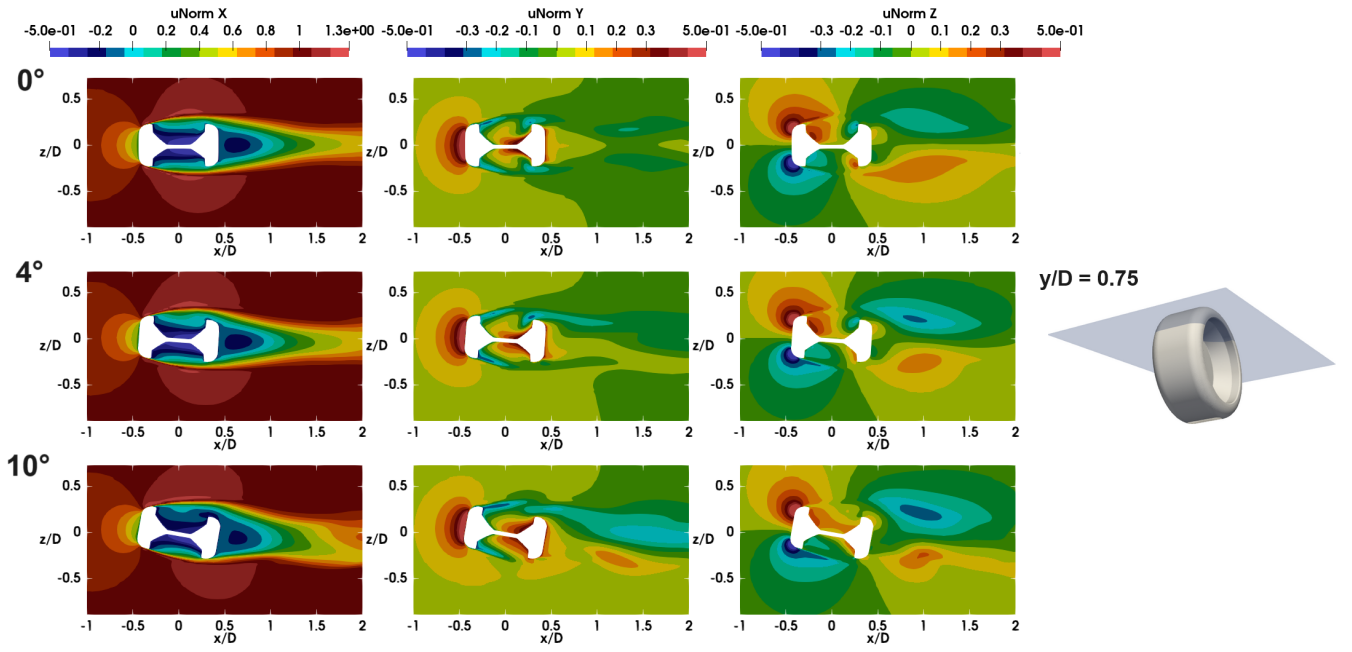


Figure 7.23: Normalised u_x , u_y and u_z by u_∞ for yaw angles of 0° , 4° and 10° at $y/D = 0.75$

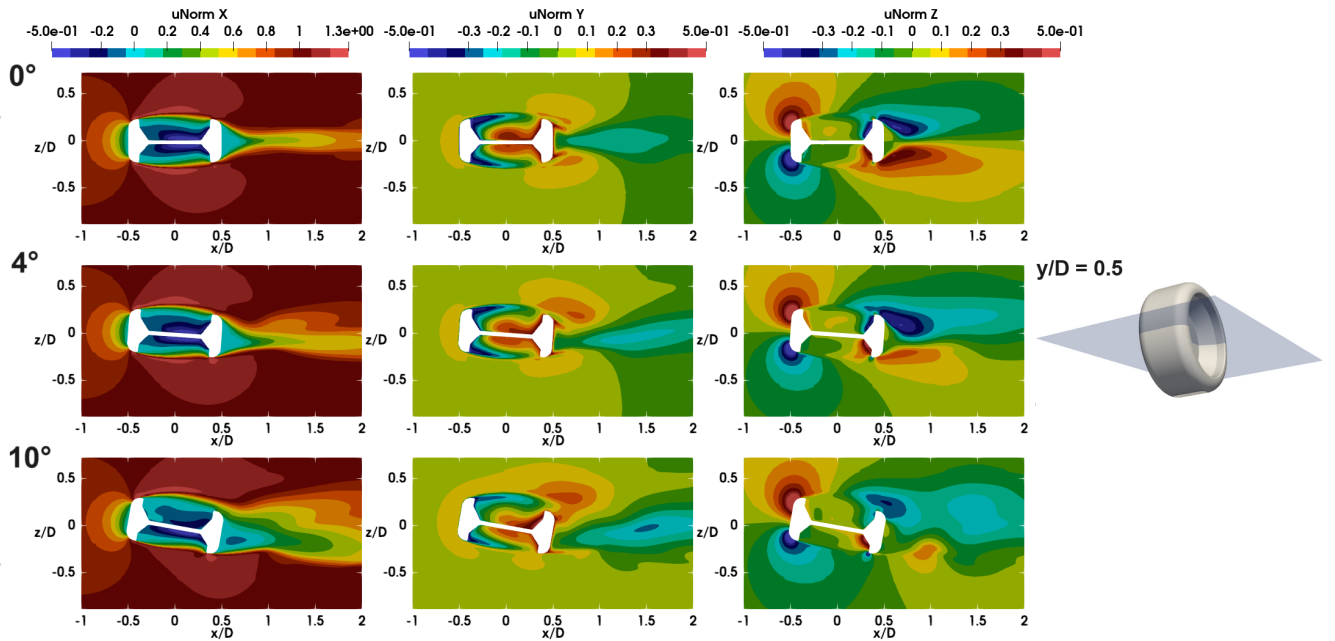


Figure 7.24: Normalised u_x , u_y and u_z by u_∞ for yaw angles of 0° , 4° and 10° at $y/D = 0.5$

Clearly, the lower wake plane $y/D = 0.25$ shows an increase in the backward flow region of the wake with an increasing angle θ . The blue area region increases in size towards the leeside of the wheel. This effect caused by the yaw is more severe in this plane than in the other y/D planes.

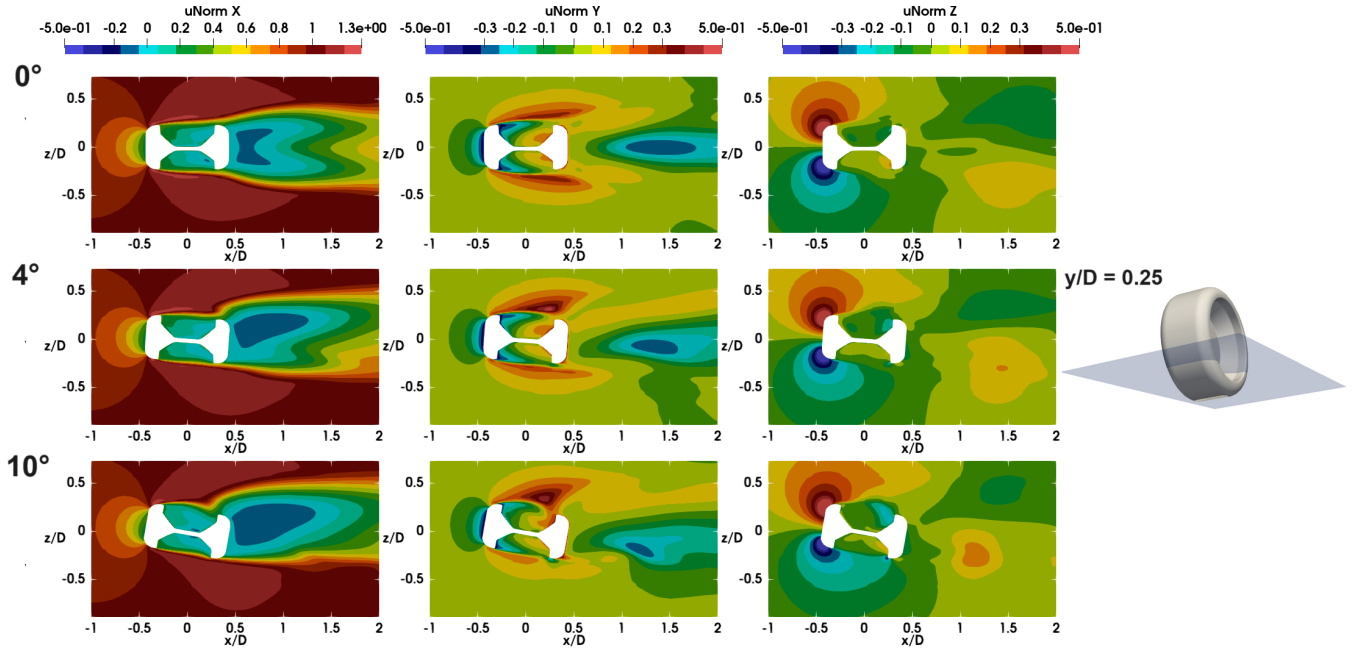


Figure 7.25: Normalised u_x , u_y and u_z by u_∞ for yaw angles of 0° , 4° and 10° at $y/D = 0.25$

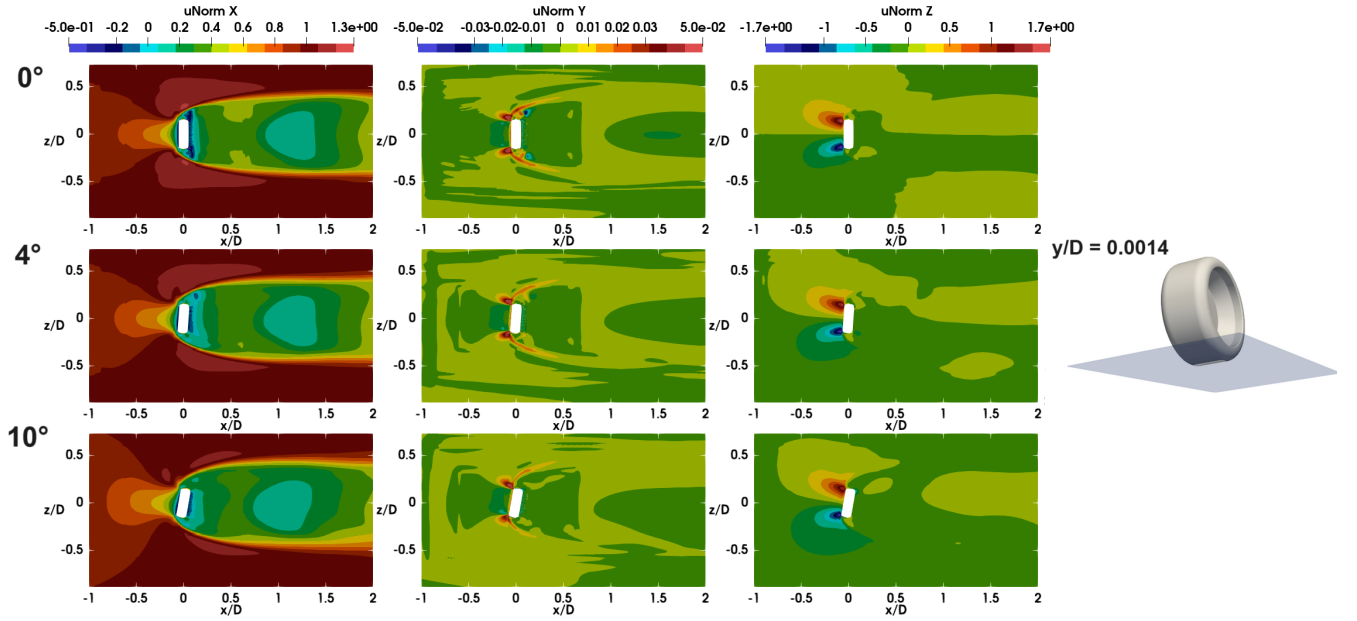


Figure 7.26: Normalised u_x , u_y and u_z by u_∞ for yaw angles of 0° , 4° and 10° at $y/D = 0.0014$

Looking at the $z/D = 0$ plane in [Figure 7.27](#) it is observed that u_y/u_∞ in the wake for $z/D = 0$ becomes less negative for an increasing yaw from 0° to 4° . Furthermore, the effect of the increase in lower wake vortex size at the leeside due to yaw is clearly visible in the u_z/u_∞ images with both the red and blue regions.

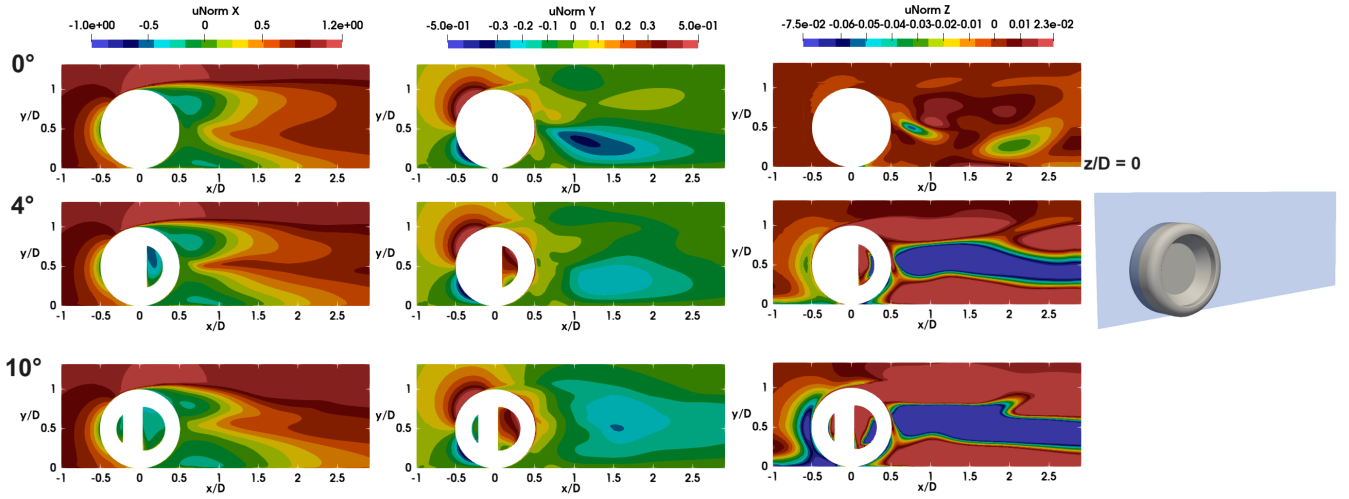


Figure 7.27: Normalised u_x , u_y and u_z by u_∞ for yaw angles of 0° , 4° and 10° at $z/D = 0$

Finally, the effect of yaw on the wake characteristics will be compared to the findings of Parfett et al. [9] to see which aspects can be captured by the RANS simulations. However, keep in mind that their results are for a different wheel geometry and they performed PIV measurements. So, an already notable difference is that they did not observe a vortex in the upper wake due to separation for the unyawed wheel.

Parfett et al. [9] found that yawing the wheel results in the stagnation point moving towards the windward side of the wheel shoulder. They found that this caused the vortex on the ground at the leeside to be strengthened while the windward ground vortex is weakened as mentioned in Section 3.2. This is the same phenomenon that can be seen in the results presented in this section. Furthermore, they also mentioned that less of the wake originated from ahead of the wheel on the windward side just as seen in Figure 7.12. Therefore, the results are in agreement with the literature and it is believed that RANS is able to capture the effects of yawing fairly well by comparing it to the experimental result of Parfett et al. [9].

7.2 Effect of the Reynolds Number

The results to investigate the effect of Re_D are presented in this section. The simulations were performed for $Re_D = 10\,000$, $Re_D = 25\,000$, $Re_D = 50\,000$, $Re_D = 100\,000$, $Re_D = 250\,000$, $Re_D = 500\,000$, $Re_D = 750\,000$ and $Re_D = 1\,000\,000$. For the flow visualisation plots, the results are visualised for $Re_D = 10\,000$, $Re_D = 100\,000$ and $Re_D = 1\,000\,000$ to clearly observe the changes in the wake. These values were chosen due to the fact that $Re_D = 10\,000$ corresponds to a speed of ≈ 1 km/h and $Re_D = 1\,000\,000$ corresponds to ≈ 126 km/h for this wheel, which is a typical operating range for cars on the road.

7.2.1 Force Coefficients

The plots containing C_D and C_L against the number of iterations are given in Figure 7.28a and Figure 7.28b respectively. From these plots, it appears that the simulations start to converge from approximately 2000 iterations after which C_D and C_L fluctuate minimally.

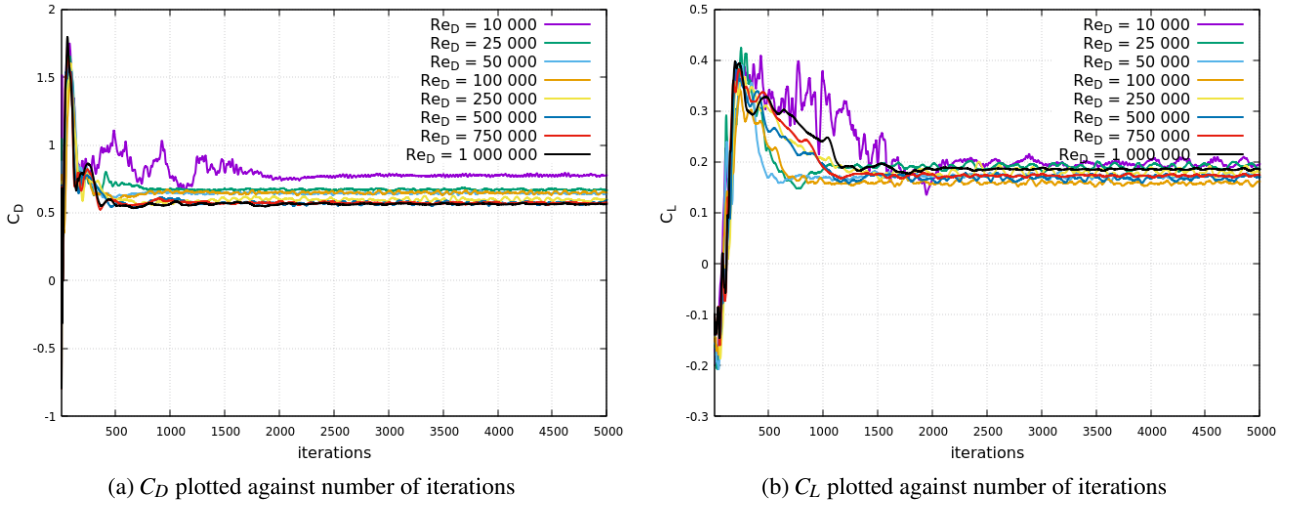


Figure 7.28: C_D and C_L convergence over 5000 iterations for different Re_D values

The results of C_D and C_L for varying Re_D values are given in Table 7.2. These results are plotted in Figure 7.29. It can be seen that the value of C_L stays approximately the same in this range with increasing Re_D . However, the value of C_D decreases with increasing Re_D . This is the most severe going from $Re_D = 10\,000$ to $Re_D = 25\,000$. Furthermore, in the regions of Re_D of 50 000 — 100 000 and 500 000 — 750 000 the C_D value seems to change minimally, indicating that in those regions the wake is most likely the same. Hence, the wake seems to experience the most changes in the following regions: 10 000 — 50 000 and 100 000 — 500 000.

Table 7.2: C_D and C_L values for different Re_D values

| Re_D [-] | C_D [-] | C_L [-] |
|------------|-----------|-----------|
| 10 000 | 0.7755 | 0.1967 |
| 25 000 | 0.6711 | 0.1911 |
| 50 000 | 0.6448 | 0.1721 |
| 100 000 | 0.6492 | 0.1586 |
| 250 000 | 0.5975 | 0.1799 |
| 500 000 | 0.572 | 0.1685 |
| 750 000 | 0.5725 | 0.1731 |
| 1 000 000 | 0.565 | 0.1855 |

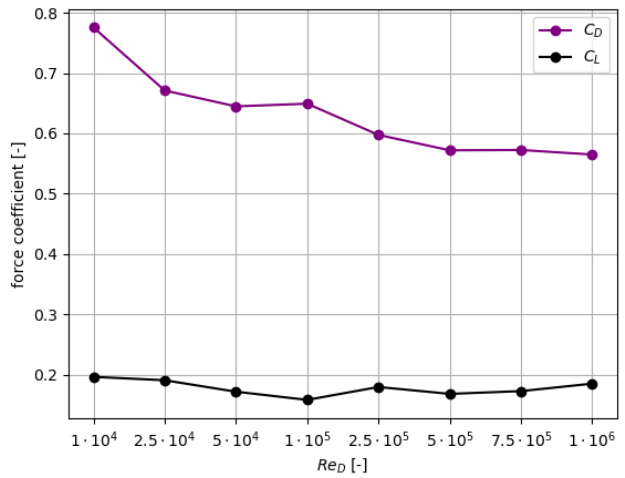


Figure 7.29: C_D and C_L plotted against different Re_D values

7.2.2 C_p Distribution

The C_p distribution along the centerline of the wheel is plotted against the angle θ as shown in Figure 7.30. Here the plots for different Re_D values are visualised. The C_p distribution does seem to slightly move upwards (more positive C_p) for a decreasing Re_D up to the contact patch region ($\theta \approx 90^\circ$). There, significant changes are observed regarding C_p values upstream and downstream of the contact patch. Upstream of the patch larger peaks are observed, whereas the value of C_p becomes more negative for lower values of Re_D downstream of the patch. The values of the positive and negative peaks are summarised in Table 7.3. Moving further along the centerline the curve seems to shift downwards (more negative C_p) for decreasing Re_D . Thus, for lower values of Re_D a lower value of base pressure is observed. Finally, moving up to the region of separation ($\approx > 260^\circ$) in Figure 7.30b it can be seen that for higher Re_D the values of C_p are more negative and the point of separation moves more downstream for a higher Re_D .

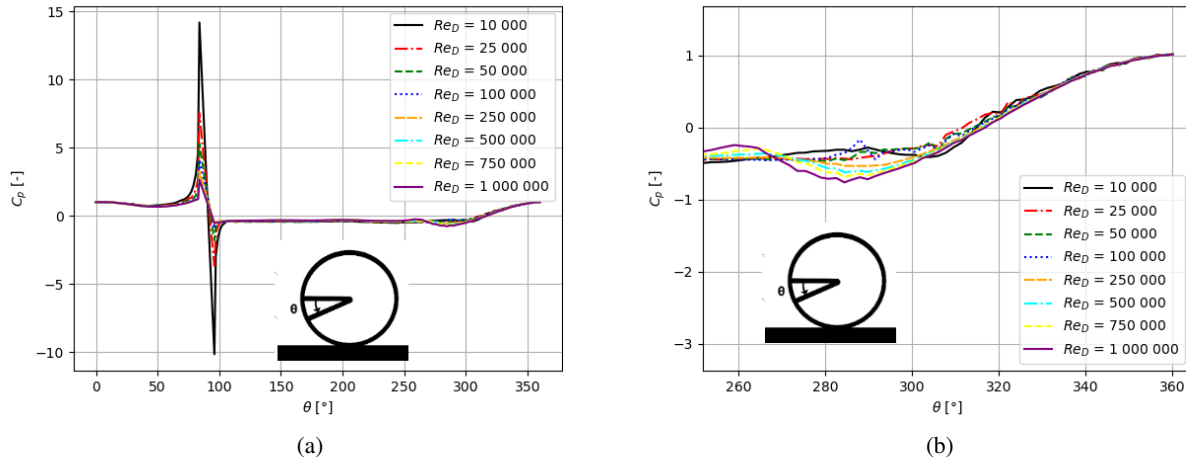


Figure 7.30: C_p distribution along the centerline for different Re_D values

Table 7.3: C_p values upstream and downstream of the contact patch area obtained for different Re_D values

| Re_D | C_p upstream | C_p downstream |
|-----------|----------------|------------------|
| 10 000 | 14.2 | -10.2 |
| 25 000 | 7.53 | -3.67 |
| 50 000 | 5.32 | -1.80 |
| 100 000 | 4.1 | -0.94 |
| 250 000 | 3.25 | -0.53 |
| 500 000 | 2.74 | -0.53 |
| 750 000 | 2.66 | -0.54 |
| 1 000 000 | 2.65 | -0.54 |

7.2.3 Streamlines

The 2D streamlines of $Re_D = 10\,000$, $Re_D = 100\,000$ and $Re_D = 1\,000\,000$ in the x/D , y/D , and z/D planes are given in [Figure 7.31](#), [Figure 7.32](#), and [Figure 7.33](#) respectively. Considering the x/D planes it becomes apparent that the streamlines behave similarly for $Re_D = 10\,000$ and $Re_D = 100\,000$. However, at $Re_D = 1\,000\,000$ the behaviour starts to become asymmetrical. This is also observed in the y/D planes. A reason could be that due to the fact that the wheel itself is asymmetric, the wake could become more sensitive to that aspect at a higher Re_D value. However, this aspect needs to be investigated further in future research. Another aspect that will be mentioned in further sections is that the wake is bigger for lower Re_D e.g. in $y/D = 0.25$ it is obvious that the vortices in the lower wake are bigger for $Re_D = 10\,000$ than $Re_D = 100\,000$.

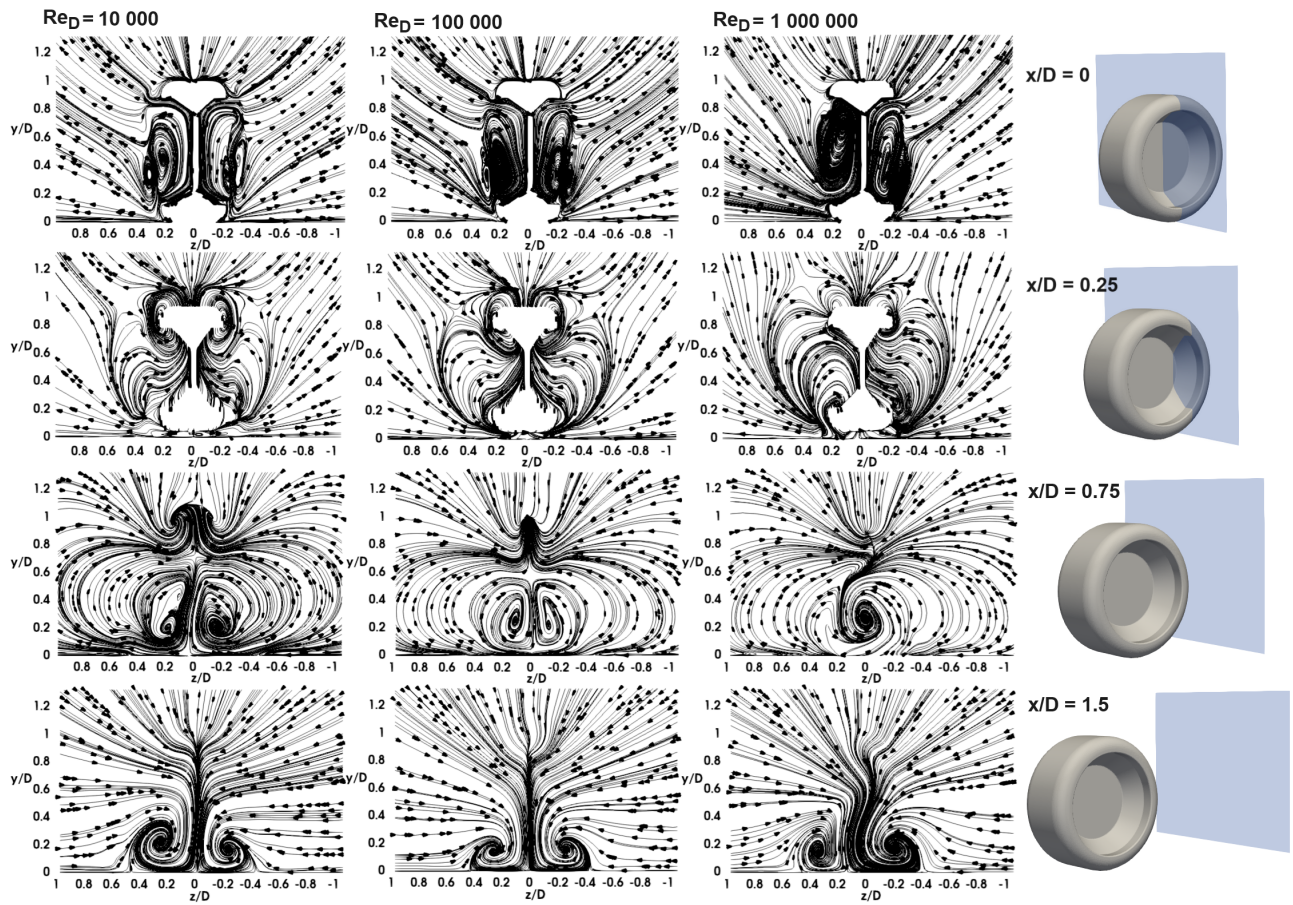


Figure 7.31: 2D streamlines for $Re_D = 10\,000$, $Re_D = 100\,000$ and $Re_D = 1\,000\,000$ at various x/D planes ($x/D = 0$, $x/D = 0.25$, $x/D = 0.75$ and $x/D = 1.5$)

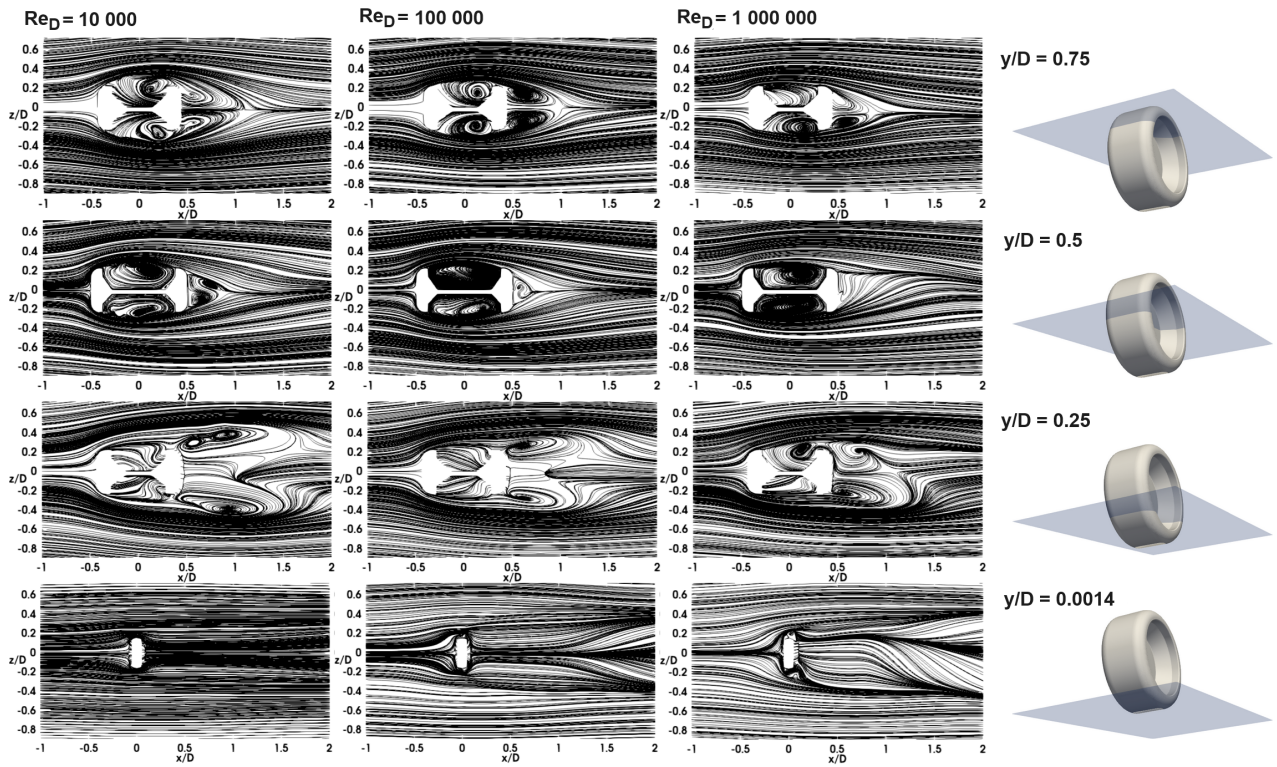


Figure 7.32: 2D streamlines for $Re_D = 10\,000$, $Re_D = 100\,000$ and $Re_D = 1\,000\,000$ at various y/D planes ($y/D = 0.0014$, $y/D = 0.25$, $y/D = 0.5$ and $y/D = 0.75$)

Figure 7.33 shows that by increasing the Re_D value, a vortex forms around the lower half of the wheel wake, which becomes more profound at higher values.

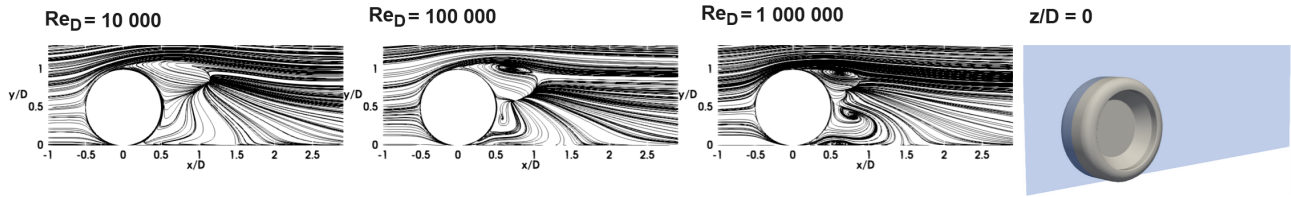


Figure 7.33: 2D streamlines for $Re_D = 10\,000$, $Re_D = 100\,000$ and $Re_D = 1\,000\,000$ at $z/D = 0$

The 3D streamlines for a front and rear view are visualised in Figure 7.34 and Figure 7.35, respectively. The 3D streamlines of the jetting vortices emerging from the contact patch are shown in Figure 7.36. These streamlines clearly show that the arch-shaped vortex and counter-rotating vortices in the lower wake are larger for smaller values of Re_D . Furthermore, the asymmetry of Re_D is clearly visible as well. Note, that in Figure 7.35 the streamlines are truncated to make the visualisation clearer.

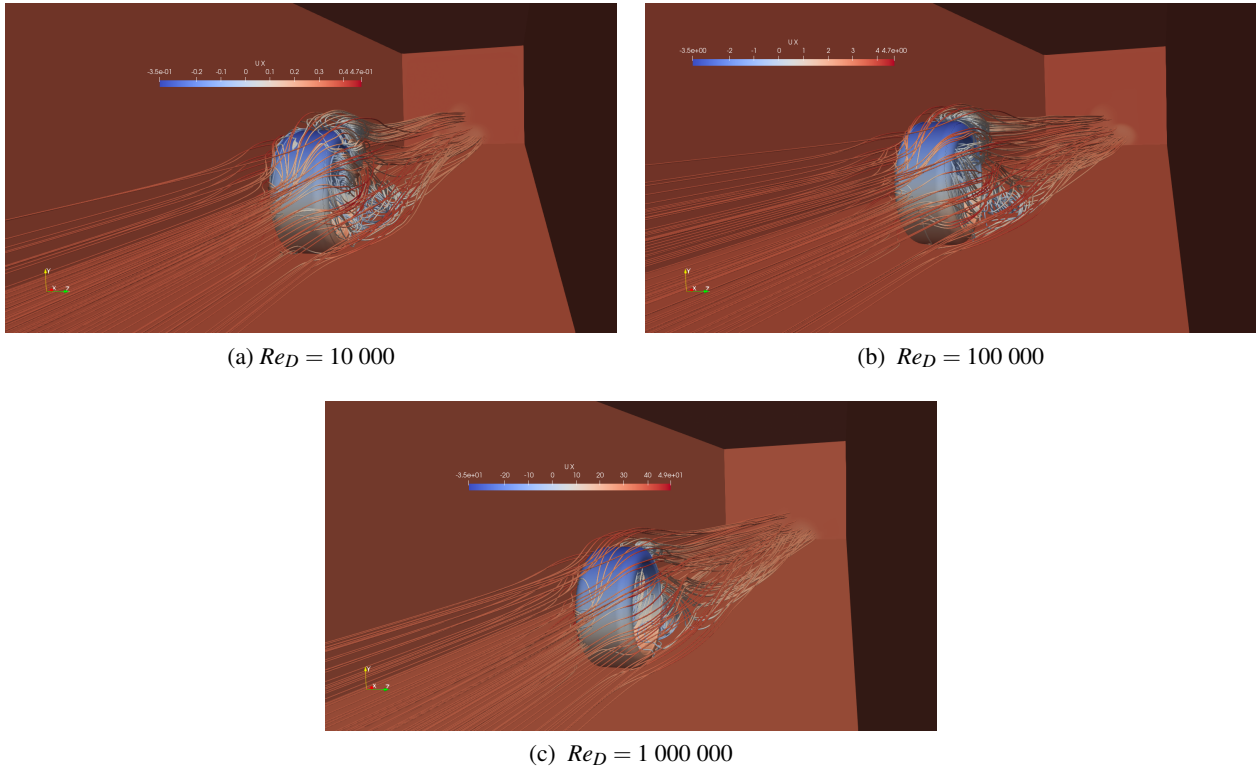
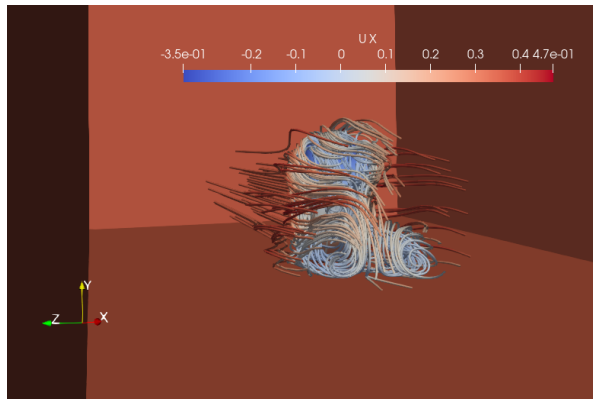
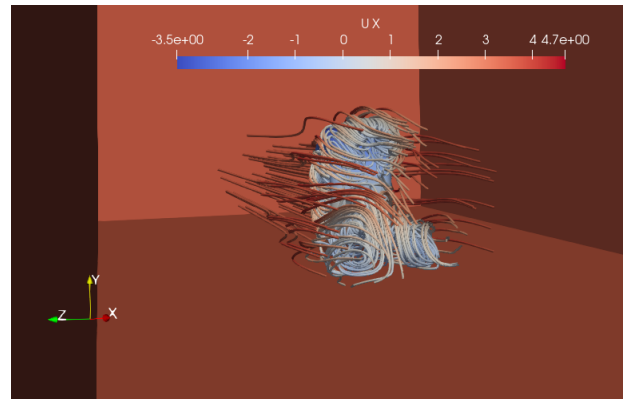


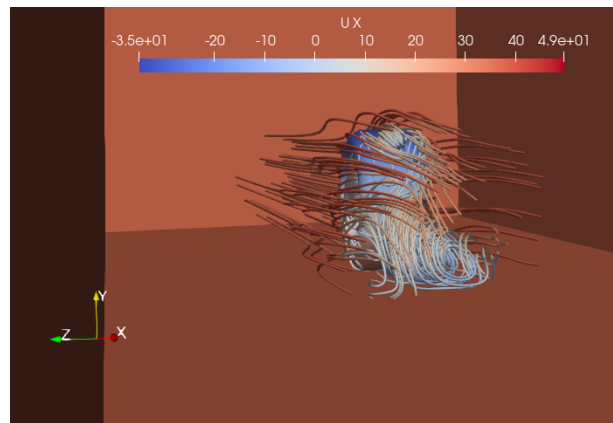
Figure 7.34: 3D streamlines front view for $Re_D = 10\,000$, $Re_D = 100\,000$ and $Re_D = 1\,000\,000$



(a) $Re_D = 10\,000$

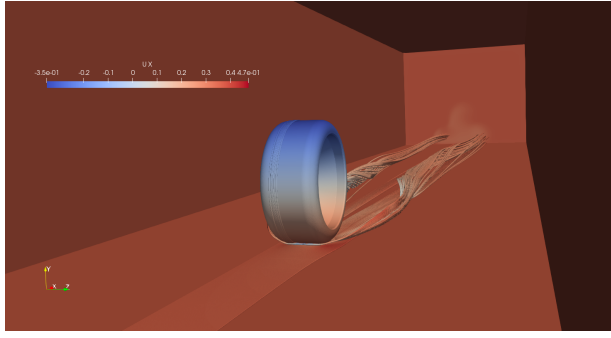


(b) $Re_D = 100\,000$

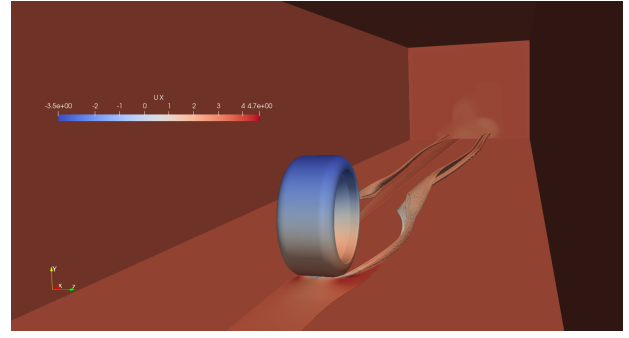


(c) $Re_D = 1\,000\,000$

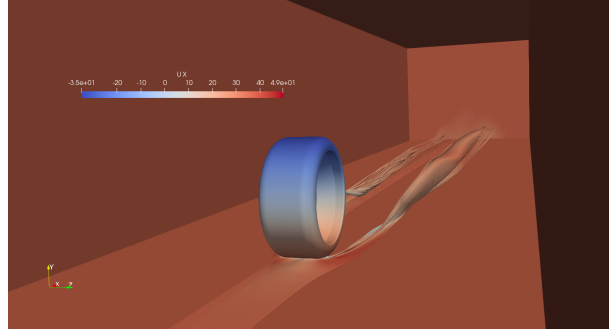
Figure 7.35: 3D streamlines rear view for $Re_D = 10\,000$, $Re_D = 100\,000$ and $Re_D = 1\,000\,000$



(a) $Re_D = 10\,000$



(b) $Re_D = 100\,000$



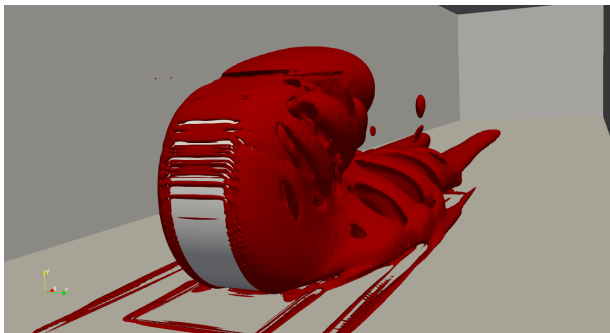
(c) $Re_D = 1\,000\,000$

Figure 7.36: 3D streamlines of the jetting vortices emerging from the contact patch for $Re_D = 10\,000$, $Re_D = 100\,000$ and $Re_D = 1\,000\,000$

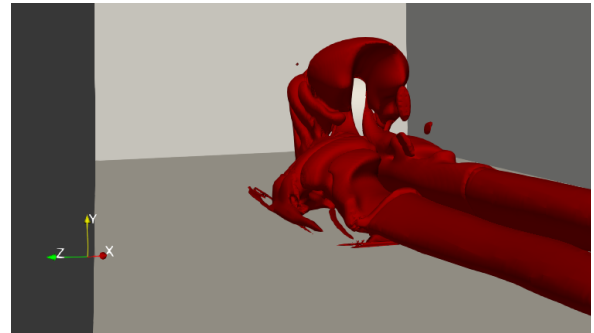
7.2.4 Q-criterion

The results of the isosurfaces of $Q = 0.1$, $Q = 50$, and $Q = 2500$ with varying Re_D values of $10\,000$, $100\,000$ and $1\,000\,000$, are given in [Figure 7.37](#), [Figure 7.38](#), and [Figure 7.39](#) respectively. Note, that different Q values are chosen due to the fact that Q is a dimensional parameter. So, for certain values, certain structures can be visualised for a particular Re_D value and not for another. This means that the structures that are moving way further downstream e.g. in [Figure 7.37](#) would also be visible for $Re_D = 100\,000$ if a smaller value for Q was chosen. However, the values were chosen in a way that the main structures are clearly visible.

Again the previously observed arc-shaped structure in the upper wake can be seen in [Figure 7.37](#), [Figure 7.38](#) and [Figure 7.39](#). It is clearly visible that for $Re_D = 1\,000\,000$ the structure is smaller than for $Re_D = 10\,000$. Furthermore, these structures clearly show that for $Re_D = 1\,000\,000$ the wake is asymmetrical, with the structure on the negative z -direction being more dominant.

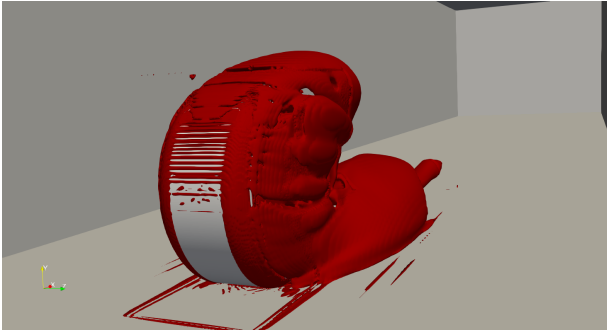


(a) front view

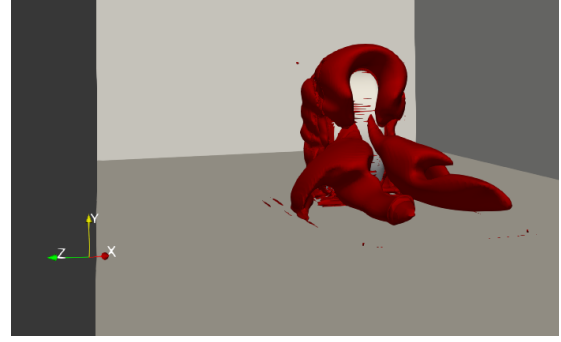


(b) rear view

Figure 7.37: Isosurface of $Q = 0.1$ contour level for $Re_D = 10\,000$

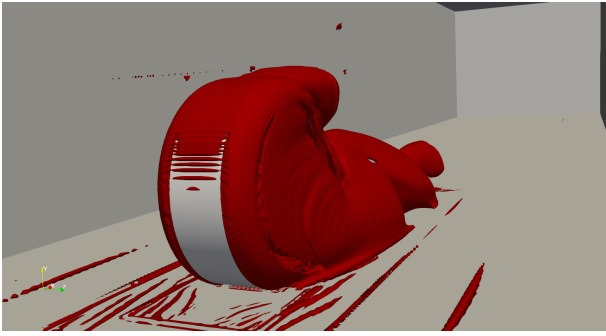


(a) front view

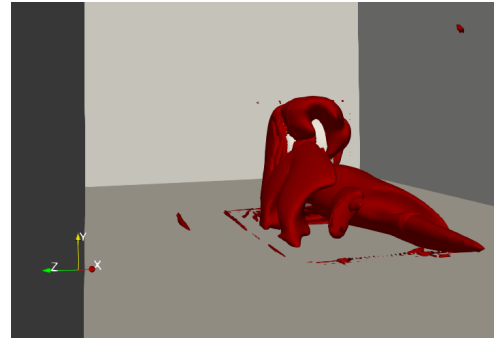


(b) rear view

Figure 7.38: Isosurface of $Q = 50$ contour level for $Re_D = 100\,000$



(a) front view



(b) rear view

Figure 7.39: Isosurface of $Q = 2500$ contour level for $Re_D = 1\,000\,000$

7.2.5 $C_{p_{total}}$ Fields

The results of the x/D planes can be found in [Figure 7.40](#). For the cases of the y/D planes and the $z/D = 0$ plane the results are presented in [Figure 7.41](#) and [Figure 7.42](#) respectively.

The results of the x/D planes show clearly that the wake is wider and taller for a lower Re_D . The wider aspect is also clearly visible in [Figure 7.41](#) and the taller in [Figure 7.42](#). In the $x/D = 0$ plane it can be seen that above the wheel for $Re_D = 10\,000$ and $Re_D = 100\,000$ there is a region with negative $C_{p_{total}}$, which indicates that the flow is already separated for these Re_D values at this plane. Moreover, the values of $C_{p_{total}}$ are more negative inside the wheel hub as well compared to $Re_D = 1\,000\,000$. The asymmetrical wake behaviour for $Re_D = 1\,000\,000$ already starts at $x/D = 0$. However, it becomes more pronounced moving downstream as can be seen for $x/D = 0.25$, $x/D = 0.75$ and $x/D = 1.5$. Also, looking at $x/D = 1.5$ it can be seen that the $C_{p_{total}}$ magnitudes in the upper half of the wake are larger for higher Re_D values.

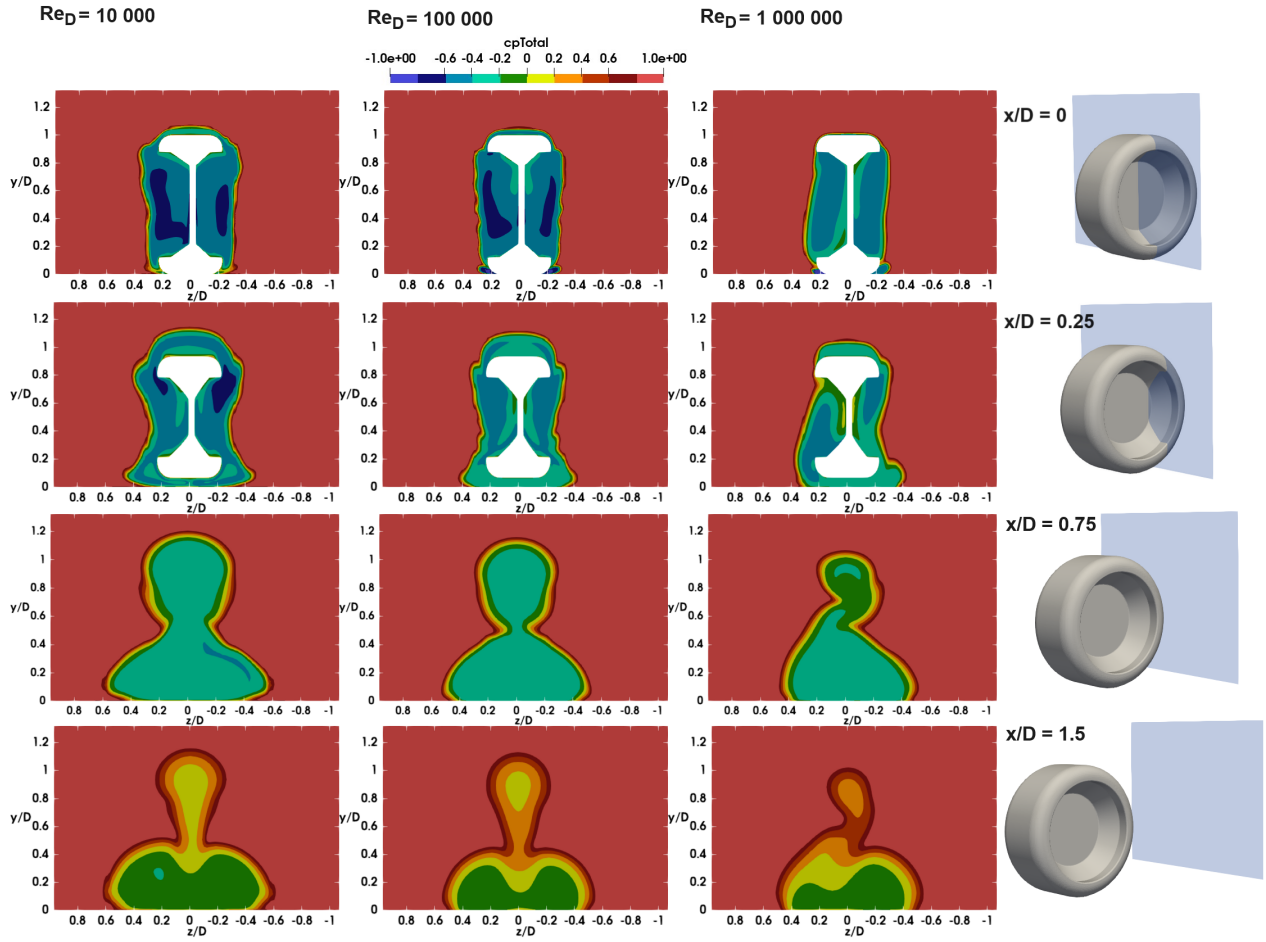


Figure 7.40: C_{pTotal} fields for $Re_D = 10\,000$, $Re_D = 100\,000$ and $Re_D = 1\,000\,000$ at various x/D planes ($x/D = 0$, $x/D = 0.25$, $x/D = 0.75$ and $x/D = 1.5$)

Apart from the wider and taller wake for lower Re_D values and the asymmetrical wake of $Re_D = 1\,000\,000$, another noticeable aspect that can be seen in Figure 7.41 is that in the plane of the contact patch $y/D = 0.0014$ the C_{pTotal} magnitudes are larger for a lower Re_D . Also, the asymmetry of the wake is the most visible in the lower part of the wake moving downstream ($y/D = 0.25$).

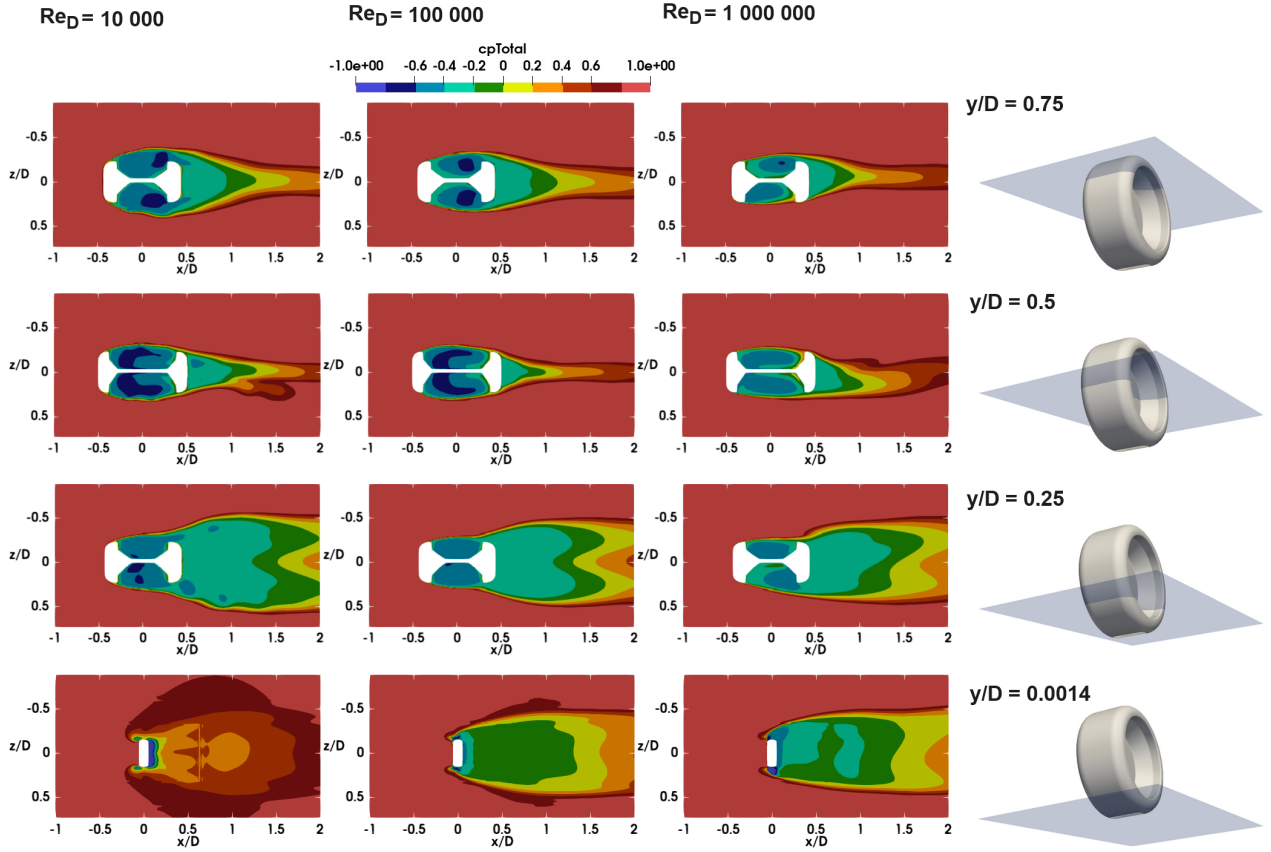


Figure 7.41: C_{pTotal} fields for $Re_D = 10\,000$, $Re_D = 100\,000$ and $Re_D = 1\,000\,000$ at various y/D planes ($y/D = 0.0014$, $y/D = 0.25$, $y/D = 0.5$ and $y/D = 0.75$)

Finally, as mentioned before [Figure 7.42](#) shows that for an increasing Re_D the wake becomes shorter. The wake becomes shorter and narrower for increasing Re_D , due to the separation point moving more downstream. Furthermore, the regions with the most negative C_{pTotal} become smaller.

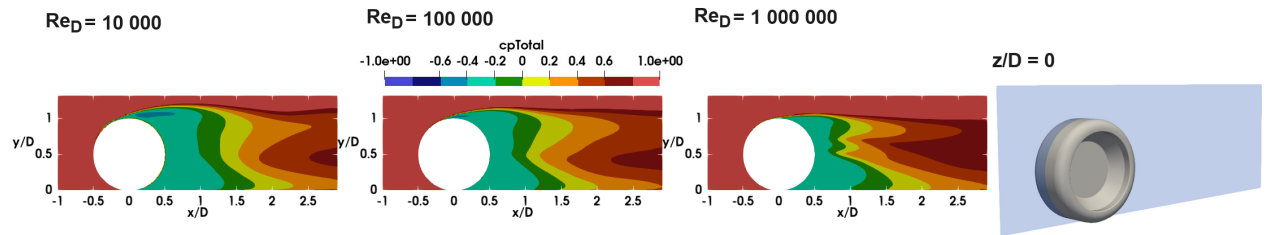


Figure 7.42: C_{pTotal} fields for $Re_D = 10\,000$, $Re_D = 100\,000$ and $Re_D = 1\,000\,000$ at $z/D = 0$

7.2.6 Velocity Fields

In this subsection, the velocity fields in the x -, y - and z -direction normalised by u_∞ for the different planes ([Figure 7.1](#)) are given. The results of the x/D planes are given in [Figure 7.43](#) - [Figure 7.46](#) and the results of the y/D planes are given in [Figure 7.47](#) - [Figure 7.50](#). Finally, the velocity fields of $z/D = 0$ are shown in [Figure 7.51](#).

From these Figures generally it can be concluded that the backward flow region in the wake becomes smaller for a bigger Re_D value. Furthermore, looking at u_y/u_∞ in [Figure 7.43](#) and [Figure 7.44](#) it is noticeable that for $Re_D = 1\,000\,000$ the dark blue area indicating (negative u_y/u_∞) flow moving downwards is inside the hub in the positive z/D region. This is contrary to what is observed for $Re_D = 10\,000$ and $Re_D = 100\,000$. Furthermore,

for $Re_D = 10\,000$ in the near-wake plane of $x/D = 0.75$ the area of reversed flow (dark green and below up to blue) is connected with the upper half of the wake and the lower part of the wake, contrary to $Re_D = 100\,000$ and $Re_D = 1\,000\,000$ where in the regions of $0.3 < \approx y/D < \approx 0.6$ and $0.4 < \approx y/D < \approx 0.6$ respectively u_x/u_∞ is positive. Additionally, the image of u_y/u_∞ of $Re_D = 1\,000\,000$ shows that at the arch-shaped vortex even though the size becomes smaller the magnitude becomes more negative. Also, the red region (positive u_y/u_∞) in the positive z/D direction becomes smaller in size while the blue region next to it moves to the direction of positive z/D for $x/D = 0.75$. The plane furthest downstream ($x/D = 1.5$) shows that there is no backwards flow in the wake anymore from that plane downstream.

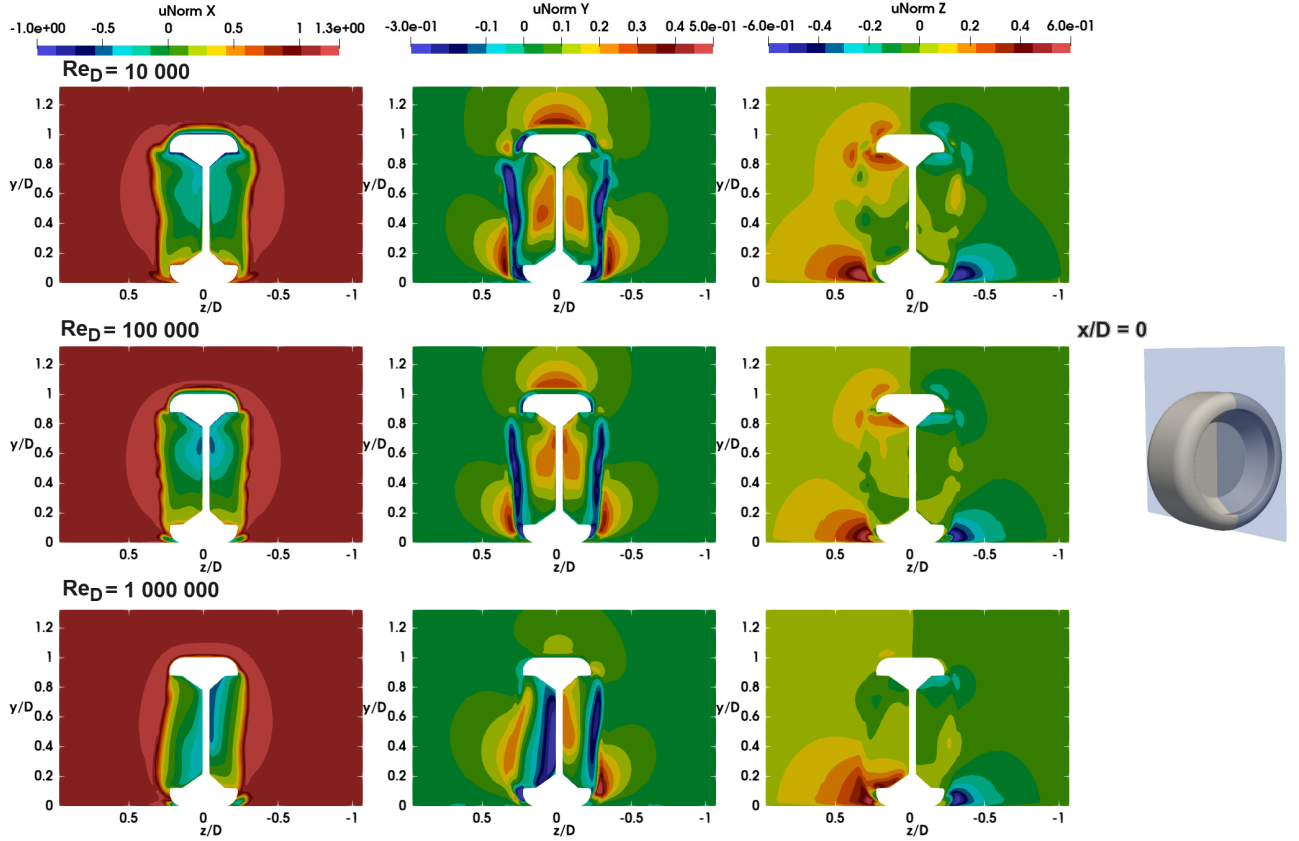


Figure 7.43: Normalised u_x , u_y and u_z by u_∞ for $Re_D = 10\,000$, $Re_D = 100\,000$ and $Re_D = 1\,000\,000$ at $x/D = 0$

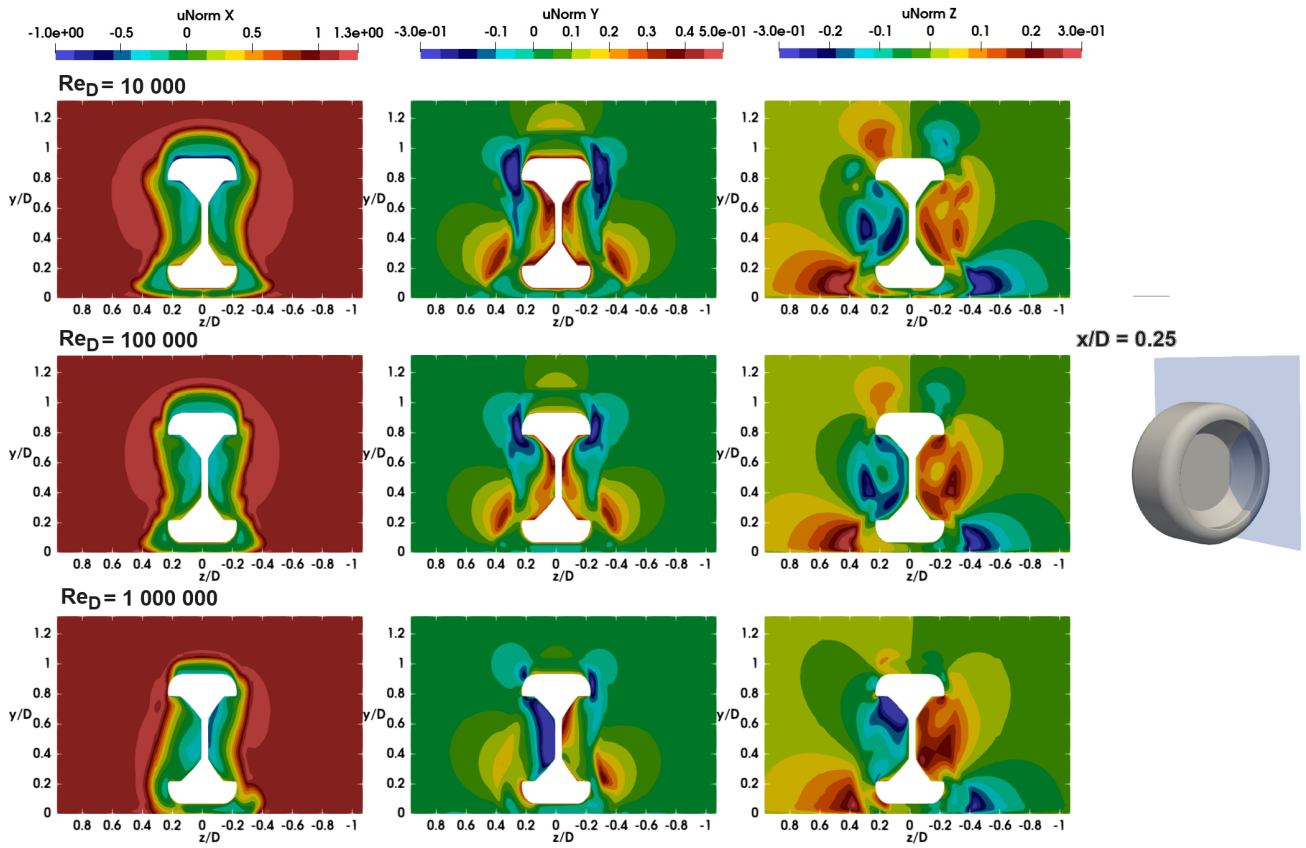


Figure 7.44: Normalised u_x , u_y and u_z by u_∞ for $Re_D = 10\,000$, $Re_D = 100\,000$ and $Re_D = 1\,000\,000$ at $x/D = 0.25$

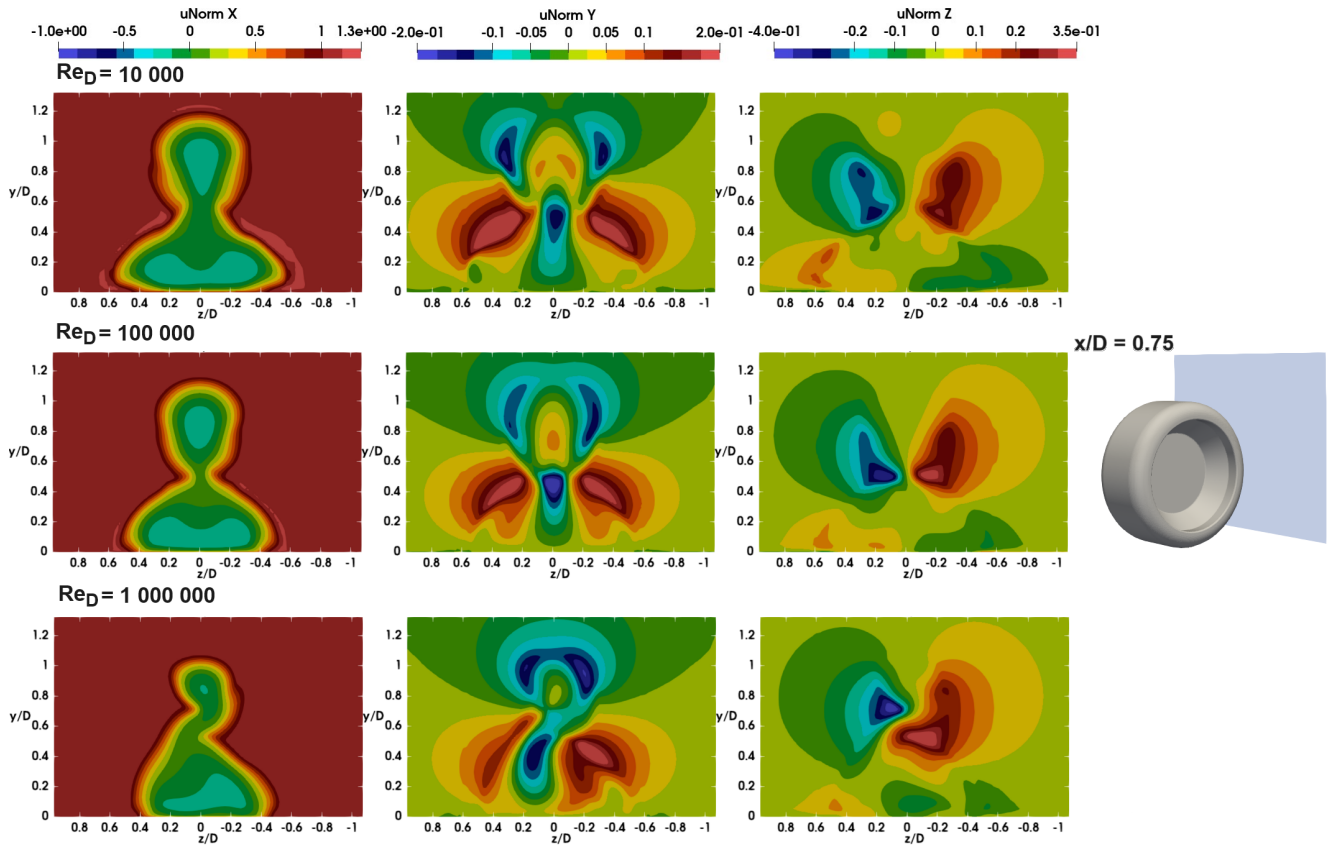


Figure 7.45: Normalised u_x , u_y and u_z by u_∞ for $Re_D = 10\,000$, $Re_D = 100\,000$ and $Re_D = 1\,000\,000$ at $x/D = 0.75$

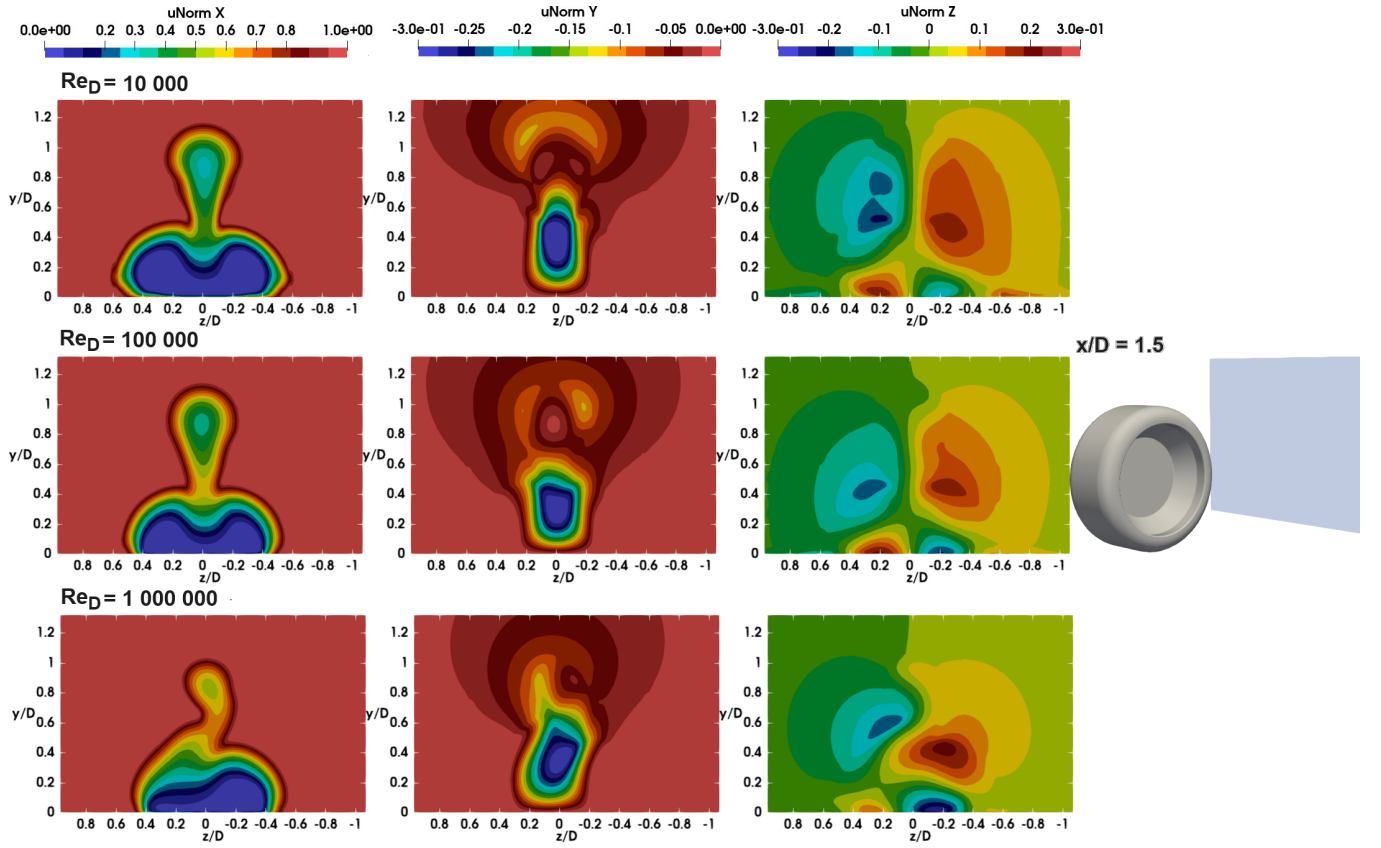


Figure 7.46: Normalised u_x , u_y and u_z by u_∞ for $Re_D = 10\,000$, $Re_D = 100\,000$ and $Re_D = 1\,000\,000$ at $x/D = 1.5$

The y/D planes show that the most backward flow is observed in the $y/D = 0.25$ plane. The backward flow is stronger in the lower part of the wake than in the upper part of the wake, due to the larger negative u_x/u_∞ observed. Furthermore, at the contact patch plane $y/D = 0.0014$ for lower Re_D the magnitude of u_x/u_∞ is bigger. This is clearly noticeable due to the red colour in the wake ($Re_D = 10\,000$), yellow colour in the wake ($Re_D = 100\,000$) and more green colour in the wake ($Re_D = 1\,000\,000$). Moreover, the plot of u_y/u_∞ shows that there is a slight increase in u_y/u_∞ upstream of the contact patch. Moreover, the regions of positive and negative u_z/u_∞ upstream of the contact patch become also bigger with increasing Re_D .

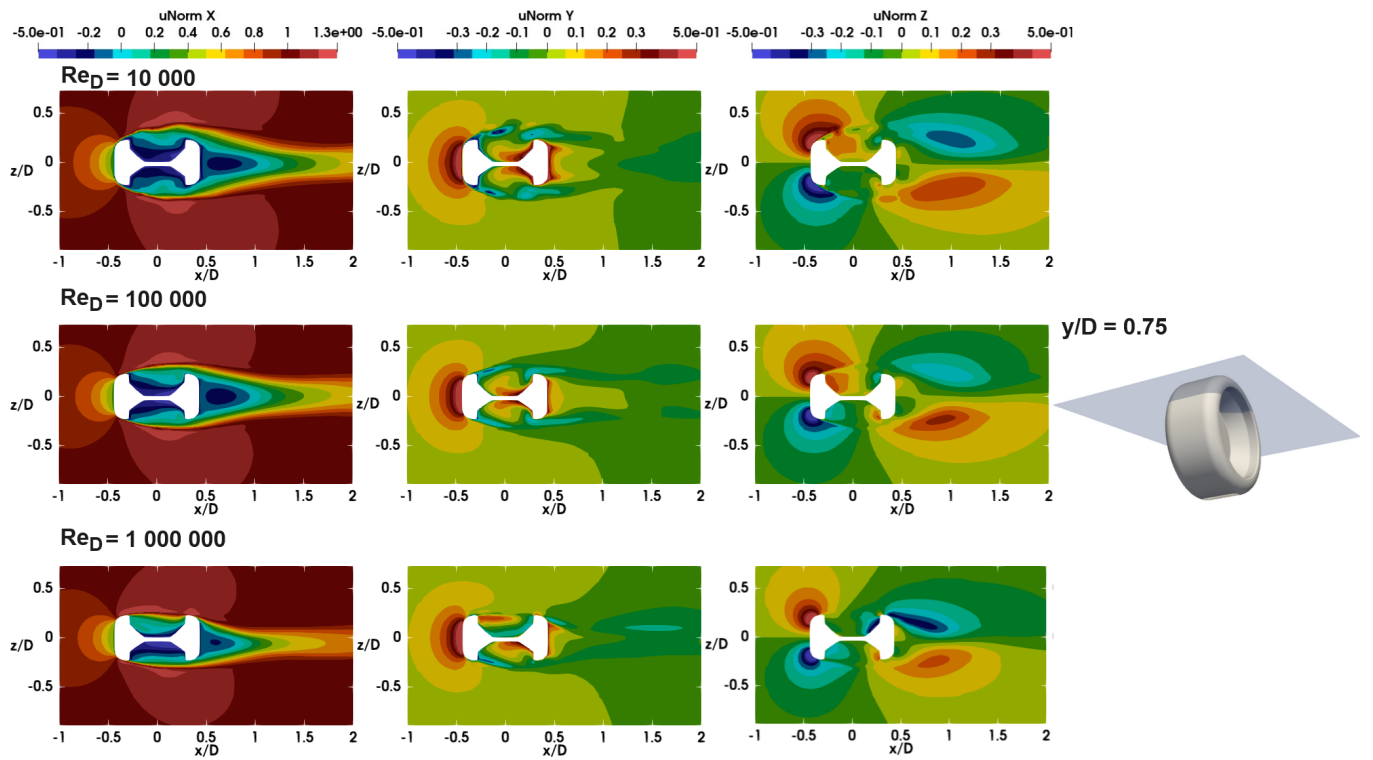


Figure 7.47: Normalised u_x , u_y and u_z by u_∞ for $Re_D = 10\,000$, $Re_D = 100\,000$ and $Re_D = 1\,000\,000$ at $y/D = 0.75$

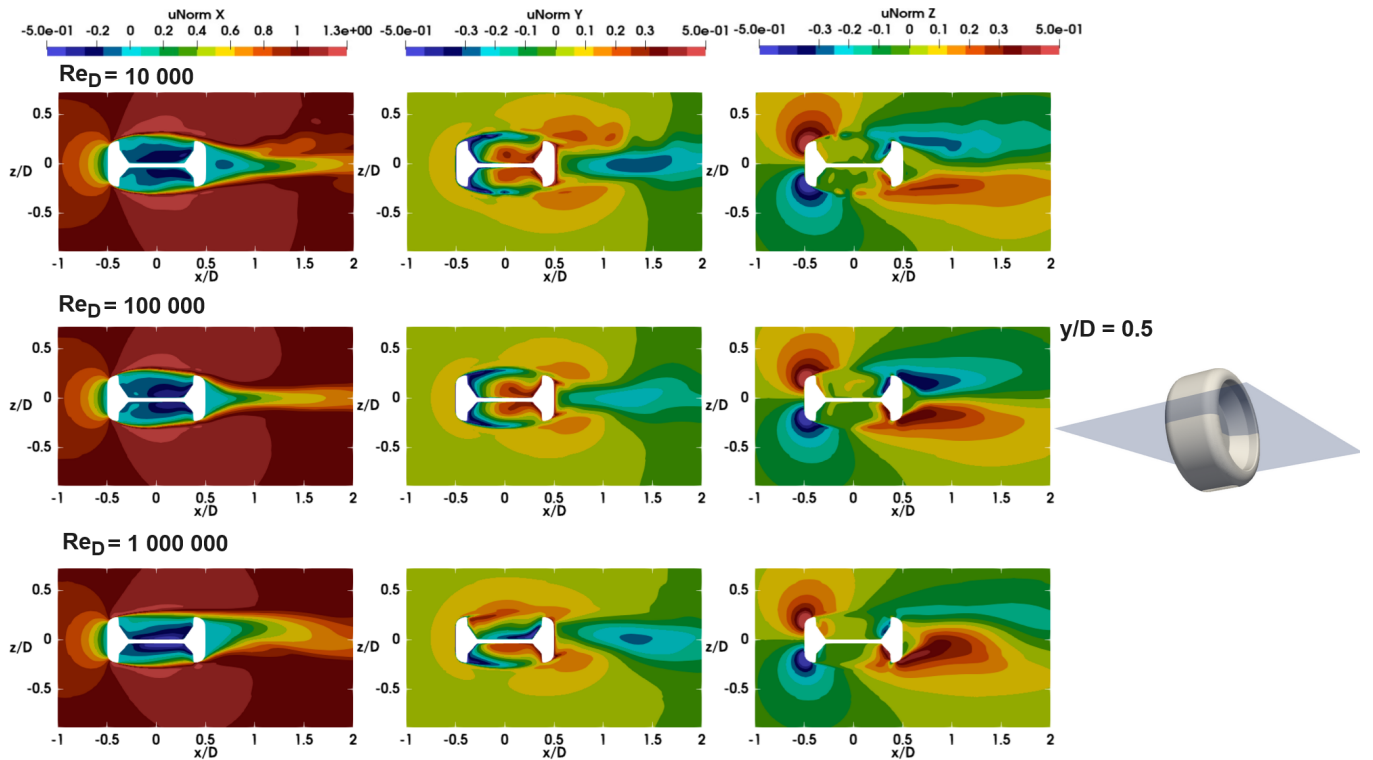


Figure 7.48: Normalised u_x , u_y and u_z by u_∞ for $Re_D = 10\,000$, $Re_D = 100\,000$ and $Re_D = 1\,000\,000$ at $y/D = 0.5$

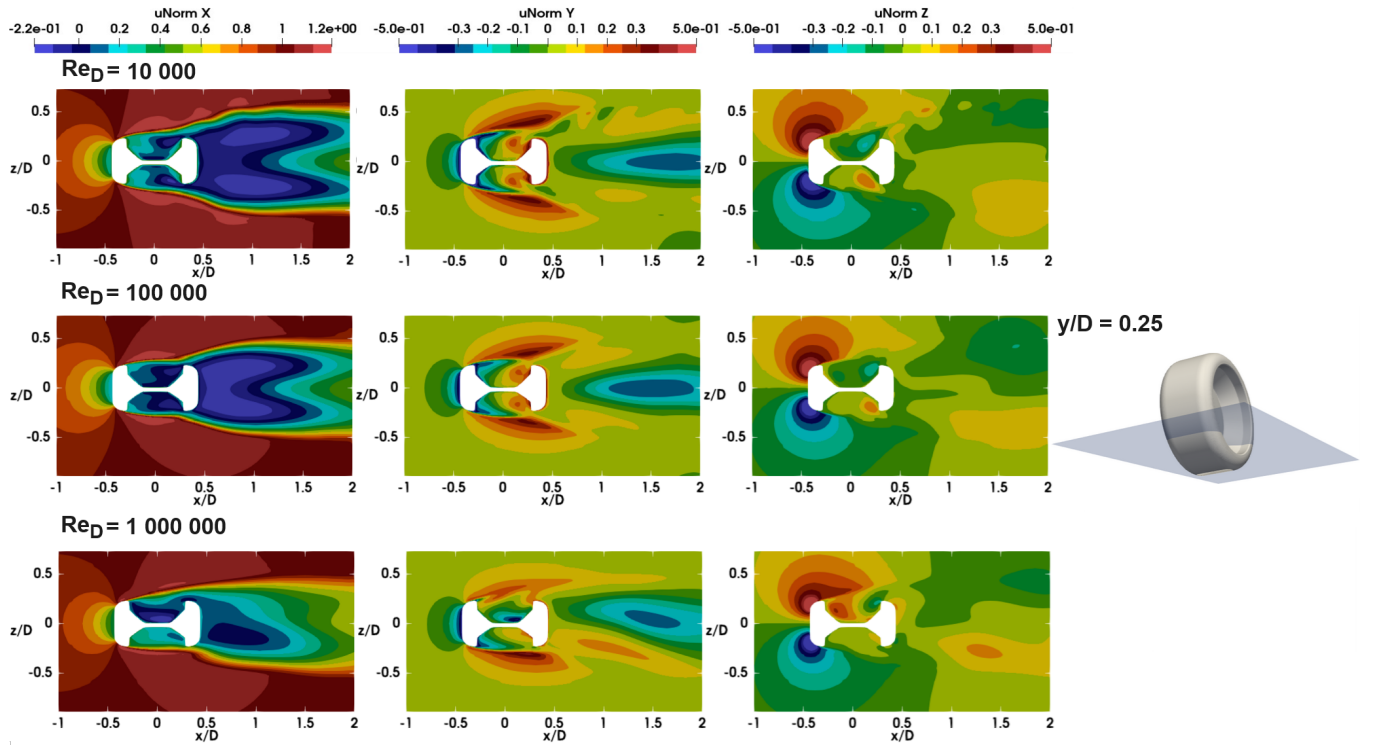


Figure 7.49: Normalised u_x , u_y and u_z by u_∞ for $Re_D = 10\,000$, $Re_D = 100\,000$ and $Re_D = 1\,000\,000$ at $y/D = 0.25$

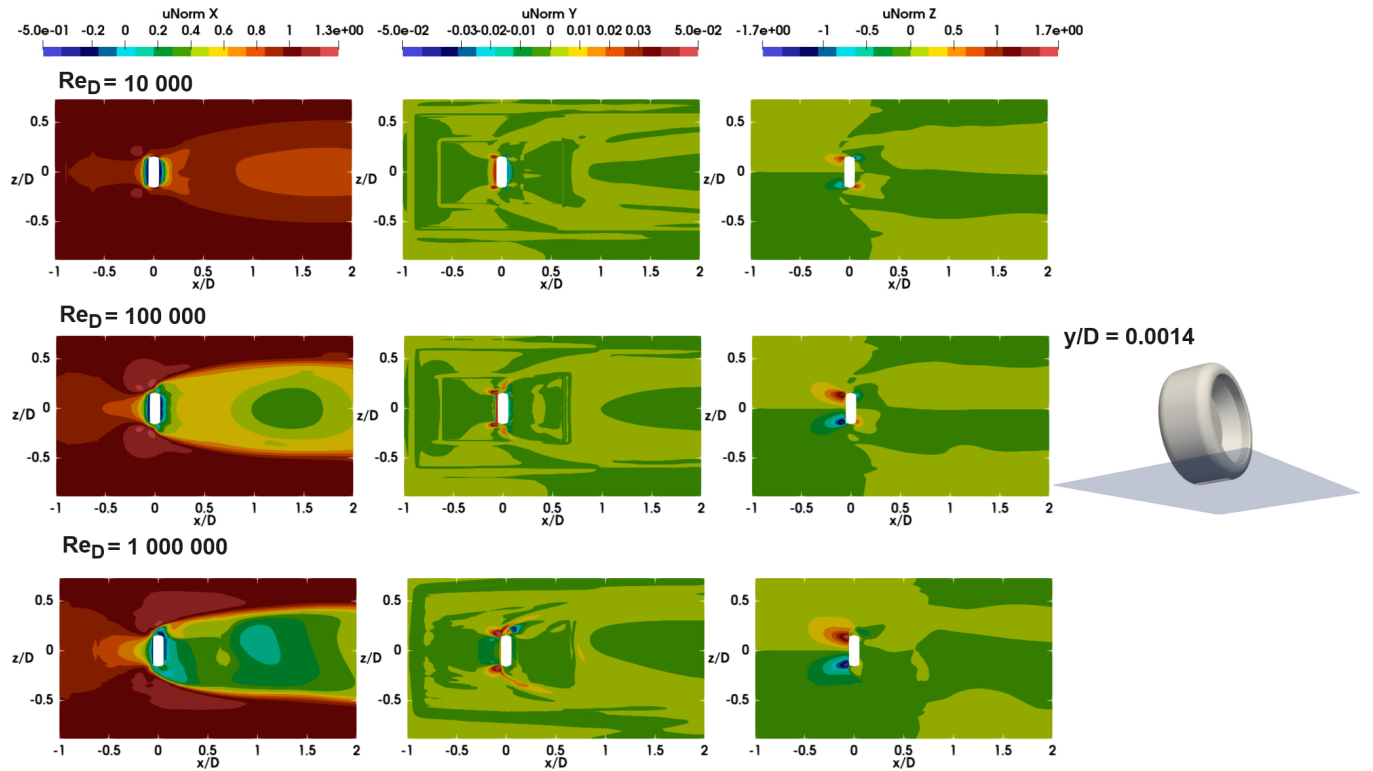


Figure 7.50: Normalised u_x , u_y and u_z by u_∞ for $Re_D = 10\,000$, $Re_D = 100\,000$ and $Re_D = 1\,000\,000$ at $y/D = 0.0014$

Finally, [Figure 7.51](#) shows that the magnitude of u_x/u_∞ becomes less negative in the upper half of the wake. Furthermore, in this plane the variation in magnitudes of u_z/u_∞ is very small.

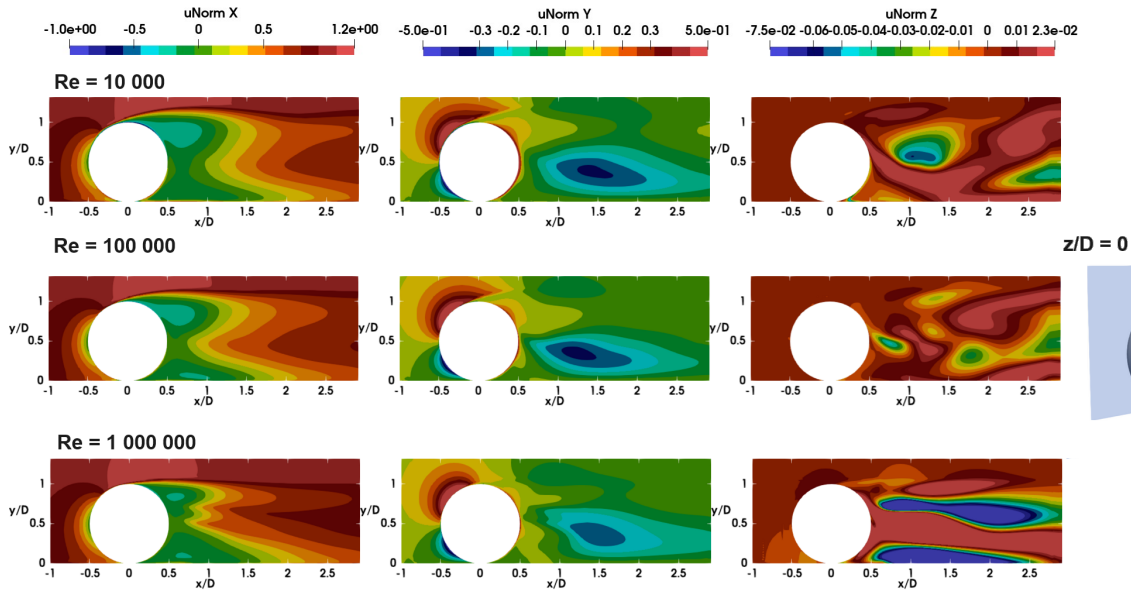


Figure 7.51: Normalised u_x , u_y and u_z by u_∞ for $Re_D = 10\,000$, $Re_D = 100\,000$ and $Re_D = 1\,000\,000$ at $z/D = 0$

8. Conclusion and Recommendations

In this chapter, a conclusion for the thesis is drawn in [Section 8.1](#). Furthermore, recommendations for future work are given in [Section 8.2](#), which will present the next steps that can be taken from this research.

8.1 Conclusion

In this thesis the effect of yawing the wheel and different Re_D values was investigated by means of RANS simulations. The results have shown that simulating a rotating wheel in contact with the ground using open-source software like cfMesh and OpenFOAM fairly good results can be attained. The obtained force coefficients, C_p distribution along the centerline and flowfield agreed with the experimental results of Fackrell [6] and the URANS simulation results of McManus and Zhang [53] and RANS simulation results of Diasinos et al. [72]. From the obtained results the following can be concluded:

- The values of the force coefficients are sensitive to the schemes chosen as was seen with the results of the RKE turbulence model with two different sets of divergence schemes chosen. Therefore, when one performs RANS simulations like performed in this research the results must always be compared to experimental results.
- The value of the C_p peaks is sensitive to the first cell height. So, this is one of the reasons that the values of the C_p peaks near the contact region differ in the literature compared to each other.
- The results obtained from the $k - \omega$ SST and RKE turbulence model are in better agreement with the experimental results than the results obtained with the S-A model.
- The size of the contact patch region seems to not affect the results when going smaller than the smallest step size that Diasinos et al. [72] could achieve of $0.0028D$. The results even showed that a step size of $0.005D$ was sufficient.

Effect of yawing the wheel

The conclusions drawn from yawing the wheel in increments of 2° up to 10° :

- Yawing the wheel results in a fairly linear increased value of C_D and C_S . A yaw angle of 10° had an increase of approximately 16.4% in C_D . At $\theta \approx 9^\circ$, the C_S became larger than C_L with a value of $C_S \approx 0.23$. Regarding the C_L only a significant increase of approximately 35.8% was observed from $\theta = 4^\circ$ to $\theta = 6^\circ$.
- Yawing the wheel results in the wake becoming asymmetric. The vortex at the leeside on the ground becomes bigger and stronger while the vortex at the windward side becomes smaller and weaker. This is also the case for the jetting vortices. This shows that RANS is able to capture the main effects of yawing since these findings agree with the experimental results of Parfett et al. [9].

Effect of the Reynolds number

The conclusion drawn from looking at the general operational range of a vehicle with the respective Re_D values of 10 000 — 1 000 000 is summarised as follows:

- For an increasing Re_D value C_D decreases and C_L stays approximately the same. The difference in C_D between $Re_D = 10\,000$ and $Re_D = 1\,000\,000$ is a decrease of approximately 27.1%. Also, in the regions of Re_D of 50 000 — 100 000 and 500 000 — 750 000 the C_D value seems to change minimally, indicating that in those regions the wake is most likely the same.
- The value of the C_p upstream and downstream of the contact patch region are bigger in magnitude for lower values of Re_D . This ranges from $C_p = 14.2$ and $C_p = -10.2$ for $Re_D = 10\,000$ to $C_p = 2.65$ and $C_p = -0.54$ for $Re_D = 1\,000\,000$. Note, that from $Re_D = 250\,000$ the values of the negative pressure downstream of the contact patch equal approximately $C_p = -0.54$. Furthermore, the results showed that the values of C_p are more negative in the separation region for an increasing Re_D .
- In the investigated range the structures in the wake are the same. However, for a smaller Re_D value the wake is larger and for $Re_D = 1\,000\,000$ an asymmetry in the wake is observed, which is probably caused

by the asymmetry of the wheel. The wake is larger for a smaller Re_D , due to the fact that the separation point moves more downstream for a higher Re_D .

8.2 Recommendations

The RANS simulations provide fairly good results for wheel simulations in contact with the ground. Therefore, for future research, one can build upon this research in the following way:

- In follow-up research, the yaw can be simulated using higher fidelity unsteady simulation methods such as DES and LES. This allows for investigation of the temporal behaviour of the structures and the RANS results can be compared to the results of the unsteady simulations.
- Another aspect that can be researched is performing the exact same simulations with a more complex detailed wheel. This will require approaches like MRF, MRFg and SM. However, automotive wheels are more detailed. So investigating the effects of yaw and Re_D with more complex wheels and methods will give a better idea of the effects in reality.
- The results of the effect of yaw or Re_D could not be compared to experiments of the same wheel. So for the future yaw and Re_D could also be investigated using experiments and simulations. This will show the shortcomings of the simulations or it will show that the results are overall well simulated. This will also confirm if the asymmetry of the wake at higher $Re_D = 1\,000\,000$ is caused by the asymmetry of the wheel or modelling errors. Note, that for future work if the capacity is there, a scanned deformed 3D CAD model of the wheel geometry during the experiment should be used for the simulations for more accurate results.

Bibliography

- [1] S. Gurunathan, P. K M, and S. Gunasekar, "Reduction of Aerodynamic Drag Force for Reducing Fuel Consumption in Road Vehicle using Basebleed," *Journal of Applied Fluid Mechanics*, vol. 11, pp. 1489–1495, 11 2018.
- [2] A. Vdovin, "Numerical and experimental investigations on aerodynamic and thermal aspects of rotating wheels," 2015.
- [3] J. Katz, "Aerodynamics of race cars," *Annu. Rev. Fluid Mech*, vol. 38, pp. 27–63, 01 2006.
- [4] G. Wickern, K. Zwicker, and M. Pfadenhauer, "Rotating Wheels - Their Impact on Wind Tunnel Test Techniques and on Vehicle Drag Results," *SAE Transactions*, vol. 106, pp. 254–270, 1997.
- [5] R. Dominy, "Aerodynamics of Grand Prix Cars," *Proceedings of The Institution of Mechanical Engineers Part D-journal of Automobile Engineering - PROC INST MECH ENG D-J AUTO*, vol. 206, pp. 267–274, 06 1992.
- [6] J. E. Fackrell, *The Aerodynamics of an Isolated Wheel Rotating in Contact with the Ground*. PhD thesis, 1974.
- [7] R. Jakhar, "Aerodynamics of trailer wheels in tandem: Experimental investigation into the effects of wheel rotation, trailer side-skirts, and wheel cavity covers," Master's thesis, Delft University of Technology, 2021.
- [8] S. Ghosh, "Experimental investigation of the effects of mudflaps on wheel aerodynamics by means of a simulated moving ground," Master's thesis, Delft University of Technology, 2022.
- [9] A. Parfett, H. Babinsky, and J. K. Harvey, "A study of the time-resolved structure of the vortices shed into the wake of an isolated F1 car wheel," *Experiments in Fluids*, vol. 63, p. 116, jul 2022.
- [10] A. Brandt, H. Berg, M. Bolzon, and L. Josefsson, "The Effects of Wheel Design on the Aerodynamic Drag of Passenger Vehicles," *SAE International Journal of Advances and Current Practices in Mobility*, vol. 1, pp. 1279–1299, apr 2019.
- [11] T. Hobeika and S. Sebben, "Tyre Pattern Features and Their Effects on Passenger Vehicle Drag," *SAE International Journal of Passenger Cars - Mechanical Systems*, vol. 11, pp. 401–413, apr 2018.
- [12] T. Hobeika and S. Sebben, "CFD investigation on wheel rotation modelling," *Journal of Wind Engineering and Industrial Aerodynamics*, vol. 174, pp. 241–251, 2018.
- [13] M. M. Zdravkovich, "Flow around circular cylinders," *Fundamentals*, vol. 1, pp. 566–571, 1997.
- [14] K. Raghavan and M. Bernitsas, "Experimental investigation of Reynolds number effect on vortex induced vibration of rigid circular cylinder on elastic supports," *Ocean Engineering*, vol. 38, no. 5-6, pp. 719–731, 2011.
- [15] S. Singh and S. Mittal, "Flow past a cylinder: shear layer instability and drag crisis," *International journal for numerical methods in fluids*, vol. 47, no. 1, pp. 75–98, 2005.
- [16] M. Van Dyke and M. Van Dyke, *An album of fluid motion*, vol. 176. Parabolic Press Stanford, 1982.
- [17] J. Fredsoe and B. M. Sumer, *Hydrodynamics around cylindrical structures (revised edition)*, vol. 26. World Scientific, 2006.
- [18] A. Roshko, "Experiments on the flow past a circular cylinder at very high Reynolds number," *Journal of fluid mechanics*, vol. 10, no. 3, pp. 345–356, 1961.
- [19] A. Porteous, "Unsteady Simulations of Flow Around a Smooth Circular Cylinder at Very High Reynolds Numbers Using OpenFOAM," 2015.

- [20] L. V. Schmidt, "Fluctuating force measurements upon a circular cylinder at Reynolds numbers up to 5×10^6 ," pp. 19–1, 1966.
- [21] E. Achenbach, "Distribution of local pressure and skin friction around a circular cylinder in cross-flow up to $Re = 5 \times 10^6$," *Journal of Fluid Mechanics*, vol. 34, no. 4, pp. 625–639, 1968.
- [22] G. W. Jones, *Aerodynamic forces on a stationary and oscillating circular cylinder at high Reynolds numbers*, vol. 300. National Aeronautics and Space Administration, 1969.
- [23] G. Schewe, "On the force fluctuations acting on a circular cylinder in crossflow from subcritical up to transcritical Reynolds numbers," *Journal of fluid mechanics*, vol. 133, pp. 265–285, 1983.
- [24] W. Shih, C. Wang, D. Coles, and A. Roshko, "Experiments on flow past rough circular cylinders at large Reynolds numbers," *Journal of Wind Engineering and Industrial Aerodynamics*, vol. 49, no. 1-3, pp. 351–368, 1993.
- [25] L. Prandtl, "Magnuseffekt und Windkraftschiff," *The science of nature*, vol. 13, no. 6, pp. 93–108, 1925.
- [26] W. Swanson, "The Magnus effect: A summary of investigations to date," 1961.
- [27] P. Tokumaru and P. Dimotakis, "The lift of a cylinder executing rotary motions in a uniform flow," *Journal of fluid mechanics*, vol. 255, pp. 1–10, 1993.
- [28] T. D. Kothalawala, *Computational investigation into the influence of yaw & rotation on the bluff-body aerodynamics of an isolated wheel*. PhD thesis, Brunel University, 2014.
- [29] M. M. Zdravkovich, *Flow around circular cylinders: Volume 2: Applications*, vol. 2. Oxford university press, 1997.
- [30] S. Mittal and B. Kumar, "Flow past a rotating cylinder," *Journal of Fluid Mechanics*, vol. 476, pp. 303–334, 2 2003.
- [31] D. Stojković, M. Breuer, and F. Durst, "Effect of high rotation rates on the laminar flow around a circular cylinder," *Physics of fluids*, vol. 14, no. 9, pp. 3160–3178, 2002.
- [32] W. Chen and C.-K. Rheem, "Experimental investigation of rotating cylinders in flow," *Journal of marine science and technology*, vol. 24, no. 1, pp. 111–122, 2019.
- [33] F. Diaz, J. Gavalda, J. Kawall, J. Keffer, and F. Giralt, "Vortex shedding from a spinning cylinder," *The Physics of fluids*, vol. 26, no. 12, pp. 3454–3460, 1983.
- [34] Y. Chew, M. Cheng, and S. Luo, "A numerical study of flow past a rotating circular cylinder using a hybrid vortex scheme," *Journal of fluid mechanics*, vol. 299, pp. 35–71, 1995.
- [35] S. Kumar, C. Cantu, and B. Gonzalez, "Flow past a rotating cylinder at low and high rotation rates," *Journal of Fluids Engineering*, vol. 133, no. 4, p. 041201, 2011.
- [36] S. Kang, H. Choi, and S. Lee, "Laminar flow past a rotating circular cylinder," *Physics of Fluids*, vol. 11, no. 11, pp. 3312–3321, 1999.
- [37] S. Karabelas, B. Koumroglou, C. Argyropoulos, and N. Markatos, "High Reynolds number turbulent flow past a rotating cylinder," *Applied Mathematical Modelling*, vol. 36, no. 1, pp. 379–398, 2012.
- [38] Q. Yao, C. Zhou, and C. Wang, "Numerical Study of the Flow past a Rotating Cylinder at Supercritical Reynolds Number," pp. 667–670, 2016.
- [39] S. Taneda, "Experimental investigation of vortex streets," *Journal of the Physical Society of Japan*, vol. 20, no. 9, pp. 1714–1721, 1965.
- [40] P. Bearman and M. Zdravkovich, "Flow around a circular cylinder near a plane boundary," *Journal of Fluid Mechanics*, vol. 89, no. 1, pp. 33–47, 1978.

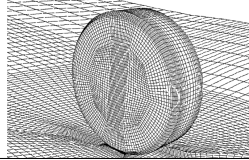
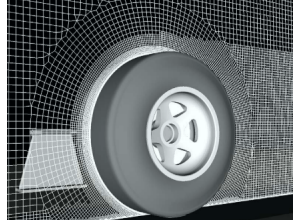
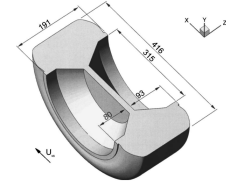
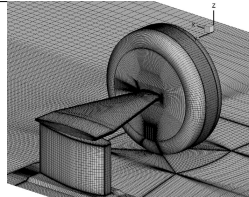
- [41] T. Nishino, *Dynamics and stability of flow past a circular cylinder in ground effect*. PhD thesis, University of Southampton, 2007.
- [42] T. Nishino, G. T. Roberts, and X. Zhang, “Unsteady RANS and detached-eddy simulations of flow around a circular cylinder in ground effect,” *Journal of Fluids and Structures*, vol. 24, pp. 18–33, 1 2008.
- [43] B. E. Stewart, *The dynamics and stability of flows around rolling bluff bodies*. PhD thesis, Université de Provence-Aix-Marseille I, 2008.
- [44] F. Houdroge, T. Leweke, K. Hourigan, and M. C. Thompson, “Two-and three-dimensional wake transitions of an impulsively started uniformly rolling circular cylinder,” *Journal of Fluid Mechanics*, vol. 826, pp. 32–59, 2017.
- [45] S. Pirozzoli, P. Orlandi, and M. Bernardini, “The fluid dynamics of rolling wheels at low Reynolds number,” *Journal of Fluid Mechanics*, vol. 706, p. 496533, 2012.
- [46] A. Morelli, “Aerodynamic Effects on an Automobile Wheel,” 1969.
- [47] W. Stapleford and G. Carr, “Aerodynamic Characteristics of Exposed Rotating Wheels,” 1970.
- [48] J. E. Fackrell and J. Harvey, “The Flow Field and Pressure Distribution of an Isolated Road Wheel,” *Advances on Road Vehicle Aerodynamics*, p. 155165, 1973.
- [49] J. E. Fackrell and J. Harvey, “The Aerodynamics of an Isolated Road Wheel,” *Proceedings of the Second AIAA Symposium of Aerodynamics of Sports and Competition Automobiles*, 1975.
- [50] A. P. Mears, R. G. Dominy, and D. B. Sims-Williams, “The Air Flow About an Exposed Racing Wheel,” *Motorsports Engineering Conference & Exhibition*, December 2002.
- [51] Mears, A. P. and Crossland, S. C. and Dominy, R. G., “An Investigation into the Flow-Field About an Exposed Racing Wheel,” *SAE 2004 World Congress & Exhibition*, March 2004.
- [52] J. V. Cánovas and A. F. Antoniadis, “Computational modelling of a solid and deformed automotive rotating wheel in contact with the ground,” *Proceedings of the Institution of Mechanical Engineers, Part D: Journal of Automobile Engineering*, vol. 234, no. 5, pp. 1413–1424, 2020.
- [53] J. McManus and X. Zhang, “A Computational Study of the Flow Around an Isolated Wheel in Contact With the Ground,” *Journal of Fluids Engineering*, vol. 128, pp. 520–530, 10 2005.
- [54] P. Dassanayake, D. Ramachandran, L. Salati, T. Barber, and G. Doig, “Unsteady computational simulation of the flow structure of an isolated wheel in contact with the ground,” 2012.
- [55] A. Cogotti, “Aerodynamic Characteristics of Car Wheels,” *International Journal of Vehicle Design*, p. 173196, 1983.
- [56] E. Mercker and H. Berneburg, “On the simulation of road driving of a passenger car in a wind tunnel using a moving belt and rotating wheels,” vol. 1, p. 992, 1992.
- [57] Bearman, P. W. and de Beer, D. and Hamidy, E. and Harvey, J.K., “The Effect of a Moving Floor on Wind Tunnel Simulation of Road Vehicles,” *Society of Automotive Engineers*, 1988.
- [58] A. J. Saddington, R. D. Knowles, and K. Knowles, “Laser Doppler anemometry measurements in the near-wake of an isolated Formula One wheel,” *Experiments in Fluids*, vol. 42, pp. 671–681, may 2007.
- [59] D. Patel, A. Garmory, and M. Passmore, “On the wake of an isolated rotating wheel: An experimental and numerical investigation,” *Journal of Wind Engineering and Industrial Aerodynamics*, vol. 227, p. 105049, 2022.
- [60] J. Axerio and G. Iaccarino, “Asymmetries in the wake structure of a formula 1 tire,” 2009.


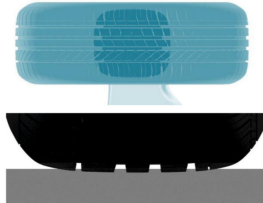
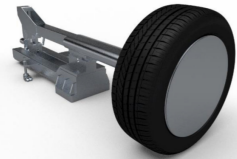

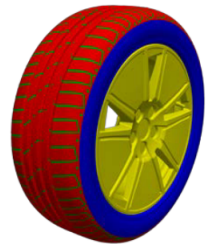
- [61] J. Heyder-Bruckner, *The aerodynamics of an inverted wing and a rotating wheel in ground effect*. PhD thesis, University of Southampton, 2011.
- [62] R. Knowles, A. Saddington, and K. Knowles, “On the near wake of rotating, 40%-scale Champ Car wheels,” *SAE Transactions*, pp. 2245–2253, 2002.
- [63] A. Wäschle, “The Influence of Rotating Wheels on Vehicle Aerodynamics - Numerical and Experimental Investigations,” *SAE World Congress & Exhibition*, April 2007.
- [64] E. Croner, H. Bézard, C. Sicot, and G. Mothay, “Aerodynamic characterization of the wake of an isolated rolling wheel,” *International Journal of Heat and Fluid Flow*, vol. 43, pp. 233–243, 2013.
- [65] T. Hobeika, S. Sebben, and L. Lofdahl, “Study of different tyre simulation methods and effects on passenger car aerodynamics,” *The International Vehicle Aerodynamics Conference*, 2014.
- [66] J. Reiß, L. Haag, and T. Indinger, “CFD investigation on fully detailed and deformed car tires,” *International Journal of Automotive Engineering*, vol. 10, pp. 324–331, 11 2019.
- [67] J. Reiß, J. Sebald, T. Indinger, L. Haag, and V. Zander, “Experimental and Numerical Investigations on Isolated, Treaded and Rotating Car Wheels,” apr 2020.
- [68] Zhou, Haichao and Jiang, Zhen and Wang, Guolin and Zhang, Shupe, “Aerodynamic Characteristics of Isolated Loaded Tires with Different Tread Patterns: Experiment and Simulation,” *Chinese Journal of Mechanical Engineering*, vol. 34, 12 2021.
- [69] C. Lew, N. Gopalaswamy, R. Shock, B. Duncan, and J. Hoch, “Aerodynamic Simulation of a Standalone Rotating Treaded Tire,” mar 2017.
- [70] T. Schütz, B. Schnepf, and T. Indinger, “Further Investigations on the Flow Around a Rotating, Isolated Wheel with Detailed Tread Pattern,” *SAE International Journal of Passenger Cars - Mechanical Systems*, vol. 8, pp. 261–274, apr 2015.
- [71] M. Mortazawy, R. Shock, D. Work, J. Sacco, and J. Hoch, “Aerodynamic Simulation of a Standalone Round and Deforming Treaded Tire,” *SAE International Journal of Advances and Current Practices in Mobility*, vol. 3, no. 2021-01-0948, pp. 2227–2235, 2021.
- [72] S. Diasinos, T. J. Barber, and G. Doig, “The effects of simplifications on isolated wheel aerodynamics,” *Journal of Wind Engineering and Industrial Aerodynamics*, vol. 146, pp. 90–101, 2015.
- [73] L. Axon, *The Aerodynamic Characteristics of Automobile Wheels CFD Prediction and Wind Tunnel Experiment*. PhD thesis, 1999.
- [74] D. Wilcox, *Turbulence Modeling for CFD*. No. v. 1 in Turbulence Modeling for CFD, DCW Industries, 2006.
- [75] P. Spalart and S. Allmaras, “A one-equation turbulence model for aerodynamic flows,” 1992.
- [76] W. Jones and B. Launder, “The prediction of laminarization with a two-equation model of turbulence,” *International Journal of Heat and Mass Transfer*, vol. 15, no. 2, pp. 301–314, 1972.
- [77] T.-H. Shih, W. W. Liou, A. Shabbir, Z. Yang, and J. Zhu, “A new k- ϵ eddy viscosity model for high Reynolds number turbulent flows,” *Computers & Fluids*, vol. 24, no. 3, pp. 227–238, 1995.
- [78] F. R. Menter, “Two-equation eddy-viscosity turbulence models for engineering applications,” *AIAA Journal*, vol. 32, no. 8, pp. 1598–1605, 1994.
- [79] OpenFOAM, *User Guide - OpenFOAM*, December 2014.
- [80] F. Jureti, *User Guide - Cfmesh*, may 2015.




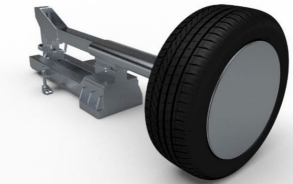
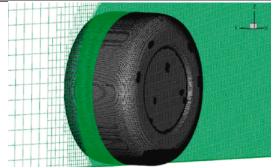
- [81] B. Rajani, A. Kandasamy, and S. Majumdar, "Numerical simulation of laminar flow past a circular cylinder," *Applied Mathematical Modelling*, vol. 33, no. 3, pp. 1228–1247, 2009.
- [82] A. Travin, M. Shur, M. Strelets, and P. Spalart, "Detached-eddy simulations past a circular cylinder," *Flow, turbulence and combustion*, vol. 63, no. 1, pp. 293–313, 2000.
- [83] P. Catalano, M. Wang, G. Iaccarino, and P. Moin, "Numerical simulation of the flow around a circular cylinder at high Reynolds numbers," *International Journal of Heat and Fluid Flow*, vol. 24, pp. 463–469, 2003.
- [84] M. C. Ong, T. Utnes, L. E. Holmedal, D. Myrhaug, and B. Pettersen, "Numerical simulation of flow around a smooth circular cylinder at very high Reynolds numbers," *Marine Structures*, vol. 22, no. 2, pp. 142–153, 2009.
- [85] R. Stringer, J. Zang, and A. Hillis, "Unsteady RANS computations of flow around a circular cylinder for a wide range of Reynolds numbers," *Ocean Engineering*, vol. 87, pp. 1–9, 2014.
- [86] F. Liu, "A thorough description of how wall functions are implemented in openfoam," *Proceedings of CFD with OpenSource Software*, vol. 34, 2016.
- [87] V. Kolář, "Vortex identification: New requirements and limitations," *International journal of heat and fluid flow*, vol. 28, no. 4, pp. 638–652, 2007.
- [88] S. Cyr, A. Wäschle, T. Kuthada, and J. Wiedemann, "Flow around an Isolated Wheel - Experimental and Numerical Comparison of Two CFD Codes," mar 2004.
- [89] P. Leśniewicz, M. Kulak, and M. Karczewski, "Aerodynamic analysis of an isolated vehicle wheel," vol. 530, no. 1, p. 012064, 2014.
- [90] L. Haag, T. Blacha, and T. Indinger, "Experimental Investigation on the Aerodynamics of Isolated Rotating Wheels and Evaluation of Wheel Rotation Models Using Unsteady CFD," *International Journal of Automotive Engineering*, vol. 8, pp. 7–14, 02 2017.
- [91] M. Soliman, A. El-Baz, M. Abdel-Aziz, N. Abdel-Aziz, O. Sugar-Gabor, *et al.*, "Numerical investigation of the effect of tread pattern on rotating wheel aerodynamics," *International Journal of Automotive and Mechanical Engineering*, vol. 17, no. 4, pp. 8234–8245, 2020.

Appendix

Table 1: Overview of numerical research performed in the literature

| Researcher(s) | year | method | model | Re_D | Rotation | Contact patch | Notes | Wheel |
|-------------------------|------|---------------------|---|-------------------|---|--|--|---|
| Axon et al. [73] | 1998 | RANS | RNG $k - \varepsilon$ | $5.3 \cdot 10^5$ | RWBC | Step approach verticals placed at 10° and 350° | <ul style="list-style-type: none"> simplified Fackrell "B2" $y^+ \approx 1$ ≈ 0.5 million cells FLUENT |  |
| Wäschle et al. [88] | 2004 | RANS URANS | RNG $k - \varepsilon$ (URANS) standard $k - \varepsilon$ with law of the wall (RANS) two layer model (RANS) | $5.37 \cdot 10^5$ | <ul style="list-style-type: none"> rim - MRF wheel surface - RWCB | Cut wheel at ground $\approx 1.5mm$ | <ul style="list-style-type: none"> Experiment EXA PowerFLOW (URANS) STAR-CD (RANS) ≈ 6.7 million cells (RANS) ≈ 17.8 million cells (URANS) URANS ($18 < y^+ < 120$) law of the wall ($30 < y^+ < 150$) two layer model ($y^+ < 3$) |  |
| McManus & Zhang [53] | 2006 | URANS | S-A RKE | $5.3 \cdot 10^5$ | RWBC | — | <ul style="list-style-type: none"> Fackrell "A2" wheel Smooth wheel $y^+ \approx 2.5$ 2.94 million cells |  |
| Dassanayake et al. [54] | 2012 | URANS DES LES | $k - \omega$ SST S-A DES WALE | $5.3 \cdot 10^5$ | RWBC | — | <ul style="list-style-type: none"> $y^+ < 1$ except contact $y^+ \approx 2.7$ 3.48 & 6.97 million cells FLUENT 13.0 | Fackrell "A2" |
| Croner et al. [64] | 2013 | URANS | $k - kL$ | $9.1 \cdot 10^5$ | RWBC | cutting wheel near ground (≈ 0.5 mm) | <ul style="list-style-type: none"> Experiment Smooth wheel $y^+ < 1$ Support modelled |  |

| Lesniewicz et al. [89] | 2014 | RANS | $k-\omega$ SST EARSM-CC (rotational reference frame) | $5.3 \cdot 10^5$ | RWCB MRF | Step size approach | <ul style="list-style-type: none">Grooved vs ungrooved studyANSYS CFX v.14.0 | Fackrell "A2" | | | | | | | | | | | | | | | | | | | | | | | | | | | | | | |
|------------------------|------|-----------------|--|------------------------|--|---|--|--|----|----|-----|----|----|-----|----|----|-----|----|----|-----|----|----|----|----|----|----|----|----|----|----|----|-----|----|----|-----|------------------|--|---|
| Diasinos et al. [72] | 2015 | RANS URANS | $k-\omega$ SST S-A RKE | $5.3 \cdot 10^5$ | RWBC | Step size: 0.0028D | <ul style="list-style-type: none">$y^+ < 1$ for attached flow8.06 million cellsANSYS FluentAlso no hub & constant R | Fackrell "A2" | | | | | | | | | | | | | | | | | | | | | | | | | | | | | | |
| Haag et al. [90] | 2016 | DDES | S-A | $7.4 \cdot 10^5$ | <ul style="list-style-type: none">Closed rim - RWBCOpen rim - SMRealistic rim - SM | Wheel intersects with ground by 0.001m | <ul style="list-style-type: none">ExperimentSupport modelledSpalding's LawOpenFOAM≈ 10 million cellssmallest cell edge length : 0.001172 m |  | | | | | | | | | | | | | | | | | | | | | | | | | | | | | | |
| Lew et al. [69] | 2017 | LBM | VLES | — | <ul style="list-style-type: none">rim - LRFwheel surface grooved - RWCBwheel surface treaded - IBM |  | <ul style="list-style-type: none">92 million cellssupport modelledexa PowerFLOW 5.4undeformed |  | | | | | | | | | | | | | | | | | | | | | | | | | | | | | | |
| Hobeika & Seben [12] | 2018 | IDDES | $k-\omega$ SST | $\approx 1 \cdot 10^4$ | <table><thead><tr><th>Wheel</th><th>Rim</th><th>Lateral grooves</th></tr></thead><tbody><tr><td>SM</td><td>SM</td><td>N/A</td></tr><tr><td>RW</td><td>SM</td><td>N/A</td></tr><tr><td>RW</td><td>RW</td><td>N/A</td></tr><tr><td>SM</td><td>RW</td><td>N/A</td></tr><tr><td>SM</td><td>SM</td><td>SM</td></tr><tr><td>RW</td><td>SM</td><td>RW</td></tr><tr><td>RW</td><td>RW</td><td>RW</td></tr><tr><td>RW</td><td>RW</td><td>MRF</td></tr><tr><td>RW</td><td>SM</td><td>MRF</td></tr></tbody></table> | Wheel | Rim | Lateral grooves | SM | SM | N/A | RW | SM | N/A | RW | RW | N/A | SM | RW | N/A | SM | SM | SM | RW | SM | RW | RW | RW | RW | RW | RW | MRF | RW | SM | MRF | 3D scanned wheel | <ul style="list-style-type: none">experimenttire deformed under load≈ 10 million cellsSTAR-CCM+ (v11.06)Wheel rotation models study |  |
| Wheel | Rim | Lateral grooves | | | | | | | | | | | | | | | | | | | | | | | | | | | | | | | | | | | | |
| SM | SM | N/A | | | | | | | | | | | | | | | | | | | | | | | | | | | | | | | | | | | | |
| RW | SM | N/A | | | | | | | | | | | | | | | | | | | | | | | | | | | | | | | | | | | | |
| RW | RW | N/A | | | | | | | | | | | | | | | | | | | | | | | | | | | | | | | | | | | | |
| SM | RW | N/A | | | | | | | | | | | | | | | | | | | | | | | | | | | | | | | | | | | | |
| SM | SM | SM | | | | | | | | | | | | | | | | | | | | | | | | | | | | | | | | | | | | |
| RW | SM | RW | | | | | | | | | | | | | | | | | | | | | | | | | | | | | | | | | | | | |
| RW | RW | RW | | | | | | | | | | | | | | | | | | | | | | | | | | | | | | | | | | | | |
| RW | RW | MRF | | | | | | | | | | | | | | | | | | | | | | | | | | | | | | | | | | | | |
| RW | SM | MRF | | | | | | | | | | | | | | | | | | | | | | | | | | | | | | | | | | | | |
| Reiß et al. [66] | 2019 | DDES | S-A Smagorinsky | $7.1 \cdot 10^5$ | <ul style="list-style-type: none">rim - SMtire shoulder - RWCBtire tread - RWCBlateral grooves - MRF | Wheel is scanned | <ul style="list-style-type: none">Spalding's Lawdetailed and deformed car tires studyOpenFOAM v1712+≈ 19 million cellssmallest cell edge length : 0.00075 m |  | | | | | | | | | | | | | | | | | | | | | | | | | | | | | | |

| | | | | | | | | |
|-----------------------|------|-------|------------------|-------------------|--|--|---|---|
| Reiß et al. [67] | 2020 | DDES | S-A Smagorinsky | — | <ul style="list-style-type: none"> rim - SM tire shoulder - RWCB tire tread - RWCB lateral grooves - MRF | Wheel model is scanned Contact patch slightly adjusted to match flat ground | <ul style="list-style-type: none"> Spalding's Law $u_\infty = 38.889$ m/s Wheel under load OpenFOAM v1712+ ≈ 38 million cells smallest cell edge length : 0.00075 m |  |
| Soliman et al. [91] | 2020 | RANS | RKE | $6.8 \cdot 10^5$ | MRF | Step size approach | <ul style="list-style-type: none"> Effect of tread pattern study $25 < y^+ < 300$ standard wall function ANSYS Fluent |  |
| Mortazawy et al. [71] | 2021 | LBM | VLES | — | IBM |  | <ul style="list-style-type: none"> 88 million cells support modelled PowerFLOW deformed |  |
| Patel et al. [59] | 2022 | IDDES | $k - \omega$ SST | $9.83 \cdot 10^5$ | RWBC | Step size: 0.1 mm | <ul style="list-style-type: none"> Wake study Smooth wheel $y^+ < 1$ 23 million cells Siemens STAR-CCM+ |  |